

IMPROVED TECHNIQUES  
FOR FLUID DIVERSION IN OIL RECOVERY

Final Report

By  
R. Seright

January 1996

Performed Under Contract No. DE-AC22-92BC14880

New Mexico Institute of Mining and Technology  
Socorro, New Mexico



**National Petroleum Technology Office**  
**U. S. DEPARTMENT OF ENERGY**  
**Tulsa, Oklahoma**

#### DISCLAIMER

This report was prepared as an account of work sponsored by an agency of the United States Government. Neither the United States Government nor any agency thereof, nor any of their employees, makes any warranty, expressed or implied, or assumes any legal liability or responsibility for the accuracy, completeness, or usefulness of any information, apparatus, product, or process disclosed, or represents that its use would not infringe privately owned rights. Reference herein to any specific commercial product, process, or service by trade name, trademark, manufacturer, or otherwise does not necessarily constitute or imply its endorsement, recommendation, or favoring by the United States Government or any agency thereof. The views and opinions of authors expressed herein do not necessarily state or reflect those of the United States Government.

This report has been reproduced directly from the best available copy.

Available to DOE and DOE contractors from the Office of Scientific and Technical Information, P.O. Box 62, Oak Ridge, TN 37831; prices available from (615) 576-8401.

Available to the public from the National Technical Information Service, U.S. Department of Commerce, 5285 Port Royal Rd., Springfield VA 22161

DOE/BC/14880-15  
Distribution Category UC-122

Improved Techniques  
for Fluid Diversion in Oil Recovery

Final Report

By  
R. Seright

January 1996

Work Performed Under Contract No. DE-AC22-92BC14880

Prepared for  
U.S. Department of Energy  
Assistant Secretary for Fossil Energy

Jerry Casteel, Project Manager  
Bartlesville Project Office  
P.O. Box 1398  
Bartlesville, OK 74005

Prepared by  
New Mexico Institute of Mining and Technology  
801 Leroy Place  
Socorro, NM 87801

## ABSTRACT

This report describes work performed during the third and final year of the project, "Improved Techniques for Fluid Diversion in Oil Recovery." This project was directed at reducing water production and increasing oil recovery efficiency. In the United States, more than 20 billion barrels of water are produced each year during oilfield operations. An average of 7 barrels of water are produced for each barrel of oil. Today, the cost of water disposal is typically between \$0.25 and \$0.50 per bbl. Therefore, there is a tremendous economic incentive to reduce water production if that can be accomplished without sacrificing hydrocarbon production. Environmental considerations also provide a significant incentive to reduce water production during oilfield operations.

This three-year project had two technical objectives. The first objective was to compare the effectiveness of gels in fluid diversion (water shutoff) with those of other types of processes. Several different types of fluid-diversion processes were compared, including those using gels, foams, emulsions, particulates, and microorganisms. The ultimate goals of these comparisons were to (1) establish which of these processes are most effective in a given application and (2) determine whether aspects of one process can be combined with those of other processes to improve performance. Analyses and experiments were performed to verify which materials are the most effective in entering and blocking high-permeability zones.

The second objective of the project was to identify the mechanisms by which materials (particularly gels) selectively reduce permeability to water more than to oil. A capacity to reduce water permeability much more than oil or gas permeability is critical to the success of gel treatments in production wells if zones cannot be isolated during gel placement.

Topics covered in this report include (1) determination of gel properties in fractures, (2) investigation of schemes to optimize gel placement in fractured systems, (3) an investigation of why some polymers and gels can reduce water permeability more than oil permeability, (4) consideration of whether microorganisms and particulates can exhibit placement properties that are superior to those of gels, and (5) examination of when foams may show placement properties that are superior to those of gels.

This project received financial support from the U.S. Department of Energy, the State of New Mexico, and a consortium of 10 oil companies. The technology developed in this project was transferred to the oil industry in several ways. First, project review meetings were held regularly, with 27 people from 13 organizations attending the most recent review (August 15-16, 1995). Second, technical progress reports were issued quarterly and annually. Third, papers were regularly presented at meetings of the Society of Petroleum Engineers (SPE) and were published in SPE and other journals (see Appendix F). Fourth, in conjunction with SPE's Distinguished Lecture Series, the presentation, "Cost-Effective Methods to Reduce Water Production," was given in 40 locations throughout the world.

## TABLE OF CONTENTS

ABSTRACT .....	iii
LIST OF FIGURES .....	ix
LIST OF TABLES .....	xv
ACKNOWLEDGEMENTS .....	xviii
EXECUTIVE SUMMARY .....	xix
1. INTRODUCTION .....	1
Project Objectives .....	1
Report Content .....	1
2. GEL PROPERTIES IN FRACTURES .....	3
Desired Gel Placement Locations .....	4
Core Characterization .....	5
Core Preparation .....	5
Correlation of Fracture Width and Permeability .....	7
Behavior of Freshly Prepared Gelants in Fractures .....	8
Resorcinol-Formaldehyde .....	9
Cr(III)-Acetate-HPAM with 1% NaCl .....	15
Cr(III)-Acetate-HPAM with 1% NaCl and 0.1% CaCl <sub>2</sub> .....	16
Summary of Previous Results During Injection of Preformed Gels into Fractures .....	18
Effect of Curing Time on Gel Extrusion Through Fractures .....	23
Gel Resistance Factors in Longer Fractures .....	25
Effect of Fracture Conductivity on Gel Extrusion Through Fractures .....	30
Effect of Gel in Fractures on Oil Flow Versus Water Flow .....	33
A Comparison of the Placement Properties of Preformed Gels and Water-Like Gelants .....	38
Fracture Model .....	38
Assumptions .....	39
Effects of Differences in Fracture Permeability and Gel Resistance Factor .....	39
Effect of Differences in Fracture Length .....	41
Effect of Differences in Gel Propagation Delay Factor .....	42
Conclusions .....	43
Conclusions from Experimental Study of Gelants in Fractures. ....	43
Conclusions from Experimental Study of Preformed Cr(III)-Acetate-HPAM Gels in Fractures. ....	44
Conclusions from Analytical Study .....	44

3. EXAMINATION OF SOME SCHEMES TO AID GEL PLACEMENT IN FRACTURES . . . . .	45
Injection of Mechanically Degraded Cr(III)-Acetate-HPAM Gels . . . . .	45
Results in a Short Fractured Core . . . . .	45
Results in a Long Fractured Core . . . . .	47
Effect of Shearing Time . . . . .	50
Injection of Cr(III) After Placement of a Mechanically Degraded Cr(III)-Acetate-HPAM Gel . . . . .	53
Injection of Cr(III) After Placement of a Hydroquinone-Hexamethylenetetramine-HPAM Gel . . . . .	54
Injection of Cr(III) After Placement of an HPAM Water-in-Oil Emulsion . . . . .	56
Conclusions . . . . .	61
4. DISPROPORTIONATE PERMEABILITY REDUCTION . . . . .	62
Water Shutoff Using Polymers Without Crosslinkers . . . . .	62
Possible Mechanisms for Disproportionate Permeability Reduction . . . . .	65
Segregated Oil and Water Pathways . . . . .	65
Experiments with an Oil-Based Gel . . . . .	65
Experiments with a Water-Based Gel . . . . .	67
Effects of Interfacial Tension and Gel Elasticity on Disproportionate Permeability Reduction . . . . .	68
Filtration Experiments . . . . .	68
Micromodel Experiments . . . . .	70
Disproportionate Permeability Reduction by a Gelled Foam . . . . .	72
First Foam Experiment . . . . .	72
Second Foam Experiment . . . . .	74
NMR Imaging Experiments . . . . .	77
Core and Fluids . . . . .	77
Experimental Procedure . . . . .	80
Screening Experiments . . . . .	80
Imaging Experiments . . . . .	82
Conclusions . . . . .	89
5. USE OF MICROORGANISMS AS BLOCKING AGENTS . . . . .	90
Selective Plugging Using Microorganisms . . . . .	90
Selective Plugging Using Spores. . . . .	90
Selective Plugging Using Ultramicrobacteria . . . . .	91
Selective Plugging in Heavy Oil Reservoirs . . . . .	94
Selective Plugging Using Indigenous Bacteria . . . . .	94
Selective Plugging by In Situ Polymer Production . . . . .	95
Simulation Study of Selective Plugging by Sequential Injection . . . . .	95
Summary. . . . .	95
Selective Placement with Rod-Shaped Microorganisms . . . . .	96

In-Depth Placement . . . . .	101
In Situ Gelation of Exopolymer . . . . .	101
Microorganism-Induced Precipitation . . . . .	101
Sequential Nutrient Injection . . . . .	101
Microencapsulation of Nutrients . . . . .	102
Permeability Reduction by Microorganisms . . . . .	102
Summary . . . . .	104
Conclusions . . . . .	104
6. EFFECTS OF PORE SIZE DISTRIBUTION ON SELECTIVE GELANT PLACEMENT USING PARTICULATES . . . . .	105
Theoretical Model . . . . .	109
Effects of Pore Size Distribution on Selective Gelant Placement Using Particulates . . . . .	109
Monodisperse Particulates . . . . .	110
Particulates with a Size Distribution . . . . .	110
Conclusions . . . . .	113
7. USE OF FOAMS AS BLOCKING AGENTS . . . . .	115
Apparatus and Experimental Procedure . . . . .	116
Coreflood Equipment . . . . .	116
Brine and Surfactant Solution . . . . .	116
Core Preparation . . . . .	116
General Experimental Procedure . . . . .	116
Cores Used . . . . .	118
Effects of Permeability, Fluid Velocity, and Foam Quality on Nitrogen-Foam Rheology . . . . .	119
Results Using the 899-, 482-, and 80-md Berea Sandstone Cores. . . . .	119
Results Using the 7.5-md Indiana Limestone Core . . . . .	119
Power-Law Correlations for Foam Rheology . . . . .	119
Implications for Selective Fluid Diversion . . . . .	127
Parameters Affecting Foam Persistence During Brine Injection . . . . .	131
Effects of Brine Velocity and Throughput . . . . .	131
Other Parameters Affecting Nitrogen-Foam Persistence . . . . .	135
Discussion of Foam Persistence During Brine Injection . . . . .	137
Comparison With Gel Treatments . . . . .	140
Placement of Foam Versus Placement of a Water-Like Gelant . . . . .	140
Relative Injectivity Losses After Foam Placement . . . . .	142
Conclusions . . . . .	144
NOMENCLATURE . . . . .	146
REFERENCES . . . . .	149

APPENDIX A	
Derivation of Eq. 5 . . . . .	157
APPENDIX B	
Data Supplement for Chapter 4 . . . . .	160
APPENDIX C	
Supplement to Chapter 7: CO <sub>2</sub> -Foam Results . . . . .	167
APPENDIX D	
Supplement to Chapter 7: Results from Tracer Studies . . . . .	174
APPENDIX E	
Supplement to Chapter 7: The Effect of Shut-In on the Residual Resistance Factor . .	189
APPENDIX F	
Technology Transfer . . . . .	191

## LIST OF FIGURES

Fig. 1. Fractures can enhance or harm oil production. . . . .	3
Fig. 2. Idealized placement locations for gels in fractures. . . . .	4
Fig. 3. Schematic of a fractured core. . . . .	6
Fig. 4. Tracer results for unfractured and fractured short (14.5-cm) and long (115-cm) Berea sandstone cores (no gel present). . . . .	6
Fig. 5. Correlation of fracture width with fracture permeability. . . . .	8
Fig. 6. Tracer results for Short Fractured Core 1: resorcinol-formaldehyde gel (placed as gelant). . . . .	9
Fig. 7. Tracer results for Short Fractured Core 3: Cr(III)-acetate-HPAM gel (placed as gelant). . . . .	9
Fig. 8. Apparent brine mobility versus PV for Long Fractured Core 6 with resorcinol-formaldehyde gel (placed as a gelant). . . . .	11
Fig. 9. Apparent brine mobility versus injection rate for Long Fractured Core 6 with resorcinol-formaldehyde (placed as a gelant). . . . .	12
Fig. 10. Tracer results for Long Fractured Core 6 with resorcinol-formaldehyde gel (placed as a gelant). . . . .	14
Fig. 11. Tracer results for Long Fractured Core 7 with Cr(III)-acetate-HPAM gel (placed as a gelant, 1% NaCl brine). . . . .	16
Fig. 12. Tracer results for Long Fractured Core 8 with Cr(III)-acetate-HPAM gel (placed as a gelant; brine: 1% NaCl, 0.1% CaCl <sub>2</sub> ). . . . .	18
Fig. 13. Tracer results before versus after placement of a 24-hr-old Cr(III)-acetate-HPAM gel in Short Fractured Core 7. . . . .	19
Fig. 14. Apparent mobility before, during, and after placement of a 24-hr-old Cr(III)- acetate-HPAM gel in Short Fractured Core 7. . . . .	20
Fig. 15. Resistance factors in Short Fractured Core 8 during placement of a Cr(III)-acetate- HPAM gel. . . . .	21

Fig. 16. Pressure gradients in Short Fractured Core 8 during placement of a Cr(III)-acetate-HPAM gel. . . . .	21
Fig. 17. Residual resistance factor versus pressure gradient after gel placement in Short Fractured Cores 5 and 6. . . . .	23
Fig. 18. Effect of gel curing time on extrusion through a single fracture. . . . .	25
Fig. 19. Gel injection into a 115-cm-long fractured core. . . . .	27
Fig. 20. Propagation of Cr(III)-acetate-HPAM gels through long fractured cores. . . . .	28
Fig. 21. The rate of gel propagation decreases as the gel penetrates deeper into the fracture. . . . .	29
Fig. 22. Effect of fracture conductivity on resistance factors for a 24-hr-old Cr(III)-acetate-HPAM gel. . . . .	30
Fig. 23. Effect of fracture conductivity on pressure gradients during injection of a 24-hr-old Cr(III)-acetate-HPAM gel. . . . .	31
Fig. 24. Resistance factor versus fracture permeability. . . . .	32
Fig. 25. Resistance factor versus fracture width. . . . .	33
Fig. 26. Tracer results before versus after placement of a 24-hr-old Cr(III)-acetate-HPAM gel in Short Fractured Core 41. . . . .	35
Fig. 27. Tracer results during brine injection after gel placement in Short Fractured Core 41 for several cycles of water/oil injection. . . . .	36
Fig. 28. Tracer results during oil injection after gel placement in Short Fractured Core 41 for several cycles of water/oil injection. . . . .	37
Fig. 29. Schematic of an injector-producer pair connected by two fractures. . . . .	38
Fig. 30. Gelants with water-like viscosities provide more favorable placement properties than preformed gels. . . . .	40
Fig. 31. Placement for preformed gels is insensitive to the fracture length ratio. . . . .	42
Fig. 32. $L_{p2}/L_{p1}$ is insensitive to the rate of gel propagation unless these rates are radically different in different fractures. . . . .	43

Fig. 33. Resistance factors and pressure gradients during placement of a sheared Cr(III)-acetate-HPAM gel in Short Fractured Core 21. . . . .	46
Fig. 34. Tracer results before versus after placement of a sheared Cr(III)-acetate-HPAM gel in Short Fractured Core 21. . . . .	47
Fig. 35. Resistance factors during gel injection into Long Fractured Core 3. . . . .	48
Fig. 36. Effluent viscosities during gel injection into Long Fractured Core 3. . . . .	49
Fig. 37. Effluent chromium concentrations during gel injection into Long Fractured Core 3 . . . . .	49
Fig. 38. Resistance factors during injection of sheared Cr(III)-acetate-HPAM gels into Short Fractured Core 33. . . . .	51
Fig. 39. Tracer results before versus after gel placement in Short Fractured Core 33. . . . .	52
Fig. 40. Resistance factors and pressure gradients during injection of a mechanically degraded Cr(III)-acetate-HPAM gel into Short Fractured Core 34. . . . .	53
Fig. 41. Tracer results before versus after gel placement in Short Fractured Core 34. . . . .	54
Fig. 42. Resistance factors and pressure gradients during injection of gel, Cr(III)-chloride solution, and brine into Short Fractured Core 35. . . . .	55
Fig. 43. Tracer results before versus after gel placement in Short Fractured Core 35. . . . .	56
Fig. 44. Viscosity versus shear rate for HPAM water-in-oil emulsion. . . . .	57
Fig. 45. Tracer results before and after placement of a crosslinked HPAM emulsion in Short Fractured Core 38. . . . .	59
Fig. 46. Tracer results before and after placement of a crosslinked HPAM emulsion in Short Fractured Core 40. . . . .	60
Fig. 47. Disproportionate permeability reduction by polymers and gels. . . . .	63
Fig. 48. Segregated oil and water pathways. . . . .	66
Fig. 49. Schematic of glass-filter experiments. . . . .	69
Fig. 50. Effect of interfacial tension on disproportionate permeability reduction. . . . .	71

Fig. 51. Brine residual resistance factor versus rate (after foam placement in Core 67). . . . 73

Fig. 52. Tracer results before and after foam placement in Core 67. . . . . 74

Fig. 53. Apparent rheology during oil and water injection. . . . . 75

Fig. 54. Tracer results before and after foam placement in Core 68. . . . . 76

Fig. 55. Image of a glass-bead core using Back-Scatter-Electron Imaging  
(low magnification). . . . . 78

Fig. 56. Image of a glass-bead core using Back-Scatter-Electron Imaging  
(high magnification). . . . . 79

Fig. 57. Core orientation during NMR imaging experiments. . . . . 83

Fig. 58. Image of the brine distribution at  $S_w = 1$ . . . . . 85

Fig. 59. Image of the oil distribution at  $S_{wr}$ . . . . . 86

Fig. 60. Image of the brine distribution after  $F_{rrw}$  measurement. . . . . 87

Fig. 61. Image of the oil distribution after  $F_{rro}$  measurement. . . . . 88

Fig. 62. Selective plugging using spores with crossflow between layers. . . . . 92

Fig. 63. Cumulative frequency plot of effective particle size for rod-shaped bacteria. . . . . 97

Fig. 64. Effect of aspect ratio of rod-shaped bacteria on selective placement . . . . . 99

Fig. 65. Effect of permeability contrast on maximum allowable aspect ratio  
of rod-shaped bacteria for selective placement. . . . . 100

Fig. 66. Effect of particle size on the degree of gelant penetration for particulates  
with a monodisperse size in porous rock with single pore sizes. . . . . 106

Fig. 67. Effect of standard deviation of particle size distribution on the degree  
of gelant penetration in porous rock with single pore size. . . . . 107

Fig. 68. Effect of permeability contrast on the maximum standard deviation  
of particle size distribution for a given selectivity. . . . . 108

Fig. 69. Effect of pore size distribution on placement of a water-like gelant with particulates having a monodisperse size. . . . .	111
Fig. 70. Effect of pore size distribution on placement of a water-like gelant with particulates having a normal size distribution. . . . .	112
Fig. 71. Effect of particle size distribution on placement of a water-like gelant in porous media with pore size distributions. . . . .	114
Fig. 72. Schematic of the foam coreflood equipment. . . . .	117
Fig. 73. Effect of quality on foam rheology, $k=899$ md. . . . .	120
Fig. 74. Effect of quality on foam rheology. $k=482$ md. . . . .	121
Fig. 75. Effect of quality on foam rheology. $k=80$ md. . . . .	122
Fig. 76. Effect of quality on foam rheology. $k=7.5$ md. . . . .	123
Fig. 77. Comparison of foam flow and two-phase flow. 50% quality foam. . . . .	124
Fig. 78. Comparison of foam flow and two-phase flow. 95% quality foam. . . . .	125
Fig. 79. Variation of foam mobility with permeability. 1.6 ft/d. . . . .	128
Fig. 80. Variation of foam mobility with permeability. 8 ft/d. . . . .	129
Fig. 81. Variation of foam mobility with permeability. 40 ft/d. . . . .	130
Fig. 82. Effects of brine throughput and velocity on foam persistence. 482 md . . . . .	132
Fig. 83. Effects of brine throughput and velocity on foam persistence. 899 md. . . . .	133
Fig. 84. Effects of brine throughput and velocity on foam persistence. 80 md. . . . .	134
Fig. 85. Factors affecting foam persistence. . . . .	136
Fig. 86. Effect of permeability on foam persistence. . . . .	138
Fig. 87. Relative permeability curve from tracer and residual resistance factor data. . . . .	139
Fig. C-1. CO <sub>2</sub> -foam generation. First set of experiments. . . . .	168

Fig. C-2. CO <sub>2</sub> -foam generation. Second set of experiments. . . . .	168
Fig. C-3. CO <sub>2</sub> -foam rheology. . . . .	169
Fig. C-4. Reproducibility of CO <sub>2</sub> -foam generation. . . . .	171
Fig. C-5. Effect of rate and throughput on CO <sub>2</sub> -foam mobilities. . . . .	171
Fig. C-6. Mobility versus velocity for nitrogen and carbon-dioxide foams. . . . .	172
Fig. D-1. Tracer results in the 899-md core, 40 ml/hr. . . . .	176
Fig. D-2. Tracer results in the 899-md core, various rates. . . . .	177
Fig. D-3. Tracer results in the 482-md core, 40 ml/hr. . . . .	180
Fig. D-4. Tracer results in the 482-md core, 100 ml/hr. . . . .	180
Fig. D-5. Tracer results in the 80-md core, 40 ml/hr. . . . .	182
Fig. D-6. Tracer results in the 80-md core, various rates. . . . .	182
Fig. D-7. Tracer results in the 7.5-md core, 40 ml/hr. . . . .	184
Fig. D-8. Tracer results in the 7.5-md core, 100 ml/hr. . . . .	184
Fig. D-9. Apparent foam viscosity in Berea cores. . . . .	186

## LIST OF TABLES

Table 1.	Properties of Long Fractured Core 6 . . . . .	10
Table 2.	Plugging 122-cm Fractures with Gels Formed In Situ from Gelants . . . . .	13
Table 3.	Properties of Long Fractured Core 7 . . . . .	15
Table 4.	Properties of Long Fractured Core 8 . . . . .	17
Table 5.	Effect of Gel Curing on Resistance Factors for Cr(III)-Acetate-HPAM Gels in 14-15-cm Fractures . . . . .	24
Table 6.	Properties of Long Fractured Core 1 . . . . .	26
Table 7.	Fracture Widths and Permeabilities from Eq. 2 . . . . .	31
Table 8.	In Fractures, Gels Can Prevent Flow of Both Water and Oil . . . . .	34
Table 9.	Properties of Long Fractured Core 3 . . . . .	48
Table 10.	Viscosities of Sheared Gels Before and After Being Forced Through Short Fractured Core 33 . . . . .	50
Table 11.	Properties of 14.5-cm Cores Used in HPAM Emulsion Experiments . . . . .	57
Table 12.	Sequences Followed During Experiments with HPAM Emulsions . . . . .	58
Table 13.	Summary of Results of Experiments with HPAM Emulsions . . . . .	58
Table 14.	Summary of $F_{rro}$ and $F_{rrw}$ for Polymers Without Crosslinkers . . . . .	64
Table 15.	Summary of $F_{rro}$ and $F_{rrw}$ For an Oil-Based Gel . . . . .	67
Table 16.	Summary of $F_{rro}$ and $F_{rrw}$ For a Water-Based Gel . . . . .	68
Table 17.	Residual Resistance Factors During Oil or Brine Injection at 15.8 ft/d . . . . .	73
Table 18.	Residual Resistance Factors During Oil or Brine Injection at 0.79 ft/d . . . . .	76
Table 19.	Summary of $F_{rrw}$ and $F_{rro}$ for Polymers in Fused Glass-Bead Cores . . . . .	81

Table 20.	Summary of $F_{rrw}$ and $F_{rro}$ for a HPAM Polymer in Fused Glass-Bead Cores . . . . .	81
Table 21.	Summary of $F_{rrw}$ and $F_{rro}$ for an Oil-Based Gel in Fused Glass-Bead Cores . . . . .	81
Table 22.	Summary of $F_{rrw}$ and $F_{rro}$ During NMR Imaging Experiments . . . . .	82
Table 23.	Parameters for Degree of Penetration Calculations . . . . .	98
Table 24.	Rock and Fluid Properties for Degree of Penetration Calculations . . . . .	109
Table 25.	General Experimental Procedure . . . . .	118
Table 26.	Properties of Cores Used . . . . .	118
Table 27.	Variation of Mobility With Darcy Velocity for Different $N_2$ -Foam Qualities . . . . .	119
Table 28.	Effect of Lithology on Foam Generation . . . . .	131
Table 29.	Effect of Different Factors on Residual Resistance Factors . . . . .	135
Table 30.	Gelant Placement Versus Foam Placement in Two-Layered Systems . . . . .	141
Table 31.	Profile Modification During Brine Injection After Foam Treatments in Two-Layered Systems (Radial Flow) . . . . .	144
Table B-1.	Summary of Endpoint Water and Oil Mobilities Before Treatment . . . . .	160
Table B-2.	Summary of Residual Resistance Factors ( $F_{rrw}$ , $F_{rro}$ )-Core SSL-100 . . . . .	163
Table C-1.	Comparison of $CO_2$ -Foam Mobilities . . . . .	170
Table C-2.	Brine $F_{rr}$ After $CO_2$ -Foam Generation . . . . .	173
Table D-1.	Sequence Followed During Tracer Studies . . . . .	174
Table D-2.	$F_{rr}$ Values Before and During Tracer Studies in the 899-md Core . . . . .	175
Table D-3.	Tracer Results in 899-md Core . . . . .	178
Table D-4.	$F_{rr}$ Values Before and During Tracer Studies in the 482-md Core . . . . .	178

Table D-5.	Tracer Results in 482-md Core . . . . .	179
Table D-6.	$F_{rr}$ Values Before and During Tracer Studies in the 80-md Core . . . . .	181
Table D-7.	Tracer Results in 80-md Core . . . . .	182
Table D-8.	Tracer Results in 7.5-md Core . . . . .	183
Table D-9.	Permeability Reduction During Foam Flow . . . . .	186
Table D-10.	Power-Law Parameters . . . . .	188
Table E-1.	Shut-In Effect . . . . .	189

## ACKNOWLEDGEMENTS

This work was financially supported by the United States Department of Energy, the State of New Mexico, Arco Exploration and Production Technology Co., British Petroleum Company, Chevron Petroleum Technology Co., Conoco Inc., Exxon Production Research Company, Marathon Oil Co., Mobil Research and Development Corp., Phillips Petroleum Co., Texaco Inc., and Unocal. This support is gratefully acknowledged. I greatly appreciate the efforts of those individuals who contributed to this project. Dr. Jenn-Tai Liang played the major role in the work described in Chapters 4, 5, and 6. Richard Schrader performed the experimental work described in Chapters 2 and 3. Hui Lin helped Richard during some of this work. John Hagstrom performed most of the experiments described in Chapter 4. The foam experiments in Chapter 4 were performed by Richard Schrader. The NMR imaging experiments (Chapter 4) were performed in collaboration with BDM-Oklahoma, Inc. (NIPER). I gratefully acknowledge BDM-Oklahoma, Inc., especially Dr. Daryl Doughty and Dr. Liviu Tomutsa, for performing the NMR imaging experiments. Dr. Hassan Nimir was principally responsible for the work described in Chapter 7. I especially appreciate the thorough review of this manuscript by Julie Ruff.

## EXECUTIVE SUMMARY

This report describes work performed during the project, "Improved Techniques for Fluid Diversion in Oil Recovery," with emphasis on the third and final year. This three-year project had two general objectives. The first objective was to compare the effectiveness of gels in fluid diversion with those of other types of processes. Several different types of fluid-diversion processes were compared, including those using gels, foams, emulsions, particulates, and microorganisms. The ultimate goals of these comparisons were to (1) establish which of these processes are most effective in a given application and (2) determine whether aspects of one process can be combined with those of other processes to improve performance. Analyses and experiments were performed to verify which materials are the most effective in entering and blocking high-permeability zones. The second objective of the project was to identify the mechanisms by which materials (particularly gels) selectively reduce permeability to water more than to oil.

### Gel Properties in Fractures

In Chapter 2 of this report, we examine the properties of gels in fractures. First, we consider idealized placement locations for gels in fractures. Second, we describe the fractured cores used in our experiments. Third, we characterize the behavior of gels formed in situ from gelants. Next, we describe how preformed gels behave in fractures as a function of injection rate, gel curing time, and fracture conductivity. Finally, these experimental results are used in a simple model to compare placement characteristics of preformed gels with those of gelants with water-like viscosities.

**Conclusions from Experimental Study of Gelants in Fractures.** The following conclusions were reached during experiments in three 122-cm-long fractured cores where approximately 2.5 fracture volumes of gelant were placed in the fractures:

1. A resorcinol-formaldehyde gelant with a water-like viscosity provided the best fracture healing of the three cases, but still did not completely heal the fracture. The gel formed from this gelant significantly damaged the first core section of a 122-cm fractured core, but healed the remaining four sections of the fracture fairly effectively.
2. A Cr(III)-acetate-HPAM gelant in a calcium brine (a) damaged the first core section of a 122-cm fractured core, (b) effectively reduced fracture conductivity in the second and third core sections, and (c) was ineffective in the fourth and fifth core sections.
3. A Cr(III)-acetate-HPAM gelant in a calcium-free brine may have effectively reduced fracture conductivity in the first core section, but was ineffective in the last four core sections.

**Conclusions from Experimental Study of Preformed Cr(III)-Acetate-HPAM Gels in Fractures.** The following conclusions were reached during experiments in fractured cores using a gel that contained 0.5% HPAM (Allied Colloids Alcoflood 935), 0.0417% Cr(III)-acetate, and 1% NaCl at pH=6 and 41°C: (The gelation time for this composition is 5 hrs at 41°C.)

1. Preformed gels can extrude through fractures without "screening out," but pressure gradients can be high, unless the fractures are very conductive.
2. Gels can effectively heal fractures with minimum leakoff.
3. Gels require a minimum pressure gradient for mobilization.
4. Gel resistance factors in fractures increase rapidly during the first 24 hours but increase more gradually during the next 200 hours.
5. Gels show flow-rate-independent residual resistance factors in fractures.
6. Gels dehydrate during extrusion through fractures, thus reducing the rate of gel propagation.
7. Gels can prevent flow of both oil and water in fractures.
8. Pressure gradients for gel extrusion vary inversely with fracture conductivity for low conductivities (e.g., < 1,100 D-cm) but are independent of conductivity in more-conductive fractures.

**Conclusions from Analytical Study.** The following conclusions were reached during an analytical study comparing the placement properties of preformed gels and water-like gelants in a simple two-fracture reservoir:

1. Generally, the ratio of the distance of gel penetration into Fracture 2 (a long, low-conductivity fracture) relative to that in Fracture 1 (a shorter, more-conductive fracture),  $L_{p2}/L_{p1}$ , is lowest for gelants with a water-like viscosity.
2. The experimentally observed variation of gel resistance factors (i.e., resistance factor increases with increasing fracture conductivity) may not aid gel placement.
3. For gels with high resistance factors,  $L_{p2}/L_{p1}$  is insensitive to differences in fracture length.
4. For gels or gelants with low resistance factors,  $L_{p2}/L_{p1}$  is very sensitive to differences in fracture length.
5.  $L_{p2}/L_{p1}$  is insensitive to the rate of gel propagation unless these rates are radically different in different fractures.

## **Examination of Some Schemes to Aid Gel Placement in Fractures**

Chapter 3 documents some of our early attempts to optimize gel placement in fractures. For the most part, these attempts were unsuccessful. We document these experiments here for the benefit of those who have wondered about the feasibility of these ideas. We investigated several schemes, including (1) injection of mechanically degraded Cr(III)-acetate-HPAM gels, (2) injection of mechanically degraded Cr(III)-acetate-HPAM gels, followed by injection of a CrCl<sub>3</sub> solution, (3) injection of a partially crosslinked hydroquinone-hexamethylenetetramine-HPAM gel, followed by a CrCl<sub>3</sub> solution, and (4) injection of an HPAM water-in-oil emulsion, preceded or followed by a CrCl<sub>3</sub> solution. We were not able to improve placement of gels in fractured cores using any of these methods. To optimize gel placement in fractured systems, many additional schemes remain to be investigated. This area will constitute an important part of our future research.

## **Disproportionate Permeability Reduction**

In Chapter 4, we attempt to determine the mechanism responsible for polymers and gels reducing the permeability to water more than that to oil. Our previous studies revealed that a capacity for blocking agents to reduce water permeability much more than oil permeability is critical to the success of water-shutoff treatments in production wells if zones cannot be isolated. Previously, we examined several possible mechanisms for this disproportionate permeability reduction. We demonstrated that the disproportionate permeability reduction is not caused by gravity or lubrication effects. Also, gel shrinking and swelling are unlikely to be responsible for this phenomenon. Our experimental results indicated that wettability may play a role that affects the disproportionate permeability reduction. Results from core experiments using an oil-based gel suggested that the disproportionate permeability reduction might be caused by oil and water following segregated pathways on a microscopic scale.

If the segregated-pathway mechanism is valid, we speculated that the disproportionate permeability reduction could be enhanced by simultaneously injecting oil with a water-based gelant or water with an oil-based gelant. For an oil-based gel, the disproportionate permeability reduction was enhanced by simultaneously injecting water with the oil-based gelant. However, simultaneously injecting oil with a water-based gelant did not result in a more pronounced disproportionate permeability reduction. This latter finding does not support the segregated-pathway mechanism.

Another mechanism that might be responsible for the disproportionate permeability reduction involves the interplay of gel elasticity and capillary forces. We propose new experiments to verify this theory. We speculate that the disproportionate permeability reduction should be reduced by lowering the oil/water interfacial tension (e.g., using a surfactant), and it should be enhanced by increasing gel elasticity (e.g., using a gelled foam). However, preliminary results using gelled foams did not support this mechanism.

Nuclear magnetic resonance (NMR) or magnetic resonance imaging (MRI) was used to observe the disproportionate permeability reduction on a microscopic scale. Preliminary results from NMR imaging experiments revealed that the technique had many limitations which prevented us from obtaining reliable pore-level images.

We also studied the feasibility of using polymers (no crosslinker) to reduce permeability to water without significantly damaging oil productivity. We examined two anionic polyacrylamide polymers (HPAM) and one cationic polyacrylamide (CPAM) polymers. These polymers suffered significant viscosity losses during the placement process. For the HPAM polymers, the residual resistance factors were low and no significant disproportionate permeability reduction was observed. The CPAM polymer reduced water permeability several times more than oil permeability. However, this polymer also caused a significant (seven-fold) reduction in oil permeability.

The mechanism responsible for the disproportionate permeability reduction remains unclear. Because of the importance of this effect, we will continue our studies in this area.

### **Use of Microorganisms as Blocking Agents**

In Chapter 5, we examine the use of microorganisms as blocking agents for fluid diversion. An extensive literature survey was conducted to determine if microorganisms can be superior to gels as blocking agents. Our literature survey revealed that selective plugging could be achieved if the nutrients or the microorganisms could be placed selectively into high-permeability thief zones. Since the flow properties of the nutrients are no different from those of gelants, their placement characteristics are similar to those of gelants. Specifically, for a given distance of penetration into a high-permeability zone, the distance of penetration into a less-permeable zone will be no less for the nutrient than for a gelant with a water-like mobility. If a viscous nutrient is used (e.g., molasses or corn syrup), nutrient penetration into less-permeable zones increases.

From one perspective, microorganisms could be viewed as particulates. Because of their narrow size distribution, certain microorganisms could, in concept, provide the advantageous placement characteristics associated with monodisperse particulates. A suspension of microorganisms could penetrate readily into a high-permeability zone, while size restrictions prevent them from entering less-permeable zones. However, most microorganisms are rod-shaped. The rod-shaped microorganisms act as particulates with a size distribution. Our theoretical analyses, based on Darcy's law and basic formation damage concepts, reveal that for a given permeability contrast, there is a maximum aspect ratio (length/diameter) that should not be exceeded for rod-shaped microorganisms to be more selective than a water-like gelant during placement. The maximum allowable aspect ratio for the rod-shaped microorganisms increases with increasing permeability contrast between high- and low-permeability zones. Maximum selectivity is achieved when the aspect ratio approaches one (i.e., near spherical). The placement characteristics of the uniformly sized, near-spherical microorganisms approach those of monodisperse particulates.

Another limiting factor when using microorganisms as blocking agents is near-wellbore plugging. Near-wellbore plugging can inhibit the in-depth placement of the biological materials in the formation. Therefore, growth, aggregation of microorganisms, and adsorption onto pore walls must be limited during placement.

Our literature survey showed that microorganisms small enough to penetrate a significant distance into a formation can cause serious formation damage. However, the literature is unclear about whether microorganisms can reduce permeability to a greater extent in high-permeability water zones than in low-permeability oil zones.

### **Effects of Pore Size Distribution on Selective Gelant Placement Using Particulates**

For particles that were suspended in a gelant, we previously used the concept of critical particle size to determine the degree of gelant penetration into formation rock. The critical-particle-size concept basically assumes that the rock has a single pore size. In reality, porous rock contains a range of pore sizes. Will the criteria for selective placement using particulates based on the single-pore-size model be too optimistic? To address this question (in Chapter 6), we assumed that the rock contains pores with normal size distributions. Our theoretical analyses indicated that selective gelant placement can be achieved in porous media with realistic pore size distributions using monodisperse particulates. The maximum allowable standard-deviation-to-mean-pore-size ratio for selective gelant placement was found to be more restrictive using particulates with a normal size distribution. Also, for a given permeability contrast, the particle size distribution does not necessarily need to be more narrow during gelant placement in rock with polydisperse pores than in rock with monodisperse pores. However, the gelant selectivity can be very sensitive to the mean and standard deviation of the particle size distribution.

### **Use of Foams as Blocking Agents**

Foams have been investigated extensively as mobility control agents—where sweep efficiency is improved by maximizing the distance of foam penetration into less-permeable, oil-productive zones. Much less work has been performed evaluating foams as blocking agents—where the objective is to maximize penetration and blocking action in high-permeability, watered-out zones while minimizing damage to oil zones. In Chapter 7, we examined whether the “limiting-capillary-pressure” concept can be exploited to aid placement of foam blocking agents. This determination required that foam mobilities be measured over a broader range of permeability and fluid velocity than previously reported. The results from our experimental studies were used during numerical analyses to establish whether foams can exhibit placement properties that are superior to those of gelants.

Using a C<sub>14-16</sub>  $\alpha$ -olefin sulfonate, we measured mobilities of a nitrogen foam in cores with permeabilities from 7.5 to 900 md (750 psi back pressure, 41°C) with foam qualities ranging from

50% to 95% and with injection rates (Darcy velocities) ranging from 0.5 to 100 ft/d. We also extensively studied the residual resistance factors provided during brine injection after foam placement. We confirmed the predictions of Khatib et al. that (1) no foam is formed in low-permeability rock (7.5 md in our case), (2) foam mobility generally decreases with increased permeability in rock with intermediate permeabilities (10 to 80 md), and (3) foam mobility increases with increased permeability in rock with high permeabilities (above 500 md). Using our experimental results and numerical analyses, we demonstrate that the foam could provide superior placement and permeability-reduction properties (compared with gels) if the offending thief zones have permeabilities of 80 md or greater and the oil zones have permeabilities less than 10 md. The foam will not be superior to gels if all zones have permeabilities that are 80 md or greater.

## 1. INTRODUCTION

In any oil recovery process, fractures and high-permeability streaks can cause early breakthrough of injected fluid and reduce oil recovery efficiency. They can also aggravate production of excess water or gas in reservoirs with water-drive or gas-drive recovery mechanisms. Several different types of processes have been proposed to reduce channeling of fluids through fractures and streaks of very high permeability. Processes that use crosslinked polymers or other types of gels have been most common. However, processes using emulsions, foams, suspended solids, precipitates, and microorganisms have also been proposed or tested. Although many of these fluid-diversion (or water or gas shutoff) projects have been very successful, many other projects have been technical failures. At present, there is no consensus on where or how the various treatments should be applied.

**Project Objectives.** This three-year project had two general objectives. The first objective was to compare the effectiveness of gels in fluid diversion with those of other types of processes. Several different types of fluid-diversion processes are being compared, including those using gels, foams, emulsions, and particulates. The ultimate goals of these comparisons were to (1) establish which of these processes are most effective in a given application and (2) determine whether aspects of one process can be combined with those of other processes to improve performance. Analyses and experiments were performed to verify which materials are the most effective in entering and blocking high-permeability zones. Another objective of the project was to identify the mechanisms by which materials (particularly gels) selectively reduce permeability to water more than to oil.

**Report Content.** This report describes work performed during the third year of the project. (Work performed during the first and second years of the project are documented in Refs. 1 and 2, respectively). In Chapter 2, we examine the properties of gels in fractures. Experiments were performed to compare the behavior of preformed gels with that of gels formed in situ from gelants. These experimental results were used in a simple model to compare placement characteristics of preformed gels with those of gelants with water-like viscosities.

In Chapter 3, we document some of our attempts to optimize gel placement in fractures. We investigated several schemes, including (1) injection of mechanically degraded Cr(III)-acetate-HPAM gels, (2) injection of mechanically degraded Cr(III)-acetate-HPAM gels, followed by injection of a  $\text{CrCl}_3$  solution, (3) injection of a partially crosslinked hydroquinone-hexamethylenetetramine-HPAM gel, followed by a  $\text{CrCl}_3$  solution, and (4) injection of an HPAM water-in-oil emulsion, preceded or followed by a  $\text{CrCl}_3$  solution.

In Chapter 4, we attempt to determine the mechanism responsible for polymers and gels reducing the permeability to water more than that to oil. Our previous studies revealed that a capacity for blocking agents to reduce water permeability much more than oil permeability is critical to the success of water-shutoff treatments in production wells if zones cannot be isolated. Previously, we examined several possible mechanisms for this disproportionate permeability reduction. We

demonstrated that the disproportionate permeability reduction is not caused by gravity or lubrication effects. Also, gel shrinking and swelling are unlikely to be responsible for this phenomenon. Our experimental results indicated that wettability may play a role that affects the disproportionate permeability reduction. Results from core experiments using an oil-based gel suggested that the disproportionate permeability reduction might be caused by oil and water following segregated pathways on a microscopic scale. In Chapter 4, we describe experiments to test whether the segregated-pathway mechanism is valid. We also consider another mechanism that involves the effects of oil/water interfacial tension and gel elasticity.

In Chapter 5, we examine the use of microorganisms as blocking agents for fluid diversion. An extensive literature survey was conducted to determine if microorganisms can be superior to gels as blocking agents. We focus on exploiting the narrow size distribution of microorganisms to maximize penetration into high-permeability zones while minimizing penetration into low-permeability zones. We also investigate (in Chapter 6) the effects of pore size distribution on selective gelant placement using particulates.

In Chapter 7, we examined whether the “limiting-capillary-pressure” concept can be exploited to aid placement of foam blocking agents. This determination required that foam mobilities be measured over a broader range of permeability and fluid velocity than previously reported. The results from our experimental studies were used during numerical analyses to establish whether foams can exhibit placement properties that are superior to those of gelants.

## 2. GEL PROPERTIES IN FRACTURES

Fractures can either enhance or harm oil production (see Fig. 1). With the proper length and orientation, fractures can increase water injectivity, oil productivity, and reservoir sweep efficiency.<sup>3-5</sup> On the other hand, with the wrong length and orientation, fractures can impair oil recovery. In waterfloods or enhanced recovery projects, fractures can cause injected fluids to channel through the reservoir. Also, when they extend out of the oil zone, fractures can aggravate production of water or gas. Crosslinked polymers and other gels have often been injected to correct these fracture problems.<sup>6-8</sup>

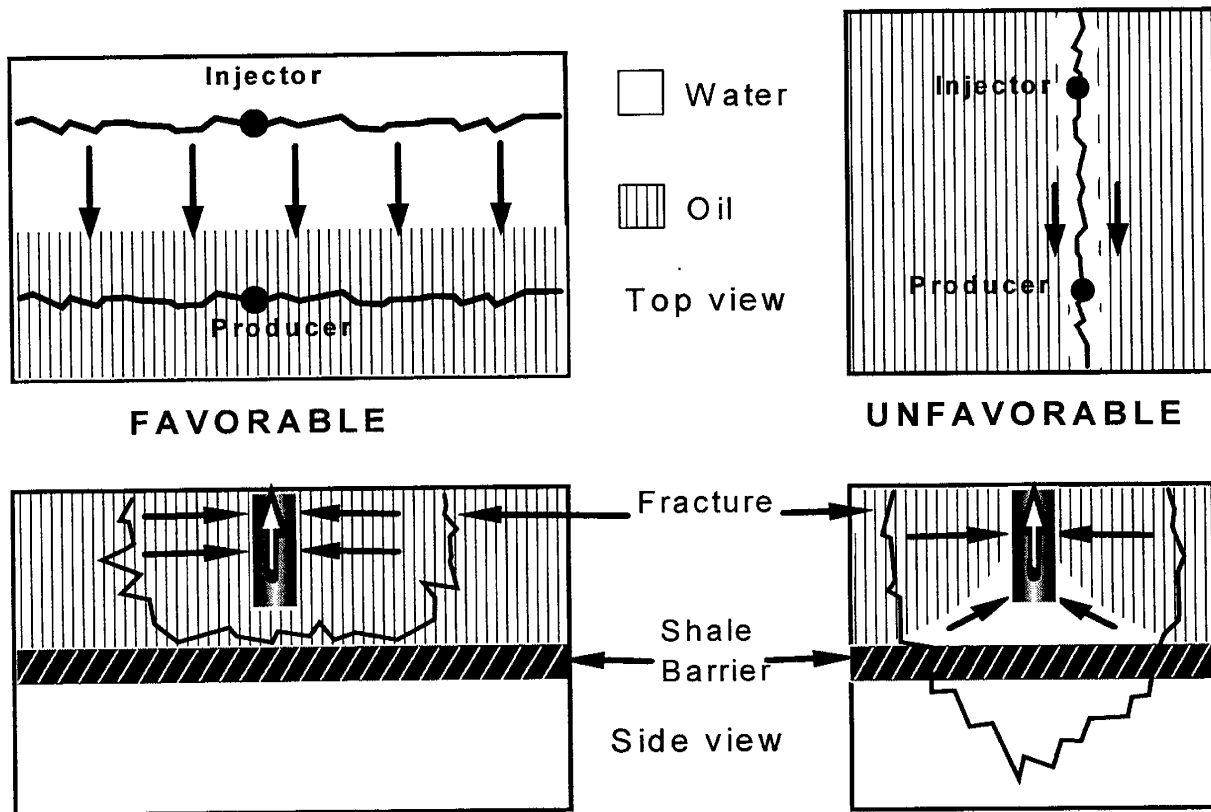


Fig. 1. Fractures can enhance or harm oil production.

In this chapter, we examine the properties of gels in fractures. First, we consider idealized placement locations for gels in fractures. Second, we describe the fractured cores used in our experiments. Third, we characterize the behavior of gels formed in situ from gelants. Next, we describe how preformed gels behave in fractures as a function of injection rate, gel curing time, and fracture conductivity. Finally, these experimental results are used in a simple model to compare placement characteristics of preformed gels with those of gelants with water-like viscosities.

## Desired Gel Placement Locations

Fig. 2 shows idealized placement locations for gels in fractures. First, consider a production well where water channels through a fracture from a nearby injection well (upper left part of Fig. 2). Ideally, the gel would be placed so that it plugs the fracture far from the wellbore, but leaves the fracture open near the well. In that way, water channeling through the fracture could be reduced while maintaining a high productivity for the well. If the gel plugs the near-wellbore portion of the fracture (in the lower left part of Fig. 2), it could reduce water channeling, but it might also reduce the productivity of the well to an unacceptably low level.

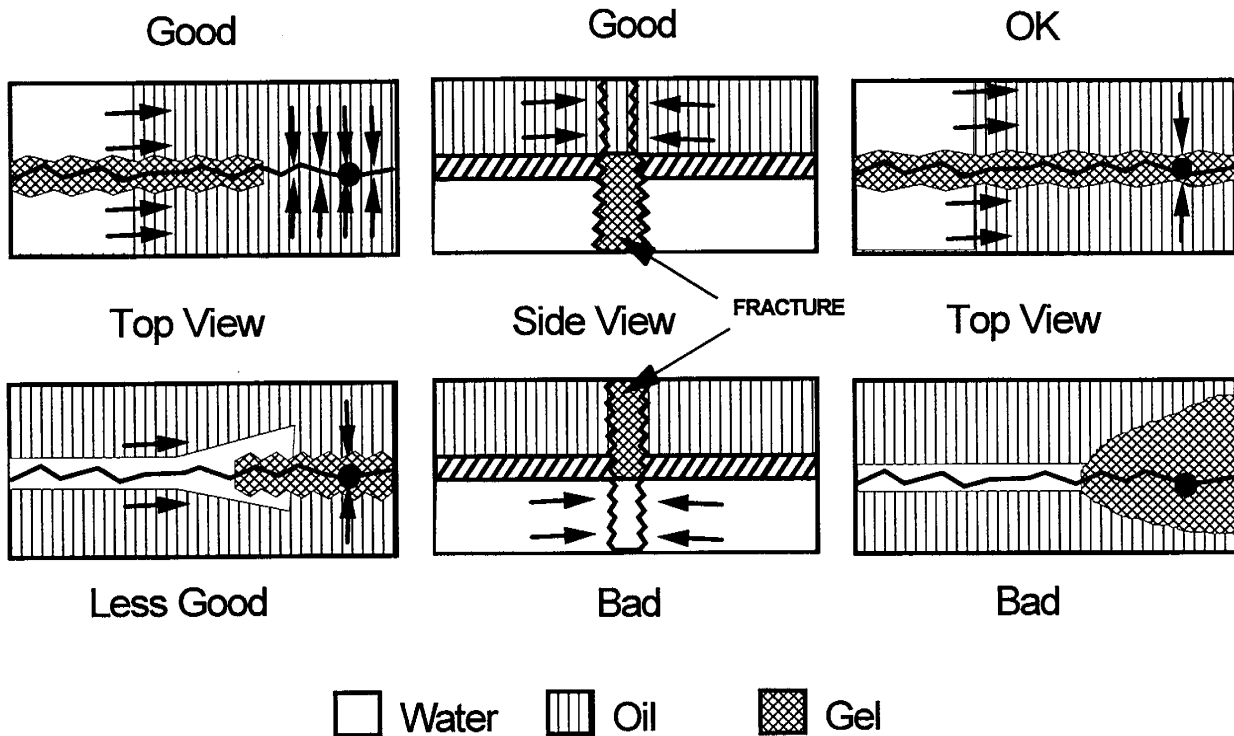


Fig. 2. Idealized placement locations for gels in fractures.

In vertical fractures that cut through multiple zones, we might want to exploit gravity and density differences to place gel in the lower part of a fracture, thereby reducing water influx from the lower zones while leaving the upper part of the fracture open to oil flow (center part of Fig. 2). In contrast, gel placement in the upper part of the fracture could be detrimental.

The amount of gelant that leaks off from a fracture face is also important (right side of Fig. 2). Ideally, the distance of gelant leakoff from the fracture face should be very small. If the leakoff distance is too great, then the near-wellbore region could be plugged, and the gel treatment could do more harm than good. A basic principle of fluid displacement in porous media is that the efficiency of the displacement increases with increasing viscosity of the injected fluid.<sup>9,10</sup> This principle suggests that other factors being equal in a fractured system, the distance of gelant

leakoff will be greater for a high-viscosity gelant than for a low-viscosity gelant. For gel treatments, this principle presents a potential problem for viscous gelants—that too much gelant may leak off from the fracture into the formation rock. So, leakoff associated with the use of viscous gelants could compromise the effectiveness of a treatment unless it is controlled.

We are interested in exploiting gelled or partially gelled material to reduce gelant leakoff. There are several important questions that must be answered when using preformed gels in fractured systems. First, can fluid diversion be improved by injecting preformed gels rather than gelants? Second, can preformed gels propagate effectively through fractures without screening out or without developing unacceptably high pressure gradients? Third, can gels be placed in selected parts of a fracture or fracture system in a controlled manner? And fourth, will gels satisfactorily resist washout after placement? We are attempting to answer these questions in our research.

### **Core Characterization**

**Core Preparation.** To answer the above questions, we performed experiments using fractured Berea sandstone cores. Before fracturing, the cores had a nominal permeability to brine of 650 md. Cores of two lengths were used. One set of cores were 14-15 cm in length and 3.56 cm in diameter. These cores were fractured lengthwise, and the two halves of the core were repositioned and cast in epoxy. Two internal pressure taps were drilled 2 cm from the inlet sandface. One tap was located 90° from the fracture to measure pressure in the porous rock, while the other tap was drilled to measure pressure in the fracture. Fig. 3 shows a schematic of the first type of fractured core. The second set of cores were 114-122 cm (3.7-4.0 ft) in length and 3.81 cm in height and width. Again, these cores were fractured lengthwise, and the two halves of the core were repositioned and cast in epoxy. Four internal pressure taps were spaced equally along the length of the fracture (i.e., to measure pressure in the fracture). During our corefloods, the fractures were always oriented vertically. All experiments were performed at 41°C.

We routinely performed water-tracer studies before and after gel placement during our experiments. These tracer studies were used to characterize pore volumes and dispersivities of the cores. These studies involved injecting a brine bank that contained potassium iodide as a tracer. The tracer concentration in the effluent was monitored at a wavelength of 230 nm. In Fig. 4, the curve with the open circles illustrates the results from a tracer study for a short (14.5-cm) unfractured Berea core that was saturated with brine. Dispersivities of unfractured Berea sandstone cores were typically 0.1 cm, and the effluent tracer concentration reached 50% of the injected concentration after injecting 1 PV of tracer solution.

The solid circles in Fig. 4 show the tracer results from a short (14.5-cm) fractured Berea core. For this fractured core, the first tracer was detected in the effluent after injecting 0.032 PV of tracer solution. In contrast, for the unfractured core, the first tracer was detected after injecting 0.8 PV.

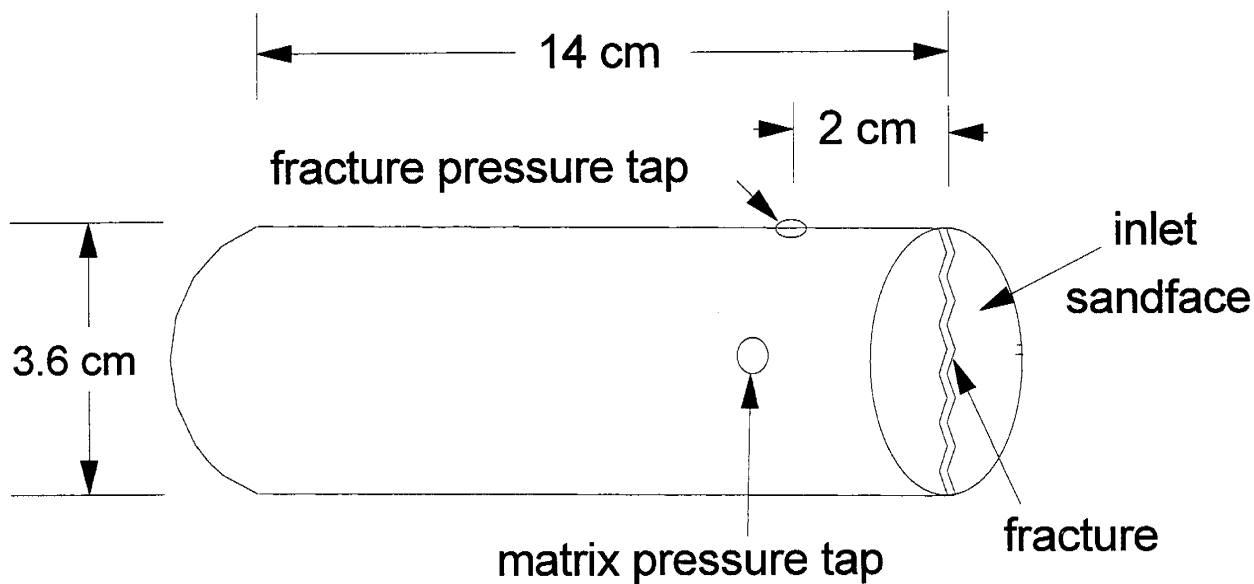


Fig. 3. Schematic of a fractured core.

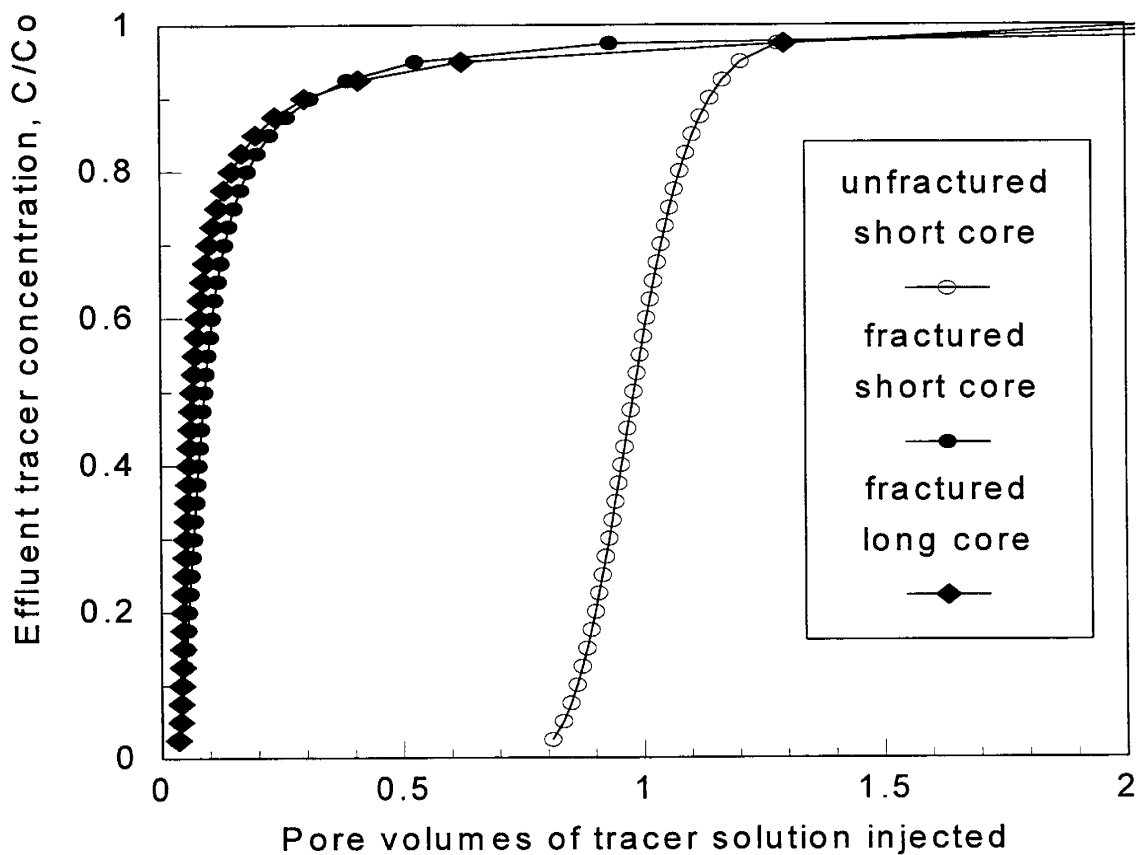


Fig. 4. Tracer results for unfractured and fractured short (14.5-cm) and long (115-cm) Berea sandstone cores (no gel present).

The solid diamonds in Fig. 4 show the tracer results from a long (115-cm) fractured Berea core. For this fractured core, the first tracer was detected in the effluent after injecting 0.035 PV of tracer solution. Fig. 4 shows that the tracer results were similar for the short and long fractured cores. The average conductivities were about the same for the short and long fractured cores (119 and 138 darcy-cm, respectively).

**Correlation of Fracture Width and Permeability.** In our work, we routinely use conductivity to characterize fractures. Fracture conductivity ( $k_f w_f$ ) is the product of fracture permeability ( $k_f$ ) and fracture width ( $w_f$ ). We report fracture conductivities because they can be determined conveniently and accurately from pressure drops, flow rates, and the Darcy equation.<sup>1</sup> For our experiments to date, fracture conductivities have ranged from 23 to 57,000 darcy-cm (D-cm).

For many people, the flow properties of fractures is understood more readily if a given fracture conductivity is separated into its components of permeability and width. To achieve this separation, one of the components must be measured by an independent method. In concept, fracture width could be measured directly if the fracture faces were smooth and parallel; unfortunately, they usually are neither.

We used results from tracer studies to make an independent estimate of the average width of the fractures in our core experiments. The cores were initially saturated with brine with no tracer. Brine with a potassium iodide tracer was then injected, and the tracer concentration in the effluent was measured spectrophotometrically. Since the flow capacities of our fractures were at least 12 times greater than the flow capacities of the adjacent rock,<sup>2</sup> the first tracer detected in the core effluent gives a good estimate of the fracture volume ( $V_f$ ). Since the lengths ( $L_f$ ) and heights ( $h_f$ ) of our fractures are known accurately, average fracture widths can be calculated using Eq. 1.

$$w_f = \frac{V_f}{L_f h_f} \quad (1)$$

By dividing fracture conductivity by fracture width, fracture permeability can be estimated. These calculations were used to generate Fig. 5, which plots fracture width versus fracture permeability for many of our fractured cores. Fracture widths ranged from 0.02 cm to 0.18 cm, and the estimated fracture permeabilities ranged from 1,650 to 360,000 darcys.

The solid line in Fig. 5 shows the relation predicted between fracture width and fracture permeability for laminar flow through a slit (parallel plates).<sup>11</sup> The theoretical relation is given by Eq. 2, where  $w_f$  is in cm and  $k_f$  is in darcys. The predictions match our data reasonably well.

$$k_f = \frac{w_f^2}{12} \times 1.013 \times 10^8 \quad (2)$$

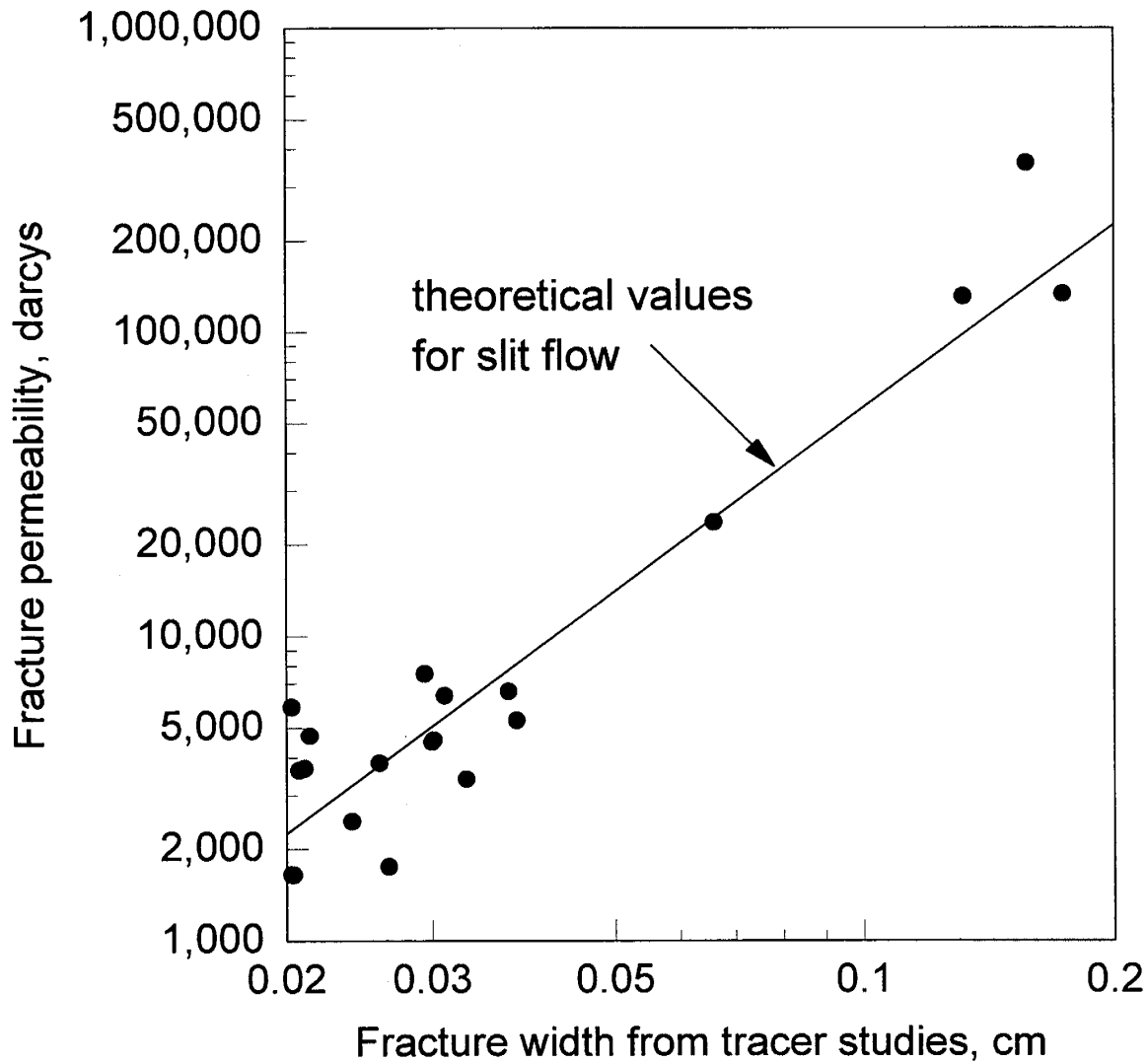


Fig. 5. Correlation of fracture width with fracture permeability.

### Behavior of Freshly Prepared Gelants in Fractures

To establish a baseline of behavior for comparing gelants to preformed gels, several experiments were performed in fractured cores using freshly prepared gelants. The results from two sets of experiments were reported earlier for resorcinol-formaldehyde and Cr(III)-acetate-HPAM gelants in short (14-15 cm) fractured cores.<sup>1,5</sup> In both cases, tracer studies indicated that the gel treatments (which each used about 10 fracture volumes or 0.3 core PV of gelant) did not improve sweep efficiency in the fractured cores. (Tracer curves obtained after gelant placement were very similar to those before gel placement—see Figs. 6 and 7.) We suspected that these gels washed too easily from the cores during brine injection after gel placement.<sup>1</sup>

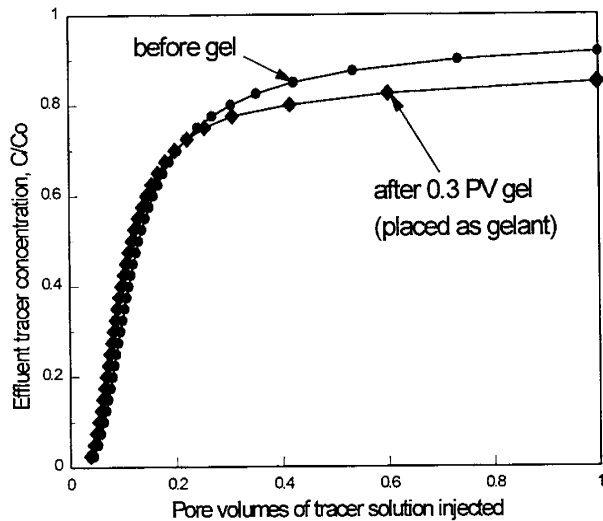


Fig. 6. Tracer results for Short Fractured Core 1: resorcinol-formaldehyde gel (placed as gelant).

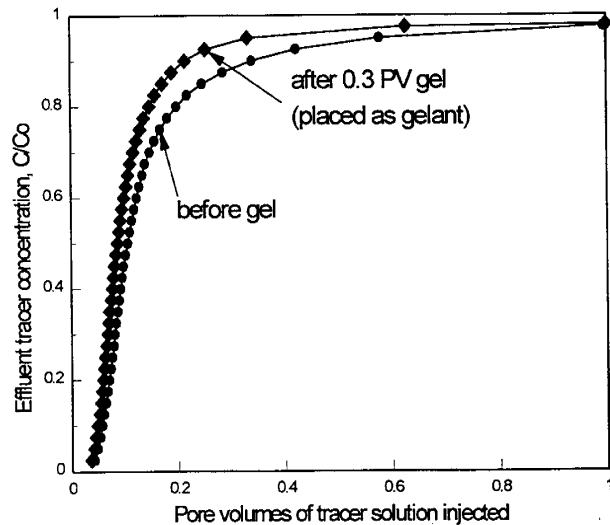


Fig. 7. Tracer results for Short Fractured Core 3: Cr(III)-acetate-HPAM gel (placed as gelant).

**Resorcinol-Formaldehyde.** We recently performed similar experiments using long (122-cm) fractured cores. Long Fractured Core 6 was used to examine the resorcinol-formaldehyde gelant. Properties of this core are listed in Table 1. The core was first saturated with a brine that contained 0.5% KCl and 0.1%  $\text{CaCl}_2 \cdot 2\text{H}_2\text{O}$  at neutral pH. The presence of calcium in the brine was important for controlling pH in the core during gelant injection. (Calcium was not present in solution during our earlier experiments in short fractured cores.<sup>1</sup>) For the present experiment, the gelant contained 3% resorcinol, 3% formaldehyde, 0.5% KCl, and 0.1%  $\text{CaCl}_2 \cdot 2\text{H}_2\text{O}$  at pH 9. This formulation forms a rigid gel within two hours at pH 9 and 41°C. However, gelation is much less complete at neutral pH.<sup>12,13</sup> If gelant without divalent cations enters the porous rock (i.e., through leakoff from the fracture), carbonates in the rock will dissolve and induce a pH value around 9 for gelant in the porous rock.<sup>12,14</sup> Thus, the gelant in the rock will form a strong gel that could ultimately harm sweep efficiency.

Ideally, we want gel to form in the fracture, not in the porous rock.<sup>5</sup> If the gelant contains calcium, carbonate dissolution will be suppressed, and the pH will not tend to rise.<sup>12-14</sup> Instead, the rock minerals (especially clays) tend to neutralize the pH of the gelant that enters the porous rock.<sup>12</sup> Hopefully, the gelant in the fracture will remain near pH 9 so that a strong gel forms.

We injected 45 ml (2.5 fracture volumes or 0.12 core PV) of resorcinol-formaldehyde gelant into Long Fractured Core 6 at a rate of 200 ml/hr. As expected (because the gelant viscosity was virtually the same as that for brine, 0.67 cp at 41°C), the resistance factor was near unity during gelant injection. After gelant injection, the core was shut in for 1 day to allow the gel to form and cure.

Table 1. Properties of Long Fractured Core 6

Core width and height = 3.81 cm		Core PV = 373 ml				
Fracture volume, $V_f$ , = 17.9 ml		Average $w_f$ = 0.038 cm, $k_f$ = 5,300 D				
Core section:	Entire core	1	2	3	4	5
Length, cm	122	24.4	24.4	24.4	24.4	24.4
$k_{av}$ , D	53.9	10.5	29.2	32.0	173.8	23.8
$k_f w_f$ , D-cm	203	37.6	108.7	119.5	660	88.0
$k_f w_f h_f / A k_m$	81.8	15.2	43.9	48.2	266	35.5

After the shut-in period, 6 PV (2,200 ml or 120 fracture volumes) of brine were injected. Brine mobilities for each of the five sections of the fractured core are plotted as a function of PV throughput in Fig. 8. After gel placement, the apparent brine mobilities in Core Sections 2 through 5 ranged from 0.35 to 1 D/cp. For a given core section (excluding Core Section 1), the mobility was fairly constant while injecting 6 PV of brine. We note that if the gel had perfectly healed the fracture, a brine mobility of about 1 D/cp ( $0.65 \text{ D rock permeability} \div 0.67 \text{ cp brine viscosity}$ ) was expected. The brine mobilities observed in Core Sections 2 through 5 suggest that the gel treatment may have been reasonably effective at healing the fracture.

In Core Section 1 (solid diamonds in Fig. 8), the brine mobility after gel placement was very low, ranging from 0.003 to 0.04 D/cp. These low values suggest that the gel seriously damaged the inlet part of the core.

Fig. 9 plots apparent mobilities after gel placement versus brine injection rate. In these experiments, a low rate was used first (10 ml/hr). Then, mobilities were determined at successively higher injection rates up to 200 ml/hr. Finally, mobilities were determined at successively lower injection rates down to 10 ml/hr. These rates correspond to superficial velocities in the core ranging from 0.54 to 10.8 ft/d. Over this range, brine mobilities were fairly insensitive to injection rate in Core Sections 2, 3, and 4 (Fig. 9). In contrast, a strong shear-thinning behavior was observed in Core Section 1. The mobility maximum for Core Section 1 (shown in Fig. 8) reflects the shear-thinning behavior. For the solid-diamond curve, the minimum mobilities (at 2.5 PV and 7.7 PV) were observed at 10 ml/hr, and the maximum mobility (at 5.5 PV) was observed at 200 ml/hr. A mild washout effect was noted in Core Section 5. We suspect that the latter observations may be related to the locations of the sections at the ends of the core.

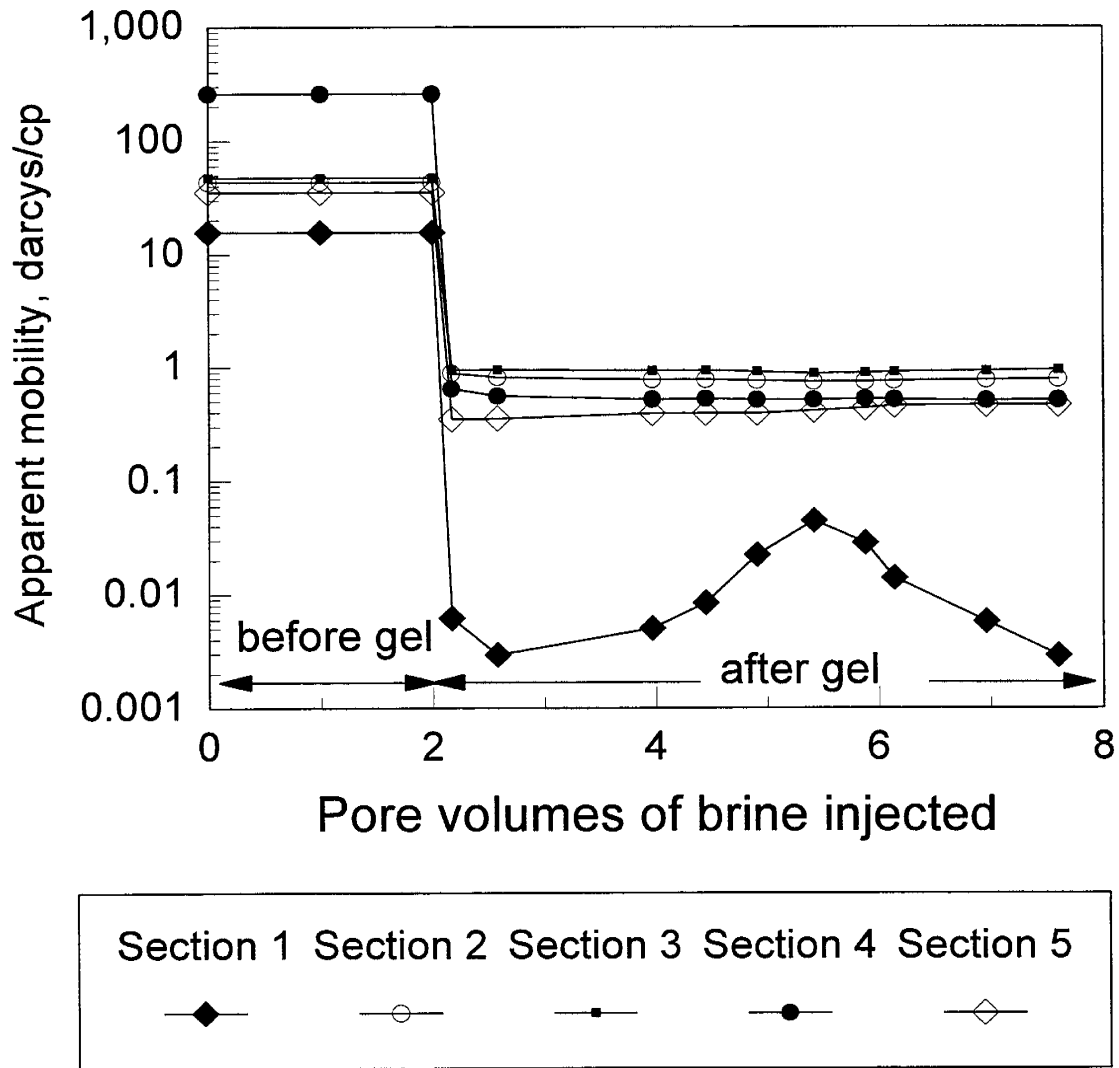


Fig. 8. Apparent brine mobility versus PV for Long Fractured Core 6 with resorcinol-formaldehyde gel (placed as a gelant).

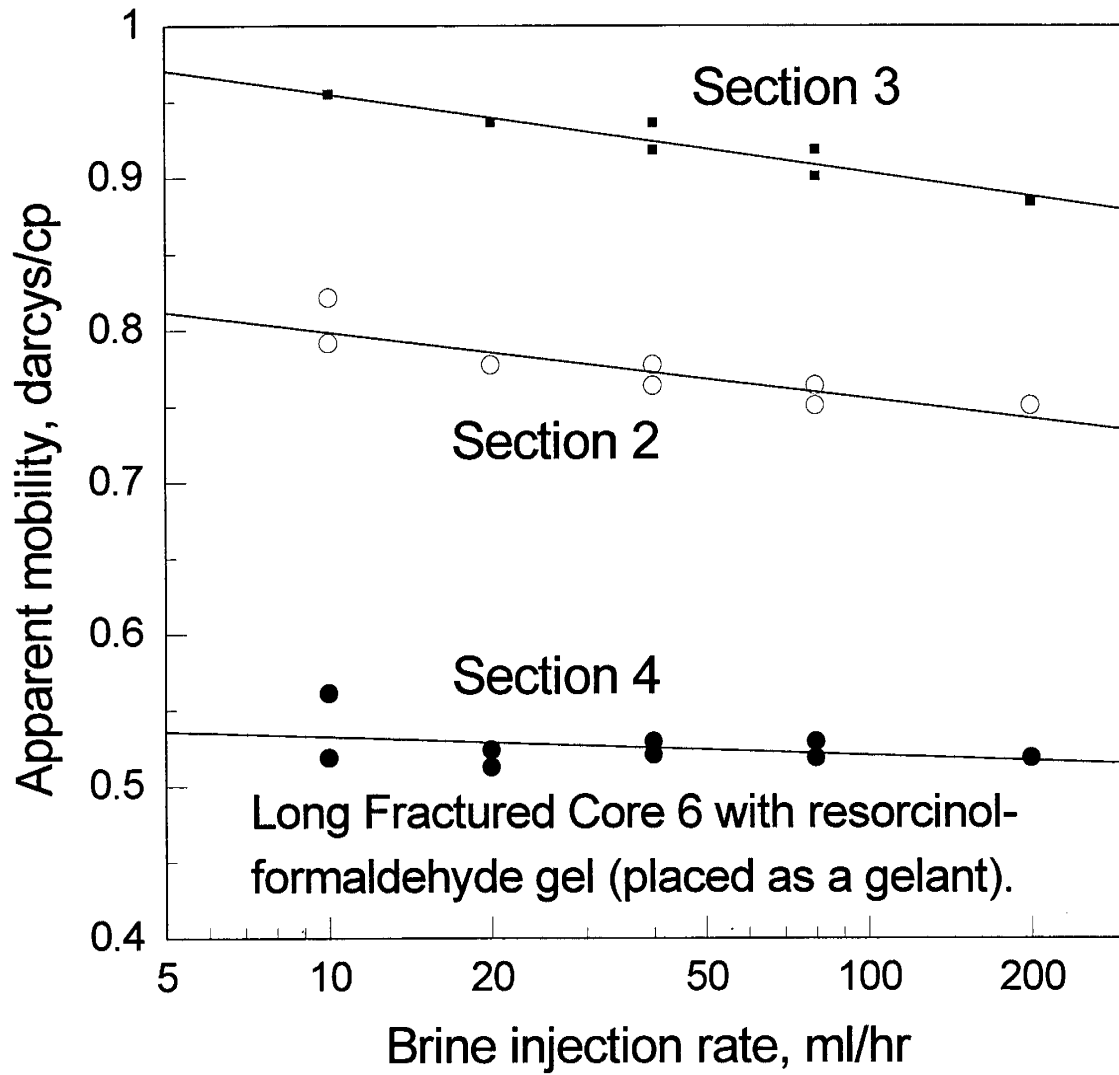


Fig. 9. Apparent brine mobility versus injection rate for Long Fractured Core 6 with resorcinol-formaldehyde (placed as a gelant).

Table 2 summarizes the results of experiments in Long Fractured Core 6 (using the resorcinol-formaldehyde gelant), as well as those from two subsequent experiments in Long Fractured Cores 7 and 8 (using Cr(III)-acetate-HPAM gelants). The central five columns list the ratio,  $(F_{rr}Ak_m)/(k_f w_f h_f)$ , for each of the five sections of the fractured cores. (The residual resistance factor is represented by the term,  $F_{rr}$ .) This ratio provides an indication of how effectively the gel healed the fracture. The ratio should have a value of unity if the fracture was perfectly healed without damaging the adjacent rock. If the ratio is significantly less than one, then the fracture is largely still open. If the ratio is much greater than one, then the gel damaged the porous rock.

Table 2. Plugging 122-cm Fractures with Gels Formed In Situ from Gelants (45 ml or  $\approx 2.5$  fracture volumes of gelant injected)

Core	Gelant	Ca <sup>2+</sup> brine?	$(F_{rr}Ak_m)/(k_f w_f h_f)$ in Core Section:					Tracer results, PV at:	
			1	2	3	4	5	Break-through	C/C <sub>o</sub> =50%
6	resorcinol-formaldehyde	yes	23	1.3	1.1	1.9	2.4	0.39	0.80
7	Cr(III)-acetate-HPAM	no	1.7	0.6	0.2	0.2	0.5	0.03	0.30
8	Cr(III)-acetate-HPAM	yes	88	1.4	0.9	0.5	0.3	0.24	0.58

For the resorcinol-formaldehyde gel in the first section of the core, the value of 23 indicates that the gel has penetrated into and significantly damaged the porous rock in the first core section. This result is not surprising since the gelant was expected to penetrate a short distance from the inlet sandface into the porous rock. In the the second and third sections of the core, the values were 1.3 and 1.1, respectively. Because they were close to 1.0, these values suggest that the gel effectively reduced the fracture conductivity in these sections. In the fourth and fifth sections, the values were 1.9 and 2.4, respectively. These values are also reasonably close to 1.0, indicating that the fracture conductivity was reduced fairly effectively.

Tracer results during brine injection after gel placement are shown in Fig. 10 for Long Fractured Core 6. Although these results (solid diamonds in Fig. 10) do not indicate perfect healing of the fracture (i.e., the open circles in Fig. 10), they do reveal that the gel treatment substantially improved sweep efficiency in the core. This result was much more positive than that reported during a similar experiment in a short fractured core (i.e., Fig. 6). One possible reason for the improved performance here is that better pH control was maintained in this experiment (because the brine contained calcium in this experiment but not in the short-core experiment).

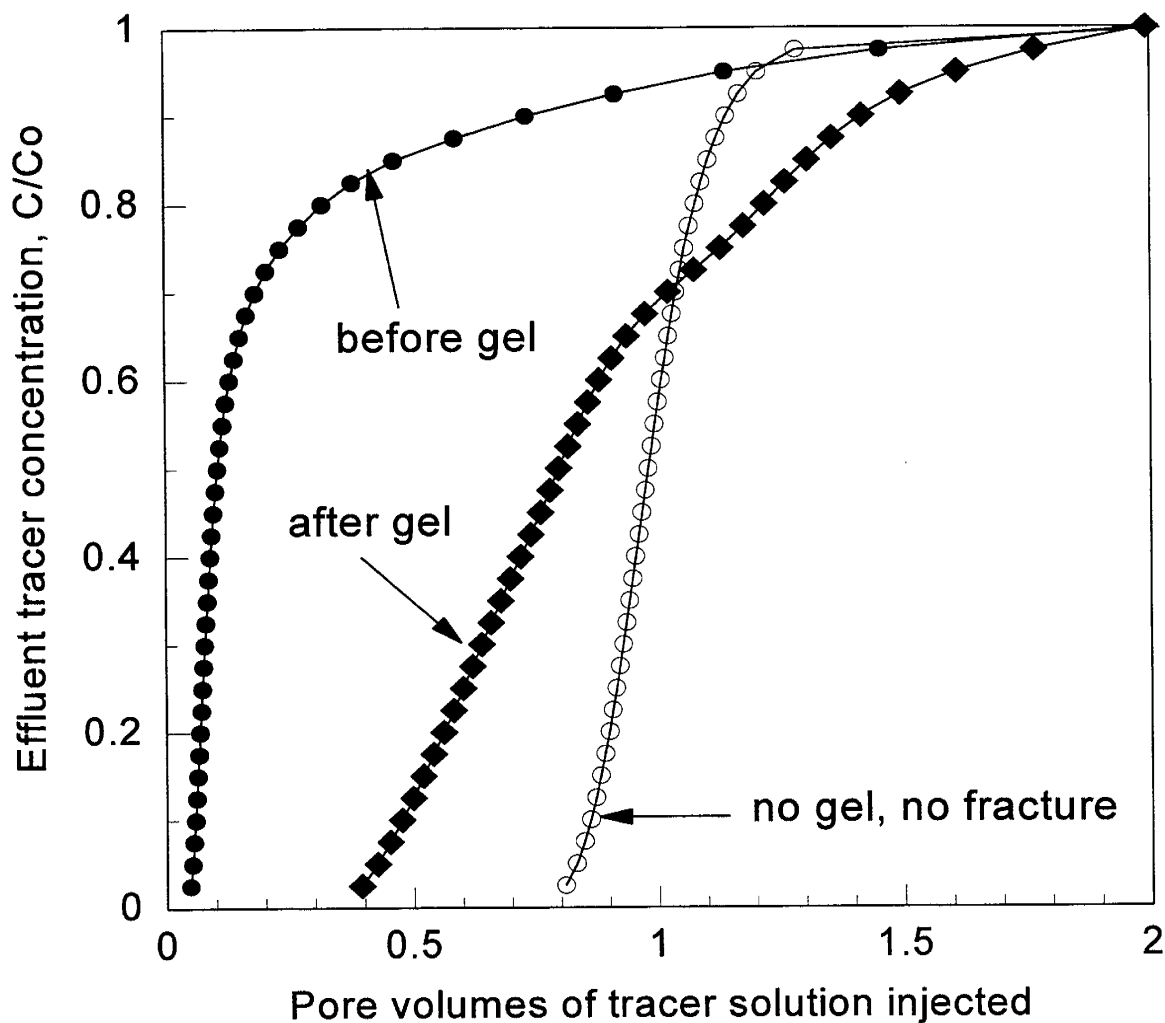


Fig. 10. Tracer results for Long Fractured Core 6 with resorcinol-formaldehyde gel (placed as a gelant).

The last two columns of Table 2 summarize the tracer results for this and the two subsequent experiments (in Long Fractured Cores 7 and 8). The “breakthrough” column indicates the PV value when tracer first arrived at the core outlet (during brine injection after gel placement). For comparison, breakthrough values are expected to be 0.05 for a fractured core without gel and 0.8 for an unfractured core without gel (or a perfectly healed fracture). The “ $C/C_o=50\%$ ” column lists the PV where the effluent tracer concentration reached 50% of the injected tracer concentration. For comparison, these values are expected to be 0.1 for a fractured core without gel and 1.0 for an unfractured core without gel (or a perfectly healed fracture).

**Cr(III)-Acetate-HPAM with 1% NaCl.** A similar set of experiments was performed in a 122-cm fractured core (Long Fractured Core 7) using a freshly prepared Cr(III)-acetate-HPAM gelant. Properties of this core are listed in Table 3. This core was first saturated with a brine that contained 1% NaCl at neutral pH. The gelant contained 0.5% HPAM (Allied Colloids Alcoflood 935®,  $M_w \approx 5 \times 10^6$  daltons, degree of hydrolysis: 5-10%), 0.0417% chromium triacetate, and 1% NaCl at pH 6. The viscosity of freshly prepared gelant was 18 cp at  $11 \text{ s}^{-1}$  and  $41^\circ\text{C}$ . The gelation time for this formulation was between 4 and 6 hours at  $41^\circ\text{C}$ .

Table 3. Properties of Long Fractured Core 7

Core width and height = 3.81 cm		Core PV = 371 ml				
Fracture volume, $V_f$ , = 15.6 ml		Average $w_f$ = 0.033 cm, $k_f$ = 3,400 D				
Core section:	Entire core	1	2	3	4	5
Length, cm	122	24.4	24.4	24.4	24.4	24.4
$k_{av}$ , D	30.3	28.8	24.7	60.5	19.8	17.6
$k_f w_f$ , D-cm	112.9	107.4	91.6	228	72.9	64.5
$k_f w_f h_f / Ak_m$	45.6	43.4	37.0	92.0	29.4	26.0

We injected 45 ml (2.9 fracture volumes or 0.12 core PV) of Cr(III)-acetate-HPAM gelant into Long Fractured Core 7 at a rate of 200 ml/hr. The apparent gelant resistance factor was 13 at the end of gelant injection. After gelant injection, the core was shut in for 3 days. After the shut-in period, 6 core PV (2,200 ml or 140 fracture volumes) of brine were injected. Results from this experiment are summarized in the second data row of Table 2. During brine injection after gel placement, the  $(F_{rr} Ak_m) / (k_f w_f h_f)$  ratio was 1.7 in the first core section, suggesting that the gel treatment may have effectively reduced the fracture conductivity in the first section. However, in the second through fifth core sections, the ratios were significantly less than one, indicating that the gel treatment was not effective in healing the fracture in those sections. Tracer results (Fig. 11 and Table 2) also indicated that the gel treatment only slightly improved sweep efficiency in the core. Two factors could have contributed to this result. First, the gelant and the brine in the core did not contain divalent cations. As mentioned earlier, this situation tends to increase the solution pH. In this case, the acetate in the crosslinker buffers the gelant (originally at pH 6) and makes the gelation reaction less sensitive to pH.<sup>15-17</sup> In other words, the acetate buffer tends to counteract the pH-increasing effect of carbonate dissolution. However, the acetate's buffering action may not always be sufficient, especially if the buffer concentration is not high enough.

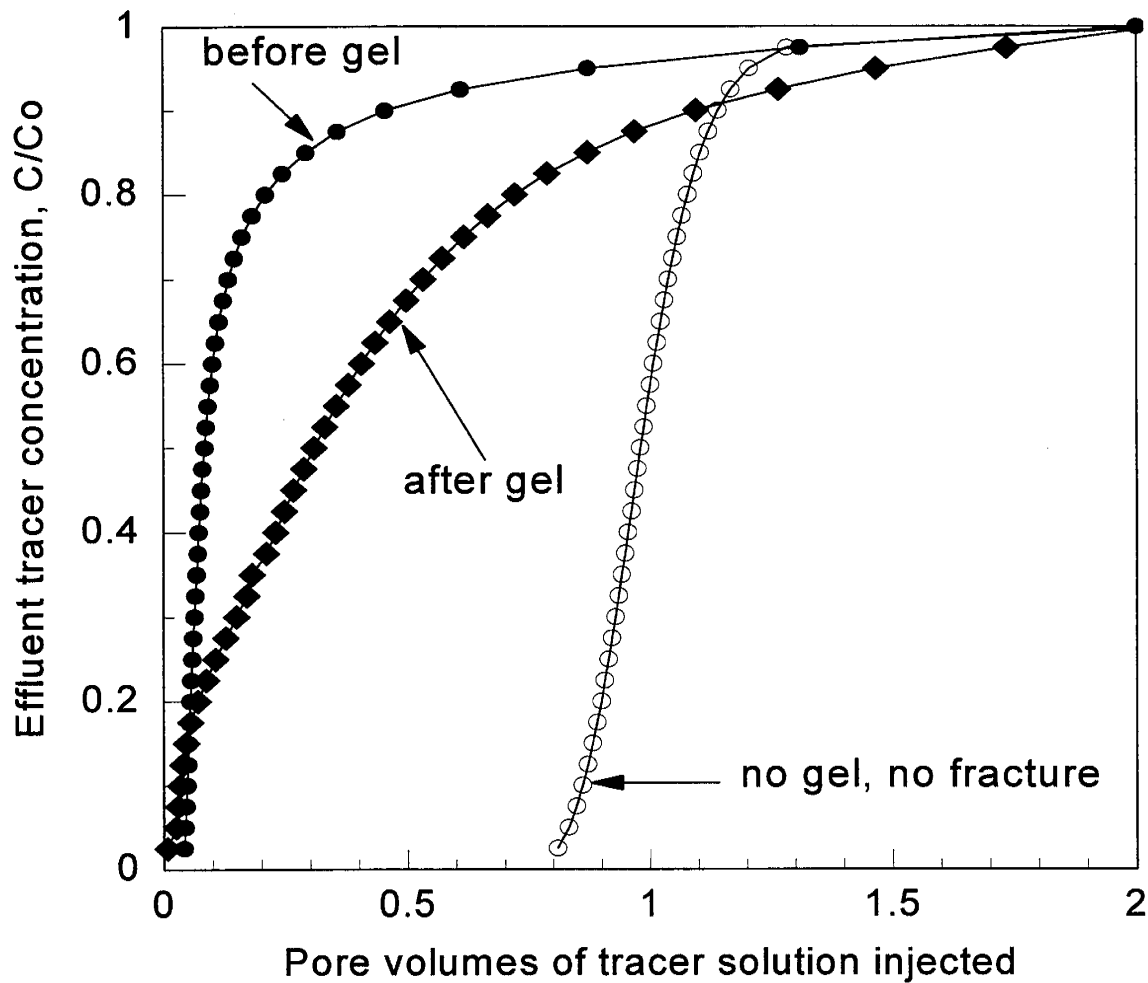


Fig. 11. Tracer results for Long Fractured Core 7 with Cr(III)-acetate-HPAM gel (placed as a gelant, 1% NaCl brine).

The second reason is tied to the viscous nature of the Cr(III)-acetate-HPAM gelant (18 cp). For a given distance of gelant penetration along the length of a fracture, more viscous gelants will penetrate (leakoff) to a greater extent into the porous rock.<sup>1,5,9</sup> This additional gelant leakoff could, in some circumstances, ultimately lead to an impairment of sweep efficiency after a gel treatment.

**Cr(III)-Acetate-HPAM with 1% NaCl and 0.1% CaCl<sub>2</sub>.** To test the importance of divalent cations on gelant performance, a second set of experiments was performed in a 122-cm fractured core (Long Fractured Core 8). We used an identical freshly prepared Cr(III)-acetate-HPAM gelant, except that the gelant and brine contained 0.1% CaCl<sub>2</sub> in addition to 1% NaCl. Properties of the core for this experiment are listed in Table 4. The viscosity of this freshly prepared gelant was 45 cp at 11 s<sup>-1</sup> and 41°C. The gelation time for this formulation was about 2 hours at 41°C. Evidently, the presence of 0.1% CaCl<sub>2</sub> decreased the gelation time and increased the gelant viscosity compared to those for the gelant without calcium.

Table 4. Properties of Long Fractured Core 8

Core width and height = 3.81 cm		Core PV = 394 ml				
Fracture volume, $V_f$ = 16.9 ml		Average $w_f$ = 0.036 cm, $k_f$ = 7,300 D				
Core section:	Entire core	1	2	3	4	5
Length, cm	122	24.4	24.4	24.4	24.4	24.4
$k_{av}$ , D	70.7	57.9	82.7	87.6	59.4	66.0
$k_f w_f$ , D-cm	267.0	218.2	312.7	331.4	223.9	248.8
$k_f w_f h_f / Ak_m$	107.8	88.1	126.3	133.8	90.4	100.5

We injected 45 ml (2.7 fracture volumes or 0.11 core PV) of Cr(III)-acetate-HPAM gelant into Long Fractured Core 8 at a rate of 200 ml/hr. The apparent gelant resistance factor was 11 at the end of gelant injection. After gelant injection, the core was shut in for 3 days. After the shut-in period, 4.5 PV (1,800 ml or 105 fracture volumes) of brine were injected. Results from this experiment are summarized in the third data row of Table 2. During brine injection after gel placement, the  $(F_{rr} Ak_m) / (k_f w_f h_f)$  ratio was 88 in the first core section, suggesting that the gelant entered and substantially damaged the porous rock of the first core section. For comparison, recall that the  $(F_{rr} Ak_m) / (k_f w_f h_f)$  ratio was 1.7 for the identical experiment without calcium (Long Fractured Core 7). The different results may be related to the differences in gelant viscosities and gelation times. The explanation for the difference in results also may be related to carbonate dissolution. In both experiments, we expected the viscous gelants to penetrate at least 2 cm from the inlet sandface into the porous rock (based on degree of penetration calculations<sup>9,21</sup>). For the gelant without calcium, carbonate dissolution may have increased the pH of gelant in the porous rock—thus, inhibiting gelation and resulting in a low residual resistance factor and a low  $(F_{rr} Ak_m) / (k_f w_f h_f)$  ratio. (The Cr(III)-acetate-HPAM gelants are usually formulated with pH values around 6.) In contrast, for the gelant with 0.1%  $CaCl_2$  (used in Long Fractured Core 8), the calcium probably suppressed carbonate dissolution—thus, leading to a stronger gel, a higher residual resistance factor, and a higher  $(F_{rr} Ak_m) / (k_f w_f h_f)$  ratio (88).

In the second and third sections of Long Fractured Core 8, the  $(F_{rr} Ak_m) / (k_f w_f h_f)$  ratios were fairly close to one (Table 2), suggesting effective healing of the fracture in these sections. However, in the fourth and fifth sections of the core, the ratios were significantly less than one, indicating that the fracture remained open in these sections. Consistent with these observations, tracer results (Fig. 12 and Table 2) indicated that the improvement in sweep efficiency was intermediate between the results obtained in Long Fractured Cores 6 and 7. Based on these results, we suspect that both gelant viscosity and divalent cation effects can play an important role in gelant placement in fractured systems.

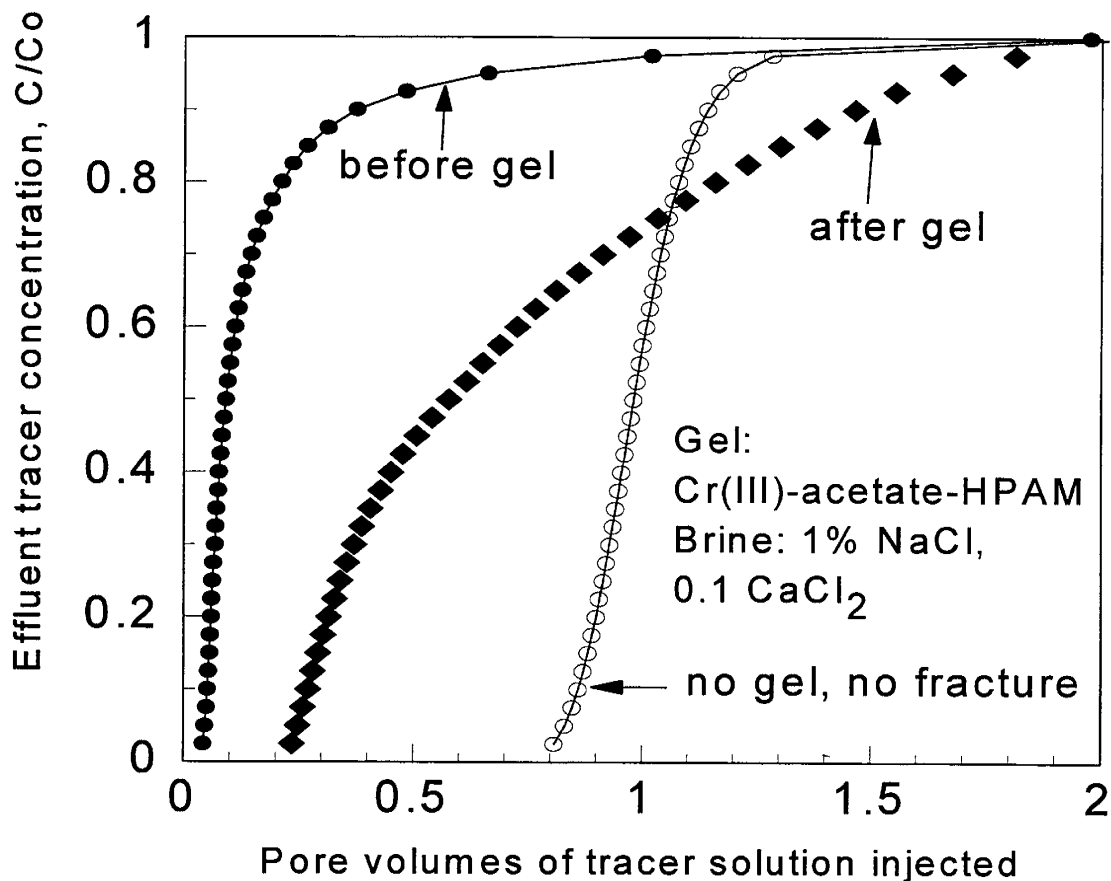


Fig. 12. Tracer results for Long Fractured Core 8 with Cr(III)-acetate-HPAM gel (placed as a gelant; brine: 1% NaCl, 0.1% CaCl<sub>2</sub>).

### Summary of Previous Results During Injection of Preformed Gels into Fractures

As mentioned earlier, we are interested in whether injection of preformed gels can provide better fluid diversion than that associated with gels formed in situ from gelants. In previous reports, we demonstrated that under the right circumstances, preformed gels can effectively heal fractures without significantly damaging the porous rock.<sup>1,2,5</sup> The experimental support for this statement comes from tracer studies combined with permeability-reduction data. Fig. 13 shows tracer results obtained before versus after placement of 17 PV (530 ml or about 500 fracture volumes) of Cr(III)-acetate-HPAM gel that was aged for 24 hours before injection. For the tracer curve that was obtained after gel placement (solid diamonds in Fig. 13), the first half of the curve was virtually identical with that for an unfractured core with no gel (open circles in Fig. 13). The deviation observed in the upper part of the tracer curves may have resulted from a capacitance effect involving the iodide tracer and the gel in the fracture. Iodide flowing near the gel could experience a delay in propagation because the tracer can diffuse into and back out of the gel.<sup>12,13</sup>

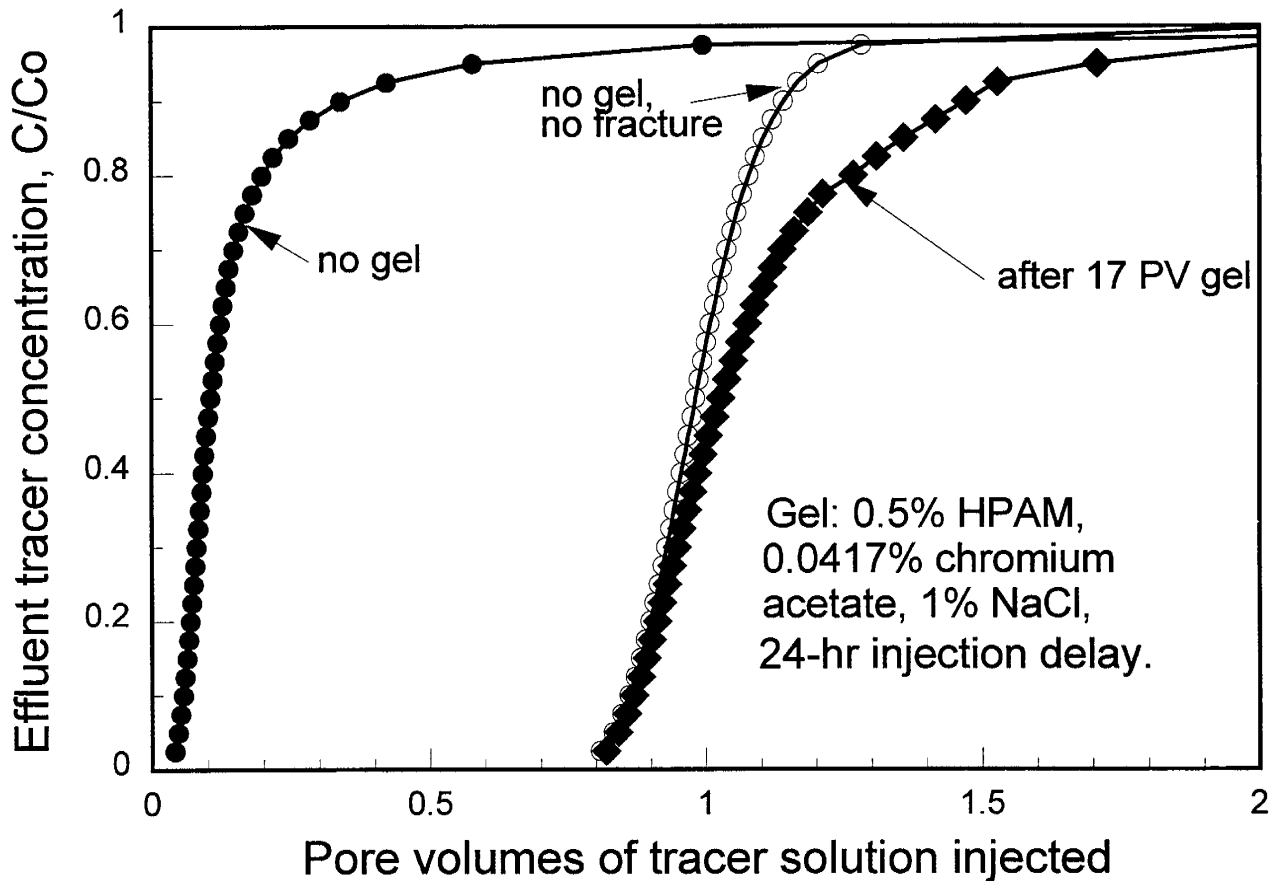


Fig. 13. Tracer results before versus after placement of a 24-hr-old Cr(III)-acetate-HPAM gel in Short Fractured Core 7.

Brine mobilities measured after gel placement also indicated that this gel treatment effectively healed the fracture. Fig. 14 shows apparent mobility data before, during, and after gel placement in Short Fractured Core 7. (We say "apparent mobility" because the values indicated include the combined effects of flow through the fracture and the porous rock.) During brine injection after gel placement, the apparent brine mobility was stable at 0.85 darcys/cp. This value was close to that expected for an unfractured core with no gel.<sup>1,2,5</sup> The stable brine mobilities indicate that the gel did not wash from the fracture under these conditions (3 psi/ft pressure gradient).

Fig. 14 also shows apparent mobilities during gel injection into Short Fractured Core 7. The original conductivity of this fracture was 53.8 D-cm.<sup>5</sup> We injected 17 PV of brine, followed by 17 PV of Cr(III)-acetate-HPAM gel (24 hrs after preparation), followed by 17 PV of brine. During these steps, the injection rate was 200 ml/hr. During the first brine injection, the apparent brine mobility was 30 darcys/cp. During the subsequent injection of gel, the apparent gel mobility stabilized at 0.01 darcys/cp. Thus, the gel was injected without plugging or "screening out" in the fracture. Since the apparent brine and gel mobilities were known (30 and 0.01 darcys/cp, respectively) and since these values were associated almost exclusively with flow in the fracture, we can calculate a resistance factor for gel in the fracture. This value was 3,000. Thus, the

effective viscosity of gel in the fracture was 3,000 times greater than that of water. The pressure gradient was 250 psi/ft during gel injection.

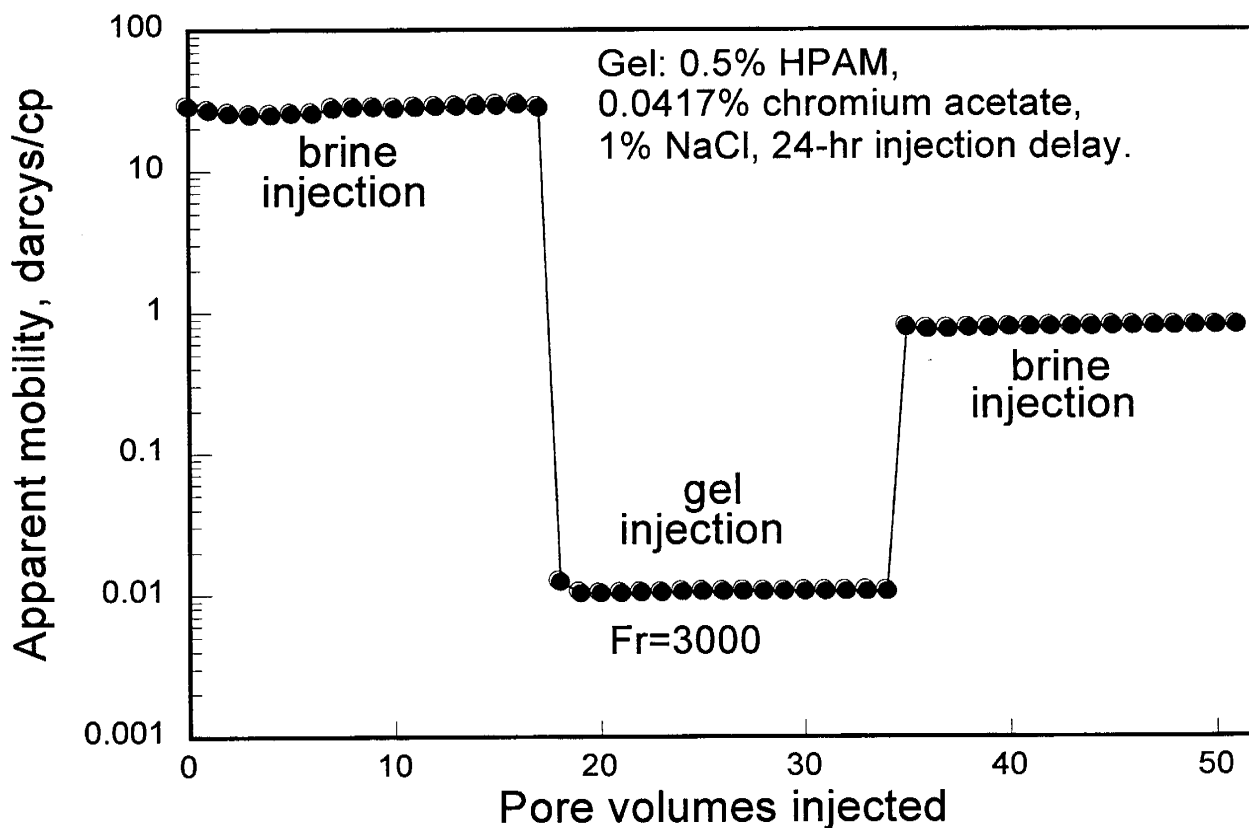


Fig. 14. Apparent mobility before, during, and after placement of a 24-hr-old Cr(III)-acetate-HPAM gel in Short Fractured Core 7.

Using Short Fractured Core 8, we examined the apparent rheology of the Cr(III)-acetate-HPAM gel in a fracture.<sup>1,5</sup> One day after the gelant was prepared, gel was injected into the fractured core at a rate of 400 ml/hr. During gel injection at this rate, the pressure gradient stabilized at about 75 psi/ft, and the resistance factor in the fracture was 1,500. After obtaining this data, the injection rate was decreased in stages. The results are shown by the solid stars in Figs. 15 and 16. At each successively lower rate down to 40 ml/hr, stabilized pressure drops were achieved and the resistance factors increased with decreasing flow rate (Fig. 15). The pressure gradient remained fairly constant between 60 and 75 psi/ft (Fig. 16). This result suggests that some minimum pressure gradient was needed to keep the gel mobilized.

When the gel injection rate was reduced to 10 ml/hr (2 hours after gel injection started and 26 hours after the gelant was prepared), the resistance factor increased to 200,000, and the pressure gradient increased to 250 psi/ft (Figs. 15 and 16). This deviation from the previous trend may have resulted from an increased degree of gelation, from the decreased injection rate, or from a

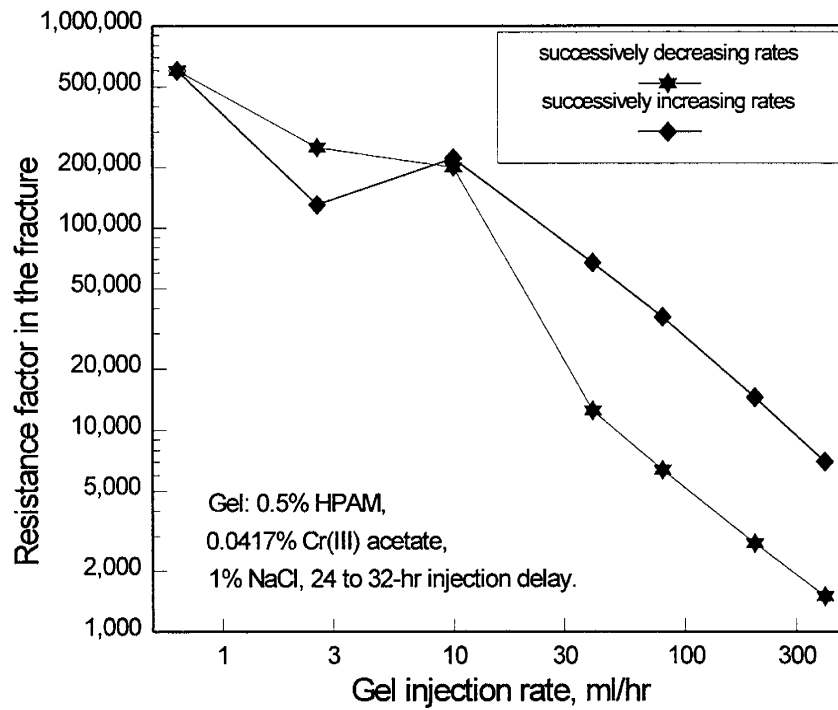


Fig. 15. Resistance factors in Short Fractured Core 8 during placement of a Cr(III)-acetate-HPAM gel.

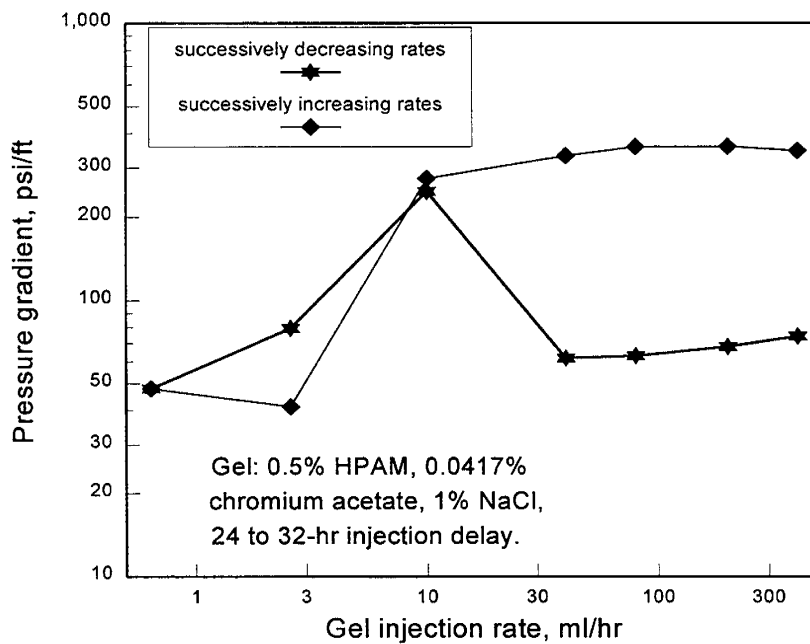


Fig. 16. Pressure gradients in Short Fractured Core 8 during placement of a Cr(III)-acetate-HPAM gel.

combination of both effects. At lower injection rates, the average pressure gradients were lower, and the resistance factors were erratic. The low-injection-rate data points in Figs. 15 and 16 show averages of these erratic values.

After reaching a low gel injection rate of 0.64 ml/hr, the injection rate was increased in stages. Results from this portion of the experiment are illustrated by the solid diamonds in Figs. 15 and 16. When the gel injection rate was increased to 10 ml/hr (6 hours after gel injection started and 30 hours after the gelant was prepared), the resistance factor was 222,000, and the pressure gradient was 280 psi/ft. These values are similar to those mentioned in the previous paragraph (associated with an injection rate of 10 ml/hr).

At higher injection rates, the resistance factors quickly stabilized at each new rate, and the pressure gradients were fairly constant around 300 psi/ft (Fig. 16). Again, this behavior suggests that some minimum pressure gradient was needed to keep the gel mobilized. However, at this point, the pressure gradient was 4 to 6 times greater than that noted earlier in the experiment. This experiment was completed 8 hours after gel injection started and 32 hours after the gelant was prepared.

The experiment described above suggests that for a given gel with a certain degree of curing in a given fracture, some minimum pressure gradient is needed to extrude the gel through the fracture. This behavior makes the gel resistance factors appear extremely shear-thinning in fractures. In contrast, during brine injection after gel placement, we usually observed Newtonian behavior. That is, permeability-reduction values or residual resistance factors were independent of flow rate or pressure gradient.<sup>1,2,5</sup> This behavior is illustrated in Fig. 17 for Cr(III)-acetate-HPAM gels in Short Fractured Cores 5 and 6. Note that the highest pressure gradient examined during brine injection was about 20 psi/ft in these cores. The gels showed no sign of washout from the fracture during the course of injecting 35 PV (1,100 ml or more than 1,000 fracture volumes) of brine. We note that the pressure gradients were much greater when the gels were placed in the fractures. It seems likely that the gel would washout from the fractures if pressure gradients were applied that approach those observed during gel placement.

The behavior of several other preformed gels in fractures can be found in Ref. 2. These gels include resorcinol-formaldehyde, Cr(III)-xanthan, Cr(III)-acetate-PAM/AMPS, Al-citrate-HPAM, Cr(VI)-redox-PAM/AMPS, and hydroquinone-hexamethylenetetramine-HPAM. Some of these gel systems extruded through fractures in a stable manner, while others did not. Also, tracer studies indicated that some of the gels effectively healed the fractures, while others washed too easily from the fractures during brine injection.<sup>2</sup> Therefore, caution must be exercised when selecting a gel—not all gels and gel compositions will be equally effective in a given application.

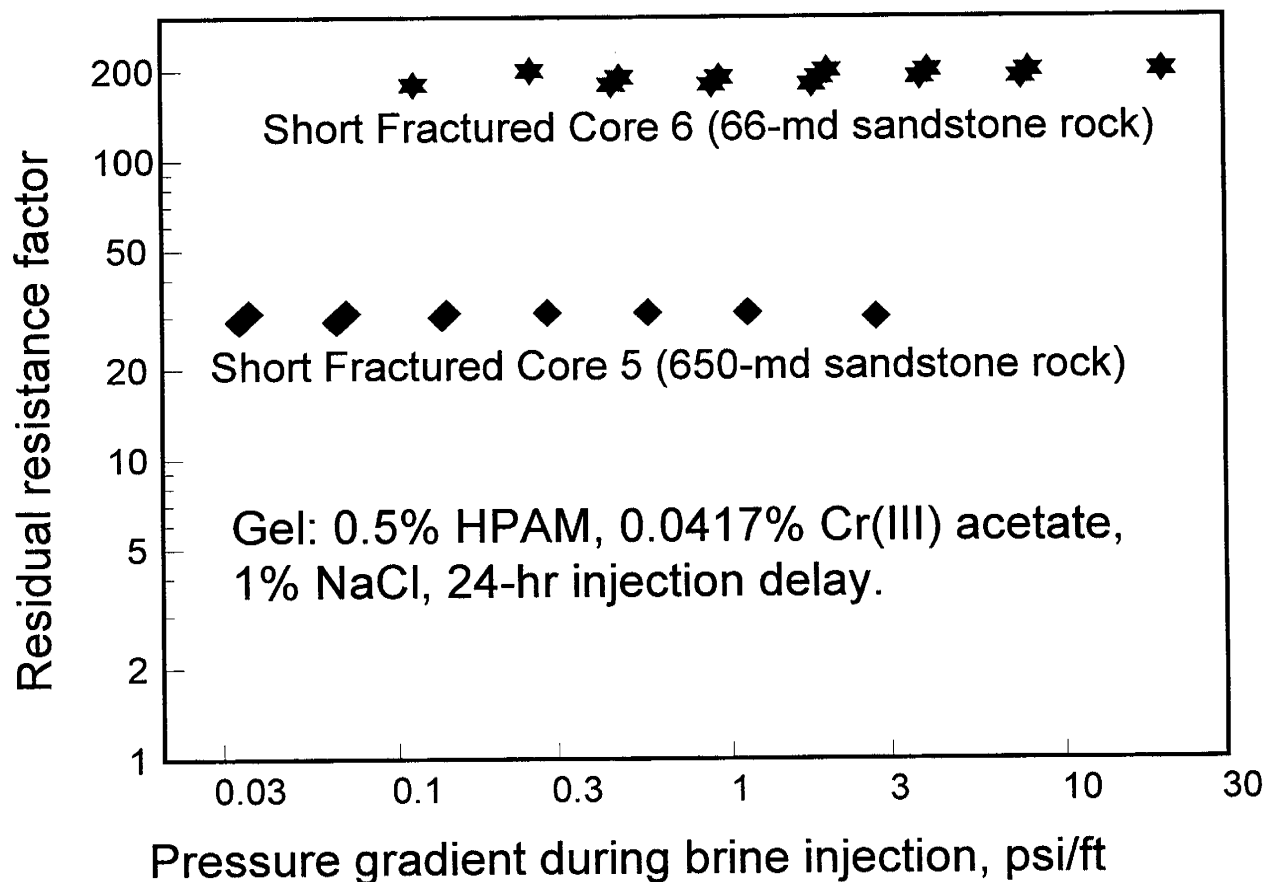


Fig. 17. Residual resistance factor versus pressure gradient after gel placement in Short Fractured Cores 5 and 6.

### Effect of Curing Time on Gel Extrusion Through Fractures

Figs. 15 and 16 suggest that the ability of a given gel to propagate effectively through a fracture depends on the degree of gelation or gel curing. We performed several experiments to study the effects of curing (i.e., continued gelation reactions after gel formation) during gel extrusion through our short (14-15 cm) fractured Berea sandstone cores. Column 3 in Table 5 lists fracture conductivities ( $k_{rw_f}$ ) for the cores used. These fracture conductivities ranged from 44.4 to 187 darcy-cm. As in the other experiments, we used a Cr(III)-acetate-HPAM gel that contained 0.5% HPAM, 0.0417% chromium triacetate, and 1% NaCl (pH=6). Remember that the gelation time for this composition was roughly 5 hours at 41°C. We injected this gel into our fractured cores after allowing different time periods to elapse. In our first set of experiments, these delay times ranged from 5 to 72 hours (see Column 1 of Table 5). During gel injection, the injection rate was fixed at 200 ml/hr. All experiments were performed at 41°C. Column 4 in Table 5 indicates that gel resistance factors (apparent gel viscosities in the fractures) increased dramatically with increased curing time up to 32 hours. However, between 32 and 72 hours, the gel resistance factors decreased substantially (from 14,500 to 340).

Table 5. Effect of Gel Curing on Resistance Factors for Cr(III)-Acetate-HPAM Gels in 14-15-cm Fractures. (First set of experiments)

Injection delay, hours	Short Core	$k_f w_f$ , darcy-cm	Resistance factor	dp/dl, psi/ft
5	28	163.4	59	2
7	28	163.4	137	4
10	20	64.3	500	35
24	8	187.0	2,750	68
32	8	187.0	14,500	357
72	11	44.4	340	34

We were concerned that the drop in resistance factor between 32 and 72 hours was an experimental artifact that occurred because different cores were used and because gels were prepared and used at different times. Therefore, we performed another experiment where only one fractured core and a single batch of gel were used. The conductivity of the fracture in this core (Core 32) was 85.9 darcy-cm. A large volume of Cr(III)-acetate-HPAM gel (same composition as that used previously) was prepared and placed in a transfer vessel between an ISCO pump and the fractured core. At predetermined times, 60 ml (60 fracture volumes) of this gel were injected into the fractured core using a constant rate of 200 ml/hr. The injection delays (time since the gelant was prepared) ranged from 5 to 240 hours. Fig. 18 shows the resistance factors and pressure gradients that were observed during the experiment. Resistance factors increased rapidly between 5 and 24 hours after gelant preparation. Thereafter, the resistance factors increased more gradually until a value of 16,240 was reached 240 hours (10 days) after gelant preparation. These results are qualitatively consistent with the results in Table 5, except for the last entry (72-hr injection delay). Thus, we feel that Fig. 18 reflects the correct effect of curing on resistance factors for this gel in fractures.

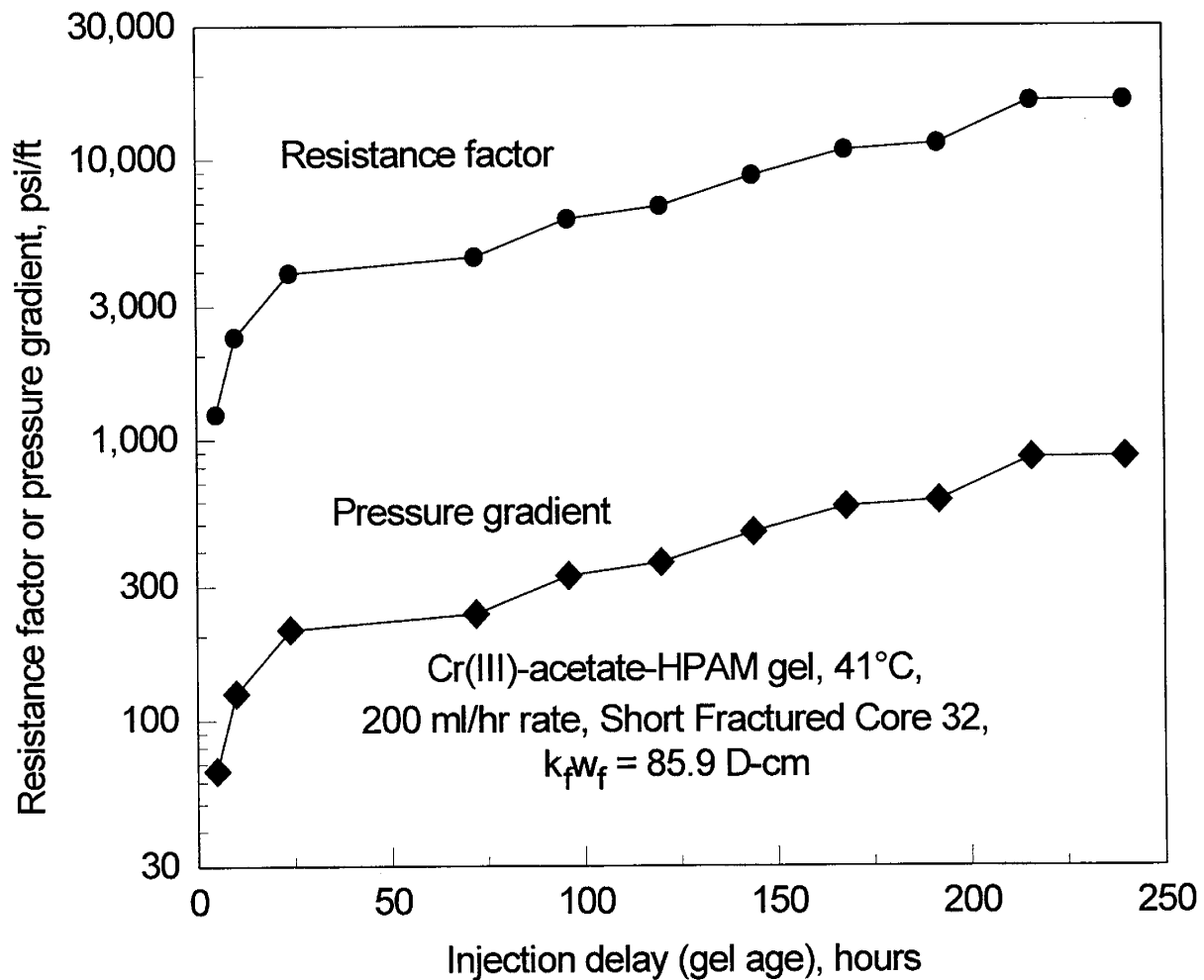


Fig. 18. Effect of gel curing time on extrusion through a single fracture.

### Gel Resistance Factors in Longer Fractures

Most of our previous experiments used fractured cores that were fairly short (14-15 cm). Of course, we are interested in assessing gel propagation through longer fractures. We performed an experiment using a fractured Berea sandstone core that was 115 cm (3.8 ft) in length and 14.5 cm<sup>2</sup> in cross-section (square). Four internal pressure taps were spaced equally along the length of the fracture. The conductivities of the five 23-cm fracture sections of the core were 129, 156, 171, 86, and 139 darcy-cm. A tracer study performed before gel injection indicated that the volume associated with the fracture was about 13 ml. Properties of this core are listed in Table 6.

Table 6. Properties of Long Fractured Core 1

Core width and height = 3.81 cm			Core PV = 376 ml			
Fracture volume, $V_f$ , = 13.1 ml			Average $w_f$ = 0.029 cm, $k_f$ = 4,500 D			
Core section:	Entire core	1	2	3	4	5
Length, cm	115	23.0	23.0	23.0	23.0	23.0
$k_{av}$ , D	36.4	34.5	41.6	45.6	23.1	37.2
$k_f w_f$ , D-cm	138.0	129.1	155.9	171.4	85.7	139.4
$k_f w_f h_f / A k_m$	54.2	52.1	62.9	69.2	34.6	52.3

Using a Cr(III)-acetate-HPAM gel with the same composition as that mentioned earlier, we aged the gel for 24 hours and then forced 880 ml of gel through the fractured core at a rate of 200 ml/hr. Resistance factors observed in the five core sections during gel injection are shown in Fig. 19 as a function of the volume of gel injected. Resistance factors in each section of the core were more or less stable after injecting 500 ml of gel. The magnitude of the stabilized values varied from section to section. In the first and last sections ( $k_f w_f = 129$  and 139 darcy-cm), the stabilized resistance factors averaged 1,700. In the second and third sections ( $k_f w_f = 156$  and 171 darcy-cm), values averaged 3,100. In the fourth section ( $k_f w_f = 86$  darcy-cm), the stabilized value averaged 2,000. End effects may have been at least partly responsible for the relatively low values observed in the first and last sections.

Interestingly, about 450 ml (35 fracture volumes) of gel were injected before gel was produced from the core. The relatively slow propagation of the gel through the fracture can be seen from the resistance factor data in Fig. 19. This slow rate of gel propagation suggests that the gel is being dehydrated as it extrudes through the core—i.e., water from the gel leaks off into the porous rock while the polymer and chromium are left behind in the fracture. This suggestion is consistent with an observation made in a previous experiment<sup>2</sup>—the gel found in a fracture (upon disassembly of the core after the experiment) was significantly more rigid (Sydansk gel code<sup>15</sup>=I) than the gel was before injection (Sydansk gel code<sup>15</sup>=D).

The slow rate of gel propagation through the fracture is consistent with field observations that were reported earlier.<sup>1</sup> In some injection-well treatments, tracer studies were first performed to determine interwell transit times for water. Very rapid transit times were observed, confirming fractures as the cause of the channeling. When a Cr(III)-acetate-HPAM gel was injected, no gel was detected at the offset producers, even though the gel volume was ten times greater than the volume associated with transit of the water tracer between the wells. We note that other factors could also account for the delayed propagation of gels through fractures in field applications.<sup>1</sup>

These factors include leakoff of the viscous gelant before gelation, and extrusion of gel into alternate fracture pathways (in naturally fractured systems).

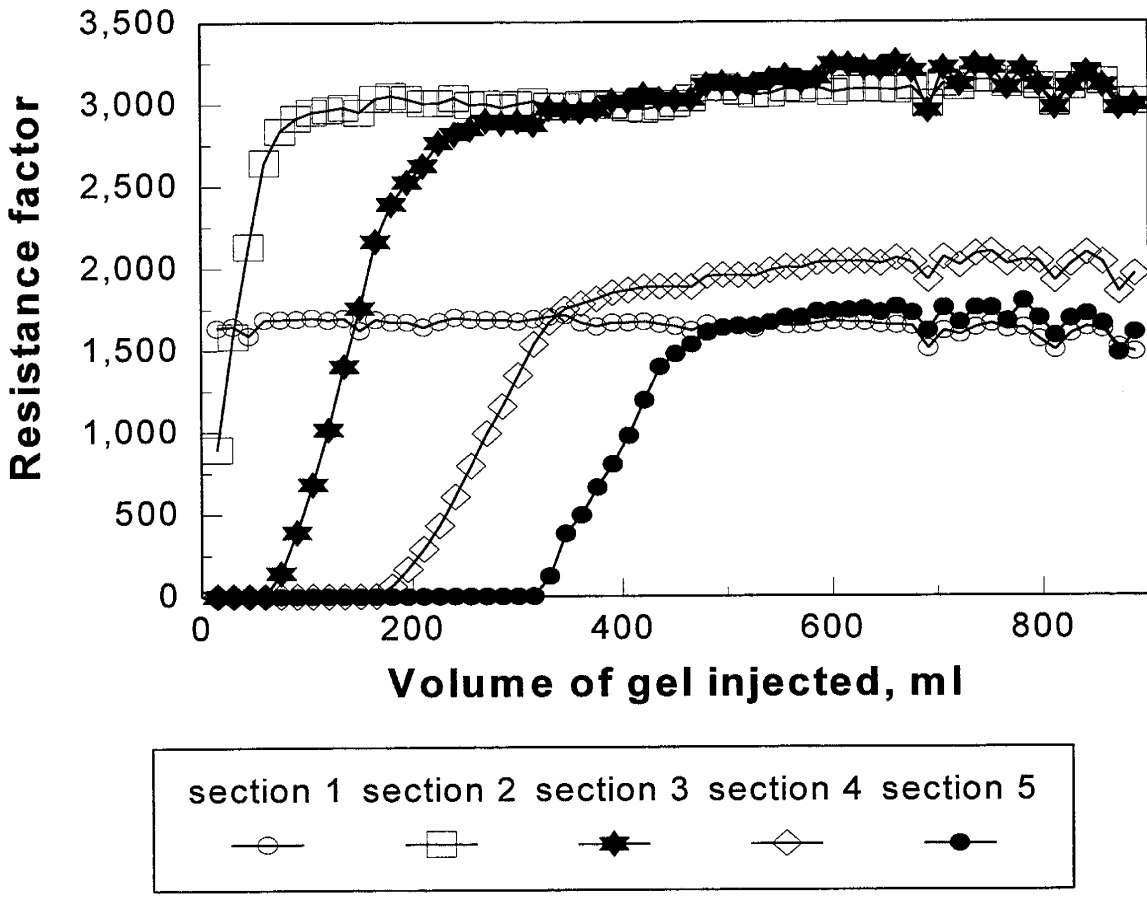


Fig. 19. Gel injection into a 115-cm-long fractured core.

We performed two similar experiments using Long Fractured Cores 4 and 5. As with Long Fractured Core 1, these cores were 115 to 122 cm in length and 14.5 cm<sup>2</sup> in cross-section (square). Four internal pressure taps were spaced equally along the length of the fracture. The average conductivities of these fractures in Cores 4 and 5 were 17,300 D-cm and 56,600 D-cm, respectively. Estimated fracture widths were 0.13 cm and 0.16 cm, respectively, and the estimated fracture permeabilities were 133,000 darcys and 360,000 darcys, respectively. Fracture volumes, determined from tracer studies, were 57.6 ml and 73.1 ml, respectively. Again, we forced preformed Cr(III)-acetate-HPAM gels through these fractures. The gels were aged at 41°C for either 10 or 24 hours before injection. By observing the effluent from a given core and the pressures along the core, we could monitor the gel front in the fracture during gel injection. Fig. 20 shows the results for experiments in Long Fractured Cores 1, 4, and 5. The positions of the gel fronts were plotted versus the fracture volumes of gel injected.

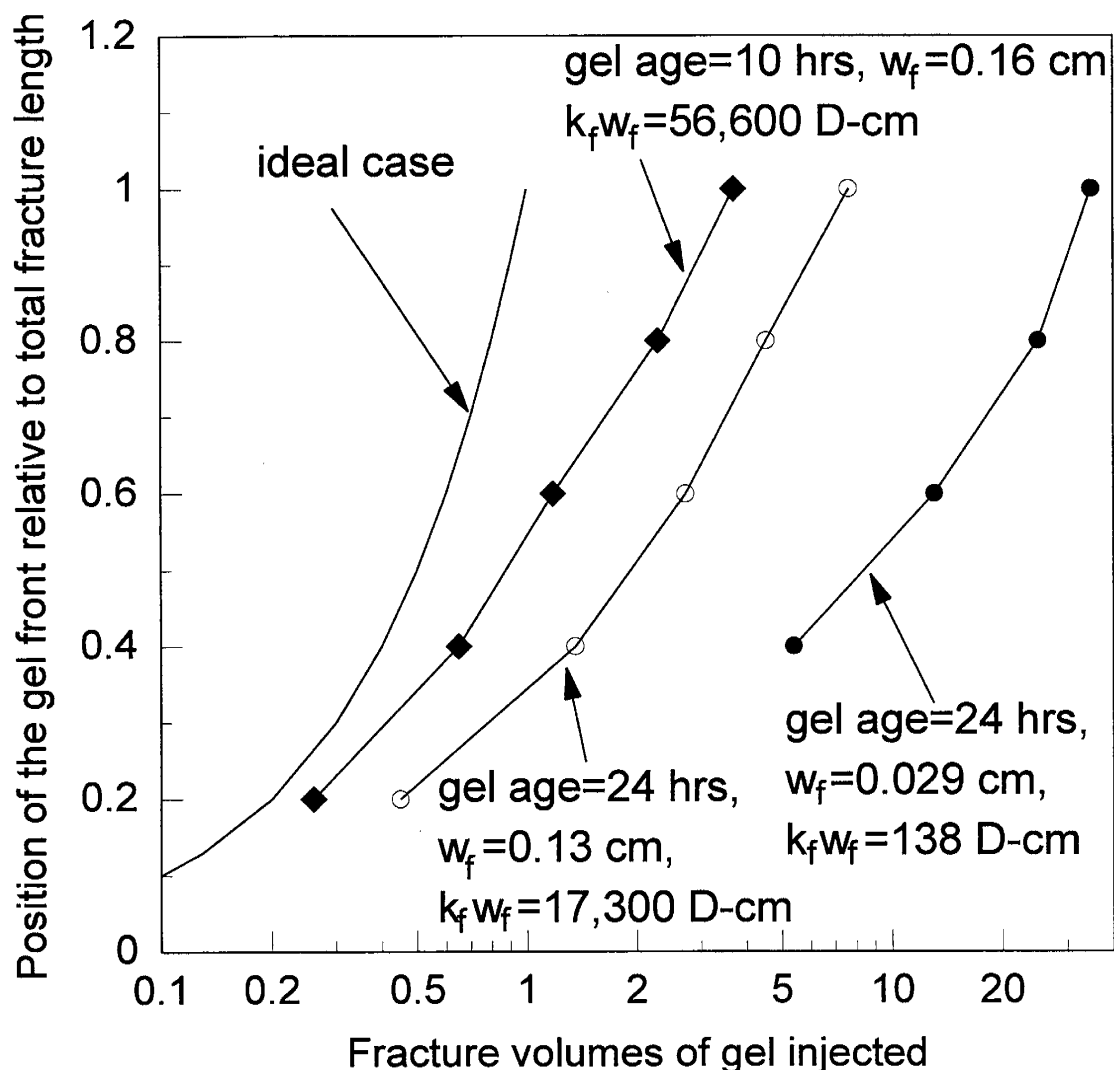


Fig. 20. Propagation of Cr(III)-acetate-HPAM gels through long fractured cores.

The curve without data points in Fig. 20 shows the ideal case expected if gel propagation was not retarded by gel dehydration or other factors (i.e., the fracture would be completely filled with gel after injecting one fracture volume of gel). For the three corefloods performed, gel transport was retarded to varying degrees, depending on the fracture conductivity and the age of the gel. The greatest retardation occurred for the 24-hr-old gel in the least conductive fracture ( $k_f w_f = 138$  D-cm). In that case, 35 fracture volumes were required for the gel to reach the end of the core (solid circles in Fig. 20). An average pressure gradient of 65.4 psi/ft was required to extrude the gel through this fracture. For comparison, a 24-hr-old gel in a fracture with  $k_f w_f = 17,300$  D-cm reached the end of the fracture after injecting 7.7 fracture volumes of gel (open circles in Fig. 20). In this case, the average pressure gradient was 10.8 psi/ft during gel injection. For the third coreflood (solid diamonds in Fig. 20), a 10-hr-old gel was extruded through a fracture with  $k_f w_f = 56,600$  D-cm. In this experiment, the gel reached the core outlet after injecting 3.7 fracture volumes of gel, and the average pressure gradient was 9.9 psi/ft. Consistent with our earlier results,<sup>5</sup> a minimum pressure gradient was required to extrude a given gel through a given

fracture. In other words, the pressure gradient was fairly insensitive to injection rate during extrusion of a given gel through a fracture.

The results in Fig. 20 indicate that the rate of gel propagation decreases and the degree of gel dehydration increases as fracture conductivity decreases. Of course, for a given injection rate, the pressure gradient increases with decreasing fracture conductivity. It seems likely that the level of gel dehydration is closely tied to the pressure gradient experienced by the gel.

Fig. 21 demonstrates that the rate of gel propagation decreases with increasing distance of penetration along a given fracture. Fig. 21 is identical to Fig. 20 except that three dashed curves have been added. For a given core experiment, the dashed line extrapolates the trend expected if gel propagated at a constant rate through the fracture. For example, for the fracture with  $k_f w_f = 138$  D-cm, the gel front was observed at the second internal pressure tap (40% of the distance through the fracture) after injecting 5.5 fracture volumes of gel. If this rate of gel propagation was constant, the gel front should have arrived at the fourth internal pressure tap (80% of the distance through the fracture) after injecting 11 fracture volumes of gel. Instead, the gel front arrived at the fourth internal pressure tap after injecting 25 fracture volumes of gel. Thus, the rate of gel propagation decreases as the gel penetrates deeper into the fracture. This behavior was evident during all three core experiments, as indicated by the positions and shapes of the dashed curves relative to the corresponding solid curves in Fig. 21.

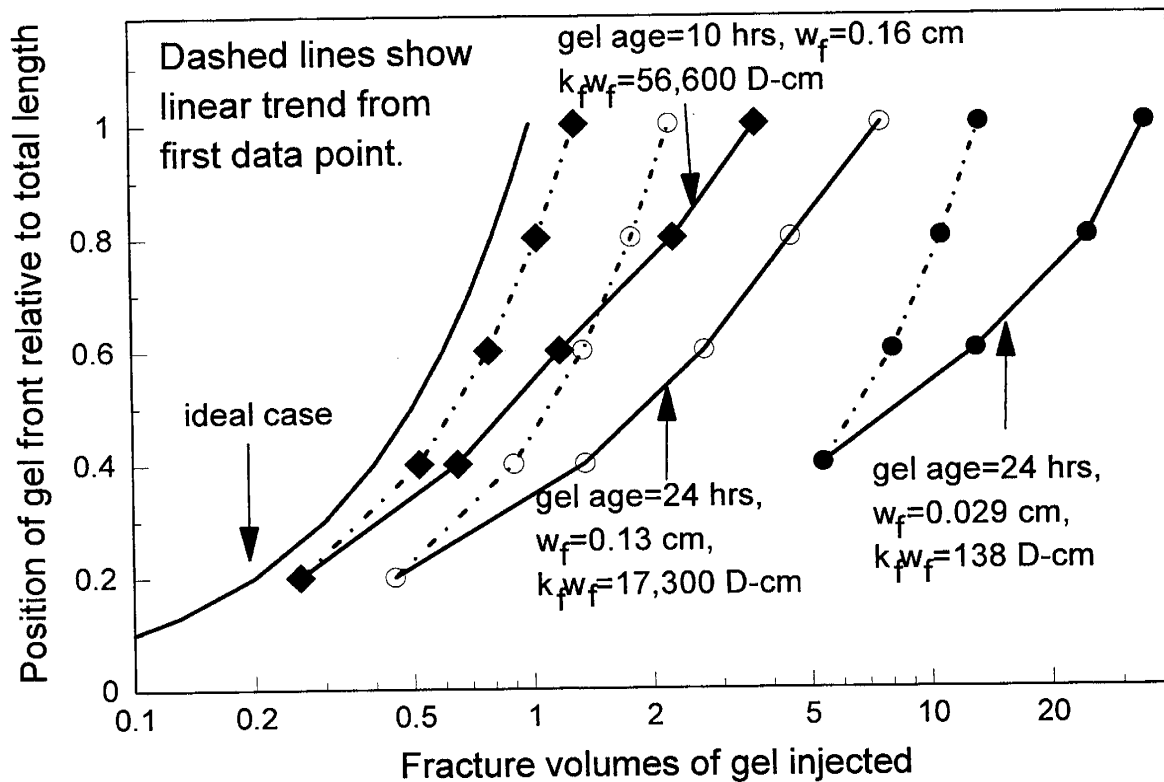


Fig. 21. The rate of gel propagation decreases as the gel penetrates deeper into the fracture.

## Effect of Fracture Conductivity on Gel Extrusion Through Fractures

An important question is, How does the ability of a given gel to extrude through a fracture vary with fracture conductivity (or fracture width or permeability)? For a Cr(III)-acetate-HPAM gel (same composition as that mentioned earlier) that was aged for 24 hours before injection, Fig. 22 plots gel resistance factor (in the fracture) versus fracture conductivity for 19 of our experiments. Similarly, Fig. 23 plots pressure gradient during gel injection versus fracture conductivity. In Fig. 22, the gel resistance factor averages about 3,000 for fracture conductivities below 1,100 D-cm (although there is a fair amount of data scatter). For fracture conductivities above 1,100 D-cm, resistance factors are proportional to fracture conductivity (in D-cm) times 2.7.

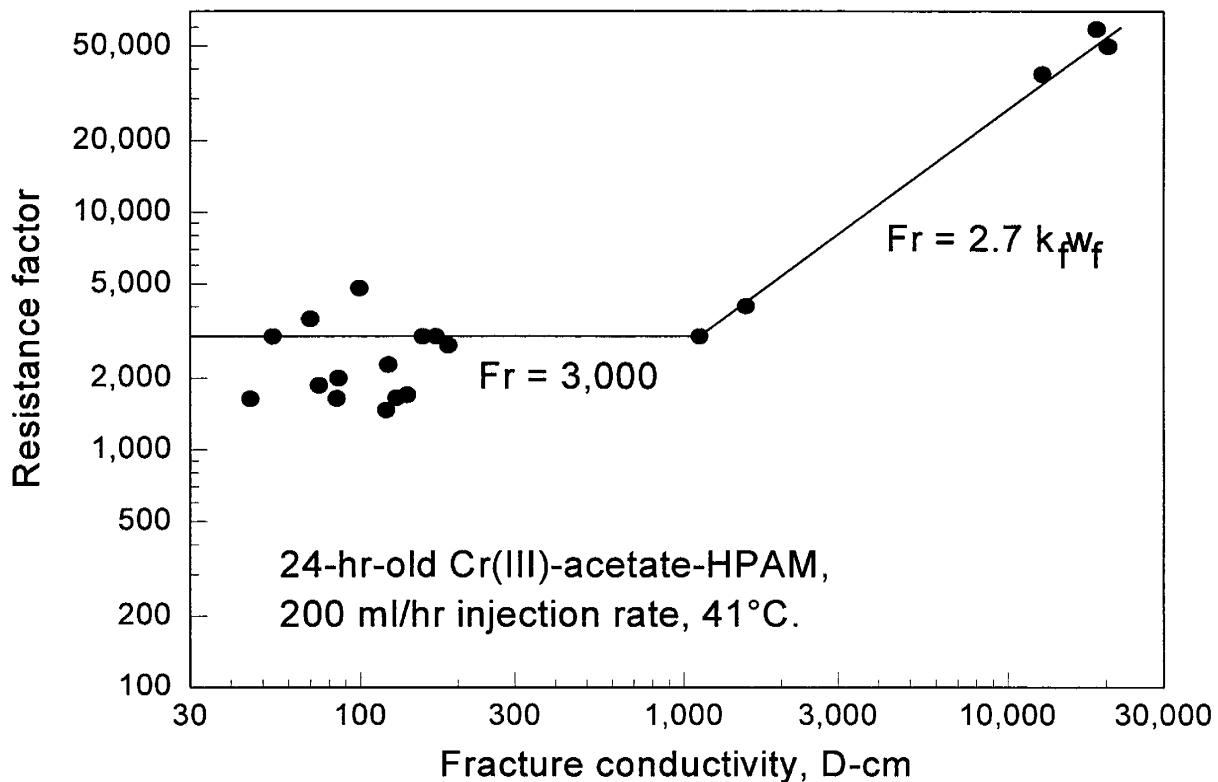


Fig. 22. Effect of fracture conductivity on resistance factors for a 24-hr-old Cr(III)-acetate-HPAM gel.

In Fig. 23, the pressure gradient averages 12 psi/ft for fracture conductivities above 1,100 D-cm. For fracture conductivities below 1,100 D-cm, pressure gradients are proportional to 13,000 divided by fracture conductivity (in D-cm). The relations illustrated in Figs. 22 and 23 provide hope that we may be able to predict gel flow properties during extrusion through fractures. (Fig. 5 and Table 7 can be used to estimate fracture widths and permeabilities from fracture conductivities. The values in Table 7 were calculated using Eq. 2.)

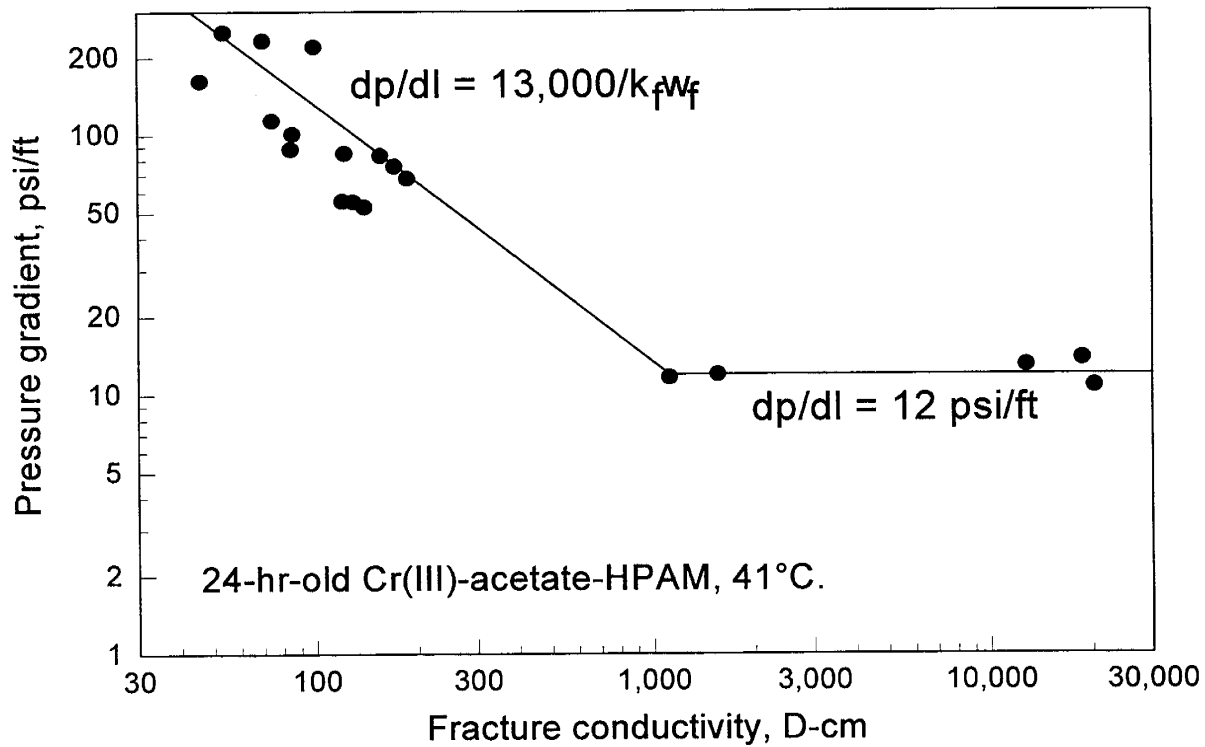


Fig. 23. Effect of fracture conductivity on pressure gradients during injection of a 24-hr-old Cr(III)-acetate-HPAM gel.

Table 7. Fracture Widths and Permeabilities from Eq. 2

$k_f w_f$ , D-cm	$w_f$ , cm	$k_f$ , darcys
$10^2$	0.0228	4,387
$10^3$	0.0491	20,360
$10^4$	0.106	94,510
$10^5$	0.228	438,700
$10^6$	0.491	2,036,000

For the most conductive fractures, the behavior observed in Fig. 22 is counter-intuitive. It seems surprising that the gel resistance factors (apparent viscosities) increase with increasing fracture conductivity (and therefore, fracture width). For comparative purposes, we replotted the resistance factors (from Fig. 22) versus fracture permeability (Fig. 24) and fracture width (Fig. 25). In Figs. 24 and 25, fracture permeabilities and widths were calculated using Eq. 2 and the

fracture conductivity data from Fig. 22. Calculated fracture permeabilities ranged from 2,600 to 152,000 darcys (Fig. 24), while the calculated fracture widths ranged from 0.017 to 0.14 cm (Fig. 25). For fracture permeabilities above 22,000 darcys, the relation between gel resistance factor and fracture permeability is described by Eq. 3.

$$F_r = 0.0011 k_f^{1.5} \tag{3}$$

For fracture widths above 0.05 cm, the relation between gel resistance factor and fracture width is described by Eq. 4.

$$F_r = 2,610,000 w_f^3 \tag{4}$$

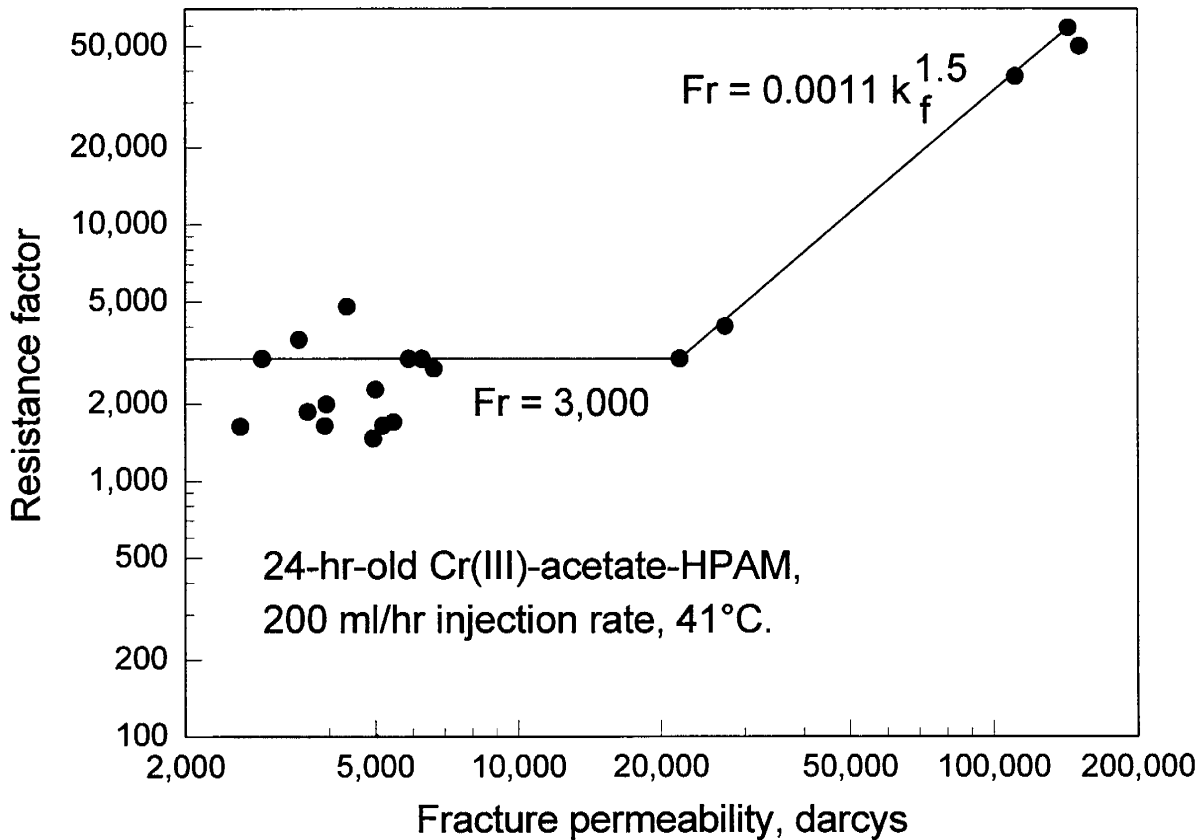


Fig. 24. Resistance factor versus fracture permeability.

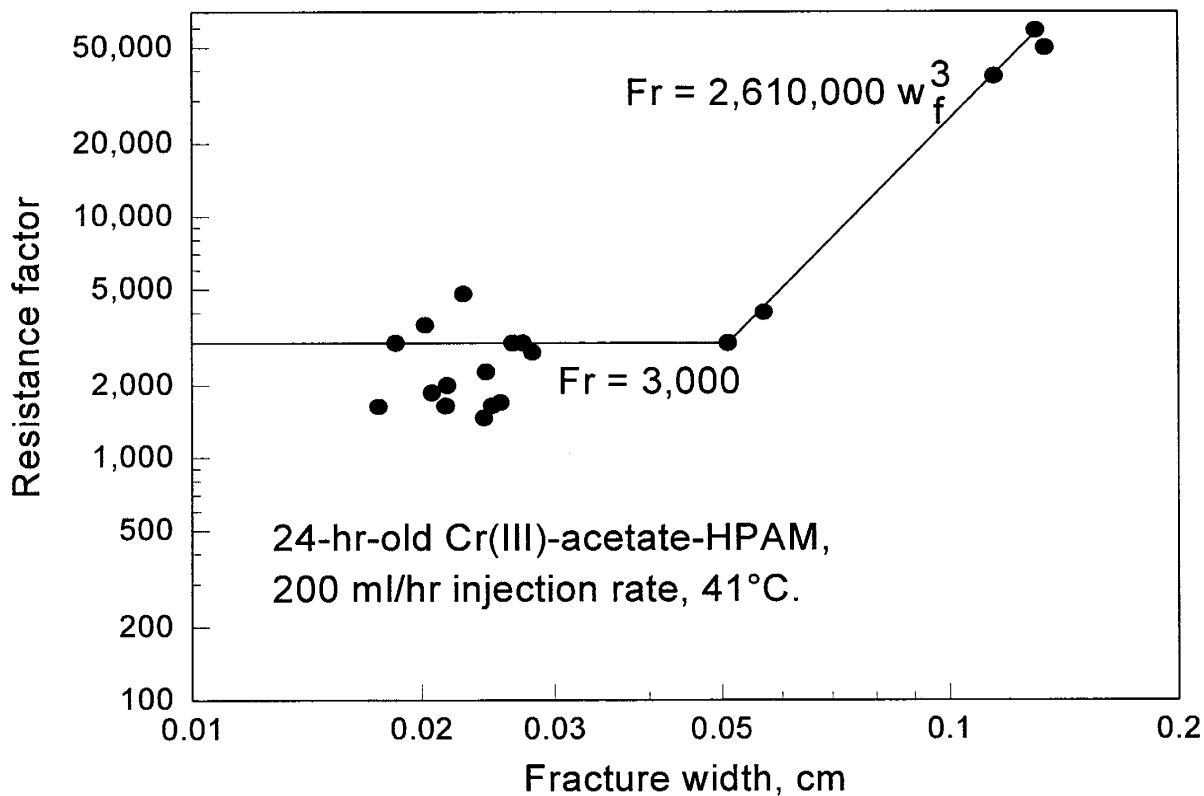


Fig. 25. Resistance factor versus fracture width.

### Effect of Gel in Fractures on Oil Flow Versus Water Flow

In porous rock, gels can reduce the permeability to water much more than to oil or gas.<sup>18-20</sup> Will gels show this same behavior in fractures? We found that a Cr(III)-acetate-HPAM gel effectively stops both water and oil flow in fractures. To demonstrate this result, we performed a comprehensive sequence of experiments in Short Fractured Core 41. This sequence is summarized in Table 8. Core 41 was 14.5 cm in length and 3.56 cm in diameter. Before fracturing, this Berea sandstone core had a nominal permeability to brine of 650 md. Since the brine viscosity was 0.67 cp at 41°C, the brine mobility was about 970 md/cp (first data row of Table 8).

After fracturing, the conductivity of the induced fracture was 99.5 D-cm, resulting in an apparent brine mobility of 54,100 md/cp. Tracer studies indicated that the fracture volume was 1.1 ml (4% of the total PV), and the average fracture width was 0.022 cm. This result suggested that the average permeability of the fracture was 4,500 darcys.

After characterizing the fracture, we injected 10 PV (317 ml or 300 fracture volumes) of a 24-hr-old Cr(III)-acetate-HPAM gel with the same composition as that mentioned earlier. The injection rate

was 200 ml/hr during this and all subsequent steps. The resistance factor ( $F_r$ ) was stable at 4,800 during gel injection. The apparent mobility was 11.3 md/cp, and the pressure gradient was 220 psi/ft. After gel placement, the core was shut in for 5 days.

Table 8. In Fractures, Gels Can Prevent Flow of Both Water and Oil.  
Short Fractured Core 41. 24-hr-old Cr(III)-acetate-HPAM gel. 200 ml/hr rate. 41°C.

Injectant	$k/\mu$ , md/cp	dp/dl, psi/ft	$S_{gel}$ , %	$S_w$ , %	$S_o$ , %	Observations
brine before fracturing	≈970	2.6	0	100	0	≈ 650-md Berea sandstone, $L=14.5$ cm, $A=10$ cm <sup>2</sup>
brine after fracturing	54,100	0.046	0	100	0	$k_f w_f = 99.5$ D-cm, $k_f w_f h_f / A k_m = 55$ , $w_f \approx 0.022$ cm, $k_f \approx 4,500$ D, $h_f = 3.56$ cm
10 PV gel	11.3	220	4	96	0	$F_r = 4,800$
20 PV brine	940	3	4	96	0	$F_{rrw} = 57 \approx k_f w_f h_f / A k_m \rightarrow$ fracture healed
20 PV oil	321	8	4	40	56	$k_{ro}$ (0.49) and $S_{wr}$ consistent with values for unfractured cores at $S_{wr}$
20 PV brine	67	37	4	60	36	$k_{rw}$ (0.07) and $S_{or}$ consistent with values for unfractured cores at $S_{or}$
20 PV oil	343	7	4	37	59	$k_{ro} = 0.53$
20 PV brine	69	36	4	60	36	$k_{rw} = 0.07$
20 PV oil	340	7	4	35	61	$k_{ro} = 0.52$
20 PV brine	70	36	4	59	37	$k_{rw} = 0.07$

After the shut-in period, gel was removed from the flow lines and scraped from the inlet and outlet sandfaces. (This is our standard procedure.<sup>2</sup>) Then, 20 PV of brine were injected. During this phase, the apparent brine mobility was 940 md/cp, and the residual resistance factor ( $F_{rrw}$ ) was 57. For comparison, values of 970 md/cp and 55, respectively, were expected for perfect healing of the fracture (see Table 8). Results from a tracer study performed during brine injection after gel placement are shown by the solid diamonds in Fig. 26. These results confirm that the gel treatment was reasonably effective at healing the fracture while causing minimal damage to the porous rock.

Next, 20 PV of Soltrol 130<sup>®</sup> oil were injected. During oil injection, the apparent mobility stabilized at 321 md/cp. Since the viscosity of this oil was 1.0 cp at 41°C, the endpoint permeability to oil (relative to the absolute brine permeability) was 0.49 ( $321$  md/cp  $\times$   $1.0$  cp  $\div$   $970$  md/cp  $\div$   $0.67$  cp). At the end of oil injection, the core pore volume contained 4% gel (presumably, all in the

fracture), 40% water, and 56% oil. These values for  $k_{ro}$  (0.49) and  $S_{wr}$  (40%) are consistent with the values expected for an unfractured Berea core, after allowing for a small amount of damage to the sandface by the gel.<sup>19</sup> This result suggests that most or all of the oil flowed through the porous rock rather than through the fracture. In other words, the gel prevented flow of oil, as well as water, through the fracture.

Next, 20 PV of brine were injected (Table 8). The apparent brine mobility stabilized at 67 md/cp, which corresponds to an endpoint relative permeability to brine ( $k_{rw}$ ) of 0.07 (67 md/cp ÷ 970 md/cp). At the end of brine injection, the core pore volume contained 4% gel, 60% water, and 36% oil. These values for  $k_{rw}$  (0.07) and  $S_{or}$  (36%) are consistent with the values expected for an unfractured Berea core, after allowing for a small amount of damage to the sandface by the gel.<sup>19</sup>

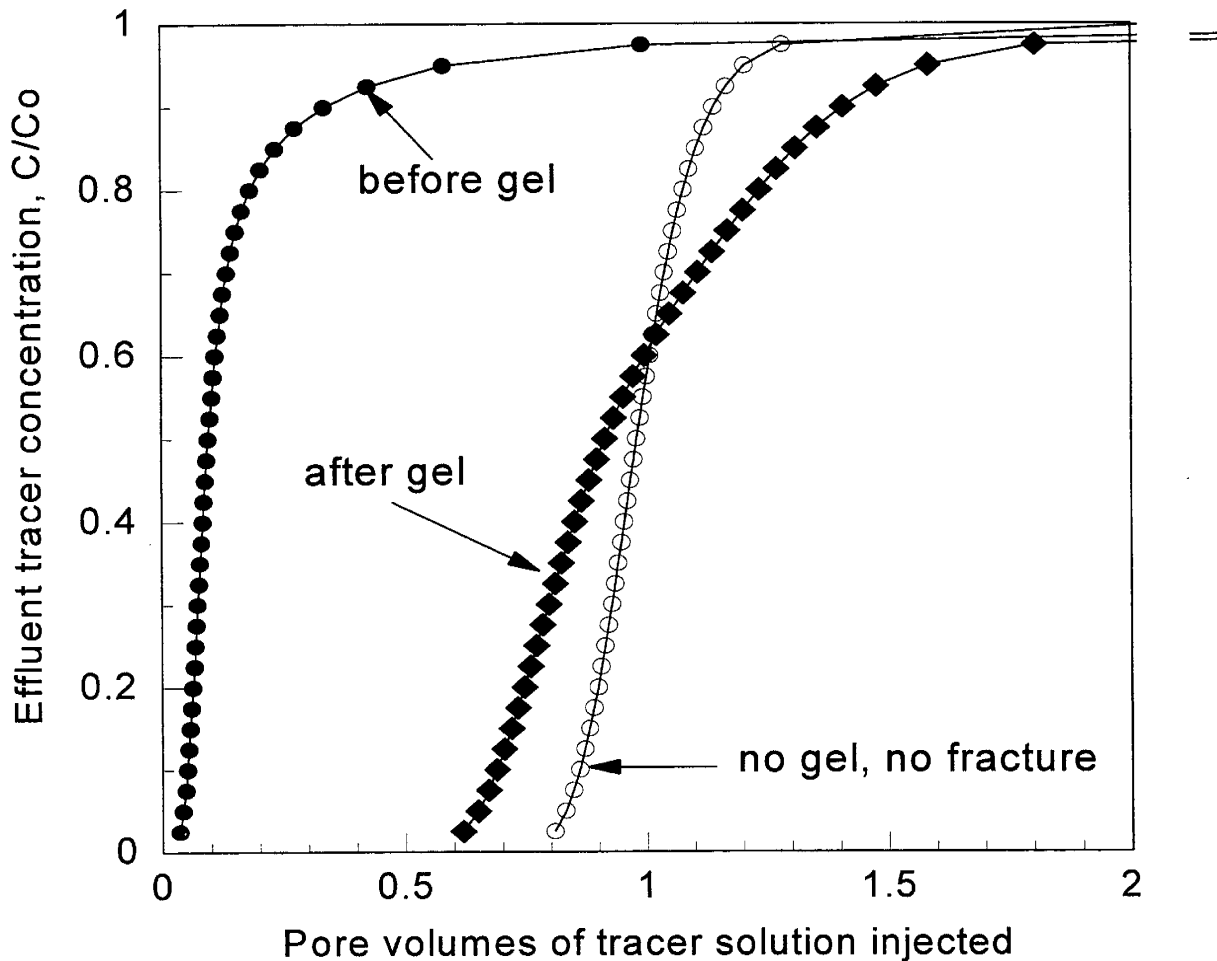


Fig. 26. Tracer results before versus after placement of a 24-hr-old Cr(III)-acetate-HPAM gel in Short Fractured Core 41.

Next, another 20 PV of oil were injected. The apparent oil mobility stabilized at 343 md/cp, which corresponds to an endpoint relative permeability to oil of 0.53 ( $343 \text{ md/cp} \times 1.0 \text{ cp} \div 970 \text{ md/cp} \div 0.67 \text{ cp}$ ). At the end of oil injection, the core pore volume contained 4% gel, 37% water, and 59% oil. These permeability and saturation values are very similar to those observed during the first cycle of oil injection.

During the next cycle of water and oil injection, the calculated endpoint permeabilities remained basically unchanged. Also, when both water and oil were present, water- and oil-tracer results remained basically unchanged during the various cycles of water and oil injection (see Figs. 27 and 28). (Details of how these tracer studies were performed have been described earlier in Refs. 13 and 18.) These results suggest that the gel did not experience significant washout during the cycles.

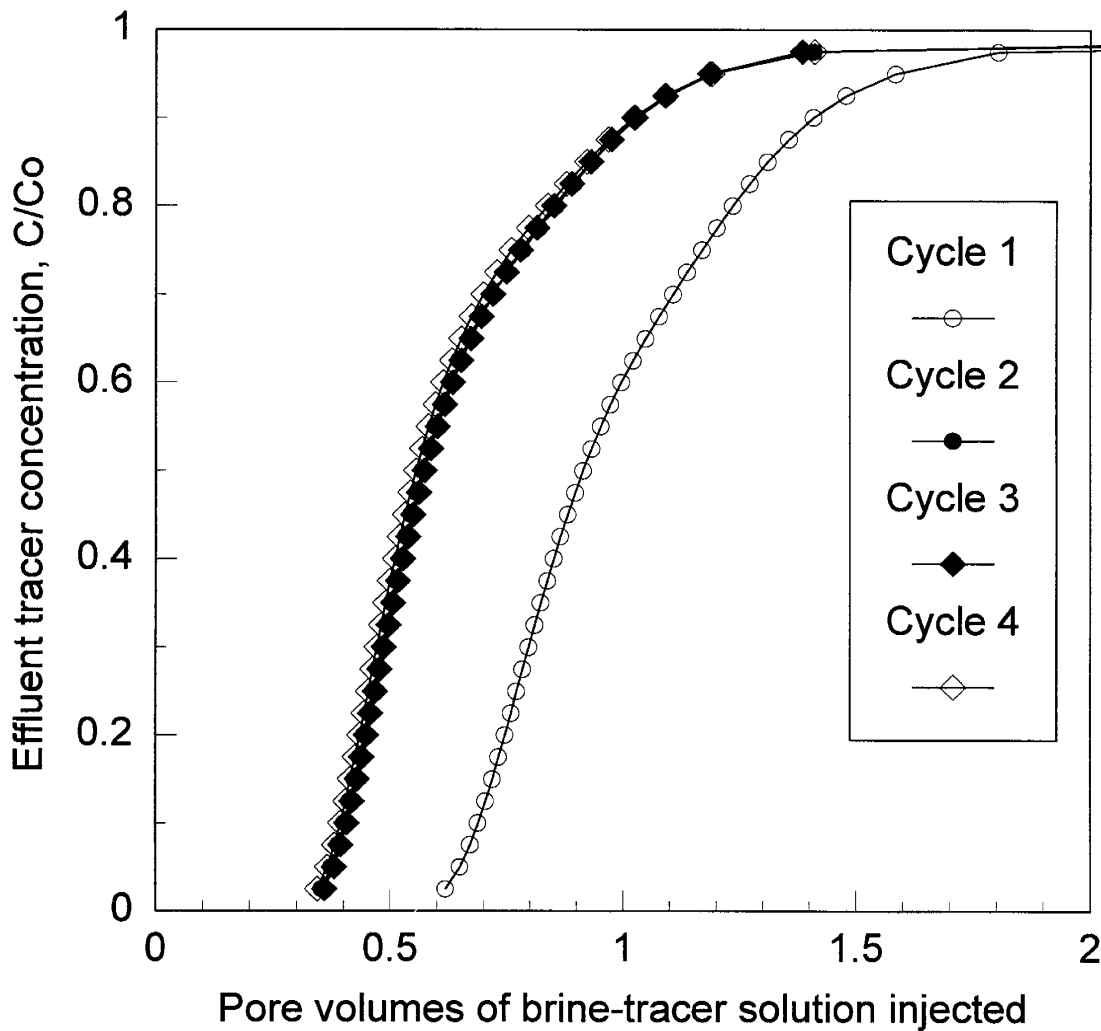


Fig. 27. Tracer results during brine injection after gel placement in Short Fractured Core 41 for several cycles of water/oil injection.

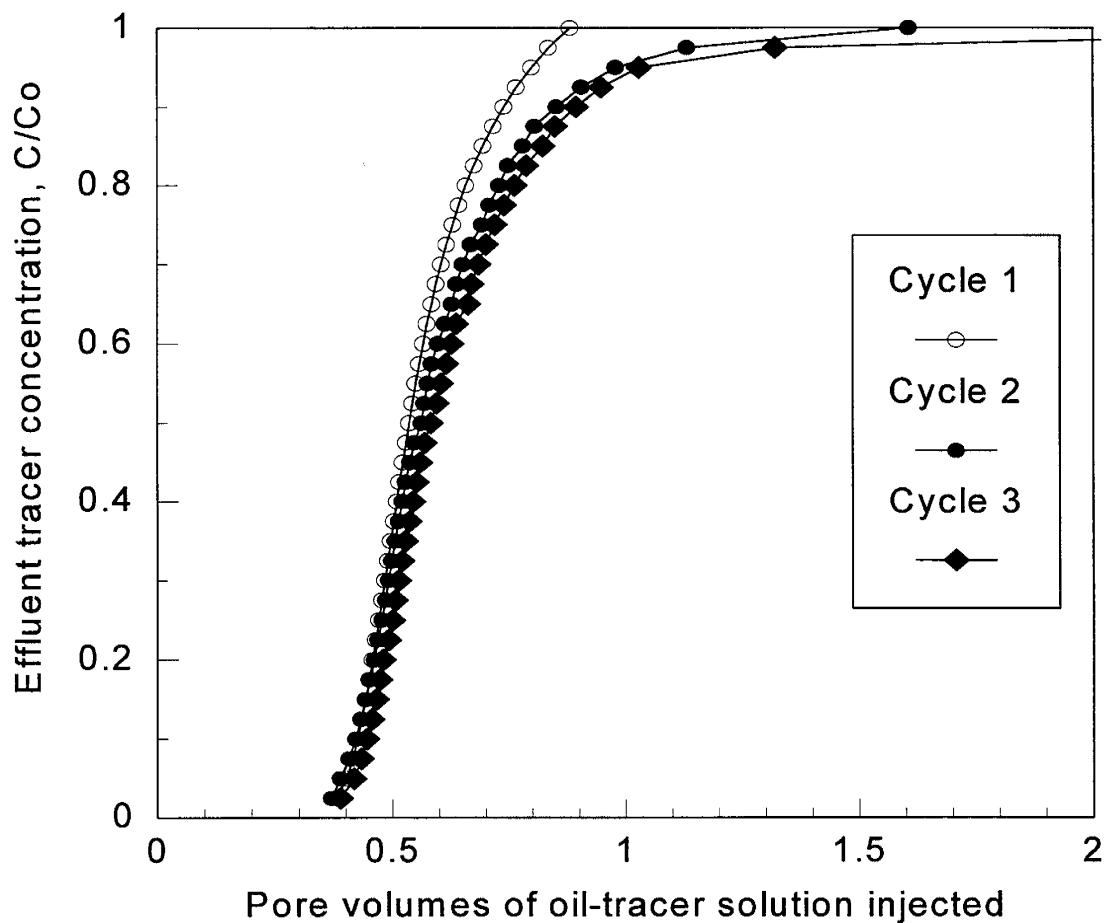


Fig. 28. Tracer results during oil injection after gel placement in Short Fractured Core 41 for several cycles of water/oil injection.

In summary, our results in Short Fractured Core 41 indicated that although the Cr(III)-acetate-HPAM gel can reduce  $k_{rw}$  much more than  $k_{ro}$  in porous media,<sup>18</sup> it effectively stops both water and oil flow in fractures.

## A Comparison of the Placement Properties of Preformed Gels and Water-Like Gelants

**Fracture Model.** We now wish to use the experimental results that were presented in the first part of this chapter to assess whether preformed gels have placement advantages over gels formed in situ from gelants. We focus on a simple model of a fractured reservoir that is illustrated in Fig. 29. Consider an injector-producer pair where Fracture 1 allows injected water to channel very directly from the injection well to the production well. Fracture 1 has an effective length,  $L_{f1}$ , and an effective permeability,  $k_1$ . This reservoir also contains a second fracture, Fracture 2, that has a beneficial role in oil recovery. Specifically, Fracture 2 meanders from the injection well to the production well in a way that is much less direct than Fracture 1. Because of its length and orientation, Fracture 2 allows the injected water to be well distributed in the reservoir and allows a high water injectivity (relative to the case where no fractures exist). (Of course, Fracture 1 also allows a high water injectivity, but most of that water simple channels directly to the production well.) Fracture 2 also acts as a conduit for oil flowing to the production well so that a relatively high oil productivity can be maintained. Fracture 2 has an effective length,  $L_{f2}$ , and an effective permeability,  $k_2$ . Generally, Fracture 2 will be longer and have a lower conductivity (lower effective fracture permeability) than Fracture 1.

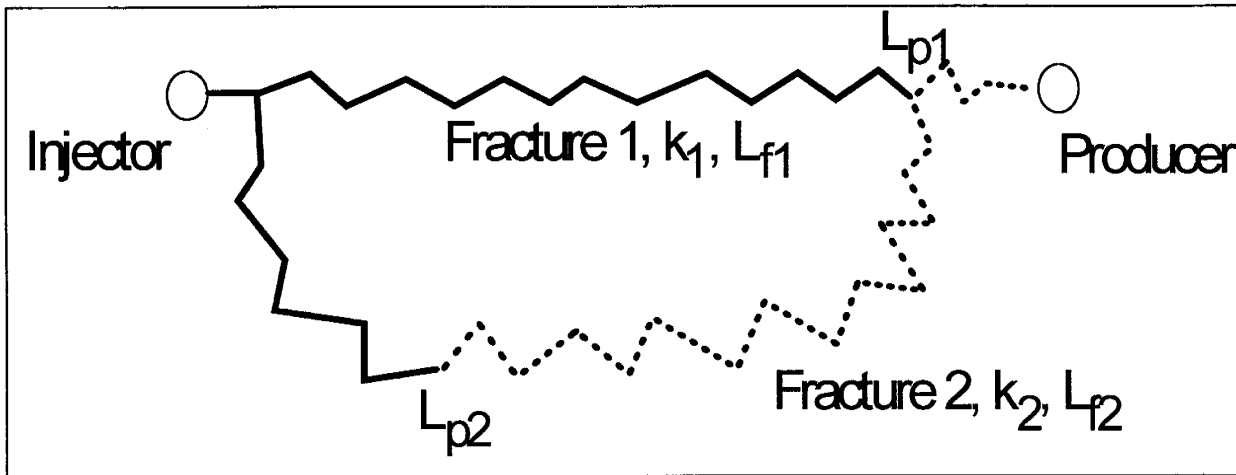


Fig. 29. Schematic of an injector-producer pair connected by two fractures.

Ideally, a gel treatment will substantially reduce the flow capacity of Fracture 1 while having little or no effect on the flow capacity of Fracture 2. Thus, we wish to maximize penetration of gel into Fracture 1 and minimize gel penetration into Fracture 2. The question is then raised, For a given distance ( $L_{p1}$ ) of gel penetration into Fracture 1, how far ( $L_{p2}$ ) will the gel penetrate into Fracture 2? In Appendix A, we derive Eq. 5, that can be used to answer this question.

$$\frac{L_{p2}}{L_{p1}} = \frac{\left[ \left( \frac{L_{f2}}{L_{p1}} \right)^2 + 2 (F_{r2} - 1) \left( \frac{k_2}{k_1} \right) \left( \frac{1 + a_{r1}}{1 + a_{r2}} \right) \left( \frac{L_{f1}}{L_{p1}} + \frac{F_{r1} - 1}{2} \right) \right]^{0.5} - \frac{L_{f2}}{L_{p1}}}{F_{r2} - 1} \quad (5)$$

**Assumptions.** The assumptions used in the derivation of Eq. 5 are as follows:

1. Fluids are incompressible.
2. Displacement is miscible and piston-like.
3. Dispersion, capillary effects, and gravity effects are negligible.
4. All factors that can retard gel propagation (such as dehydration, leakoff, adsorption, and mechanical entrapment) are included in the propagation delay factor,  $a_r$ .
5. In a given fracture,  $a_r$ ,  $k_f$ ,  $w_f$  (fracture width),  $h_f$  (fracture height), and gel resistance factor are constant. (These parameters may have different values in different fractures.)
6. Flow of gel in a given fracture is effectively linear.
7. The fractures are initially filled with fluids with water-like viscosities.

The form and derivation of Eq. 5 are very similar to those for the equations predicting gelant placement in linear flow systems.<sup>21</sup> Certainly, there are limitations associated with the use of Eq. 5. For example, the equation assumes that the gel propagation delay factor,  $a_r$ , is independent of the distance of penetration into the fracture. Earlier in this chapter, we demonstrated that this assumption is not correct. Even so, Eq. 5 provides a means to give a rough idea of the placement properties of preformed gels. An important area for future work will involve testing how the predictions from our simple model change when the above assumptions are relaxed.

In the meantime, Eq. 5 allows one to estimate placement of preformed gels as a function of differences in fracture permeability, fracture length, gel resistance factor, and gel propagation delay factor.

**Effects of Differences in Fracture Permeability and Gel Resistance Factor.** In most circumstances, Fracture 1 is expected to be more permeable than Fracture 2. So, how does the degree of gel penetration,  $L_{p2}/L_{p1}$ , vary with the fracture permeability ratio? Fig. 30 answers this question for several cases of gel resistance factor. (In this figure, which was generated using Eq. 5, both fractures were assumed to have the same length.) The curve with the solid diamonds illustrates the case where the gel resistance factor is fixed at a value of 3,000. (Recall from Figs. 22 and 24 that a 24-hr-old Cr(III)-acetate-HPAM gel provided an average resistance factor of 3,000 for fracture conductivities below 1,100 D-cm and for fracture permeabilities below 22,000 darcys.) In this case, when Fracture 1 is 10 times more permeable than Fracture 2, the gel penetrates 31.6% as far in Fracture 2 as it does in Fracture 1 ( $L_{p2}/L_{p1}=0.316$ ).

For comparison, the best case illustrated in Fig. 30 involves the use of a gelant with a water-like viscosity, where  $F_r=1$ . In that case, when Fracture 1 is 10 times more permeable than Fracture 2, the gel penetrates 10.0% as far in Fracture 2 as it does in Fracture 1 ( $L_{p2}/L_{p1}=0.10$ ). [Both of the above cases assume that the gel propagation delay factor is the same in both fractures (i.e.,  $a_{r1}=a_{r2}$ ).] This result is particularly interesting because it suggests that water-like gelants may have much better placement properties than preformed gels when treating naturally fractured reservoirs.

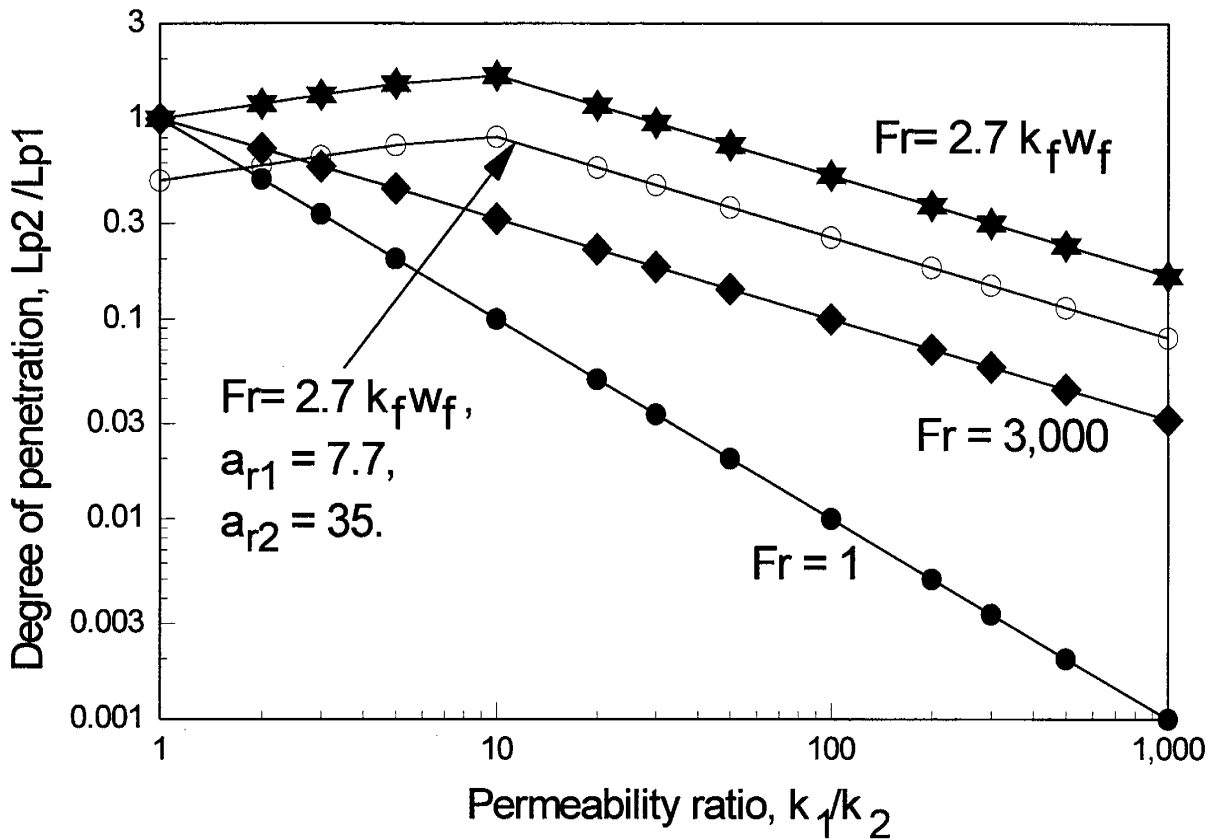


Fig. 30. Gelants with water-like viscosities provide more favorable placement properties than preformed gels.

The curve with the solid stars in Fig. 30 illustrates a third case, where the gel resistance factors followed the behavior shown in Fig. 22. In this case, the conductivity of Fracture 1 was assumed to be 30,000 D-cm, and the resistance factor was assumed to be 81,000 (i.e.,  $2.7 \times 30,000$ ). For a given ratio,  $k_1/k_2$ , the conductivity of Fracture 2 was calculated using Eq. 2. If the conductivity of Fracture 2 was between 1,100 and 30,000 D-cm, the resistance factor in Fracture 2 was calculated using  $F_r = 2.7 k_f w_f$ . If the conductivity of Fracture 2 was less than 1,100 D-cm, a value of 3,000 was used for the resistance factor in Fracture 2. The curve with the solid stars in Fig. 30 shows that  $L_{p2}/L_{p1}$  actually increases with increasing permeability ratio until  $k_1/k_2$  reaches a value around 10 (where the conductivity of Fracture 2 has a value of 1,100 D-cm). In other words, the behavior shown on the right side of Fig. 22 causes the gel to penetrate farther into Fracture 2 than into the more-permeable Fracture 1. Thus, the behavior where  $F_r = 2.7 k_f w_f$  is detrimental to gel placement.

In the three cases considered above, the gel propagation delay factor ( $a_r$ ) was assumed to be the same in Fractures 1 and 2. However, for a given preformed gel, Fig. 20 indicates that the  $a_r$  value should decrease with increasing fracture conductivity. In particular, Fig. 20 suggests that the  $a_r$  values are 7.7 and 35 when  $k_f w_f$  values are 17,300 D-cm and 138 D-cm, respectively. (In

other words, 7.7 fracture volumes of gel must be injected to fill the 17,300 D-cm fracture, while 35 fracture volumes of gel must be injected to fill the 138 D-cm fracture.) The curve with the open circles in Fig. 30 was generated using the same resistance factor relation as that used to generate the curve with the solid stars, except  $a_{r1}$  (in Eq. 5) was assigned a value of 7.7 and  $a_{r2}$  was valued at 35. When  $k_1/k_2=1$ ,  $L_{p2}/L_{p1}$  was reduced from a value of 1 for the case where  $a_{r1}=a_{r2}$ , to a value of 0.492 for the case where  $a_{r1}$  is 7.7 and  $a_{r2}$  is 35. Thus, at first glance, the difference in  $a_r$  values appears to have a significant beneficial effect on the degree of penetration. However, remember that these particular gel propagation delay factors (7.7 and 35, respectively) applied only when the fracture conductivity ratio was 17,300 to 138—which translates to a fracture permeability ratio of 25 [i.e.,  $(17,300/138)^{2/3}$ ]. In Fig. 30, for  $k_1/k_2=25$ , the open-circle curve is substantially above the solid-circle curve. Therefore, the placement properties for a gelant with a water-like resistance factor appear to be significantly better than those for the preformed gel. This conclusion assumes that all other factors are equal. Of course, differences in such factors as gravity effects and gelation chemistry could ultimately change this conclusion.

**Effect of Differences in Fracture Length.** In the above discussion, we assumed that Fractures 1 and 2 had the same length. In reality, Fracture 1 (the most direct channel between the wells) will probably be significantly shorter than Fracture 2. How will the degree of gel penetration,  $L_{p2}/L_{p1}$ , be affected by the fracture length ratio,  $L_{f2}/L_{f1}$ ? This question is addressed in Fig. 31 for a fixed fracture permeability ratio,  $k_1/k_2=10$ . The curve with the open circles plots  $L_{p2}/L_{p1}$  versus  $L_{f2}/L_{f1}$  for the case where the resistance factor in both fractures has a constant value of 3,000. Interestingly,  $L_{p2}/L_{p1}$  is insensitive to  $L_{f2}/L_{f1}$  for  $L_{f2}/L_{f1}$  values below 300. This result indicates that for preformed gels with high  $F_r$  values,  $L_{p2}/L_{p1}$  is insensitive to differences in total fracture length. This result occurs simply because the resistance to flow in the gel-filled portions of the fracture is much larger than that in the portions of the fracture that do not contain gel.

In Fig. 31, the curve with the solid circles plots  $L_{p2}/L_{p1}$  versus  $L_{f2}/L_{f1}$  for the case where a gelant is used that has a water-like resistance factor ( $F_r=1$ ). For all fracture length ratios considered,  $L_{p2}/L_{p1}$  is substantially less than the case where  $F_r=3,000$ . Also,  $L_{p2}/L_{p1}$  decreases substantially with increasing  $L_{f2}/L_{f1}$  values. These observations further indicate merit in considering water-like gelants in naturally fractured reservoirs.

The three intermediate curves in Fig. 31 illustrate cases where the resistance factors for preformed gels vary from 2 to 100. As expected, these cases demonstrate that  $L_{p2}/L_{p1}$  increases with increasing gel resistance factor. These curves should be considered hypothetical since we have not identified real, effective preformed gels that provide these low resistance factors. In our work to date, we have observed preformed gels with resistance factors as low as 100, but these gels were ineffective because they washed out of the fracture too easily during brine flow after gel placement. Of course, gelants are known that will provide resistance factors between 2 and 100, but these viscous gelants can leak off from the fracture in a way that is not taken into account during the calculations that generated Fig. 31.

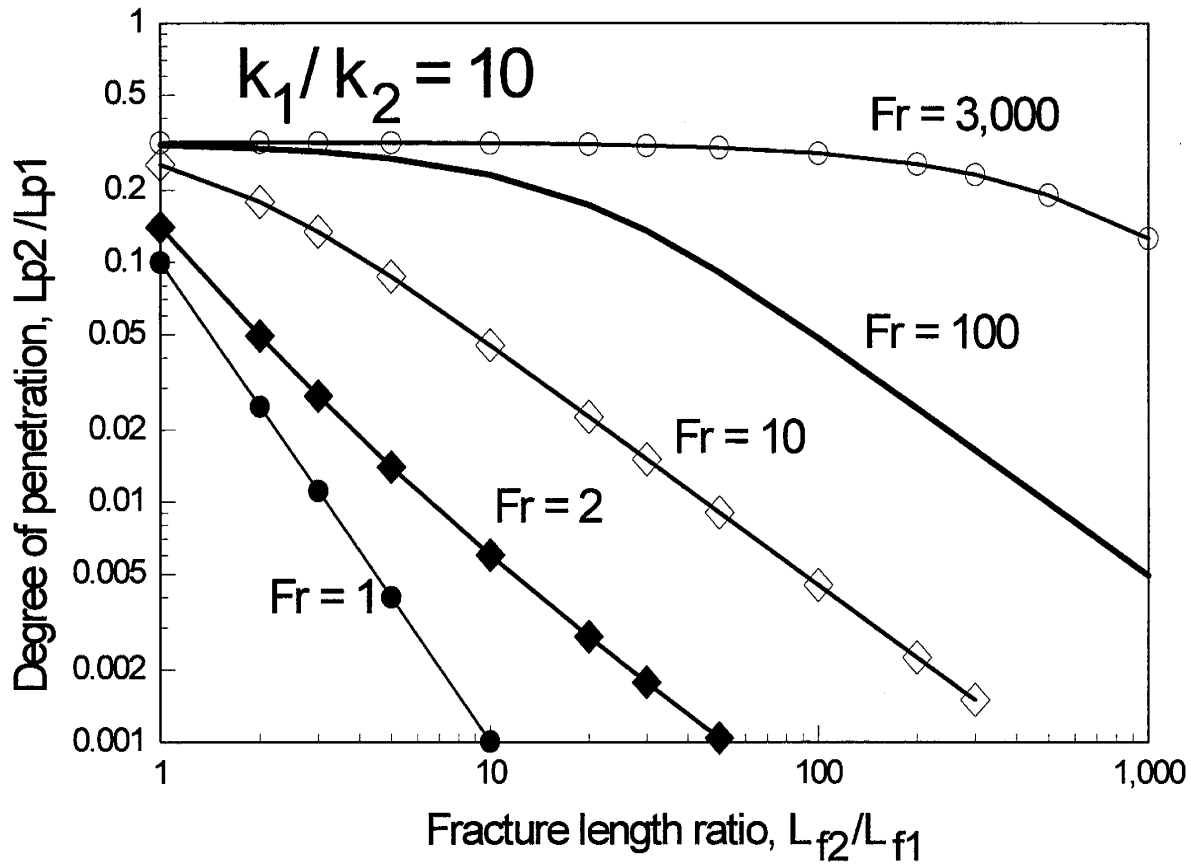


Fig. 31. Placement for preformed gels is insensitive to the fracture length ratio.

**Effect of Differences in Gel Propagation Delay Factor ( $a_r$ ).** In most of the previous discussion, we assumed that if gel transport in Fracture 1 was delayed (e.g., because of dehydration, adsorption, or leakoff), gel transport would be delayed by the same factor in Fracture 2. In this section, we examine the effect of differences in gel propagation delay factor ( $a_r$ ) on the relative distances of gel propagation,  $L_{p2}/L_{p1}$ . Fig. 32 plots the degree of penetration versus the delay factor for gel propagation in Fracture 1 ( $a_{r1}$ ). These results apply to a fixed fracture permeability ratio ( $k_1/k_2=10$ ), a constant gel resistance factor ( $F_r=3,000$ ), and the same lengths for Fractures 1 and 2. Three cases are illustrated in Fig. 32: (1)  $a_{r2}=a_{r1}$ , (2)  $a_{r2}=2a_{r1}$ , and (3)  $a_{r2}=10a_{r1}$ . In all three cases,  $L_{p2}/L_{p1}$  is not sensitive to  $a_{r1}$  for practical values of the delay factor. Also, the degree of penetration is only moderately affected by differences in the delay factor. For example, a 10-fold difference in delay factor only causes a 3-fold reduction in the degree of penetration. (Compare the open-circle curve in Fig. 32 with the curve without symbols.) Recall from Fig. 20 that a 125-fold fracture-conductivity difference (17,300 D-cm versus 138 D-cm) resulted in less than a 5-fold difference in  $a_r$  value (35 versus 7.7). Therefore, we do not expect differences in gel propagation delay factors to have a large effect on  $L_{p2}/L_{p1}$  unless these differences are extreme (which would indicate that the differences in fracture conductivity are even more extreme).

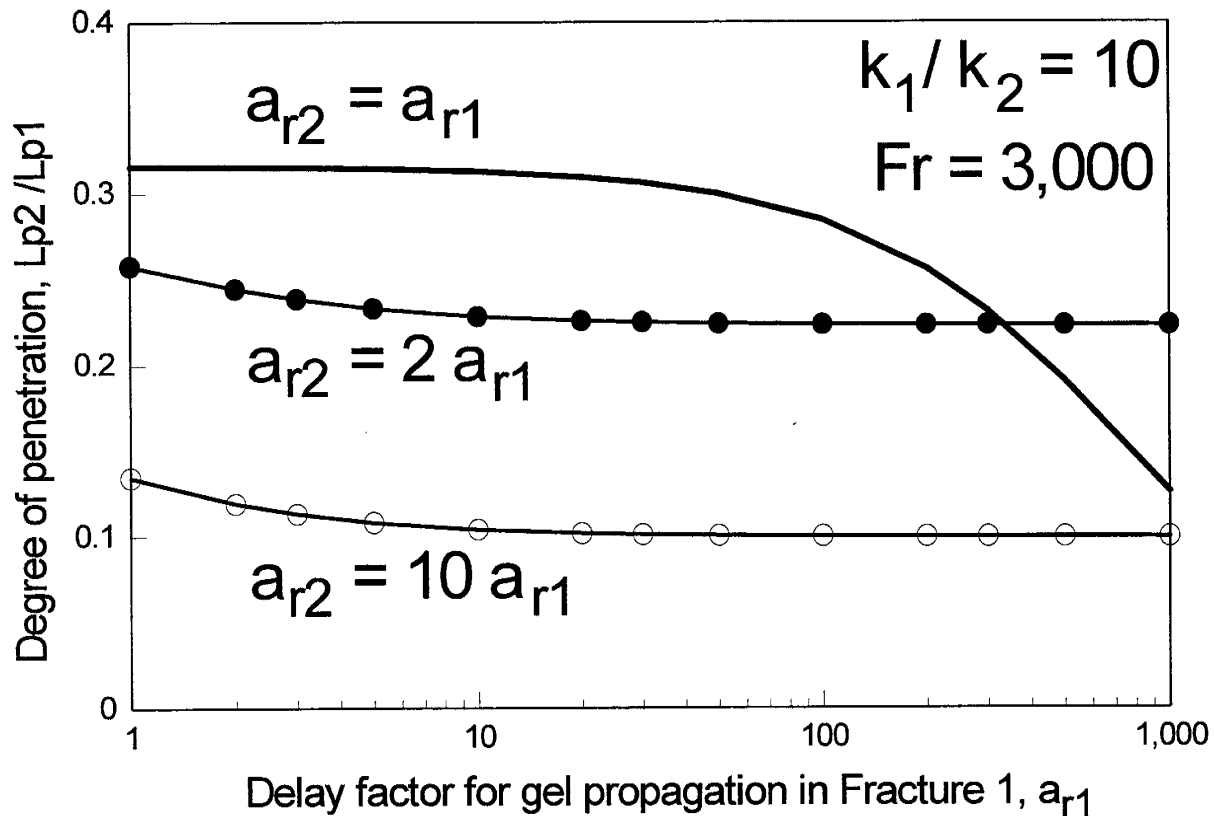


Fig. 32.  $L_{p2}/L_{p1}$  is insensitive to the rate of gel propagation unless these rates are radically different in different fractures.

## Conclusions

**Conclusions from Experimental Study of Gelants in Fractures.** The following conclusions were reached during experiments in three 122-cm-long fractured cores where approximately 2.5 fracture volumes of gelant were placed in the fractures:

1. A resorcinol-formaldehyde gelant with a water-like viscosity provided the best fracture healing of the three cases, but still did not completely heal the fracture. The gel formed from this gelant significantly damaged the first core section of a 122-cm fractured core, but healed the remaining four sections of the fracture fairly effectively.
2. A Cr(III)-acetate-HPAM gelant (45 cp) in a calcium brine (a) damaged the first core section of a 122-cm fractured core, (b) effectively reduced fracture conductivity in the second and third core sections, and (c) was ineffective in the fourth and fifth core sections.
3. A Cr(III)-acetate-HPAM gelant (18 cp) in a calcium-free brine may have effectively reduced fracture conductivity in the first core section, but was ineffective in the last four core sections.

**Conclusions from Experimental Study of Preformed Cr(III)-Acetate-HPAM Gels in Fractures.** The following conclusions were reached during experiments in fractured cores using a gel that contained 0.5% HPAM (Allied Colloids Alcoflood 935), 0.0417% Cr(III)-acetate, and 1% NaCl at pH=6 and 41°C: (The gelation time for this composition is 5 hrs at 41°C.)

1. Preformed gels can extrude through fractures without "screening out," but pressure gradients can be high, unless the fractures are very conductive.
2. Gels can effectively heal fractures with minimum leakoff.
3. Gels require a minimum pressure gradient for mobilization.
4. Gel resistance factors in fractures increase rapidly during the first 24 hours but increase more gradually during the next 200 hours.
5. Gels show flow-rate-independent residual resistance factors in fractures.
6. Gels dehydrate during extrusion through fractures, thus reducing the rate of gel propagation.
7. Gels can prevent flow of both oil and water in fractures.
8. Pressure gradients for gel extrusion vary inversely with fracture conductivity for low conductivities (e.g., < 1,100 D-cm) but are independent of conductivity in more conductive fractures.

**Conclusions from Analytical Study.** The following conclusions were reached during an analytical study comparing the placement properties of preformed gels and water-like gelants in a simple two-fracture reservoir:

1. Generally,  $L_{p2}/L_{p1}$  is lowest for gelants with a water-like viscosity.
2. The observed variation of gel resistance factors (i.e.,  $F_r$  increases with increasing fracture conductivity) may not aid gel placement.
3. For gels with high resistance factors,  $L_{p2}/L_{p1}$  is insensitive to differences in total fracture length.
4. For gelants with low resistance factors,  $L_{p2}/L_{p1}$  is very sensitive to differences in total fracture length.
5.  $L_{p2}/L_{p1}$  is insensitive to the rate of gel propagation unless these rates are radically different in different fractures.

### 3. EXAMINATION OF SOME SCHEMES TO AID GEL PLACEMENT IN FRACTURES

This chapter documents some of our early attempts to optimize gel placement in fractures. For the most part, these attempts were unsuccessful. We document these experiments here for the benefit of those who have wondered about the feasibility of these ideas. We investigated several schemes, including (1) injection of mechanically degraded Cr(III)-acetate-HPAM gels, (2) injection of mechanically degraded Cr(III)-acetate-HPAM gels, followed by injection of a CrCl<sub>3</sub> solution, (3) injection of a partially crosslinked hydroquinone-hexamethylenetetramine-HPAM gel, followed by a CrCl<sub>3</sub> solution, and (4) injection of an HPAM water-in-oil emulsion, preceded or followed by a CrCl<sub>3</sub> solution.

#### Injection of Mechanically Degraded Cr(III)-Acetate-HPAM Gels

A concern during injection of preformed gels is that the gel may “screen out” or develop excessive pressure gradients. In one approach to reduce this concern, we allowed the gelation reaction for a conventional gel to proceed to completion and then mechanically degraded the gel to a desired fluidity. We examined the performance of a 5-day-old Cr(III)-acetate-HPAM gel that was sheared in a blender. Our objective was to determine whether this mechanical degradation can reduce gel resistance factors while still providing effective fluid diversion in a fractured core. In this work, we used the same composition of Cr(III)-acetate-HPAM gel that was described in Chapter 2 (0.5% Allied Colloids Alcoflood 935® HPAM, 0.0417% chromium triacetate, 1% NaCl, pH 6). All experiments described in this chapter were performed at 41°C. After preparation, the gel was allowed to set for 5 days at 41°C. Then, it was sheared for 1 minute in a Waring blender at 75% of full power. After shearing, the product had a smooth consistency (no chunks).

**Results in a Short Fractured Core.** We injected 10 PV (315 ml or about 300 fracture volumes) of sheared Cr(III)-acetate-HPAM gel through a fractured Berea sandstone core (Core 21). As with other cores, Core 21 had a nominal permeability to brine of 650 md before fracturing, and the core was 14.7 cm in length and 3.6 cm in diameter. After fracturing, the average core permeability was 8.81 darcys, the fracture conductivity was 22.8 D-cm, and the  $k_{fw}h_f/Ak_m$  value was 12.6.

Fig. 33 shows resistance factors and pressure gradients during gel injection at a rate of 200 ml/hr. During injection of 10 PV of gel, the resistance factor steadily increased from 45 to 200, while the pressure gradient increased from 9 to 38 psi/ft. These values are lower (and therefore more desirable) than most previous values that we observed. These low values are especially encouraging because Core 21 had one of the least conductive fractures that we studied (22.8 D-cm). However, the steady increase in these values still raises a concern that unacceptably high pressure gradients could develop unless the fractures are very conductive.

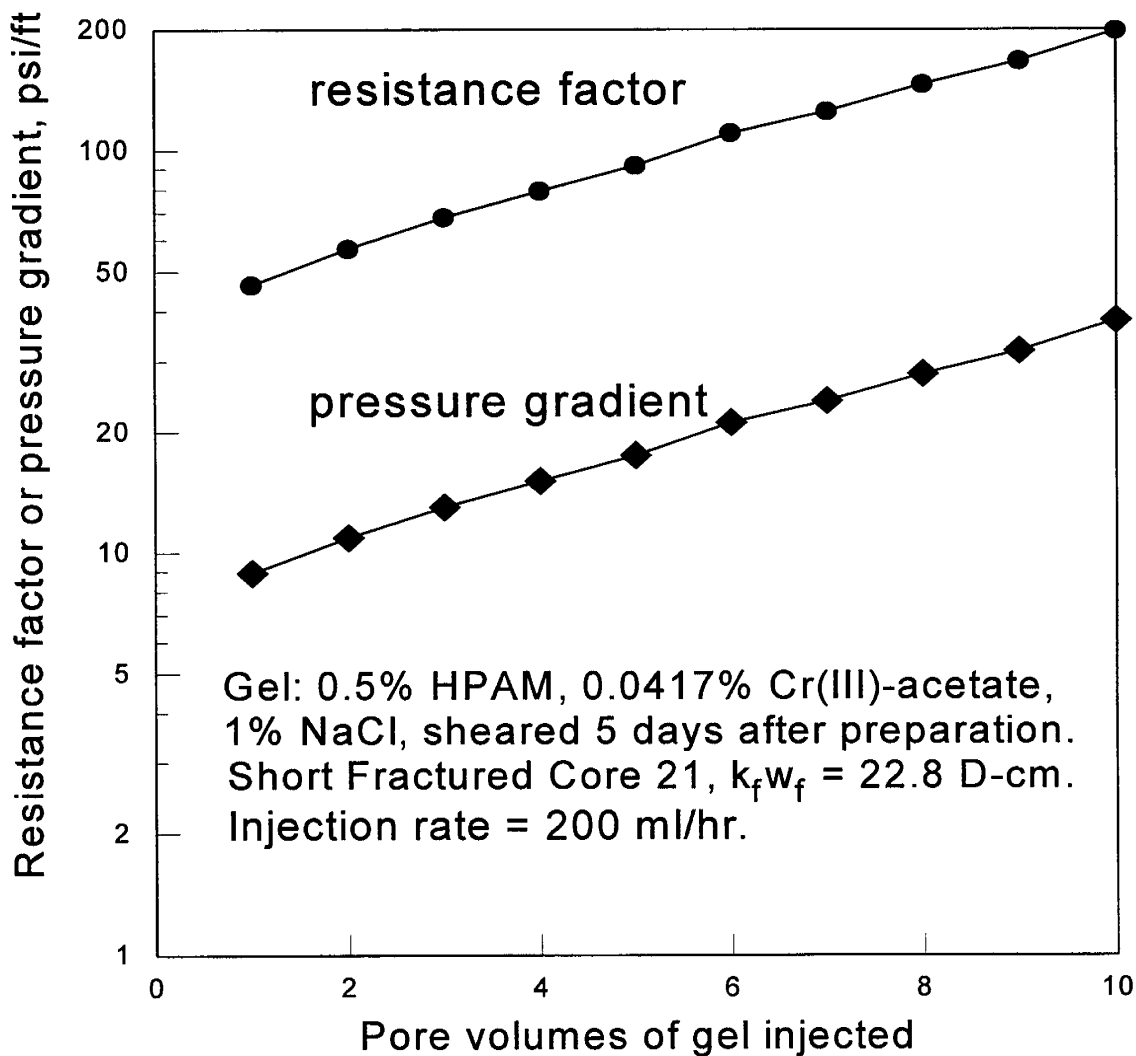


Fig. 33. Resistance factors and pressure gradients during placement of a sheared Cr(III)-acetate-HPAM gel in Short Fractured Core 21.

The solid diamonds in Fig. 34 show tracer results that were obtained during brine injection after gel placement. In this study, tracer breakthrough occurred at 0.345 PV and  $C/C_o=50\%$  at 0.505 PV. Thus, the treatment improved sweep efficiency somewhat in the core, but the fracture was not healed.

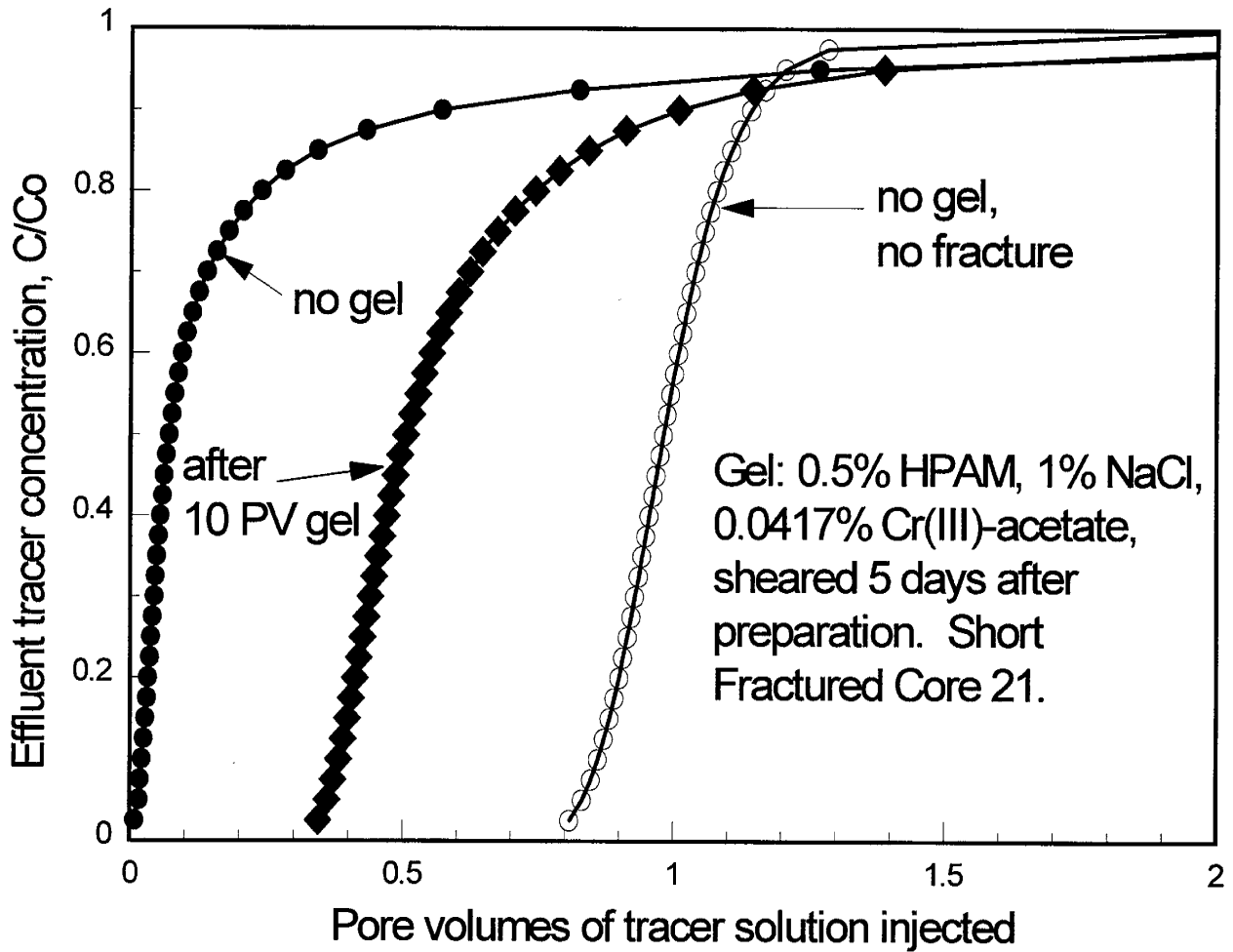


Fig. 34. Tracer results before versus after placement of a sheared Cr(III)-acetate-HPAM gel in Short Fractured Core 21.

**Results in a Long Fractured Core.** We repeated the above experiment using a fractured core (Long Fractured Core 3) that was 114.5 cm in length (compared to the 14.7-cm core that was used in the previous experiment). Table 9 lists the properties of Long Fractured Core 3. We used a Cr(III)-acetate-HPAM gel with the same composition and aging time (5 days at 41°C) as that used in Short Fractured Core 21. The gel was also sheared in a Waring blender in the same way (1 minute at 75% of full power). We injected 750 ml (2.1 core PV or 60 fracture volumes) of sheared gel at a rate of 400 ml/hr. Fig. 35 plots resistance factor versus the throughput of gel. Figs. 36 and 37 show the viscosities and chromium concentrations in the effluent during gel injection. Fig. 35 shows that progressive plugging occurred in all five sections of the fractured core. The resistance factors reached the highest values in the first two sections, exceeding 1,000. Figs. 36 and 37 confirm the low rate of gel propagation through the fracture. Fig. 36 shows that the effluent viscosity gradually rose to about 5 cp (75% of the viscosity of the sheared gel before injection) after injecting 300 ml (24 fracture volumes) of gel. However, after injecting 500 ml (40 fracture volumes) of gel the effluent viscosity decreased until it matched the solvent viscosity

Table 9. Properties of Long Fractured Core 3

Core width and height = 3.81 cm		Core PV = 353 ml				
Fracture volume, $V_f$ = 12.4 ml		Average $w_f$ = 0.028 cm, $k_f$ = 1,600 D				
Core section:	Entire core	1	2	3	4	5
Length, cm	114.5	22.9	22.9	22.9	22.9	22.9
$k_{av}$ , D	12.7	7.2	7.1	20.2	11.5	17.3
$k_f w_f$ , D-cm	45.7	24.8	24.4	74.5	41.4	63.5
$k_f w_f h_f / Ak_m$	18.5	10.0	9.9	30.1	16.7	25.6

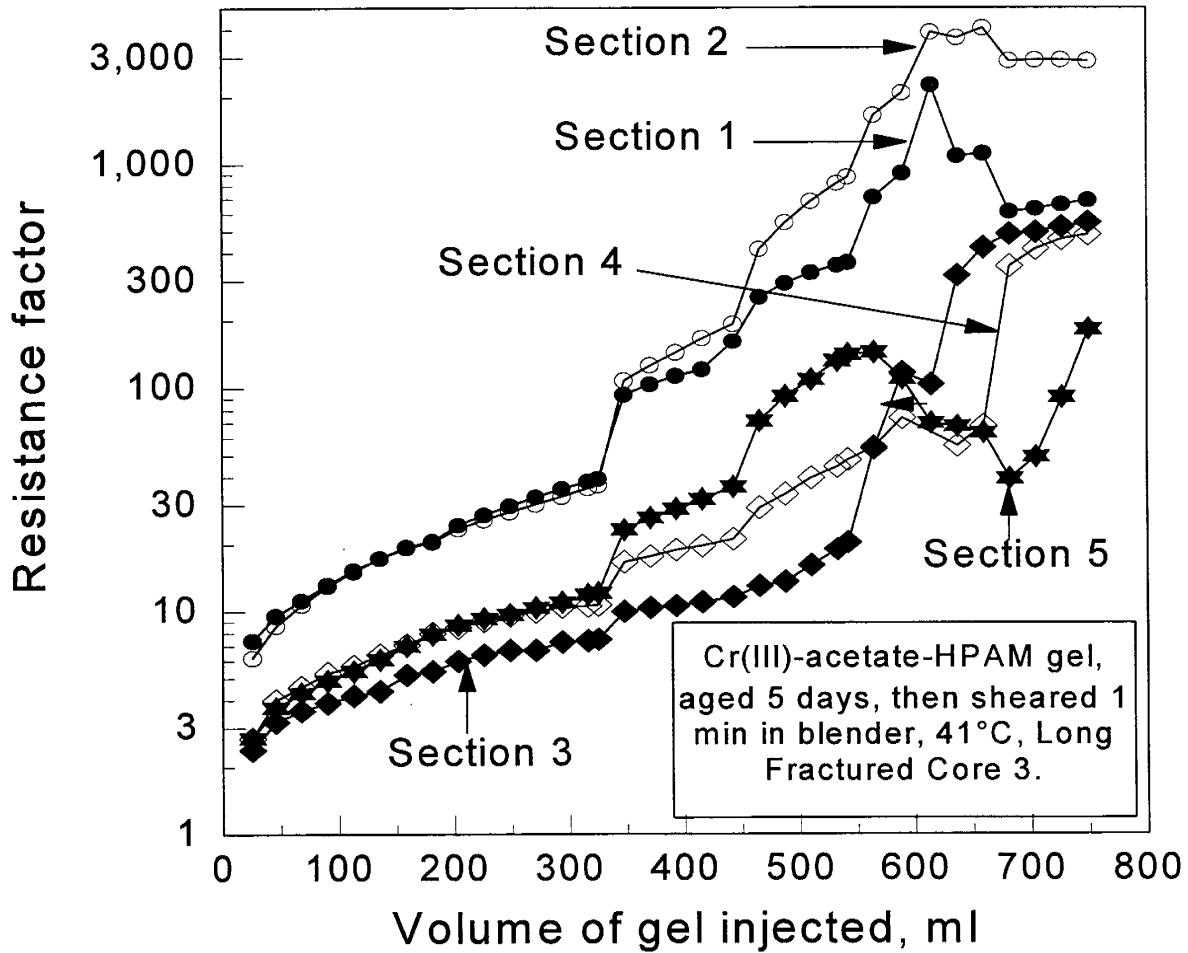


Fig. 35. Resistance factors during gel injection into Long Fractured Core 3.

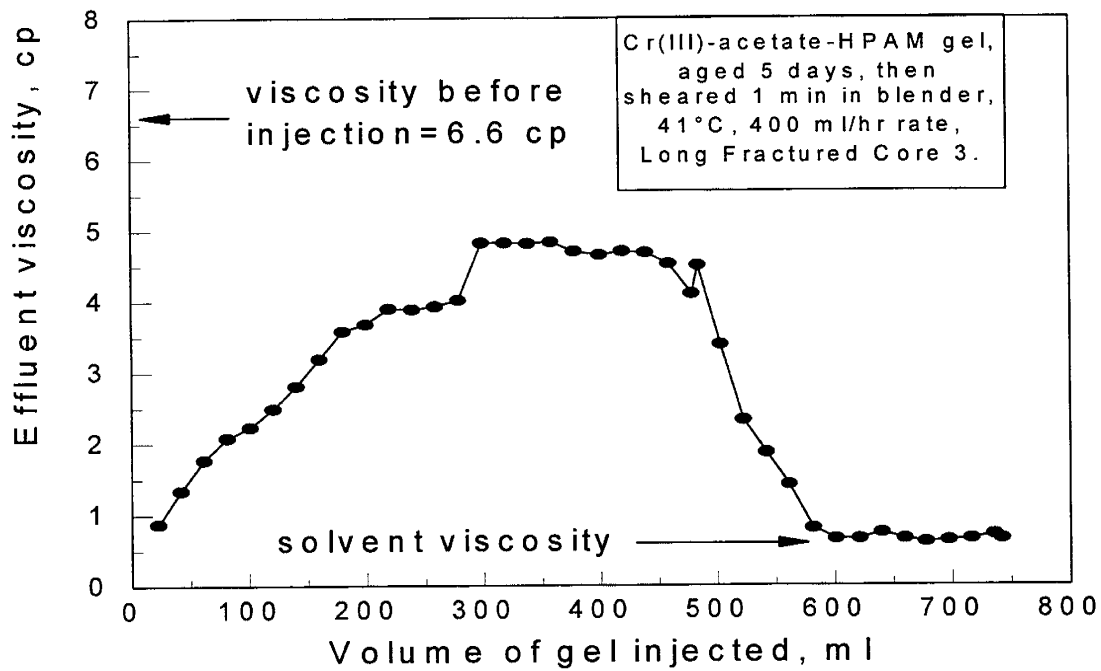


Fig. 36. Effluent viscosities during gel injection into Long Fractured Core 3.

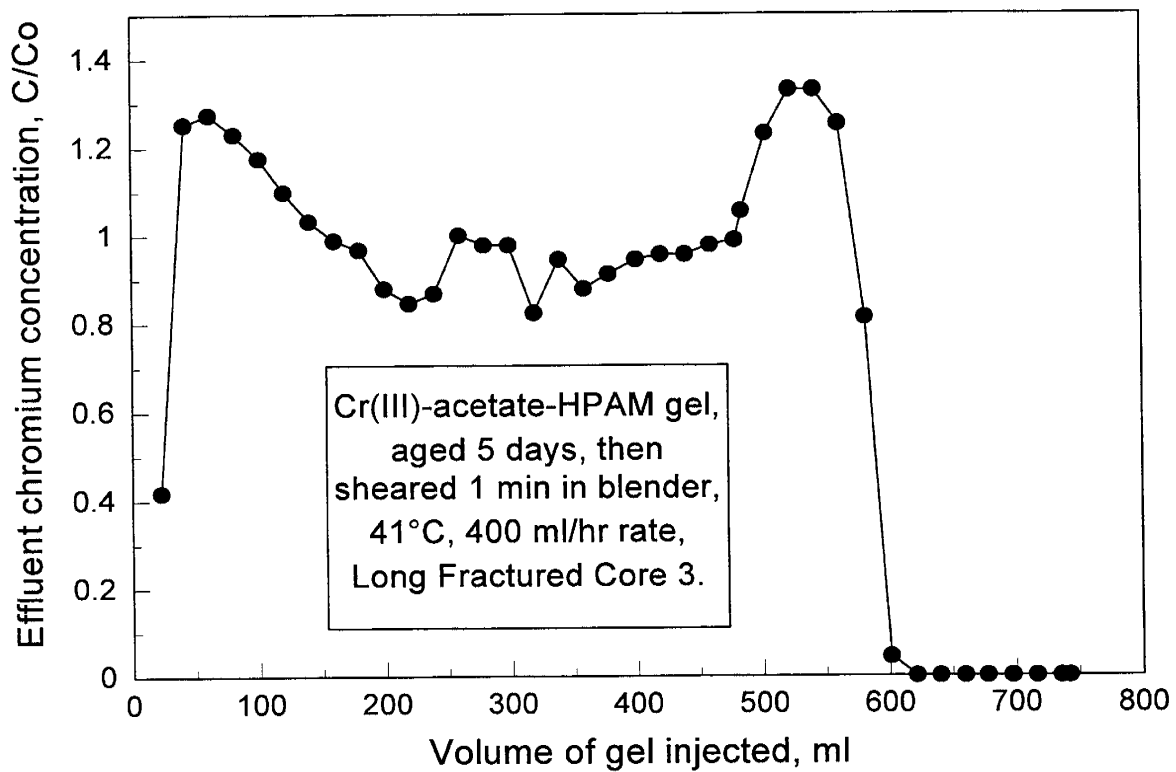


Fig. 37. Effluent chromium concentrations during gel injection into Long Fractured Core 3.

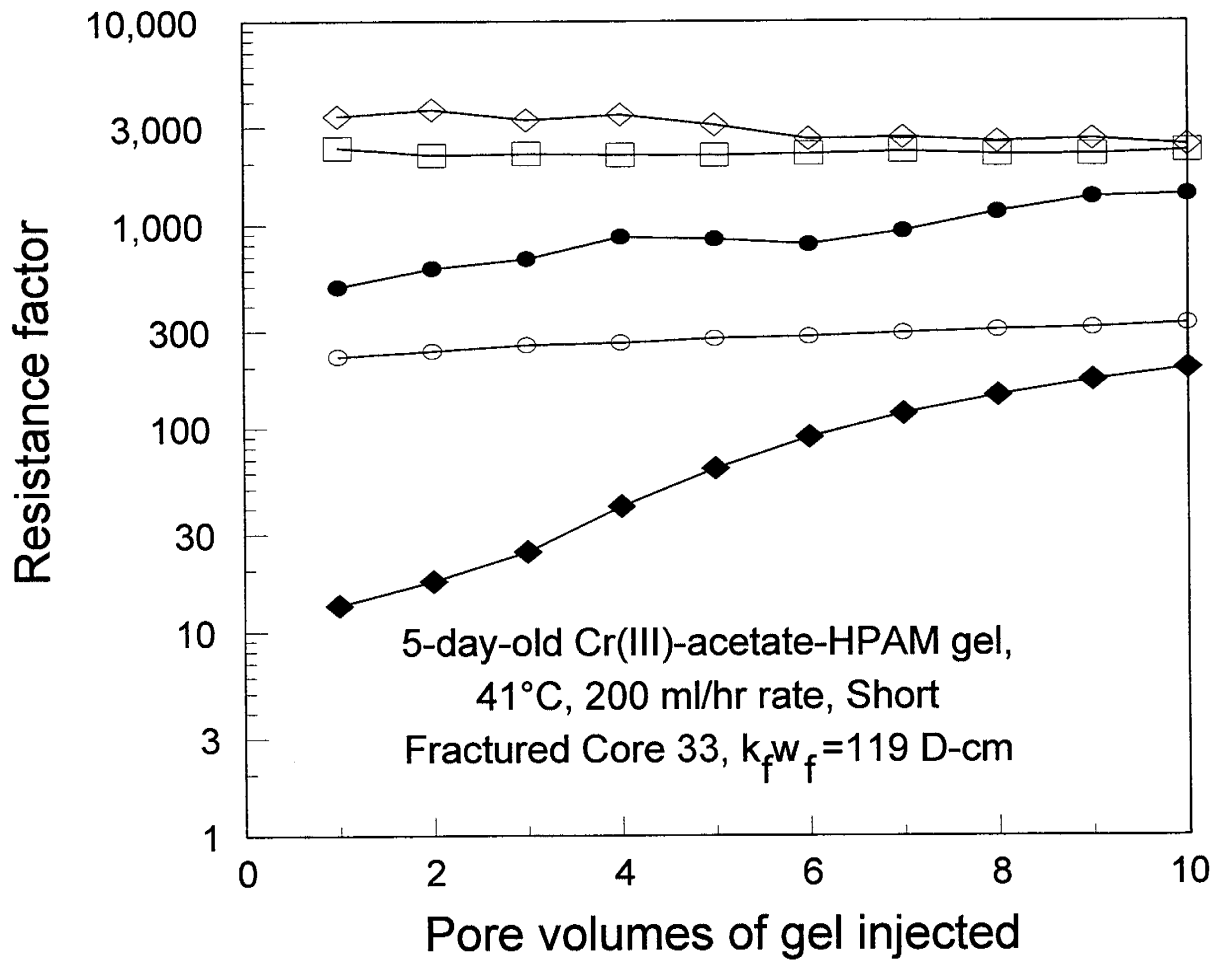
(after injecting 600 ml or 48 fracture volumes of gel). This result indicated that gel no longer propagated through the fracture after injecting 48 fracture volumes of gel. The effluent chromium concentrations (Fig. 37) confirm this conclusion. After injecting 600 ml of gel, the effluent chromium concentration fell abruptly to zero. Interestingly, Fig. 37 shows that the chromium propagated rapidly through the fracture when gel was first injected—with the effluent exceeding the injected chromium concentration after injecting about 40 ml or 3 fracture volumes of gel.

**Effect of Shearing Time.** Using gel that had been sheared for 1 minute in a Waring blender, the above results suggest that gel propagation through fractures is still a potential problem. How does the gel resistance factor vary with shearing time? To answer this question, we performed a series of experiments using Short Fractured Core 33. This core was 14.4 cm in length. After fracturing, the average core permeability was 42.6 darcys, the fracture conductivity was 119 D-cm, and the  $k_{fw}h_f/Ak_m$  value was 65.6. (Note that the conductivity of this core was significantly greater than that for either Short Fracture Core 21 or Long Fractured Core 3, which were used in the previous experiments.) A Cr(III)-acetate-HPAM gel was prepared with the same composition as that mentioned earlier, and this gel was again aged for five days at 41°C. This gel was separated into five batches of equal size. Then, each batch was sheared in a Waring blender at 75% of full power for time periods ranging from 15 to 90 seconds. Table 10 lists the shearing times and the viscosities of the sheared gels before and after being forced through Short Fractured Core 33.

Table 10. Viscosities of Sheared Gels Before and After Being Forced Through Short Fractured Core 33

Shearing time, seconds	Viscosity before injection, cp	Viscosity after injection, cp
90	8.1	6.9
60	9.8	12.2
45	12.5	12.2
30	61	63
15	---	169

After preparation, we injected 10 PV (326 ml or about 300 fracture volumes) of each batch of sheared gel into Short Fractured Core 33 using a rate of 200 ml/hr. Table 10 indicates the order of injection, with the most sheared gel injected first and the least-sheared gel injected last. Fig. 38 shows the resistance factors that were observed during gel injection. While injecting 10 PV (300 fracture volumes) of gel, the resistance factors steadily increased from 11 to 200 for the 90-second-sheared gel, from 230 to 330 for the 60-second-sheared gel, and from 450 to 1,600 for the 45-second-sheared gel. For the 30-second-sheared gel and the 15-second-sheared gel, the resistance factors were fairly stable—averaging 2,200 and 3,100, respectively. Thus, as expected, the average resistance factor decreases with increasing shearing time.



Time sheared in a Waring blender before injection:

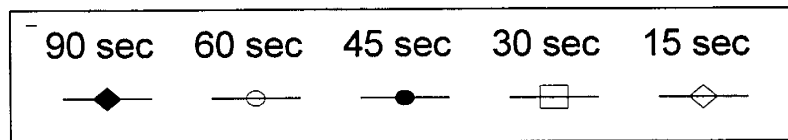


Fig. 38. Resistance factors during injection of sheared Cr(III)-acetate-HPAM gels into Short Fractured Core 33.

In contrast to Fig. 36, Table 10 shows that the gel viscosities were not reduced much after being forced through the core. We also note that the gel resistance factors appeared to be more stable in Fig. 38 than in Fig. 35. The difference in results may be partly due to the higher conductivity for Short Fractured Core 33 (119 D-cm) than for Long Fractured Core 3 (45.7 D-cm).

After injecting the sheared gels, we injected 650 ml (20 core PV or 600 fracture volumes) of brine. During brine injection, the residual resistance factor was stable at value of 132, which is about twice the value expected for a perfectly healed fracture. Fig. 39 shows tracer results before and after gel placement in Short Fractured Core 33. The solid diamonds indicate that the gel treatment significantly improved sweep efficiency in the core, but it did not completely heal the fracture.

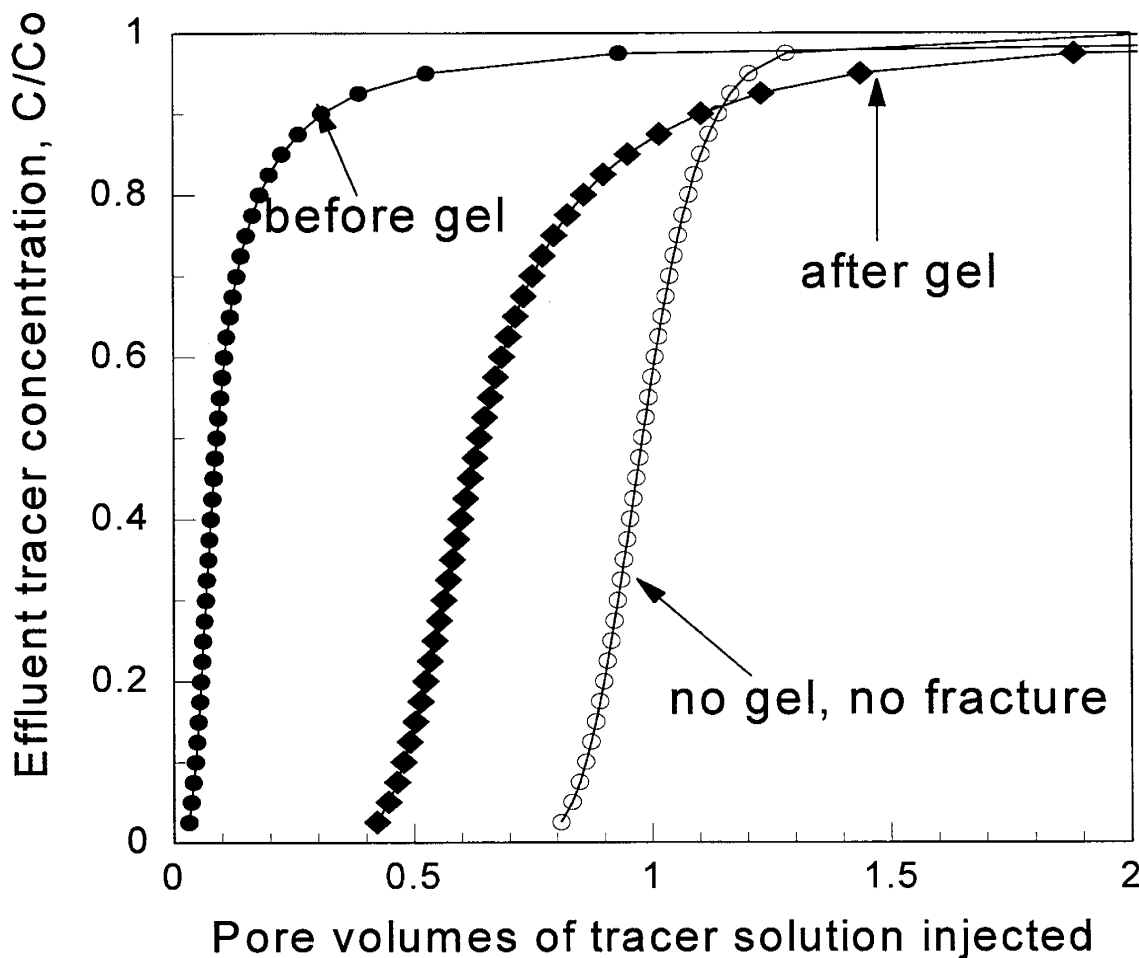


Fig. 39. Tracer results before versus after gel placement in Short Fractured Core 33.

In summary, our investigation has not shown sheared preformed gels to be superior to preformed gels that were not sheared. However, our studies have not been extensive enough to abandon hope that sheared gels may prove useful.

## Injection of Cr(III) After Placement of a Mechanically Degraded Cr(III)-Acetate-HPAM Gel

Another approach that we investigated involved injecting a sheared gel, followed by a crosslinker solution. In concept, the sheared gel could exhibit a low resistance factor and pressure gradient during gel injection. Then, when a crosslinker solution was injected after gel placement, hopefully, a more effective gel could be formed that might plug the fracture. We investigated this idea using Short Fractured Core 34. This core was 14.4 cm in length. After fracturing, the average core permeability was 28.4 darcys, the fracture conductivity was 77.6 D-cm, and the  $k_f w_f h_f / Ak_m$  value was 42.7. We used a Cr(III)-acetate-HPAM gel with the same composition and aging time (5 days at 41°C) as that used in previous experiments. The gel was also sheared in a Waring blender in the same way (1 minute at 75% of full power). After shearing, the viscosity of this gel was 6.6 cp. We injected 10 PV (317 ml or 300 fracture volumes) of sheared gel at a rate of 200 ml/hr. The left side of Fig. 40 shows how the resistance factor and pressure gradient increased while injecting 10 PV of gel.

After gel placement, we immediately injected 10 PV (317 ml or 300 fracture volumes) of a crosslinker solution that contained 0.0288% CrCl<sub>3</sub> and 1% NaCl. The right side of Fig. 40 shows that the resistance factor and pressure gradient continued to increase, but not as rapidly as during gel injection.

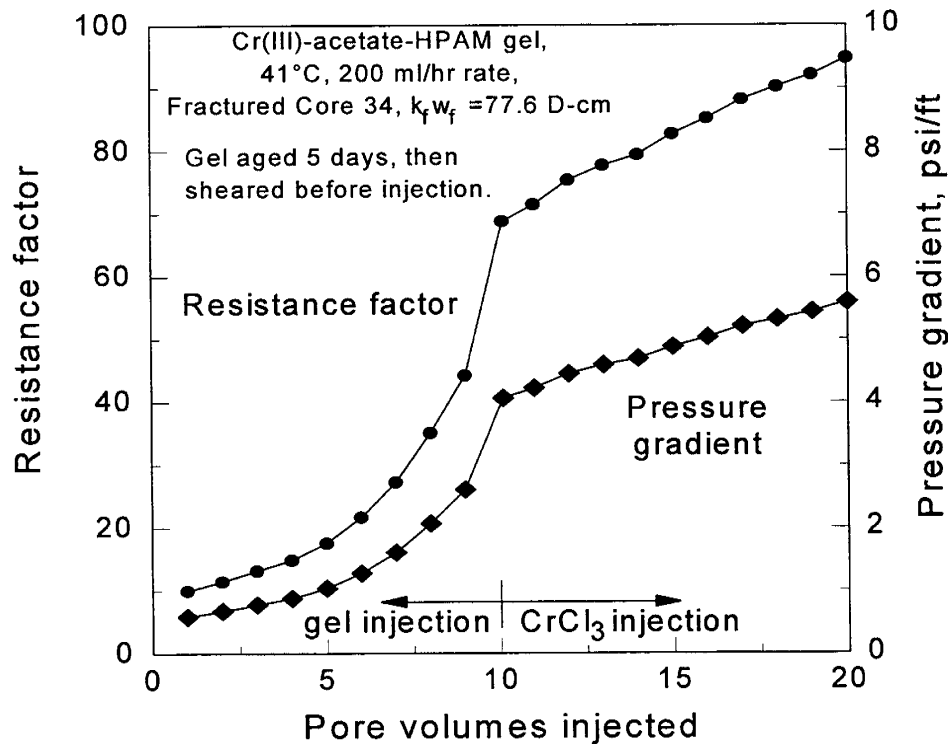


Fig. 40. Resistance factors and pressure gradients during injection of a mechanically degraded Cr(III)-acetate-HPAM gel into Short Fractured Core 34.

After injecting the crosslinker solution, the core was shut in for three days. Then, we injected 25 PV of brine, followed by a tracer study. Fig. 41 shows the tracer results. The solid diamonds demonstrate that this treatment had no beneficial effect on sweep efficiency.

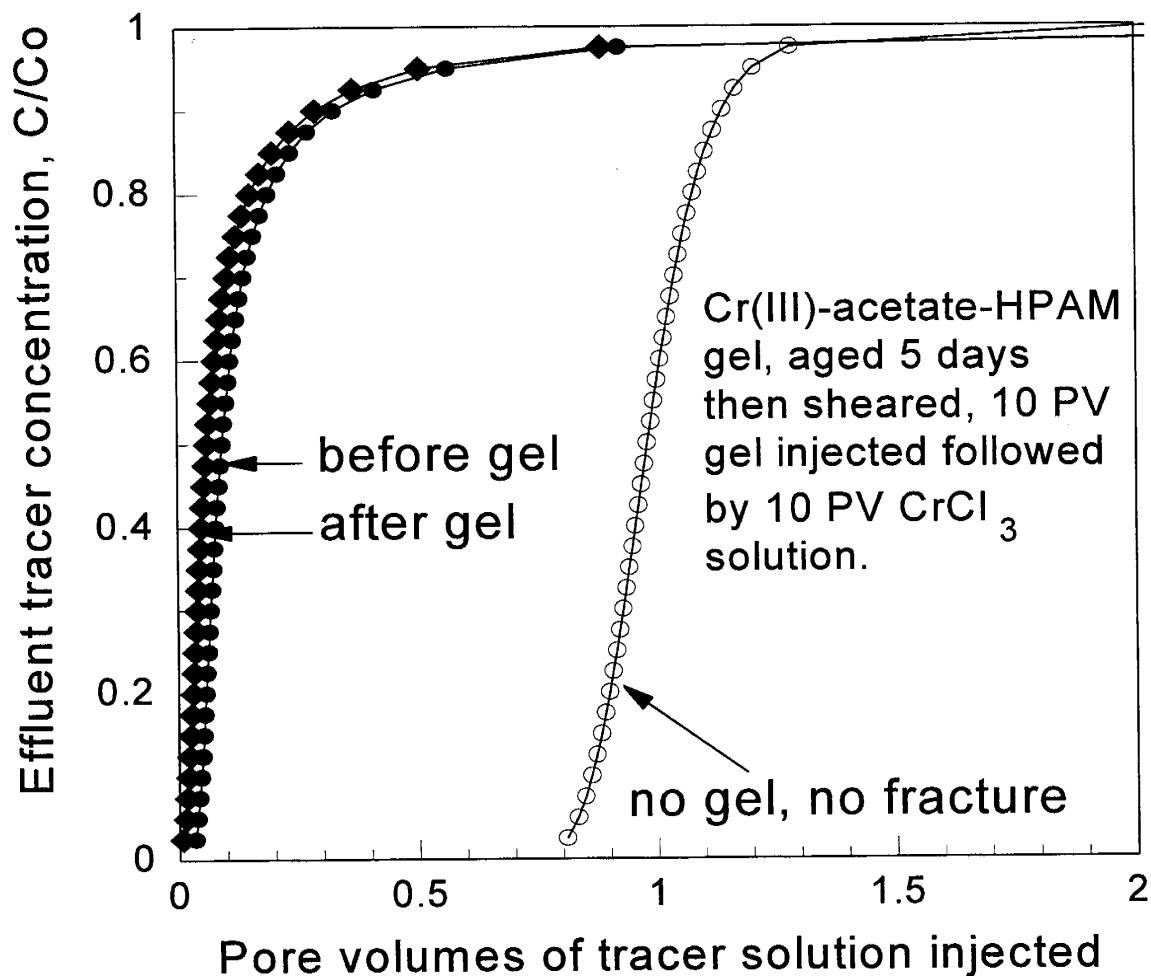


Fig. 41. Tracer results before versus after gel placement in Short Fractured Core 34.

### Injection of Cr(III) After Placement of a Hydroquinone-Hexamethylenetetramine-HPAM Gel

Following similar logic to that described above, we performed another experiment where a hydroquinone-hexamethylenetetramine-HPAM gel was injected instead of a sheared Cr(III)-acetate-HPAM gel. The gelant contained 0.5445% Allied Colloids Alcofluid® 935 HPAM, 0.25% hydroquinone, 0.1% hexamethylenetetramine, and 1%  $\text{NaHCO}_3$ . This gelant requires high temperatures for the gelation reaction to proceed at a significant rate. Based on our previous experience,<sup>2</sup> we aged the gelant for 18 hours at 110°C, followed by quenching to 41°C, to make

a gel that exhibits fairly low resistance factors and pressure gradients during injection. Then, we injected 10 PV (325 ml or 300 fracture volumes) of this gel into Short Fractured Core 35 using a rate of 200 ml/hr. This core was 14.5 cm in length. After fracturing, the average core permeability was 36.7 darcys, the fracture conductivity was 100.8 darcy-cm, and the  $k_f w_f h_f / Ak_m$  value was 55.5.

During gel injection, the resistance factor was stable at 340, and the pressure gradient was stable at 15 psi/ft (left side of Fig. 42). After gel injection, we injected 10 PV of crosslinker solution that contained 0.0288%  $\text{CrCl}_3$  and 1%  $\text{NaCl}$ . (Throughout this experiment, the rate was maintained constant at 200 ml/hr.) During injection of the crosslinker solution, the residual resistance factor and pressure gradient averaged 21 and 1 psi/ft, respectively. Next, 20 PV of 1%- $\text{NaCl}$  brine (without crosslinker) were injected. During this brine injection, the resistance factor and pressure gradient were about the same as those observed during crosslinker injection (Fig. 42). After brine injection, an additional 10 PV of crosslinker solution (same composition as before) were injected, with no effect on the resistance factor or pressure gradient. Then, the core was shut in for 3 days, followed by injection of an additional 20 PV of 1%- $\text{NaCl}$  brine. Again, the resistance factor and pressure gradient were unaffected. Finally, a tracer study was performed. As in the previous experiment, the tracer study indicated that the gel treatment did not improve sweep efficiency in the core (compare Figs. 41 and 43).

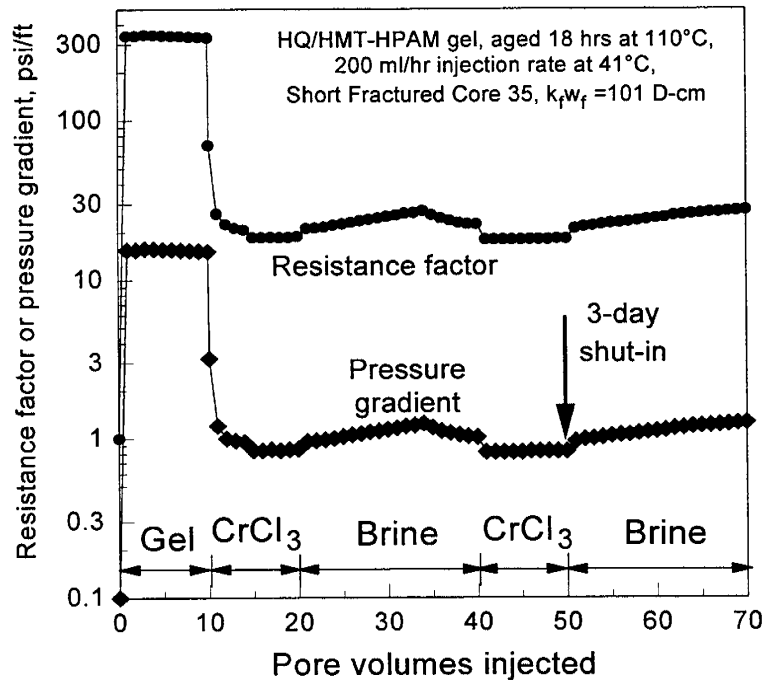


Fig. 42. Resistance factors and pressure gradients during injection of gel, Cr(III)-chloride solution, and brine into Short Fractured Core 35.

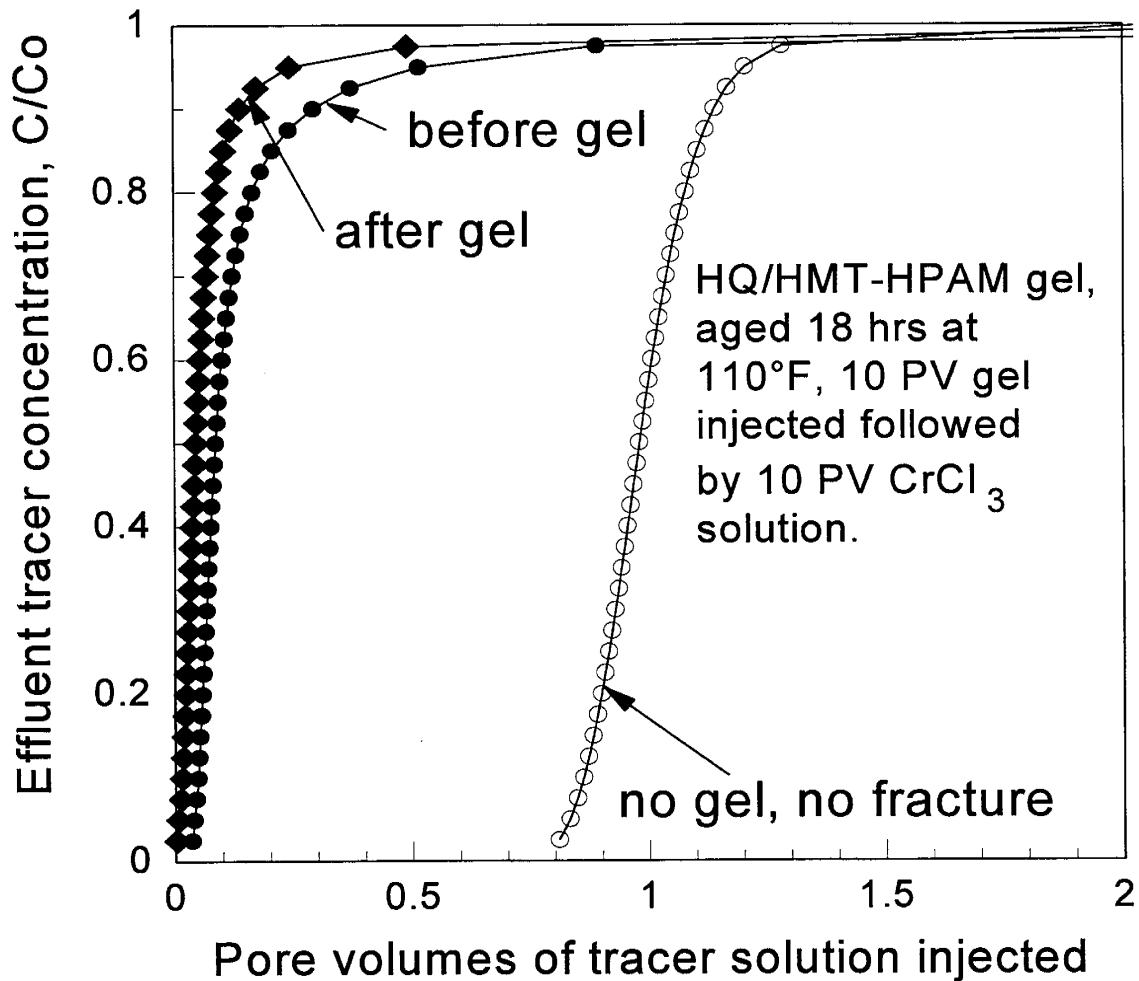


Fig. 43. Tracer results before versus after gel placement in Short Fractured Core 35.

#### Injection of Cr(III) After Placement of an HPAM Water-in-Oil Emulsion

We also investigated whether fractures can be treated by injecting a concentrated HPAM water-in-oil emulsion, followed by injection of a crosslinker solution. We used the emulsion-form polymer, Allied Colloids Alcomer® 123L. This product consists of 25% HPAM that is dispersed in water, that is, in turn, dispersed in oil. This water-in-oil emulsion was used directly as supplied from the manufacturer. Fig. 44 plots the viscosity versus shear rate for this emulsion at 41°C. This emulsion is shear-thinning and exhibits a viscosity of 76 cp at  $11 \text{ s}^{-1}$  and 41°C.

We performed experiments with this emulsion in five short fracture cores ( $\approx 14.5 \text{ cm}$  in length). Properties of the five fractured cores are listed in Table 11. Table 12 lists the injection sequence for each of these experiments. All experiments were performed at 41°C. Table 13 summarizes the experimental results.

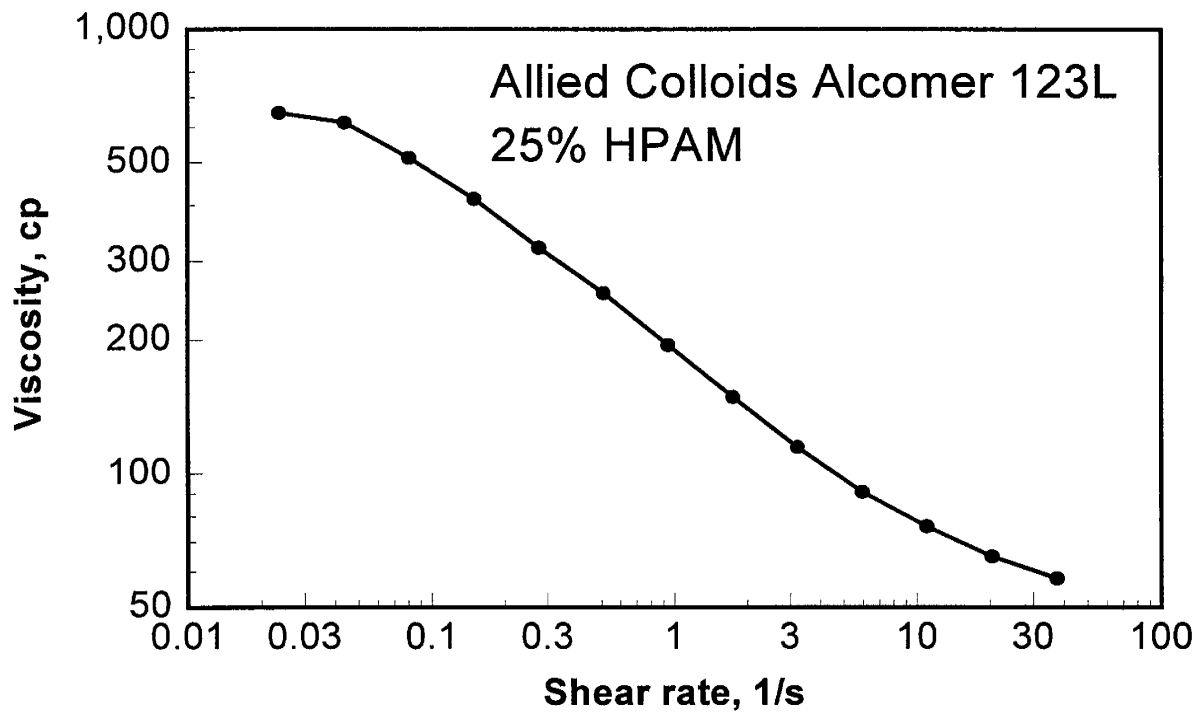


Fig. 44. Viscosity versus shear rate for HPAM water-in-oil emulsion.

Table 11. Properties of 14.5-cm Cores Used in HPAM Emulsion Experiments

Core no.	36	37	38	39	40
$k_{av}$ , D	27.6	12.7	17.0	14.3	21.3
$k_f w_f$ , D-cm	75.4	33.6	45.8	38.2	59.4
$k_f w_f h_f / Ak_m$	41.5	18.5	25.2	21.0	32.7
$V_f$ , ml	1.0	1.0	0.8	0.8	1.2
$w_f$ , cm	0.020	0.020	0.016	0.016	0.024
$k_f$ , D	3,900	1,700	2,900	2,400	2,500

Table 12. Sequences Followed During Experiments with HPAM Emulsions (41°C)

Step	Core 36	Core 37	Core 38	Core 39	Core 40
1	brine saturated	brine saturated	oil saturated	oil saturated	brine saturated, 10 PV CrCl <sub>3</sub>
2	1 PV emulsion	1 PV emulsion	2 PV emulsion	1 PV emulsion	0.25 PV emulsion
3	34 PV brine	1 day shut-in	10 PV CrCl <sub>3</sub>	0.7 PV CrCl <sub>3</sub> *	1 day shut-in
4	10 PV CrCl <sub>3</sub> , 1-day shut-in	10 PV CrCl <sub>3</sub> , 1 day shut-in	26 PV oil	20 PV oil	27 PV brine
5	11 PV brine	22 PV brine	oil tracer	oil tracer	brine tracer

\* CrCl<sub>3</sub> placement occurred at 0.32 ml/hr injection rate during this experiment only. In the other experiments, CrCl<sub>3</sub> placement occurred at 200 ml/hr injection rate.

Table 13. Summary of Results of Experiments with HPAM Emulsions (41°C)

	Core 36	Core 37	Core 38	Core 39	Core 40
Maximum $F_r$ during emulsion injection	85	77	30	52	80
Maximum $F_{rr}$ during CrCl <sub>3</sub> injection	4,000	370	28	85,000	--
Maximum $F_{rr}$ during water or oil injection	3,700	105	5	4,000	91
Tracer indicates sweep improvement?	not available	not available	no	no	no

Short Fractured Core 36 was first saturated with brine (1% NaCl). Then, 31 ml (1 core PV or 31 fracture volumes) of Alcomer 123L HPAM emulsion were injected. (Unless stated otherwise, the injection rate was 200 ml/hr.) The resistance factor in the second section of the fracture reached a value of 85 during emulsion injection (Table 13). For comparison, the emulsion viscosity approaches 50 cp at high shear rates (Fig. 44). After emulsion injection, 34 PV of 1%-NaCl brine were injected. During this step, the maximum residual resistance factor ( $F_{rrw}$ ) was 130. Next, 10 PV of crosslinker solution (0.0288% CrCl<sub>3</sub>, 1% NaCl) were injected. During this step,  $F_{rrw}$  reached a maximum of 4,000. After injecting the crosslinker solution, the core was shut in for 1 day, followed by injection of 11 PV of brine. During this final step,  $F_{rrw}$  was 3,700.

Unfortunately, we could not perform a tracer study at the end of this experiment because emulsified polymer was continually produced—interfering with our tracer detector.

The above experiment was repeated in Short Fractured Core 37, with certain modifications (see Table 12). Again, the core was first saturated with brine (1% NaCl), and 1 PV of HPAM emulsion was injected (resulting in a maximum  $F_r$  of 77), followed by a 1-day shut-in. Then, 10 PV of crosslinker solution were injected, resulting in a maximum  $F_{rw}$  value of 370. After a 1-day shut-in period, 22 PV of brine were injected, resulting in a maximum  $F_{rw}$  value of 105. At the end of this experiment, produced emulsion, again, precluded a successful tracer study.

In an attempt to minimize the production of emulsion from the core (so that a post-treatment tracer study could be performed), two floods were conducted using oil-saturated cores (Short Fractured Cores 38 and 39). These cores were first completely saturated with Soltrol 130 oil. In Core 38, the  $F_r$  value reached a maximum value of 30 during injection of 2 PV (60 fracture volumes) of emulsion (Tables 12 and 13). Then, 10 PV of  $CrCl_3$  crosslinker solution (again, containing 0.0288%  $CrCl_3$  and 1% NaCl) were injected, resulting in a maximum  $F_{rw}$  value of 28. During the subsequent injection of 26 PV of Soltrol 130 oil, the residual resistance factor fell to a value of 5. Finally, we were able to complete oil-tracer studies both before and after placement of the crosslinked emulsion. Fig. 45 shows that this emulsion treatment was completely ineffective at improving sweep efficiency in Core 38.

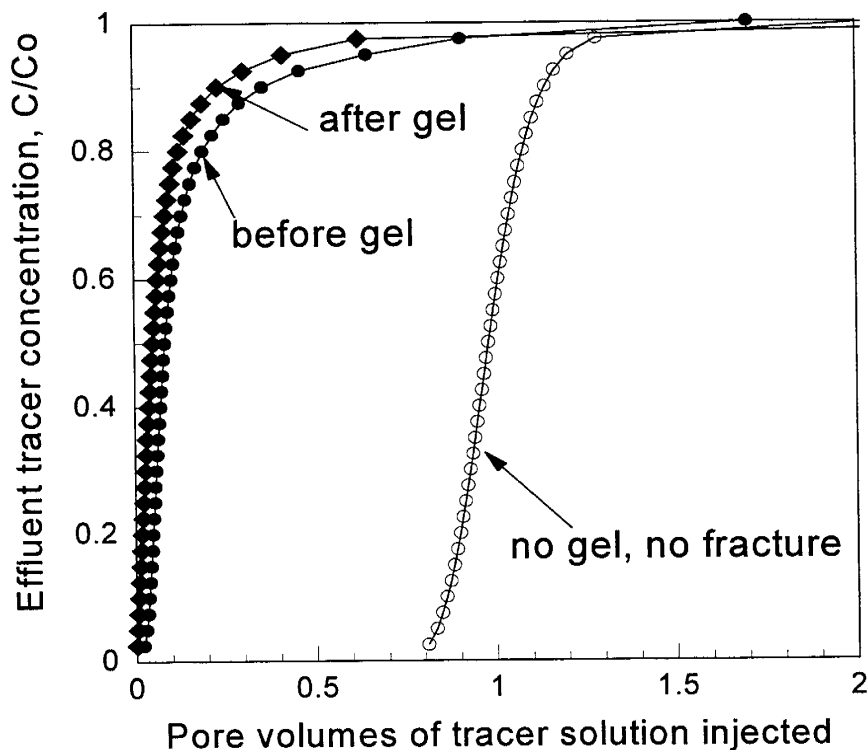


Fig. 45. Tracer results before and after placement of a crosslinked HPAM emulsion in Short Fractured Core 38.

The above experiment was repeated in Short Fractured Core 39, with certain modifications. The core was first saturated with Soltrol 130 oil. Then, 1 PV (30 fracture volumes) of HPAM emulsion was injected at a rate of 200 ml/hr. The maximum  $F_r$  was 52 during this step. Next, 0.7 PV of  $CrCl_3$  crosslinker solution was injected at a rate of 0.32 ml/hr. This slow rate was chosen to maximize diffusion into and reaction with the HPAM. The residual resistance factor reached a very high value (85,000) during this step. After injecting the crosslinker, 20 PV of Soltrol 130 oil were injected at 200 ml/hr, resulting in an  $F_{rw}$  value of 4,000. Finally, an oil-tracer study was conducted. Unfortunately, the tracer results indicated that the crosslinked-emulsion treatment was ineffective.

The final experiment was performed in Short Fractured Core 40. This core was first saturated with brine (1% NaCl), and then, 10 PV of  $CrCl_3$  crosslinker solution were injected. Our intent was to saturate the core with crosslinker before the emulsion was placed. (All steps in this experiment used a rate of 200 ml/hr.) Next, 0.25 PV (6 fracture volumes) of emulsion were injected, resulting in a maximum  $F_r$  value of 80. This  $F_r$  value is comparable to those observed during emulsion placement in Cores 36 and 37 (see Table 13). This result suggests that the HPAM did not react extensively with the resident  $CrCl_3$  crosslinker during the placement process. After emulsion placement, Core 40 was shut in for 1 day, followed by injection of 27 PV of brine. The  $F_{rw}$  during brine injection was 91. Finally, we were able to complete a brine-tracer study at the end of this experiment. Unfortunately, as shown in Fig. 46, this crosslinked-emulsion treatment was also ineffective at improving sweep efficiency in the fractured core.

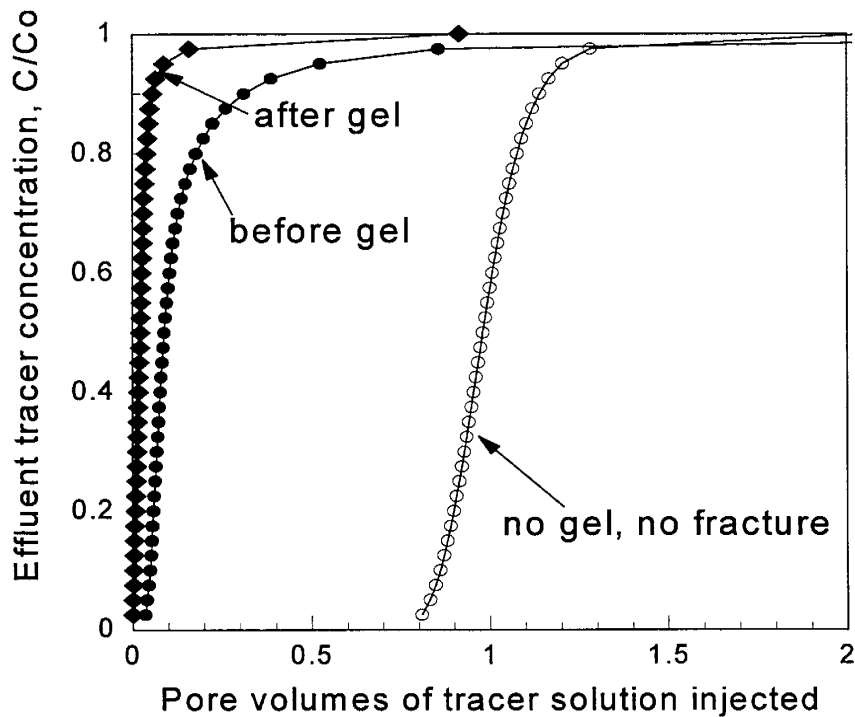


Fig. 46. Tracer results before and after placement of a crosslinked HPAM emulsion in Short Fractured Core 40.

## Conclusions

In summary, we were not able to improve the placement of gels in fractured cores using (1) mechanically degraded Cr(III)-acetate-HPAM gels, (2) mechanically degraded Cr(III)-acetate-HPAM gels, followed by CrCl<sub>3</sub> crosslinker solutions, (3) partially crosslinked hydroquinone-hexamethylenetetramine-HPAM gels, followed by CrCl<sub>3</sub> crosslinker solutions, or (4) HPAM emulsions, preceded or followed by CrCl<sub>3</sub> crosslinker solutions. To optimize gel placement in fractured systems, many additional schemes remain to be investigated.

## 4. DISPROPORTIONATE PERMEABILITY REDUCTION

Several researchers<sup>19,22-29</sup> reported that some polymers and gels can reduce water permeability more than oil permeability. This property is critical to the success of gel treatments in production wells when zones cannot be isolated during gelant placement.<sup>30,31</sup> However, a plausible explanation for this phenomenon is not yet available. In our previous studies,<sup>2,18</sup> we examined several possible mechanisms for this disproportionate permeability reduction. We demonstrated that the disproportionate permeability reduction is not caused by gravity or lubrication effects. Also, gel shrinking and swelling are unlikely to be responsible for this phenomenon. Our experimental results indicated that wettability may play a role that affects the disproportionate permeability reduction. Results from core experiments using an oil-based gel suggest that the disproportionate permeability reduction might be caused by oil and water following segregated pathways. If the segregated-pathway mechanism is valid, we speculated that the disproportionate permeability reduction could be enhanced by simultaneously injecting oil with a water-based gelant or water with an oil-based gelant. In our second annual report,<sup>2</sup> we showed that the disproportionate permeability reduction was enhanced by simultaneously injecting water and an oil-based gelant using a 50/50 volume ratio. In this chapter, we continue our study of this theory by simultaneously injecting oil and a water-based gelant using a 50/50 volume ratio during gelant placement. NMR imaging was also used to observe the disproportionate permeability reduction on a microscopic scale. Based on a micromodel study by Dawe and Zhang,<sup>32</sup> we discuss how gel elasticity and interfacial tension might affect the disproportionate permeability, and we propose new experiments to verify this theory. We also studied the feasibility of using polymers (no crosslinker) to reduce permeability to water without significantly damaging oil productivity. The objectives of our research in this area are to determine why some polymers and gels selectively reduce water permeability more than oil permeability and to identify conditions that maximize this phenomenon.

### Water Shutoff Using Polymers Without Crosslinkers

Results from the literature and our own coreflood experiments<sup>19,22-29</sup> showed that many gels can reduce water permeability significantly more than oil permeability (Fig. 47). As shown in Fig. 47, the most pronounced disproportionate permeability reduction was found for a Cr(III)-HPAM gel, where the residual resistance factor for water ( $F_{rrw}$ ) was 50,000 and the residual resistance factor for oil ( $F_{rro}$ ) was 50. However, in unfractured wells, a gel with  $F_{rro} = 50$  creates essentially the same result as that for a gel with  $F_{rro} = 1,000,000$ ; both gels effectively stop flow.<sup>30</sup> Ideally, we would like a blocking agent to provide a significant permeability reduction to water without causing any damage to the oil permeability.<sup>31</sup> Several researchers suggested that adsorbed polymers may perform in this manner.<sup>24,33,34</sup> Therefore, we wish to study and confirm the ability of adsorbed polymers to reduce water permeability with minimum reduction of oil permeability.

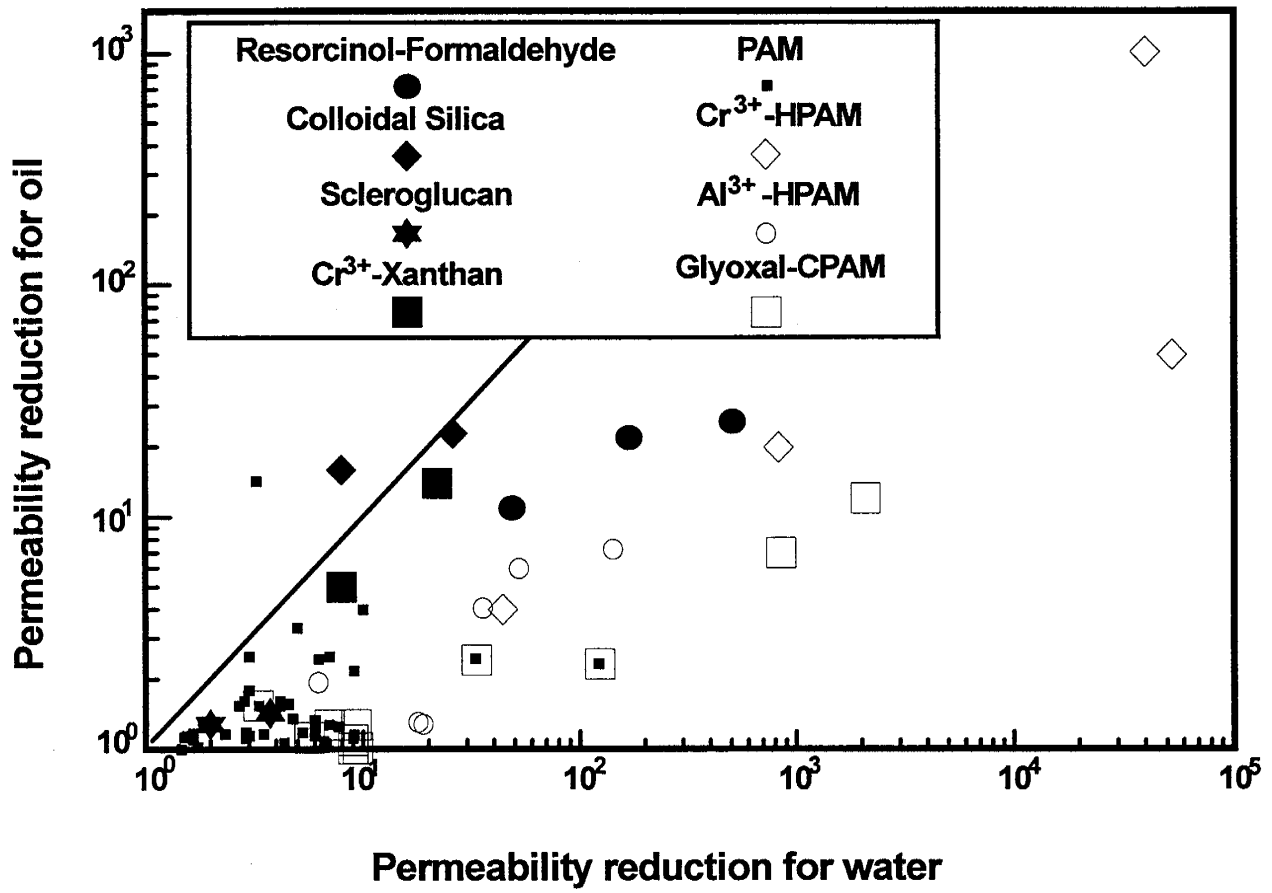


Fig. 47. Disproportionate permeability reduction by polymers and gels.

In this study, we examined two anionic polyacrylamide (HPAM) polymers and one cationic polyacrylamide (CPAM) polymer. The HPAM polymers were Allied Colloids Alcoflood® 935 and 1175A. The CPAM polymer was Pfizer Floperm® 500P. (The polymer and brine concentrations are summarized in Table 14.) Low-permeability Berea sandstone cores were used as the porous media. (We chose low-permeability Berea sandstone to minimize polymer washout.) For each experiment, the core was first saturated with brine, and porosity and permeability were determined. The core was then oilflooded, followed by waterflooding. The endpoint water and oil mobilities were measured at residual oil and water saturations, respectively. (Please refer to Table 15 in Ref. 2 for a detailed description of the coreflood procedure.) The endpoint mobilities at different stages of the core experiments are summarized in Tables B-1c through B-1e in Appendix B.

Table 14. Summary of  $F_{rro}$  and  $F_{rrw}$  for Polymers Without Crosslinkers  
Cores: Low-Permeability Berea Sandstone, 41 °C

Core ID	Polymer	1st $F_{rrw}$	1st $F_{rro}$	2nd $F_{rrw}$	2nd $F_{rro}$
SSL-100	0.5% HPAM (Alcoflood 935), 1% NaCl	4	5	3	3
SSL-102	0.1% HPAM (Alcoflood 1175A), 1% NaCl	$6.7 u^{-0.39}$	4	4	
SSL-103	0.4% CPAM, (Floperm 500P), 2% KCl	$39 u^{-0.81}$	7	$18 u^{-0.54}$	7

Ten PV of the polymer solution were then injected into the core at residual oil saturation. During polymer injection, effluent samples were collected and the viscosities were measured using a Contraves LS30 low-shear viscometer. For all polymers tested, the effluent viscosities leveled off after injecting 2 PV of polymer solution. In all cases, the effluent viscosity at the end of the polymer injection never reached the viscosity of the uninjected samples. For the 0.5%-Alcoflood 935 HPAM, the viscosity of the uninjected sample was 28 cp. After injecting 10 PV of the polymer solution, the final effluent viscosity was 20 cp. For the 0.1%-Alcoflood 1175A HPAM, the viscosity of the uninjected sample was 5 cp. After injecting 10 PV of the polymer solution, the final effluent viscosity was 3.5 cp. Similar behavior was observed for the 0.4%-Floperm 500P CPAM. The viscosity of the uninjected sample and the final effluent viscosity after injecting 10 PV of the polymer solution were 16 cp and 9 cp, respectively. These are indications that polymers are being removed or degraded during the placement process. There are several possible reasons for the viscosity losses, including filtration, adsorption, and mechanical degradation. Since a constant pressure gradient of 200 psi/ft was used during polymer injection, mechanical degradation is certainly a possible cause for the viscosity losses. However, at this time, we do not have enough information to rule out other possibilities.

After polymer injection, residual resistance factors were determined at different flow rates. For the Alcoflood 935 HPAM, Table 14 shows that the residual resistance factors were low after treatment. These residual resistance factors ( $F_{rw}$  and  $F_{ro}$ ) were independent of flow rate. For the Alcoflood 1175A HPAM, only the  $F_{rw}$  values measured immediately after treatment showed a non-Newtonian behavior—described by a power-law equation ( $F_{rw} = 6.7 u^{-0.39}$ ). Neither HPAM provided a significant disproportionate permeability reduction. In contrast, the CPAM reduced water permeability several times more than oil permeability (Table 14). However, this polymer also resulted in a seven-fold reduction in oil permeability. As shown in Table 14, the  $F_{rw}$  for the CPAM exhibited a strong shear-thinning behavior that can be described by a power-law equation. For all the polymers tested, the  $F_{ro}$  values were Newtonian. Please refer to Tables B-2a through B-2c in Appendix B for detailed information regarding residual resistance factors.

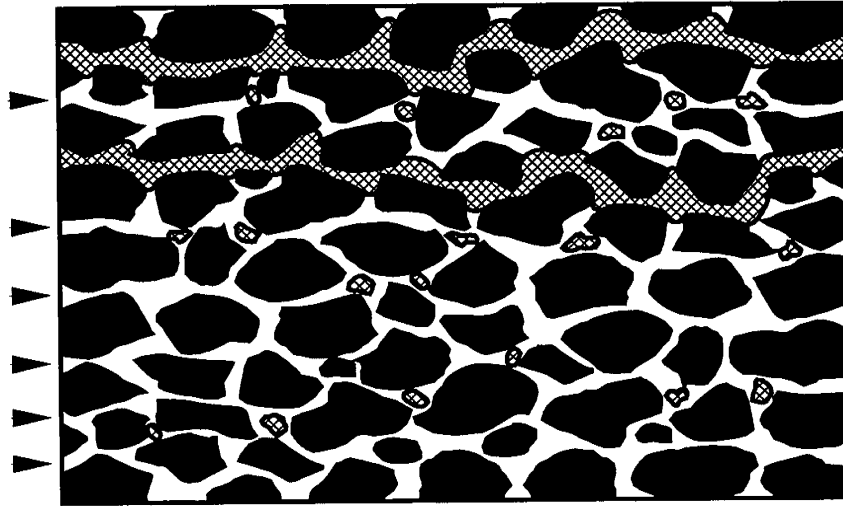
In summary, the polymers examined in this work suffered significant viscosity losses during the placement process. For the HPAM polymers, the residual resistance factors were low, and no significant disproportionate permeability reduction was observed after treatment. The CPAM reduced water permeability several times more than oil permeability. However, this polymer also resulted in a significant (seven-fold) reduction in oil permeability after treatment.

## **Possible Mechanisms for Disproportionate Permeability Reduction**

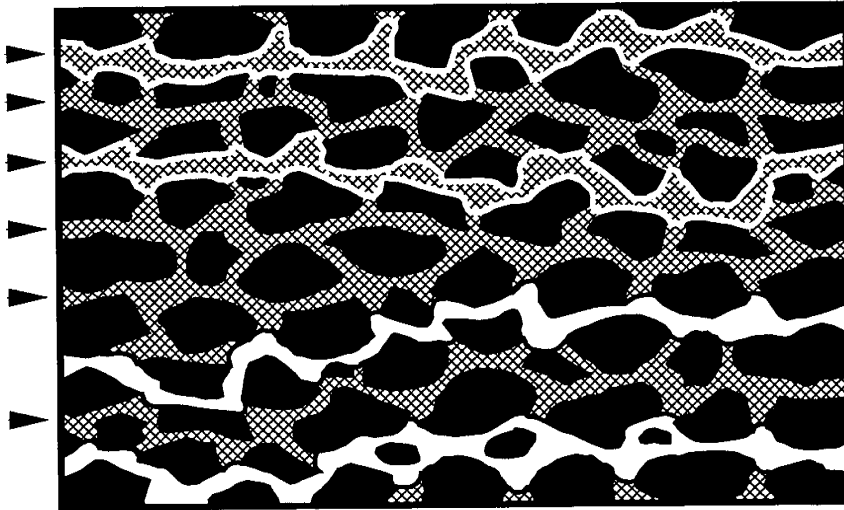
### **Segregated Oil and Water Pathways**

In our second annual report,<sup>2</sup> we proposed that the disproportionate permeability reduction might be caused by water and oil following segregated pathways on a microscopic scale. As illustrated in Fig. 48, during high water fractional flow, water flows through most of the open pathways while some of the pathways remain connected by oil and inaccessible to water. If, on a microscopic scale, a water-like gelant primarily follows the water pathways, many of the oil pathways could remain connected and gel-free after treatment. In this way, the water-based gel could reduce water permeability more than oil permeability. Following the same logic, if an oil-based gel primarily follows the oil pathways, many of the water pathways could remain connected and gel-free after treatment. Therefore, if this theory is valid, an oil-based gel should reduce oil permeability more than water permeability.

**Experiments with an Oil-Based Gel.** In our second annual report,<sup>2</sup> we used an oil-based gel consisting of 12-hydroxystearic acid and Soltrol 130 to test the segregated-pathway theory. During core experiments using this oil-based gel, oil permeability was reduced significantly more than water permeability. This result suggests that the gel restricted oil pathways much more than water pathways.



High Water Fractional Flow



High Oil Fractional Flow

Water
  Oil
  Oil Only
  Rocks

Fig. 48. Segregated oil and water pathways.

If the segregated-pathway mechanism is valid, we speculated that the disproportionate permeability reduction could be enhanced by simultaneously injecting oil with a water-based gelant or water with an oil-based gelant. Presumably, simultaneous injection of oil and a water-based gelant should allow a larger fraction of oil pathways to remain open than if a water-based gelant is injected by itself. Using similar logic, simultaneous injection of water and an oil-based gelant should allow a larger fraction of water pathways to remain open than if an oil-based gelant is injected by itself. We used an oil-based gel containing 18% 12-hydroxystearic acid in Soltrol 130 to verify this theory. Two core experiments were performed using high-permeability Berea sandstone cores. (Ref. 2 contains a detailed description of the experiments.) For the base case, the oil-based gelant was injected at residual oil. In the second experiment, the gelant was injected with brine using a 50/50 volume ratio. Table 15 shows that for the case where brine was injected with the gelant during placement, the  $F_{rrw}$  value ( $F_{rrw}=5$ ) was much lower than that for the case where no brine was injected with the gelant ( $F_{rrw}=34$ ). Interestingly,  $F_{rro}$  values were comparable for both cases (Table 15). These findings support the segregated-pathway theory.

Table 15. Summary of  $F_{rro}$  and  $F_{rrw}$  For an Oil-Based Gel  
 Core: High-Permeability Berea Sandstone, 41 °C  
 Gelant: 18% 12-Hydroxystearic Acid in Soltrol 130

Core ID	Gelant-injection strategy during placement	1st $F_{rrw}$	1st $F_{rro}$	2nd $F_{rrw}$
SSH-85	Gelant injected @ $S_{or}$	34	300	30
SSH-86	50/50 gelant/brine volume ratio during placement	5	225	14

**Experiments with a Water-Based Gel.** We performed similar core experiments using a water-based gel to confirm the validity of the segregated-pathway theory. The water-based gel contained 0.5% HPAM (Allied Colloids 935), 0.1667% chromium triacetate, and 1% NaCl. High-permeability Berea sandstone cores were used as the porous media. (The endpoint water and oil mobilities are summarized in Tables B-1a and B-1b.) To minimize injectivity problems during placement, the gelant was injected at room temperature (26 °C). (The remainder of the core experiments were performed at 41 °C.) For the base case, 8 PV of the gelant were injected at residual water saturation. After gelant injection, the core was shut in for three days at 41 °C. After shut-in, oil was first injected into the core to determine the residual resistance factor for oil ( $F_{rro}$ ). To minimize gel breakdown,  $F_{rro}$  was determined using a single flow rate, 0.32 ml/hr. Next, brine was injected at the same flow rate to determine  $F_{rrw}$ . Then, oil was injected again at 0.32 ml/hr to verify that the disproportionate permeability reduction was not caused by gel breakdown. The first data row of Table 16 shows that the gel reduced water permeability about three times more than oil permeability.

In the second core experiment, the aqueous gelant was injected with Soltrol 130 oil using a 50/50 volume ratio. As shown in the second data row of Table 16, this change in injection strategy

resulted in  $F_{rro}$  and  $F_{rrw}$  values that were approximately three times less than those in the first data row of Table 16. These findings suggest that the water and oil pathways after treatment were both less restricted compared to the case where the aqueous gelant was injected alone. Contrary to the case for oil-based gelant injected with water, simultaneous injection of oil with a water-based gelant did not result in a more pronounced disproportionate permeability reduction. Also, the  $F_{rro}$  value increased significantly during the second oil injection after shut-in (last column of Table 16). A similar behavior was observed in the previous case with the oil-based gel (Table 15). Specifically, the  $F_{rrw}$  value measured during the second water injection cycle after shut-in was significantly higher than during the first water injection cycle. At this point, we do not know why this happened. More work is needed to resolve this issue.

Table 16. Summary of  $F_{rro}$  and  $F_{rrw}$  For a Water-Based Gel  
 Core: High-Permeability Berea Sandstone, 41 °C  
 Gelant: 0.5% HPAM, 0.1667% Cr(III)-Acetate, 1% NaCl

Core ID	Gelant-injection strategy during placement	1st $F_{rro}$	1st $F_{rrw}$	2nd $F_{rro}$
SSH-91	Gelant injected @ $S_{wr}$	1,250	3,000	1,250
SSH-92	50/50 gelant/oil volume ratio during placement	360	990	660

### Effects of Interfacial Tension and Gel Elasticity on Disproportionate Permeability Reduction

**Filtration Experiments.** Dawe and Zhang<sup>32</sup> proposed that the disproportionate permeability reduction is caused by gels shrinking in contact with oil and swelling in contact with water. In their study, filtration experiments were first performed to study the behavior of gels in the presence of oil and water. In their experiments, Dawe and Zhang<sup>32</sup> used glass-frit filters commonly used for polymer filtration. The gelant used in their glass-filter experiments contained 0.2% xanthan (Pfizer's Flocon 4800), 80-ppm  $CrCl_3$  (Pfizer's X-link 1000), and 2% NaCl. Fig. 49 is a schematic of the glass-filter experiments. For each experiment, they first prepared the gelant in a beaker and waited until the gelant was nearly gelled. Then, they poured 25 ml (30 mm in height) of the nearly gelled gelant into an empty glass filter. After gelation, they put 125 ml (150 mm in height) of a dyed brine on top of the gel. The brine had the same composition as that used for gelant preparation. The experiment was repeated with the same amount of dyed oil on top of the gel. (The oil was a heavy distillate oil with a viscosity of 2 cp.) Dawe and Zhang reported that the brine diffused into the gel, but no significant gel-volume change was observed. In contrast, the gel under the oil collapsed to a thin cake, and the oil did not diffuse into the gel or pass through the filter. Dawe and Zhang<sup>32</sup> suggested that the oil caused the gel to synerese. However, results from their glass-filter experiments were not consistent with our observations. Based on previous experiments, we are convinced that oil does not necessarily cause gels to shrink. Therefore, we tried to reproduce the glass-filter experiments of Dawe and Zhang.<sup>32</sup>

**Gel Composition: 0.2% Xanthan (Flocon-4800),  
80-ppm  $\text{CrCl}_3$  (X-link 1000), 2% NaCl**

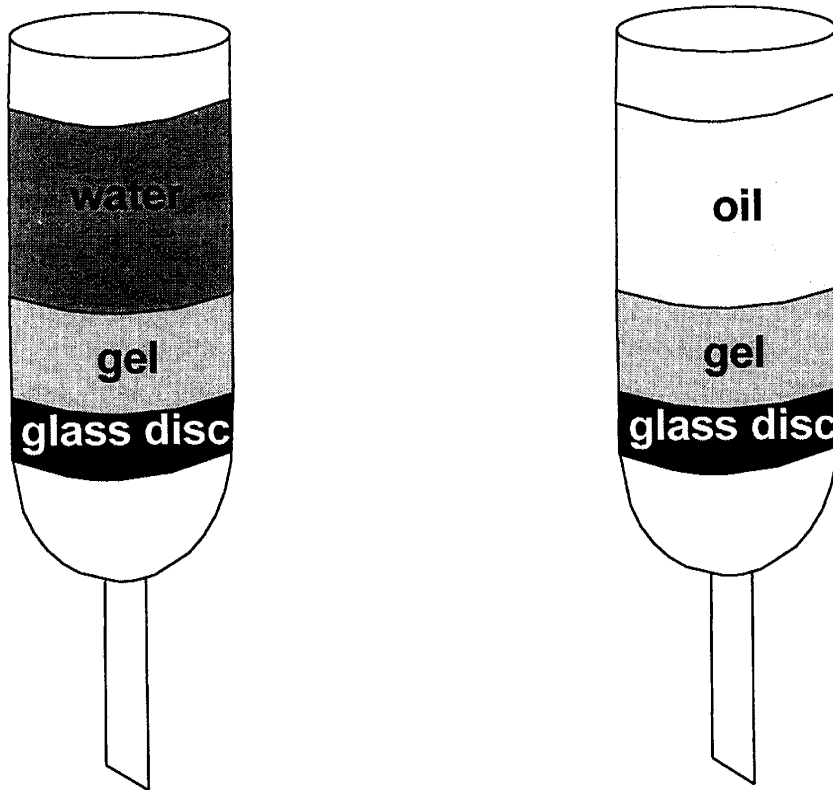
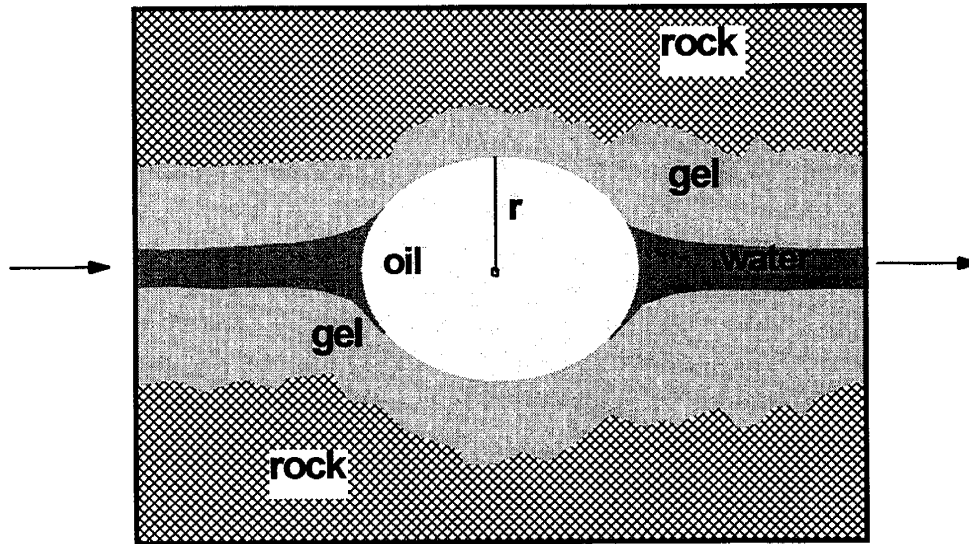


Fig. 49. Schematic of glass-filter experiments.

We repeated the same experiments and observed that the gel shrank (syneresed) by about the same amount (more than 50%) under both oil and brine. Our observations were consistent with our past experience and yet very different from the results reported by Dawe and Zhang.<sup>32</sup> The fact that the gel shrank by about the same amount under both oil and water indicates that the oil, by itself, did not cause the gel to synerese. This result is a critical issue which affects our assessment of the correct mechanism for the disproportionate permeability reduction.

**Micromodel Experiments.** Based on visual micromodel experiments, Dawe and Zhang<sup>32</sup> concluded that oil passes through a gel by fingering through the center of the pores, and then widens the pathways by taking water away from inside the gel (syneresis). In contrast, water diffuses through a gel and reduces the width of the pathways by swelling the gel. Therefore, the gel could reduce water permeability more than oil permeability. Dawe and Zhang were kind enough to send us a copy of the video recording of their visual micromodel study. In reviewing the video, we agreed that oil forced its way through the gel by creating a channel through the center of the pores; however, the oil did not widen the pathways by syneresing the gel. Pathways were widened by physical gel breakdown, not syneresis. Also, during waterflooding, we observed that gel swelling was a minor effect. In the video, we also observed that when oil drops forced their way through an aqueous gel, the gel acted like an elastic material, creating just enough room for the oil drops to squeeze through. We suspect that this phenomenon was a result of interfacial tension between oil and the aqueous phase. As illustrated in Fig. 50, when an oil droplet is extruding through an aqueous gel, there are two competing forces acting against each other. On the one hand, a capillary force is trying to force open the channel. On the other hand, the confining force exerted by the gel on the oil droplet is trying to close the channel. The final radius of the channel around the oil droplet depends on the balance between the two forces. The greater the radius of the flow path around the oil droplet, the higher the effective permeability to oil. In contrast, when water flows through the same channel, there is no capillary force to force open the channel. Hence, the effective permeability to water should be less than that to oil. To us, results from Dawe and Zhang's micromodel experiments suggest that interfacial tensions and the elasticity of the gel might contribute to the disproportionate permeability reduction.

There are two possible ways to test this theory. One way is to vary the oil/water interfacial tension by adding a surfactant to the oil phase during an oil-water experiment in a strongly water-wet core. According to the equation in Fig. 50, the capillary pressure across the interface,  $P_c$ , is proportional to the interfacial tension,  $\sigma$ , divided by the oil-drop radius,  $r$ . Reducing the interfacial tension will decrease the capillary pressure, decrease the radius of the oil droplets flowing through the gel (because of the elastic counterforce applied by the gel), and decrease the radius of the channels through an elastic gel. Therefore, if this theory is valid, lowering the interfacial tension should result in a lower permeability to oil while the water permeability should not be affected. In other words, the disproportionate permeability reduction should decrease if the oil-water interfacial tension is reduced.



$$P_c \propto \frac{\sigma}{r}$$

where  $P_c$  : capillary pressure across the interface  
 $\sigma$  : interfacial tension  
 $r$  : oil-drop radius

Fig. 50. Effect of interfacial tension on disproportionate permeability reduction.

Another way to test this theory is to change the gel elasticity. In concept, increasing gel elasticity should allow the capillary force to force open a larger path, resulting in a higher effective permeability to oil. One way to increase the elasticity of a gel is to incorporate gas into the system. Therefore, if this theory is valid, we expect a gelled foam to show a more pronounced disproportionate permeability reduction. Experiments are being conducted to verify this theory.

### Disproportionate Permeability Reduction by a Gelled Foam

To test the above theory, we examined the ability of a gelled foam to reduce permeability to water and oil. Because gelled foams are very compressible, we expected a large disproportionate-permeability-reduction effect. We performed two core experiments, both in 700-md Berea sandstone. In both experiments, the cores were first saturated with a brine that contained 1% NaCl and 0.1%  $\text{CaCl}_2 \cdot 2\text{H}_2\text{O}$ . In both cases, the gelant/surfactant solution contained 0.5% Allied Colloids Alcoflood® 935 HPAM, 0.0417% Cr(III) acetate, 1% NaCl, 0.1%  $\text{CaCl}_2 \cdot 2\text{H}_2\text{O}$ , and 0.3% Stepan Bio-Terge® AS-40 (a  $\text{C}_{14-16}$  alpha-olefin sulfonate). Nitrogen was the gas used for foaming.

**First Foam Experiment.** In the first core experiment, 5 PV (161 ml) of gelant/surfactant solution were forced through Core 67 using a rate of 200 ml/hr (15.0 ft/d). To slow the gelation reaction, this placement step occurred at 26°C. Next, 66 ml of nitrogen were injected with an injection pressure of about 30 psi. (Atmospheric pressure existed at the core exit.) During gas injection, 16.5 ml of liquid were produced. Then, to allow gelation to occur, the core temperature was raised to 41°C, and the core was shut in for five days.

After the shut-in period, 14.3 PV (460 ml) of brine were injected at a variety of rates, as indicated in Fig. 51. This figure shows that an apparent shear-thinning behavior was observed during brine injection. At a Darcy velocity of 15.8 ft/d, the brine residual resistance factor was 61. Fig. 51 indicates that the gelled foam was degraded to some extent when subjected to the rate sequence shown. After obtaining the data shown in Fig. 51, we performed several cycles of oil and water injection, as shown in Table 17. This table shows oil and water residual resistance factors during these cycles. Throughout the cycles, the water residual resistance factors were significantly greater than the oil residual resistance factors. However, the disproportionate permeability reduction was not particularly large. For this foamed gel,  $F_{\text{rw}}/F_{\text{ro}}$  was about 2 (later cycles of Table 17). For comparison,  $F_{\text{rw}}/F_{\text{ro}}$  (measured at 15.8 ft/d) was about 2 for gels (without foam or gas) that provided  $F_{\text{ro}}$  values of 10.<sup>18</sup>

Fig. 52 shows the results from tracer studies that were performed during each of the brine injection steps listed in Table 17. The open-circle curve shows tracer results before any gelled foam was placed in the core. The solid-circle curve shows tracer results during brine injection after placement of the gelled foam (but before oil injection). This curve indicates that the gelled foam occupied about 60% of the pore space in the core (because the tracer  $C/C_0 = 50\%$  about 0.4 PV). The solid-diamond curve shows tracer results during brine injection after the first oil cycle,

while the open-diamond curve shows tracer results during brine injection after the second oil cycle. Consistent with the resistance-factor data in Table 17, these curves indicated some breakdown of the gelled foam during successive cycles of oil and water injection.

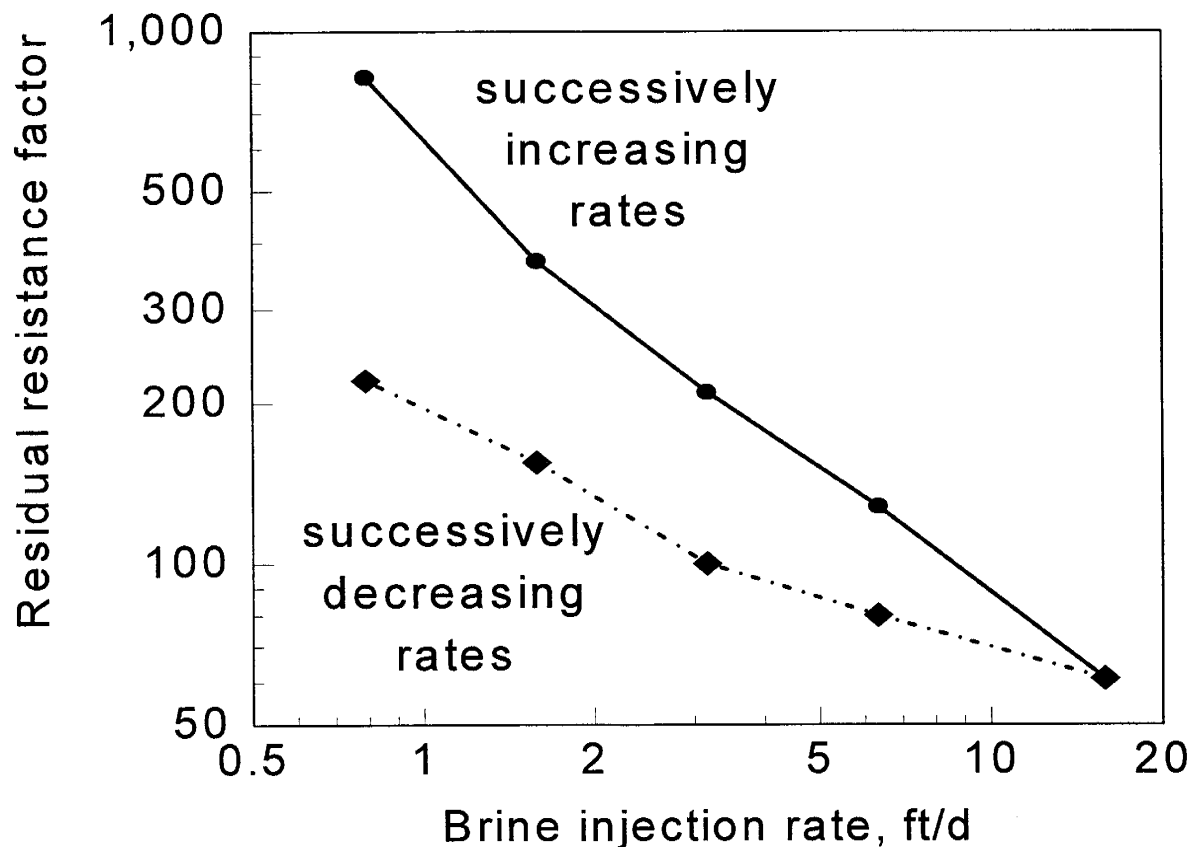


Fig. 51. Brine residual resistance factor versus rate (after foam placement in Core 67).

Table 17. Residual Resistance Factors During Oil or Brine Injection at 15.8 ft/d (Core 67)

Injectant	PV injected	Residual resistance factor
brine	14.3	61.0
oil	15.3	12.0
brine	11.5	20.0
oil	10.0	10.4
brine	10.6	18.9
oil	11.1	9.0

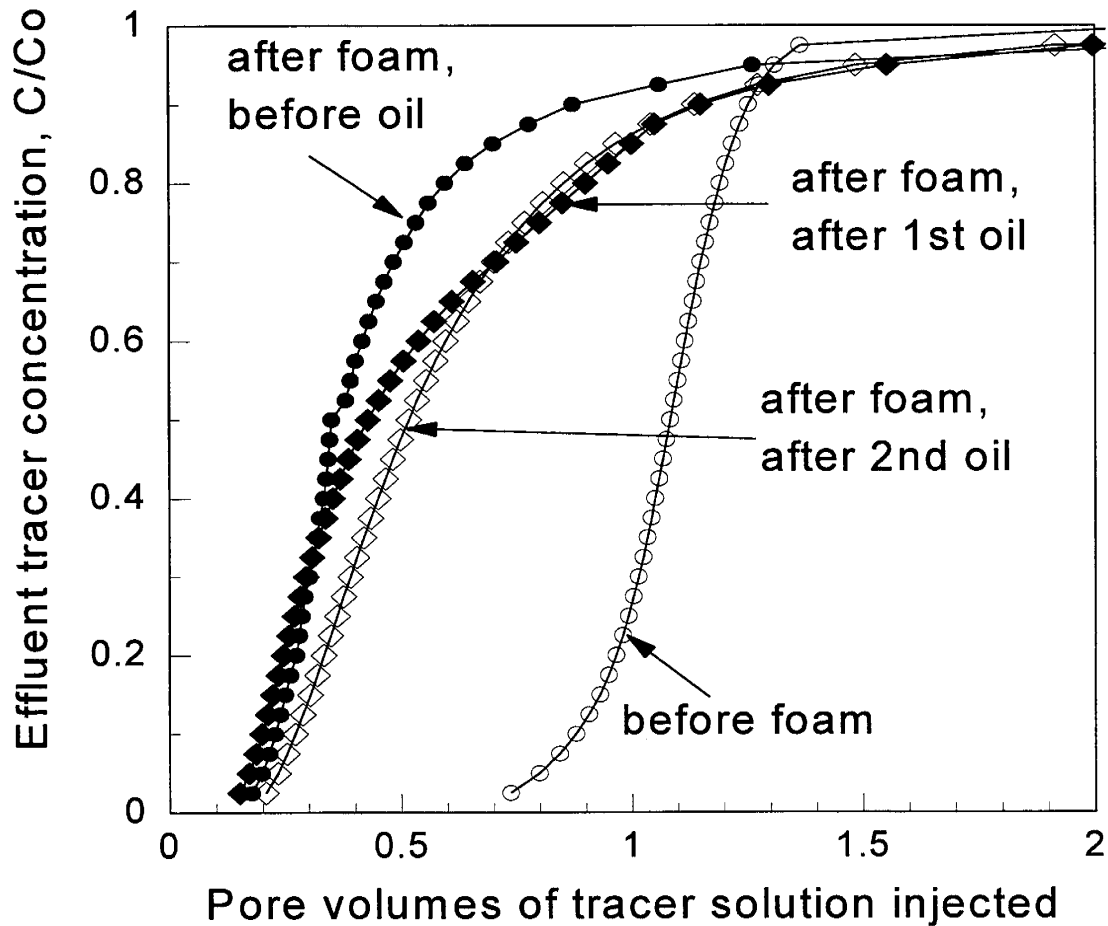


Fig. 52. Tracer results before and after foam placement in Core 67.

**Second Foam Experiment.** In the second core experiment, 6.6 PV (196 ml) of gelant/surfactant solution were forced through Core 68 using a rate of 200 ml/hr (15.8 ft/d). Again, placement occurred at 26°C. Next, 53 ml of nitrogen gas were injected with an injection pressure of about 17 psi. During gas injection, 18.3 ml of liquid were produced. Then, the core temperature was raised to 41°C, and the core was shut in for four days.

After the shut-in period, several cycles of brine and oil were injected using a fixed rate of 10 ml/hr (0.791 ft/d). Table 18 lists  $F_{rw}$  and  $F_{ro}$  values measured during these cycles. Table 18 shows that the ratio,  $F_{rw}/F_{ro}$ , ranged from 5 to 9 during this experiment. A comparison of Tables 17 and 18 suggests the disproportionate permeability reduction is most pronounced at low flow rates. This result is consistent with our earlier observations of the behavior of gels without gas or foam. For example, Fig. 53 (taken from Fig. 1 of Ref. 18) shows that  $F_{rw}/F_{ro}$  has values of 7 and 2 at velocities of 0.791 ft/d and 15.8 ft/d, respectively. Therefore, to date, the disproportionate permeability reduction does not appear to be more pronounced for a gelled foam than for a gel without foam or gas. These findings do not support our speculation that gel elasticity contributes to the disproportionate permeability reduction.

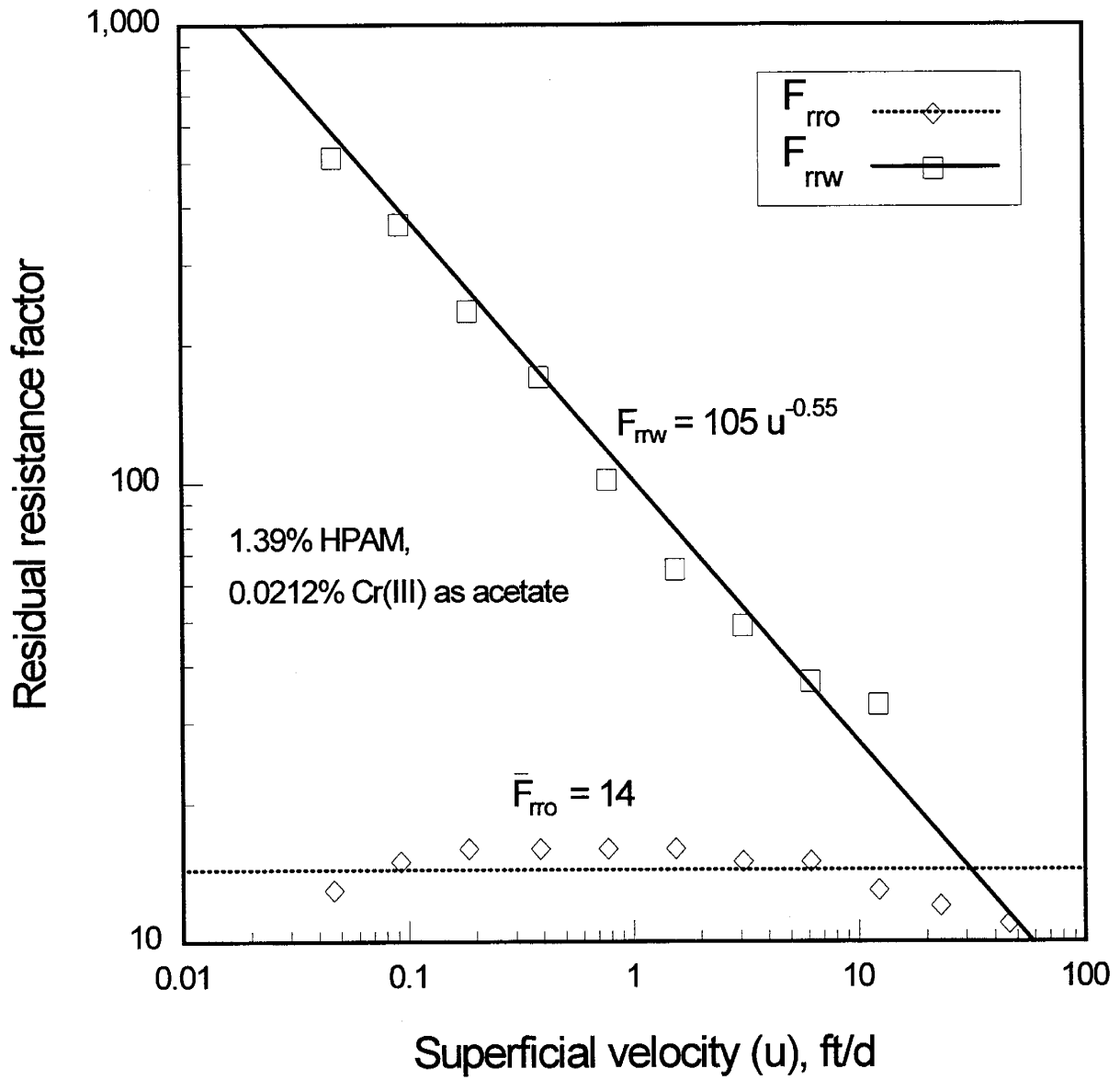


Fig. 53. Apparent rheology during oil and water injection.

Table 18. Residual Resistance Factors During Oil or Brine Injection at 0.79 ft/d (Core 68)

Injectant	PV injected	Residual resistance factor
brine	15.6	205
oil	7.7	35
brine	7.6	157
oil	8.1	22
brine	8.0	94
oil	8.0	11
brine	8.8	50
oil	10.5	11

Fig. 54 shows the results from water- and oil-tracer studies that were performed during this experiment. The open-circle curve shows tracer results during brine injection, before any gelled foam was placed in the core. The solid-circle curve shows brine-tracer results during the last brine-injection step of Table 18, while the solid-diamond curve shows oil-tracer results during the last oil-injection step of Table 18. The last two curves exhibited similar breakthrough times.

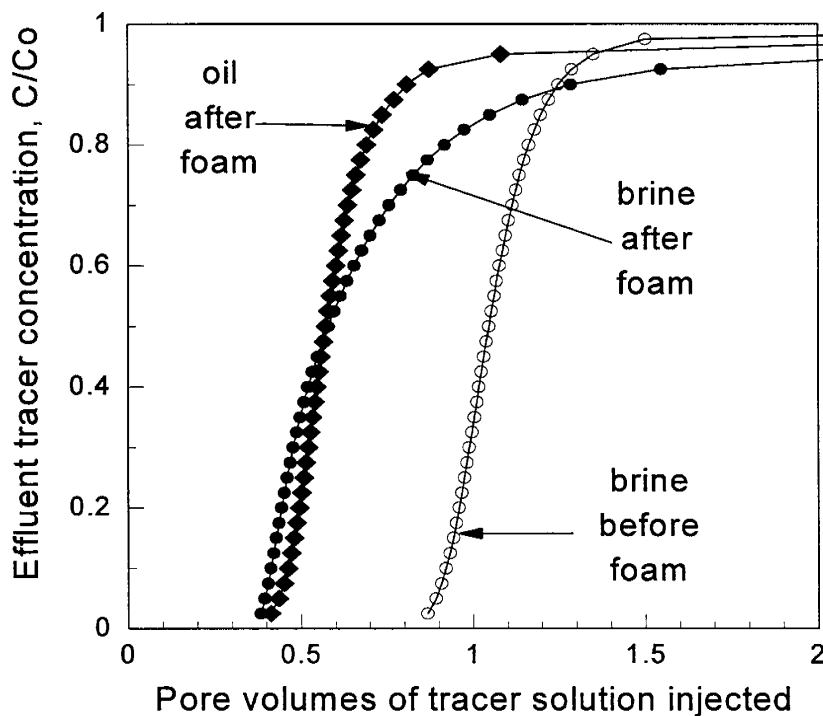


Fig. 54. Tracer results before and after foam placement in Core 68.

## NMR Imaging Experiments

The objective of our NMR imaging experiments was to observe the disproportionate permeability reduction on a microscopic scale. In this section, we report our first attempt using NMR imaging to visualize water and oil pathways after a polymer treatment. Prior to these experiments, we have relied on macroscopic parameters, such as pressure drops, tracer-breakthrough times, and effluent concentrations, to study the disproportionate permeability reduction. NMR imaging provides a means to study the phenomenon on a microscopic scale.

**Core and Fluids.** In this study, we used fused glass-bead cores as the porous media. Before fusing, the Pyrex beads ranged from 20 to 38  $\mu\text{m}$  in diameter. The cores were 2.7 cm in length with a cross-sectional area of 0.113  $\text{cm}^2$ . The cores has a nominal permeability to water of 1,000 md. Due to the small core size, we could only estimate the pore volume to be about 0.1 ml. Also, the dead volume was several times larger than the estimated pore volume. Therefore, tracer tests were not feasible with the glass-bead cores. We chose the fused glass-bead cores because most conventional cores (e.g., Berea sandstone) contain too much metal that interferes with the NMR measurements. Figs. 55 and 56 are images of a glass-bead core from electron microscopy. They show images of the glass-bead core at two different magnifications using the Back-Scatter-Electron-Imaging technique. During sample preparation, some glass beads fell off the thin section. The black craters seen on these pictures indicate the missing beads. As shown in these images, most of the glass beads remained spherical in shape with a relatively smooth surface. These images also show that the porous medium was clean and clay free. Results from an image analysis revealed that the beads had a mean particle size of about 35  $\mu\text{m}$ , which is consistent with the manufacturer's numbers (20 to 38  $\mu\text{m}$  in diameter). The pore sizes varied from 18  $\mu\text{m}$  to 174  $\mu\text{m}$ . Results from an Amott test showed that the glass-bead core had a Amott water index of about 0.5. This result is surprising since we generally expect a glass porous medium to be strongly water wet (Amott water index = 1).

The brine used in the NMR imaging experiments contained 1% NaCl and 0.025%  $\text{MnCl}_2$ . The purpose of using  $\text{MnCl}_2$  was twofold. First,  $\text{MnCl}_2$  accelerates the relaxation time for protons in the brine phase and, therefore, reduces the time required to finish a scan. (With  $\text{MnCl}_2$  in the brine phase, a 3-D scan required about 18 hours. Without  $\text{MnCl}_2$ , about 68 hours are required to complete a 3-D scan.) Second, since  $\text{MnCl}_2$  only affects the relaxation time of protons in the brine phase, interference is minimized from protons in the oil phase. Originally, we planned to use fluorine scans with 3,5-bis(trifluoromethyl)bromobenzene to image the oil phase. However, the idea was abandoned because we discovered (at the last minute) that the imaging probe was not capable of delivering the required resolution. Instead, we performed proton scans only. Since the core was held in place throughout the imaging experiment, the image of the oil distribution at residual water saturation could be calculated by subtracting the brine image at residual water saturation from the brine image when the core was completely saturated with the water phase. However, the subtraction process could affect the signal to noise ratio and render the image less reliable. The polymer used in this study was 0.1% Allied Colloids 1175A HPAM.

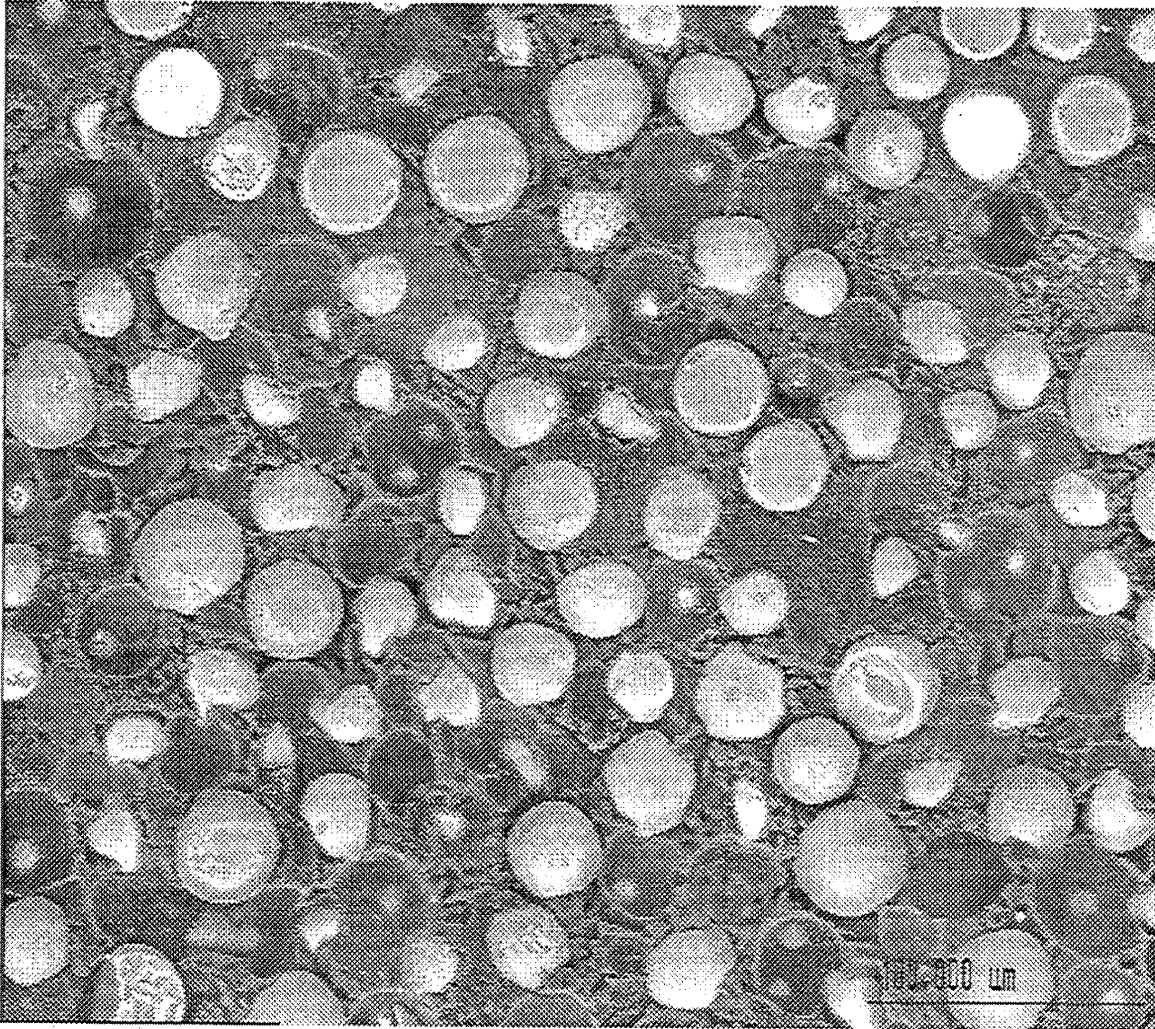


Fig. 55. Image of a glass-bead core using Back-Scatter-Electron Imaging (low magnification).

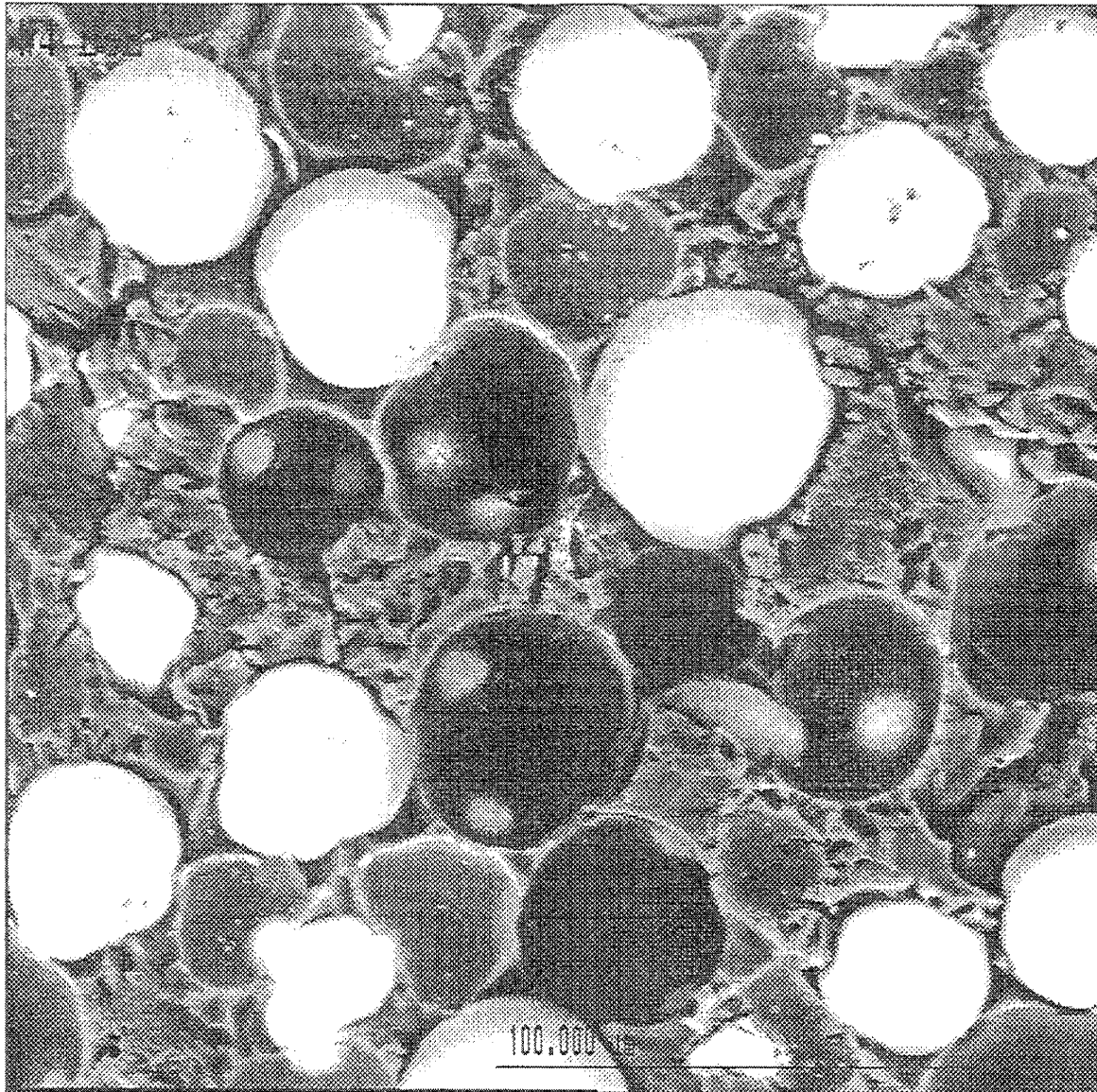


Fig. 56. Image of a glass-bead core using Back-Scatter-Electron Imaging (high magnification).

**Experimental Procedure.** For each NMR imaging experiment, the core was first saturated with brine and the brine permeability was measured. The core was then loaded into an imaging probe and placed into the NMR imaging device. After loading the core into the imaging device, a proton scan was performed to image the brine distribution in the core. Then, the core was oilflooded, followed by waterflooding to determine the endpoint oil and water permeabilities at  $S_{wr}$  and  $S_{or}$ , respectively. During each flood, a constant pressure of 15 psi was applied across the core. The permeability measurements were performed at a constant flow rate without exceeding the pressure constraint (to avoid mobilizing the residual phases). After each flood, a proton scan was performed to determine the brine distribution in the core. As discussed previously, the image of the oil distribution at  $S_{wr}$  was determined through subtraction. Since our main objective was to see the oil and water pathways after treatment, the polymer solution was prepared in  $D_2O$  to minimize the interference from the resident brine. The polymer solution was injected into the core at  $S_{or}$ . After polymer injection, brine was injected into the core at 0.32 ml/hr to determine the residual resistance factor for water ( $F_{rrw}$ ). Then, oil was injected into the core at the same flow rate to determine the residual resistance factor for oil ( $F_{rro}$ ). Proton imaging was performed after each residual-resistance-factor measurement to image the water and oil pathways after treatment. However, a potential problem here is that the polymer also contained protons. Although the polymer concentration was very low (0.1%), we could not distinguish between the injected brine and the retained polymer. All imaging experiments were performed at room temperature (26°C).

**Screening Experiments.** Before we actually performed the imaging experiments, several screening experiments were conducted in the glass-bead cores to characterize the rock-fluid system. The experimental procedure was the same as that discussed in the previous paragraph, except that no actual imaging was performed. Unless otherwise specified, the screening experiments were performed at 41°C. Also, in these experiments, Soltrol 130 was used as the oil phase. (The endpoint mobilities for all glass-bead cores are summarized in Tables B-1f through B-1m of Appendix B.) Since the glass-bead cores could not sustain a high pressure drop, we focused our efforts on finding a polymer that can provide reproducible disproportionate permeability reduction. We examined three different polymers, including Allied Colloids' Alcoflood® 935 and 1175A HPAM polymers, and Pfizer's Floperm® 500P CPAM polymer. Table 19 summarizes the results from these screening experiments. As shown in Table 19, the core treated with the Alcoflood 935 HPAM did not show reproducible residual resistance factors. The core treated with Floperm 500P CPAM provided low residual resistance factors. This result indicated polymer washout. Surprisingly,  $F_{rro}$  values were greater than the  $F_{rrw}$  values for the CPAM.

Table 19 also shows that the Alcoflood 1175A HPAM reduced oil permeability about five times more than water permeability. To ensure that this result was not an experimental artifact, we repeated the same experiment using xylene as the oil phase. We chose xylene because it is very similar in molecular structure to the oil, 3,5-bis(trifluoromethyl)bromobenzene, that was used during the NMR imaging experiments. Since 3,5-bis(trifluoromethyl)bromobenzene was very expensive (over \$1 per gram), we chose xylene for screening tests. These experiments were performed at room temperature (26°C). Tables 19 and 20 show that the Alcoflood 1175A HPAM

consistently reduced oil permeability five to ten times more than water permeability. This is opposite of the trend that we expected, and we do not know why this happened. In spite of this polymer's unusual behavior, we decided to use it for our preliminary NMR imaging experiments for two reasons. First, we did not have a suitable alternative that provided a reproducible disproportionate permeability reduction in the glass-bead cores. Second, determining why this polymer behaves differently might be valuable in understanding why the disproportionate permeability reduction occurs.

Table 19. Summary of  $F_{rrw}$  and  $F_{rro}$  for Polymers in Fused Glass-Bead Cores  
Oil: Soltrol 130, Brine: 1% NaCl, 41°C

Core ID	Polymer	1st $F_{rrw}$	1st $F_{rro}$	2nd $F_{rrw}$	2nd $F_{rro}$	3rd $F_{rrw}$
NB-9	0.5% HPAM (Alcoflood 935)	2	11	20	7	2
NB-12	0.4% CPAM (Floperm 500P)	3	6	4	9	3
NB-11	0.1% HPAM (Alcoflood 1175A)	2	11	3	12	2

Table 20. Summary of  $F_{rrw}$  and  $F_{rro}$  for a HPAM Polymer in Fused Glass-Bead Cores  
Polymer: 0.1% HPAM (Alcoflood 1175A)  
Oil: Xylene, Brine: 1% NaCl, 26°C

Core ID	1st $F_{rrw}$	1st $F_{rro}$	2nd $F_{rrw}$	2nd $F_{rro}$	3rd $F_{rrw}$
XB-4	3	26	3	30	2
XB-5	3	30	6	26	3

A similar experiment was performed using an oil-based gel consisting of 12-hydroxystearic acid and Soltrol 130. Table 21 shows that gels with 8% and 18% 12-hydroxystearic acid in Soltrol 130 reduced oil permeability significantly more than water permeability ( $F_{rro}/F_{rrw}=5$ ). This result is consistent with the results that we observed in Berea sandstone cores. (Please refer to Ref. 2 for a more detailed description of the oil-based gel.)

Table 21. Summary of  $F_{rrw}$  and  $F_{rro}$  for an Oil-Based Gel in Fused Glass-Bead Cores  
Oil: Soltrol 130, Brine: 1% NaCl, 41°C

Core ID	Gel	1st $F_{rro}$	1st $F_{rrw}$	2nd $F_{rro}$
NB-17	8% 12-hydroxystearic acid in Soltrol 130	200	40	180
NB-16	18% 12-hydroxystearic acid in Soltrol 130	216	60	300

**Imaging Experiments.** The NMR imaging experiments were performed in collaboration with BDM-Oklahoma, Inc. (NIPER). We gratefully acknowledge BDM-Oklahoma, Inc., especially Daryl Doughty and Liviu Tomutsa, for performing the NMR imaging experiments. Fig. 57 shows a schematic of the core orientation during a scan. The direction of flow was along the y-axis. The part of the core covered by the RF (radio frequency) coil was about 11-mm long. In the imaging experiments, a three-dimensional projection-reconstruction-NMR-imaging method was used. The core was placed in a very strong and homogeneous magnetic field. The protons in water resonate at the same frequency in the magnetic field, resulting in a sharp peak for water in the NMR spectrum. By superimposing a linear magnetic gradient on the homogenous field, a spatial differentiation of the water molecules can be made from the different resonate-frequency responses. Water protons on the side of the sample exposed to the lower field will resonate at lower frequencies. (The resonate frequency is proportional to the field intensity.) By changing the orientation of the intensity gradient in a three-dimensional manner, information about the location of all water protons can be obtained and images of the water distribution can be reconstructed. A more detailed discussion of the methodology of NMR microscopy can be found in Ref. 35. (Due to a software deficiency, no fluid saturation numbers are available for our scans.)

Table 22 summarizes results from the residual-resistance-factor measurements during the NMR imaging experiments. In this case, we used 3,5-bis(trifluoromethyl)bromobenzene as the oil phase, and all measurements were conducted at room temperature (26°C). As shown in Table 22, the brine mobility was 1,100 md/cp when the glass-bead core was saturated with brine only. The endpoint oil and brine mobilities were 453 md/cp and 540 md/cp, measured at  $S_{wr}$  and  $S_{or}$ , respectively. Ten pore volumes of 0.1%-Alcoflood 1175A HPAM were injected into the core at  $S_{or}$ . To minimize the interference from the resident brine, the polymer solution was prepared in  $D_2O$ . Table 22 shows that the polymer reduced oil permeability ten times more than water permeability. This is consistent with our previous observations in this type of fused glass-bead core.

Table 22. Summary of  $F_{rrw}$  and  $F_{rro}$  During NMR Imaging Experiments  
 Oil: 3,5-Bis(trifluoromethyl)bromobenzene, Brine: 1% NaCl  
 Polymer: 0.1% HPAM (Alcoflood 1175A)

Core ID	$(k/\mu)_w$ , md/cp @ $S_w = 1.0$	$(k/\mu)_o$ , md/cp @ $S_{wr}$	$(k/\mu)_w$ , md/cp @ $S_{or}$	$F_{rrw}$	$F_{rro}$
XB-6	1,100	453	540	2	21

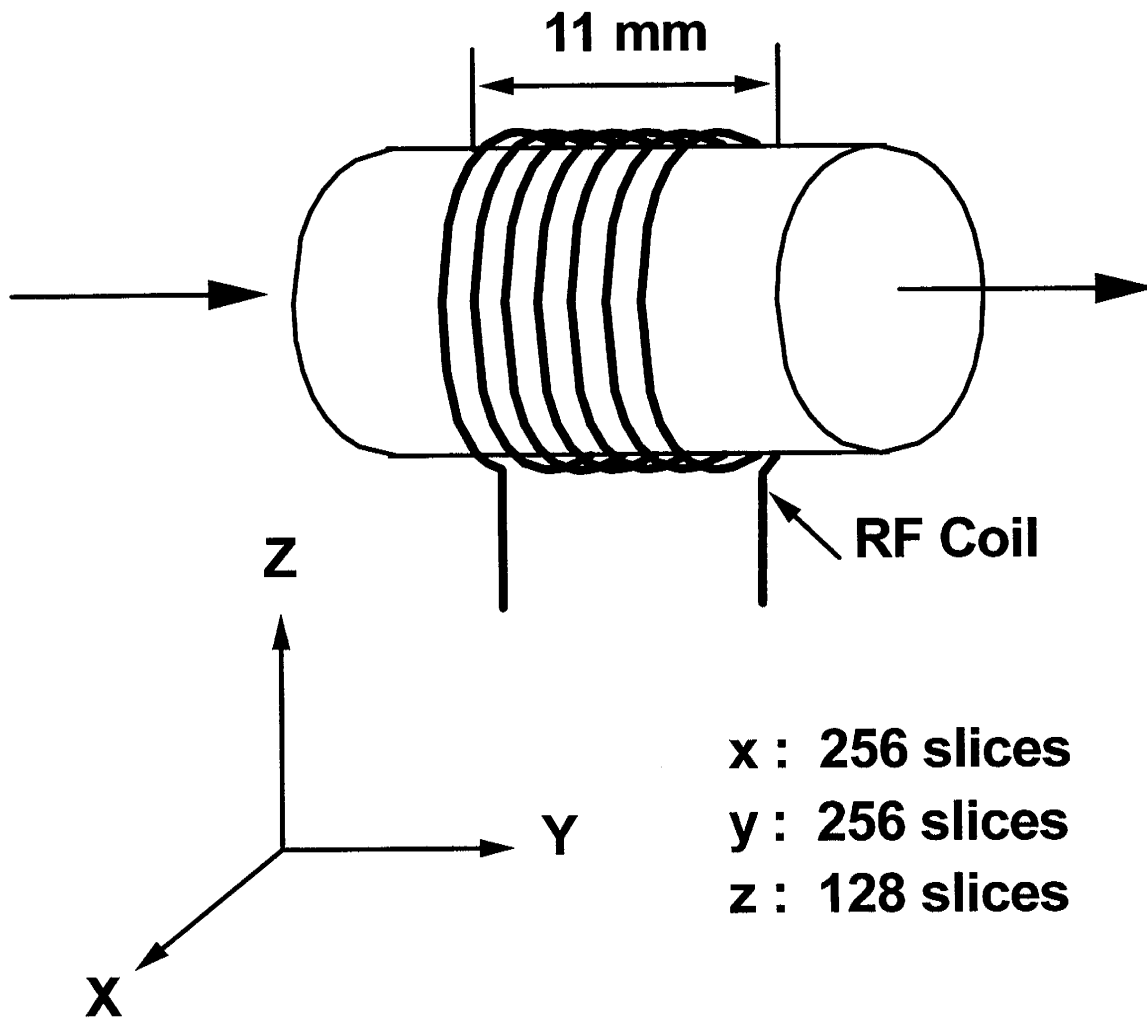


Fig. 57. Core orientation during NMR imaging experiments.

Figs. 58 through 61 are images of a horizontal slice located at the center of the core along the x-y plane taken at different stages of the experiment. The flow direction was from the bottom to the top of the image. Fig. 58 is an image of the core saturated with brine only. The gray scale on the bottom of each image represents fluid saturations, with the brightness increasing with increasing fluid saturation. From the number of pixels on the image, we estimated that the image has a resolution of about  $23 \mu\text{m}$  in the horizontal direction (x-direction) and a resolution of about  $90 \mu\text{m}$  in the vertical direction (y-direction). Fig. 58 shows that the brine was distributed fairly evenly throughout the core. The large black holes in the image are chunks of fused glass beads. Following the brine-distribution imaging, the core was oilflooded to residual water saturation. Fig. 59 is an image of the oil distribution in the core at residual water saturation. This image was obtained by subtracting the water image taken at residual water saturation from the water image taken when the core was saturated with brine only. As discussed earlier, the subtraction process results in a lower signal to noise ratio. Hence, the oil image generated in this way is less reliable. The image in Fig. 59 shows that the oil phase is distributed evenly throughout the core. Next, the core was flooded with brine to residual oil saturation. Due to a malfunction in the data acquisition computer, the next imaging scan failed. Therefore, no image was available of the water distribution at residual oil saturation. After the waterflood, 10 PV of polymer solution were injected at residual oil saturation. The resistance factor during the polymer injection was 70. (For comparison, the viscosity of the solution was 5 cp.) After polymer injection, brine was injected at a constant flow rate of 0.32 ml/hr to determine  $F_{rrw}$ . Fig. 60 is the image taken after the  $F_{rrw}$  measurement. As shown in Fig. 60, the brine was distributed evenly throughout the core, and the brine saturation was high. We can barely distinguish the connecting water pathways in the image. After the  $F_{rrw}$  measurement, oil was injected into the core at the same flow rate (0.32 ml/hr) to determine  $F_{rro}$ . Fig. 61 shows that the oil saturation was extremely low after the  $F_{rro}$  measurement, and the oil was sparsely distributed throughout the core. Remember that this polymer reduced oil permeability significantly more than water permeability ( $F_{rro}/F_{rrw} = 10$ ). By comparing Figs. 60 and 61, we might be tempted to conclude that the oil permeability was reduced more than water permeability because the number of pathways available for water flow after polymer treatment was significantly greater than that for oil after treatment. However, as we discussed earlier, there are several problems with our current experimental procedure. First, we cannot distinguish polymer retained in the porous medium from the brine injected after treatment. Therefore, the high water saturation seen in Fig. 60 might be misleading if a significant amount of polymer was retained in the porous medium. Second, the oil images were generated indirectly through subtraction. The lower signal/noise ratio resulting from the subtraction process renders the images less reliable. Also, the resolution of the NMR imaging technique was still not high enough to see clearly at the pore level. In light of the limitations mentioned above, we need a more suitable imaging technique that can provide reliable pore-level images of oil and water flow in porous media. While continuing a search for suitable imaging techniques, our efforts will focus on other methods to study disproportionate permeability reduction.

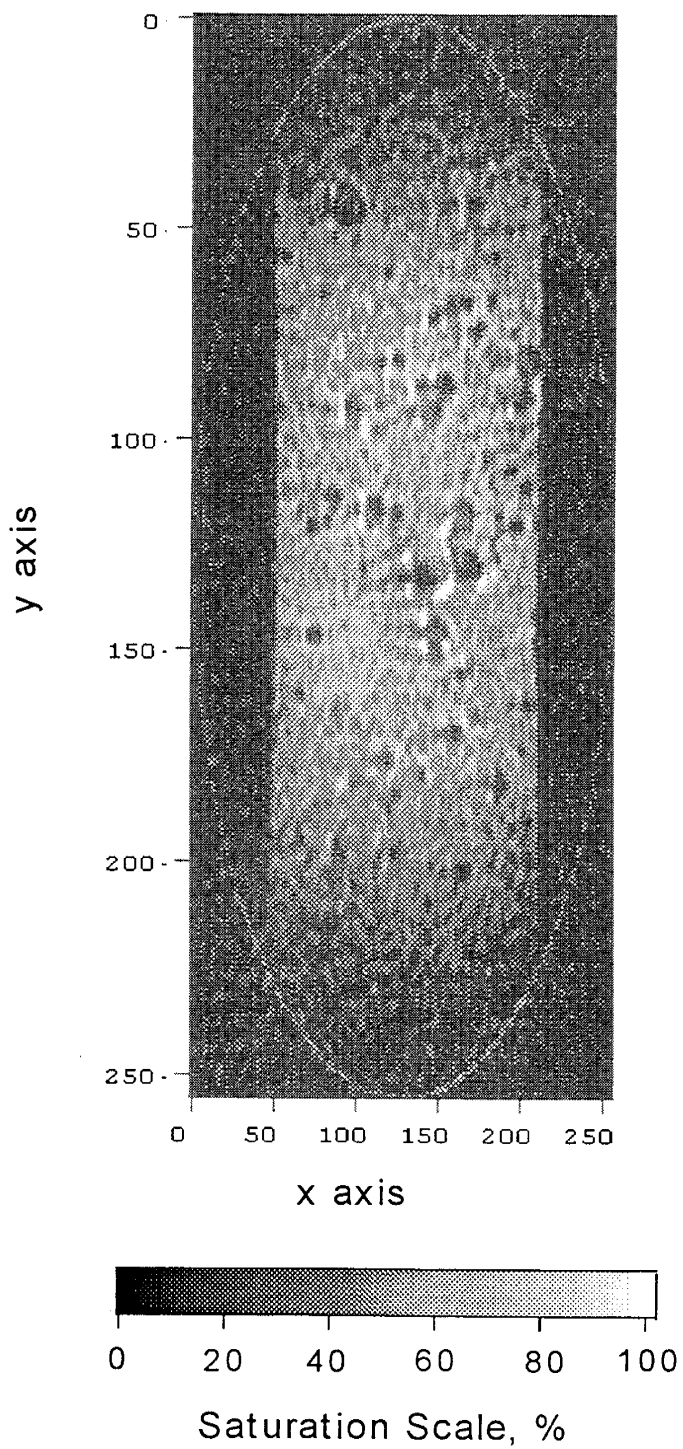


Fig. 58. Image of the brine distribution at  $S_w=1$ .

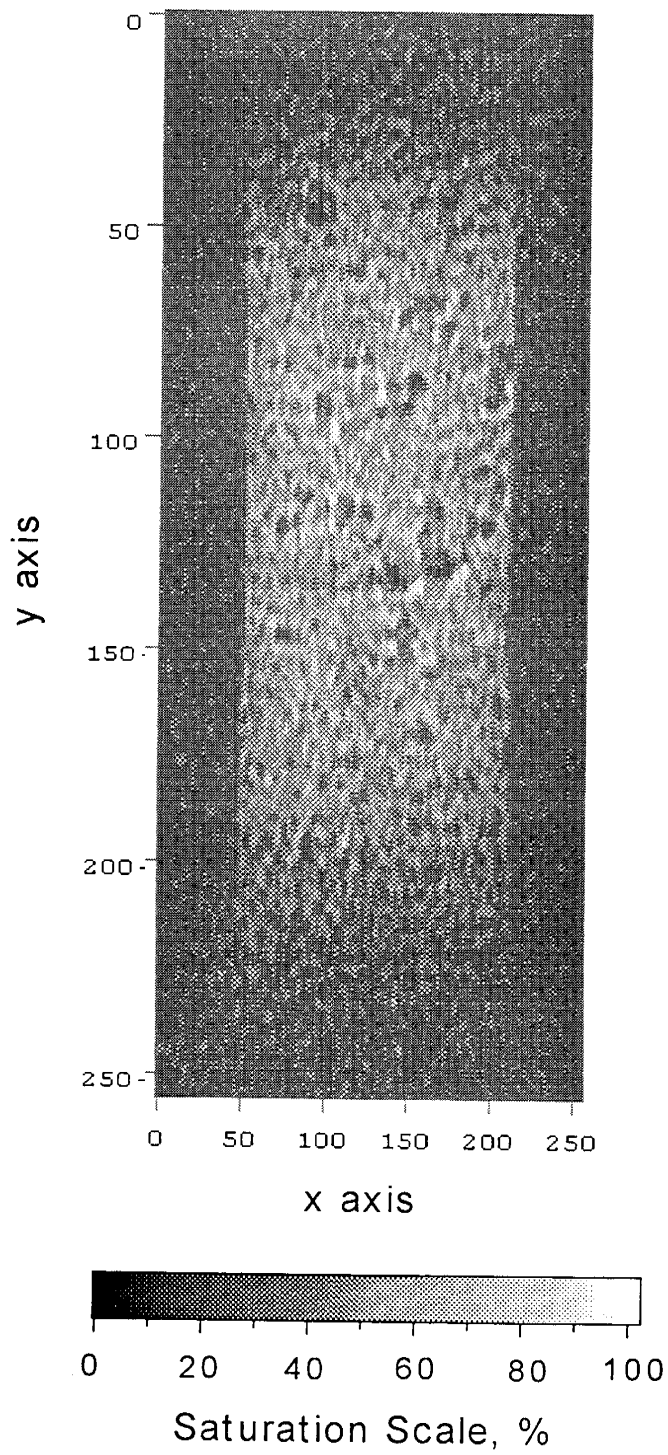


Fig. 59. Image of the oil distribution at  $S_{wr}$ .

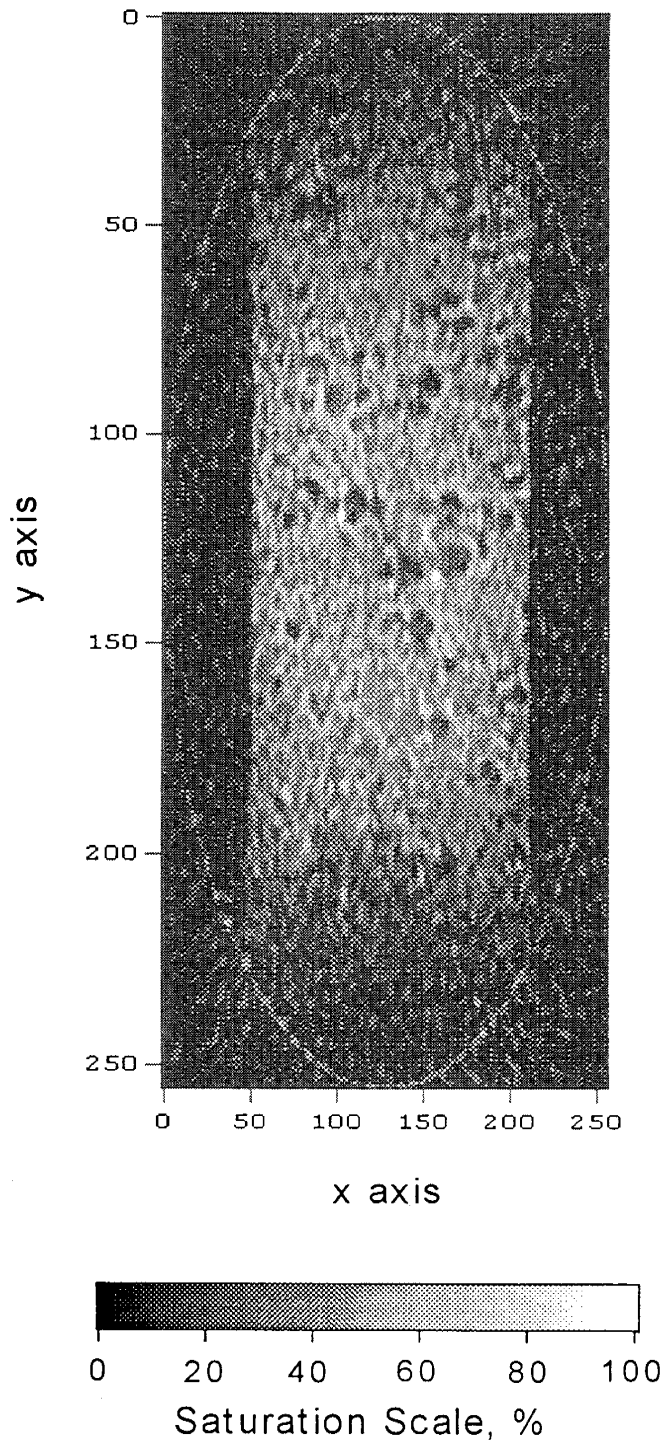


Fig. 60. Image of the brine distribution after  $F_{rw}$  measurement.

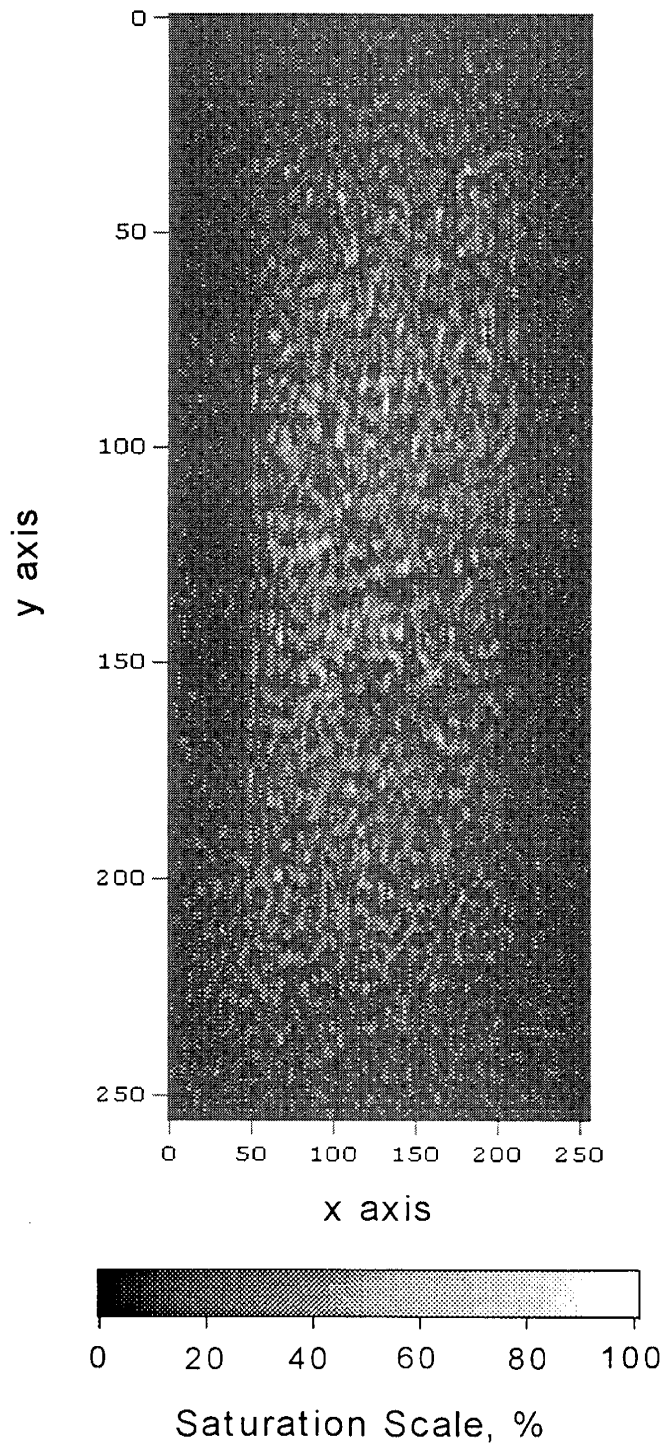


Fig. 61. Image of the oil distribution after  $F_{ro}$  measurement.

## Conclusions

1. In our second annual report,<sup>2</sup> based on results from core experiments using an oil-based gel, we proposed that the disproportionate permeability reduction might be caused by oil and water following segregated pathways on a microscopic scale. If the segregated-pathway mechanism is valid, we speculated that the disproportionate permeability reduction could be enhanced by simultaneously injecting oil with a water-based gelant or water with an oil-based gelant. For an oil-based gel, the disproportionate permeability reduction was enhanced by simultaneously injecting water with the oil-based gelant. This result supports the segregated-pathway mechanism. However, simultaneously injecting oil with a water-based gelant did not result in a more pronounced disproportionate permeability reduction. This latter finding does not support the segregated-pathway mechanism.
2. One mechanism that might be responsible for the disproportionate permeability reduction involves the effects of oil/water interfacial tension and gel elasticity. This concept can be tested by varying the oil/water interfacial tension during flow of water and oil through an aqueous gel in a strongly water-wet core. A second type of experiment to test this concept involves varying the elasticity of the blocking agent. Core experiments are being conducted to verify this theory. Preliminary results using gelled foams did not support this mechanism.
3. While examining HPAM and CPAM polymers in Berea sandstone, the polymer solutions suffered significant viscosity losses during the placement process. For the HPAM polymers, the residual resistance factors were low, and no significant disproportionate permeability reduction was observed after treatment. The CPAM polymer reduced water permeability several times more than oil permeability. However, this polymer also caused a significant (seven-fold) reduction in oil permeability.
4. HPAM and CPAM polymers reduced oil permeability more than water permeability in glass-bead cores (that we developed for the NMR imaging experiments). This behavior is the opposite of the result that we expected. More work is needed to understand why this happened.
5. Preliminary results from NMR imaging experiments revealed that our imaging technique had many limitations which prevented us from obtaining reliable pore-level images. We will continue to search for suitable imaging techniques to study the disproportionate permeability reduction on a microscopic scale. In the mean time, our efforts will focus on other methods to study the disproportionate permeability reduction.

## 5. USE OF MICROORGANISMS AS BLOCKING AGENTS

Several people<sup>36-57</sup> proposed the use of microorganisms as blocking agents. In this study, we conducted an extensive literature survey to determine if microorganisms can be superior to gels as blocking agents. Our analyses focused on the placement and permeability-reduction characteristics. We investigated the ability of microorganisms to selectively enter and block high-permeability thief zones without damaging the low-permeability, oil-productive zones. We also examined the permeability-reduction characteristics of microorganisms in porous media. Specifically, we want to determine if microorganisms can reduce permeability to a greater extent in high-permeability water zones than in low-permeability oil zones.

### Selective Plugging Using Microorganisms

**Selective Plugging Using Spores.** Bae *et al.*<sup>36</sup> investigated the use of spores for profile modification. The spores were produced by an endospore-forming bacteria called Salton-1. In its native state (not as spores), the bacteria resembled *Bacillus licheniformis*. The molecular weight of an exopolymer produced by the bacteria was between 2 and 3 million daltons. The spores produced by the bacteria were spherical with a diameter of about 0.2-0.3  $\mu\text{m}$  (private conversation with Bae). Bae *et al.* stated that the spores are small and therefore easier to propagate through the porous media. From one perspective, the spherical-shaped spores could be viewed as particulates. A suspension of particulates could penetrate readily into a high-permeability zone, while size restrictions prevent them from entering less-permeable zones.<sup>2</sup> Therefore, spores could conceptually provide better placement characteristics than gels.

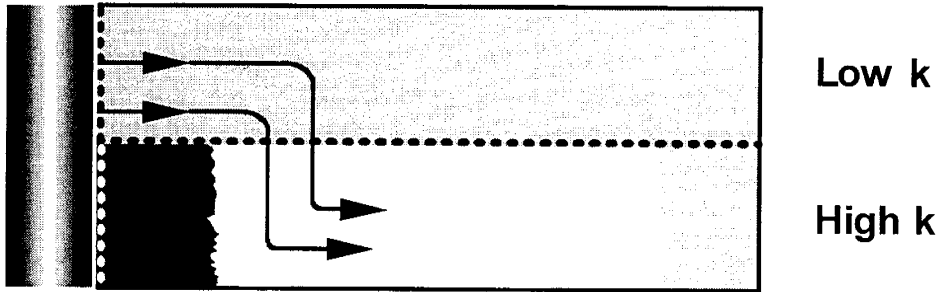
Bae *et al.*<sup>36</sup> performed coreflood experiments in Berea sandstone cores with permeabilities ranging from 100 md to 1,820 md. The treatment process involved injecting a slug of spores, followed by a nutrient slug. Two sets of experiments were performed in this study. First, Bae *et al.* studied spore transport in the porous media by injecting 1 PV of spore suspension followed by another 1 PV of nutrient-free brine. Results from effluent analyses indicated that the spores propagated through Berea cores with permeabilities greater than 710 md. However, a careful examination of the data reveals that a large fraction of the spores were retained in the high-permeability cores. For cores with permeabilities less than 380 md, no spores were detected in the effluent. In the second set of core experiments, a slug of spores was injected followed by a nutrient slug of the same size. The core permeabilities ranged from 1,150 md to 1,820 md. Different slug sizes were used in the coreflood experiments. Depending on the amount of spores and nutrients injected, the treatments reduced permeability by 10% to 100% (complete plugging). The degree of permeability reduction decreased with decreasing amount of spores and nutrients injected. The core experiments with less than 0.6 pore volumes of spores and nutrients injected caused only an average of 20 to 30% permeability reduction. Based on these results, the authors suggested that in field applications, the small amount of spores that penetrated into the low-permeability zones might not cause any significant formation damage.

Bae *et al.* proposed a scheme which takes advantage of crossflow in a reservoir to achieve a selective placement. Conceptually, selective placement of spores could be achieved if the spores are small enough to penetrate deep into the high-permeability zones and yet large enough to form filter cakes on the rock faces of the low-permeability zones.<sup>2</sup> After spore injection, the filter cakes could be removed by jet-washing the wellbore. During subsequent nutrient injection, the near-wellbore region in the high-permeability zones would be damaged by microbial growth. As shown in Fig. 62, the near-well plugging in the high-permeability zones would then divert the subsequently injected nutrient solution into the low-permeability zones. The nutrients would then crossflow into the high-permeability zones after bypassing the damaged area and promote the growth of the spores trapped beyond the damaged area. In this way, selective plugging of the high-permeability channels could be extended deep into the reservoir without damaging the low-permeability oil-productive zones. The proposed scheme is most likely to succeed when the permeability contrasts between high- and low-permeability zones are high.<sup>2</sup>

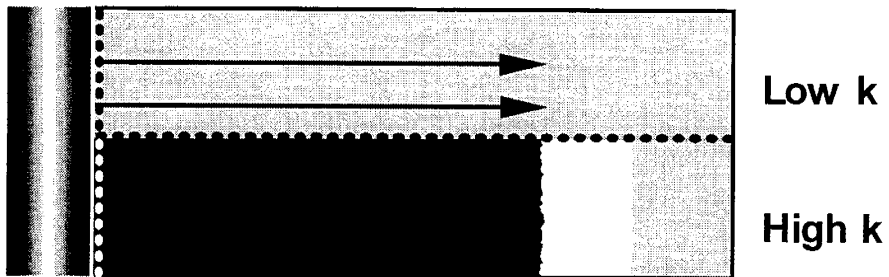
Another process using spores was proposed by Silver *et al.*<sup>37</sup> Silver *et al.* developed bacteria consisting of two strains of *Bacillus licheniformis* for injection profile modification. The authors speculated that selective placement could be achieved by injecting spores small enough to penetrate into high-permeability thief zones, but not the low-permeability oil zones. The spore injection was then followed by nutrient injection. After germination and growth, their biomass and the exopolymer produced in situ could then reduce the permeability of the high-permeability thief zones without damaging the low-permeability oil zones. Their coreflood examples demonstrated that the bacteria can enter and damage cores with permeabilities ranging from 124 to 6,700 md. The authors asserted that the microbial process is most effective in cores with permeabilities greater than 600 md. However, their coreflood data did not contain enough details to support this claim. Also, the authors did not provide any information about the spore sizes.

**Selective Plugging Using Ultramicrobacteria (UMB).** A series of studies<sup>38-41</sup> were conducted using ultramicrobacteria (UMB) for in-depth selective plugging of high-permeability thief zones. The UMB are the reduced-sized bacteria of certain bacterial strains (e.g., *Pseudomonas putida*) formed in a starvation regime. Costerton *et al.*<sup>38</sup> reported that the typical size of the UMB ranges from 0.2 to 0.4  $\mu\text{m}$  (determined by direct light and electron microscopy). However, they did not specify the shape of the UMB. The reintroduction of nutrients can revive the starved bacteria from the dormant state to the vegetative adherent biofilm-forming state. To achieve in-depth placement, Costerton *et al.*<sup>38</sup> proposed a two-stage sequential injection technique. In their method, UMB are injected into the formation followed by a slug of nutrient. Their experimental data showed that the UMB caused a significant permeability reduction in a 3.3-darcy sandpack. However, they did not provide any data to support the claim of selective plugging.

UMB could be viewed as particulates as well. With a typical size ranging from 0.2 to 0.4  $\mu\text{m}$ , they could penetrate readily into formations with a permeability greater than 1 md.<sup>2</sup> Selective plugging is therefore dictated by the placement of nutrients. Since the flow properties of the nutrients are no different from those of gelants, their placement characteristics are similar to those



i) nutrients bypass the damaged area and crossflow into the high-permeability zone from the low-permeability zone.



ii) in-depth plugging of the high-permeability zone without damaging the low-permeability zone.

Damaged area     
  Spores only     
  Brine

Fig. 62. Selective plugging using spores with crossflow between layers.<sup>36</sup>

of gelants. Specifically, for a given distance of penetration into a high-permeability zone, the distance of penetration into a less-permeable zone will be no less for the nutrient than for a gelant with a water-like mobility. If a viscous nutrient is used (e.g., molasses or corn syrup), nutrient penetration into less-permeable zones increases.<sup>9,21,31</sup> Hence, this process suffers from the same placement limitations that gels experience.

Cusack *et al.*<sup>39</sup> injected UMB into a three-dimensional sandpack model. The authors noted that the injected UMB were found in every area of the sandpack. After nutrient injection, the UMB resuscitated and produced exopolymer in situ. The authors did not provide any information regarding the extent of permeability reduction after treatment. Also, the experimental data did not support the claim of selective plugging.

In a different study, Cusack *et al.*<sup>40</sup> used a sandstone core (16.2 cm × 10.2 cm) extracted from a Westcoast Suffield field to demonstrate the effectiveness of using UMB to enhance oil recovery. The core had a permeability of 1,058 md and a porosity of 29.5%. The core was conditioned to residual oil saturation before treatment ( $S_{or}=0.45$ ). Their coreflood data showed an increased pressure drop during the treatment process. Also, more than 90% of the residual oil was recovered during the process. The authors attributed the incremental oil recovery to selective plugging of the high permeability zones in the sandstone core. However, it is not possible to demonstrate selective plugging using such a small core (16.2 cm × 10.2 cm) with a single coreflood experiment. It is more likely that the exopolymer produced in situ and the increased pressure drop observed during the treatment process contributed to the additional oil recovery.

In another study, Cusack *et al.*<sup>41</sup> used a 45-cm × 38-cm sandpack embedded with a Berea sandstone core to demonstrate selective plugging using UMB. The sandpack was built with 125-mesh Ottawa sand with a permeability of 3,800 md. Permeability of the Berea core was 400 md. During the experiment, 1.5 PV of the UMB were injected into the test pack, followed by multiple batches of 1-PV sodium citrate medium (SCM). The pressure drop across the test pack increased significantly during the UMB and SCM injections. At the end of the experiment, the test pack was dismantled and cell numbers and polymer production in different parts of the test pack were determined. The results showed that the cells were uniformly distributed in the low-permeability Berea sandstone core, with a concentration of  $10^6$  cells/gram. The cell distribution in the sandpack was less uniform, ranging from  $10^6$  to  $10^8$  cells/gram. Polymer production in the high-permeability sandpack was 100 times higher than that in the low-permeability Berea core. Scanning electron microscopy (SEM) showed that the cells were encased in extracellular polymer in the high-permeability zone but not in the low-permeability zone. Based on this information, the authors speculated that the UMB could selectively plug the high-permeability zones in a real formation. However, the results clearly indicated that a significant amount of UMB ( $10^6$  cells/gram) penetrated into the low-permeability Berea core. Also, the authors did not provide any information regarding the extent of formation damage in the low-permeability Berea core.

**Selective Plugging in Heavy Oil Reservoirs.** Jack *et al.*<sup>42</sup> proposed the use of *Leuconostoc mesenteroides* NRRL B523 bacteria to plug water channels generated by viscous fingering during

waterflooding of heavy oil reservoirs (API gravity 13° to 17°). The lithology of the target reservoirs was a clean unconsolidated sand formation with an average permeability in excess of 1 darcy. The authors stated that the bacteria have a unique property of producing a water-insoluble polysaccharide only when sucrose is present in the culture medium. According to Lappan and Fogler,<sup>52</sup> the bacteria resemble colloidal particles with a size distribution of 0.5 to 1.2  $\mu\text{m}$ . Hence, the bacteria could conceptually be viewed as particulates with a size distribution. Due to the narrow size distribution and the small particle size, the bacteria can propagate through formations with a permeability greater than 15 md.<sup>2</sup> During placement, Jack *et al.* suggested first injecting the bacteria in a culture medium free of sucrose until the desired depth of penetration is achieved. Then, the same culture medium with enough sucrose to stimulate polymer production is injected into the porous medium. The authors speculated that the biomass and the polymer produced in situ by the bacteria could plug the water channels, thereby improving the sweep efficiency. The proposed scheme is most applicable to unfractured reservoirs with high (unfavorable) water/oil mobility ratios. However, the benefit from such a treatment will be temporary. At some point during the subsequent brine injection after treatment, viscous fingering will develop new water channels through the reservoir.<sup>58</sup> Jack's coreflood data revealed that the biomass and the polymer produced in situ did not provide much resistance to the subsequent brine injection. The plugging materials generated by the microbial process could only sustain about 6 psi across a 6.5-darcy fused glass-bead core during the subsequent injection of nutrient-free brine. The placement characteristics of the proposed process in heavy oil reservoirs are similar to those of gels.<sup>58</sup>

In a separate paper,<sup>43</sup> results from a parallel-linear coreflooding experiment were used to demonstrate the selectivity of the microbial process. However, results from parallel-linear coreflooding experiments are unreliable indicators of the selectivity of a treatment process.<sup>13</sup> The proposed microbial system was injected into a watered-out well to plug the high-permeability water zones. Chemical analyses of the produced water showed microbial activity underground. However, no significant change in oil/water ratio was observed after the treatment.

**Selective Plugging Using Indigenous Bacteria.** Knapp *et al.*<sup>44</sup> conducted a microbially enhanced oil recovery field pilot. Bacteria indigenous to the reservoir were identified. Tracer tests were performed before treatment to identify the source of fluid channeling. Sodium fluorescein was used as a tracer. Fourteen days after tracer injection, fluorescein was detected in a production well outside of the pilot area, 1,870 ft away from the injection well. The tracer results suggest that fractures were responsible for fluid channeling in the reservoir. Nutrients (molasses and ammonium nitrate) were then injected into the reservoir to stimulate bacterial growth. After treatment, tracer tests were performed again to determine the effect of microbial growth on the injection profile. The authors reported that no tracer was detected in the production well 123 days after tracer injection. This result indicates that the microbial activity had reduced the conductivity of the fractures. Results from pressure interference tests also suggest that the microbial growth process resulted in a more uniform permeability distribution in the treated region. A total of 22.5 bbls of incremental oil was produced as a result of the treatment. The authors attributed the small amount of incremental oil to the low initial oil saturation before treatment.

The proposed scheme relies on the injection of nutrients to stimulate the growth of indigenous bacteria. Since nutrients and gelants have similar placement characteristics, this process suffers from the same placement limitations that gels experience.

**Selective Plugging by In Situ Polymer Production.** Li *et al.*<sup>45</sup> studied the use of *Alcaligenes eutrophus* for formation plugging. *Alcaligenes eutrophus* are capable of producing a large amount (70% of the cell weight) of intracellular polyester–poly-3-hydroxybutyrate (PHB). Results from sandpack experiments showed that both living cells and the PHB produced by the bacteria could cause significant formation plugging. (Sandpack permeabilities were not provided in the paper.) The cells are rod-shaped. They are about 0.7  $\mu\text{m}$  in diameter and 1.8–2.6  $\mu\text{m}$  in length. The authors speculated that the elongated shape could assist selective placement. However, they did not provide evidence to support this idea. The rod-shaped bacteria act as particulates with a size distribution. As will be shown later, a broad size distribution could severely limit the selectivity of the microorganisms during placement.

**Simulation Study of Selective Plugging by Sequential Injection.** Chang *et al.*<sup>46</sup> performed a simulation study of the transport of microbes through porous media. A modified black oil model was used to simulate the microbial process. The simulated treatment involved injecting a slug of microbes followed by a nutrient slug. After a 3-day shut-in period, water was injected to determine the effectiveness of the treatment. The example case involved a two-layer reservoir with crossflow between layers. The high-permeability layer was 20-ft thick with a permeability of 1,000 md. The low-permeability layer was 10-ft thick with a permeability of 100 md. The simulation showed that the microbial process could only temporarily improve the sweep efficiency. Without continual injection of microbes and the required nutrients, the benefit from the microbial process was very short-lived. The simulation also showed that clogging or adsorption of the microbes on the rock faces could severely impede the transportation of microbes and nutrients in the porous medium. In a separate example, microbes and nutrients were injected into the high-permeability layer only during placement. The change in injection strategy resulted in a more immediate response in fluid diversion during the subsequent fluid injections. However, the change in injection strategy did not result in a longer effective treatment life. The effect on water-oil ratio after treatment was similar to that using unrestricted injection during placement.

**Summary.** Selective plugging could be achieved if the nutrients or the microorganisms could be placed selectively into high-permeability thief zones. Since the flow properties of the nutrients are no different from those of gelants, their placement characteristics are similar to those of gelants. Specifically, for a given distance of penetration into a high-permeability zone, the distance of penetration into a less-permeable zone will be no less for the nutrient (and the microorganisms) than for a gelant with a water-like mobility. If a viscous nutrient is used (e.g., molasses or corn syrup), nutrient penetration into less-permeable zones increases.<sup>9,21,31</sup>

From one perspective, microorganisms could be viewed as particulates. Because of their narrow size distribution, certain microorganisms could, in concept, provide the advantageous placement characteristics associated with monodisperse particulates.<sup>2</sup> A suspension of microorganisms could

penetrate readily into a high-permeability zone, while size restrictions prevent them from entering less-permeable zones. However, most microorganisms are rod-shaped. The rod-shaped microorganisms act like particulates with a size distribution. A broad size distribution could severely limit the selectivity of microorganisms during placement.<sup>2</sup> In the following section, we investigate the effect of rod-shaped microorganisms on selective placement.

### Selective Placement with Rod-Shaped Microorganisms

The effective particle size of a rod-shaped microorganism is determined by the orientation of the microorganism relative to the direction of flow at a pore entrance. The effective particle size,  $d_p$ , can be calculated from the following equation,

$$d_p = L \sin \theta + d \cos \theta, \quad \text{if } 0 \leq \theta \leq \tan^{-1}\left(\frac{L}{d}\right)$$

$$d_p = \sqrt{L^2 + d^2} \quad \text{if } \tan^{-1}\left(\frac{L}{d}\right) \leq \theta \leq \frac{\pi}{2} \quad (6)$$

where  $d$  is the diameter of the microorganism,  $L$  is the length of the microorganism, and  $\theta$  is the angle between the long axis of the microorganism and the direction of flow at the pore entrance. According to Eq. 6, the effective particle size is  $d$  when the long axis of the microorganism aligns with the direction of flow at a pore entrance (i.e.,  $\theta=0$ ). The effective particle size,  $d_p$ , then increases with increasing  $\theta$ . In this study, we assume that the rod-shaped microorganisms can rotate freely in a suspension. Therefore, there is an equal probability for a microorganism to assume any orientation in a suspension. Fig. 63 is a cumulative frequency plot of the effective particle size of a suspension of microorganisms. (Results in Fig. 63 were generated by Eq. 6.) The microorganisms in this example are 90- $\mu\text{m}$  long with a diameter of 18  $\mu\text{m}$ . (We assume in this study that all the microorganisms have the same dimensions.) As shown in Fig. 63, the rod-shaped microorganisms act like particulates with a size distribution. The effective particle size in this case ranges from 18  $\mu\text{m}$  (rod diameter) to 91.78  $\mu\text{m}$  (measured diagonally from one end of the rod to the other).

To study the effect of rod-shaped microorganisms on selective placement, consider injecting a suspension of microorganisms into two parallel homogeneous cores of equal length from a common injection port. The high-permeability core (Core 1) has a permeability of 10,000 md and the low-permeability core (Core 2) has a permeability of 100 md. The carrier fluid has water-like

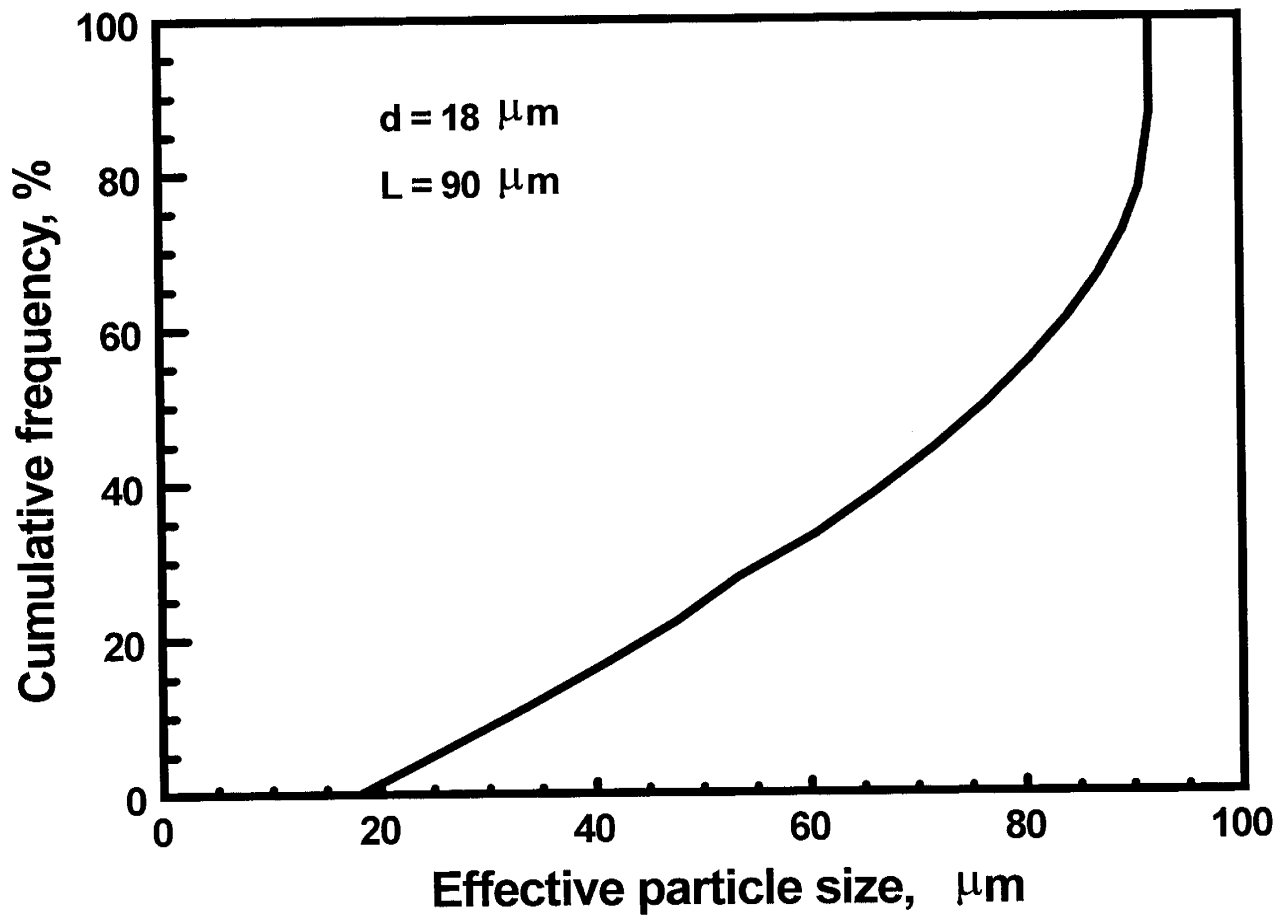


Fig. 63. Cumulative frequency plot of effective particle size for rod-shaped bacteria.

density and viscosity. The parameters used in this example are summarized in Table 23. A theoretical model developed in a previous study<sup>2</sup> for particulates is used here to examine the placement characteristics of rod-shaped microorganisms. (Please refer to Ref. 2 for a detailed description of this theoretical model.) Since our objective is to determine if microorganisms can be made to work better than gels as blocking agents, we use the performance of gels as a basis of comparison. In this example, we arbitrarily chose the average of the critical particle sizes of the high- and low-permeability cores  $[(33.33 \mu\text{m} + 3.33 \mu\text{m})/2 = 18 \mu\text{m}]$  as the rod diameter. We compared the selectivity of rod-shaped microorganisms having different aspect ratios (length/diameter) with a water-like gelant. Fig. 64 illustrates the effect of aspect ratio on selective placement of the rod-shaped microorganisms. As shown in Fig. 64, for a given permeability contrast, there is a maximum aspect ratio (in this case, 1.6:1) that should not be exceeded for the rod-shaped microorganisms to be more selective than a water-like gelant during placement. The maximum selectivity is achieved when the aspect ratio approaches one (i.e., near spherical). When the microorganisms are near spherical, the placement characteristics of the microorganisms approach those of monodisperse particulates. Next, we examine the effect of permeability contrast on the maximum allowable aspect ratio for selective placement. In this example, the low-permeability core has a permeability of 10 md and the rod diameter is  $1.5 \mu\text{m}$ . (With the exception of the permeability values, the other parameters remain the same as those in Table 23.) We increase the permeability contrast by increasing the permeability of the high-permeability core. Again, a water-like gelant was used as the base case for comparison. Fig. 65 shows that the maximum allowable aspect ratio for the rod-shaped microorganisms to be more selective than a water-like gelant increases with increasing permeability contrast between high- and low-permeability zones.

Table 23. Parameters for Degree of Penetration Calculations

d	= 18 $\mu\text{m}$		
k <sub>1</sub>	= 10,000 md	k <sub>2</sub>	= 100 md
d <sub>crit1</sub>	= 33.33 $\mu\text{m}$	d <sub>crit2</sub>	= 3.33 $\mu\text{m}$
$\phi_1$	= 0.2	$\phi_2$	= 0.2
L <sub>t</sub>	= 50 ft	$\alpha_o$	= 0.21
k <sub>c</sub>	= 1 md	$\phi_c$	= 0.2
S <sub>w1</sub>	= 1.0	S <sub>w2</sub>	= 1.0
$\mu_w$	= 1 cp	$\mu_p$	= 1 cp

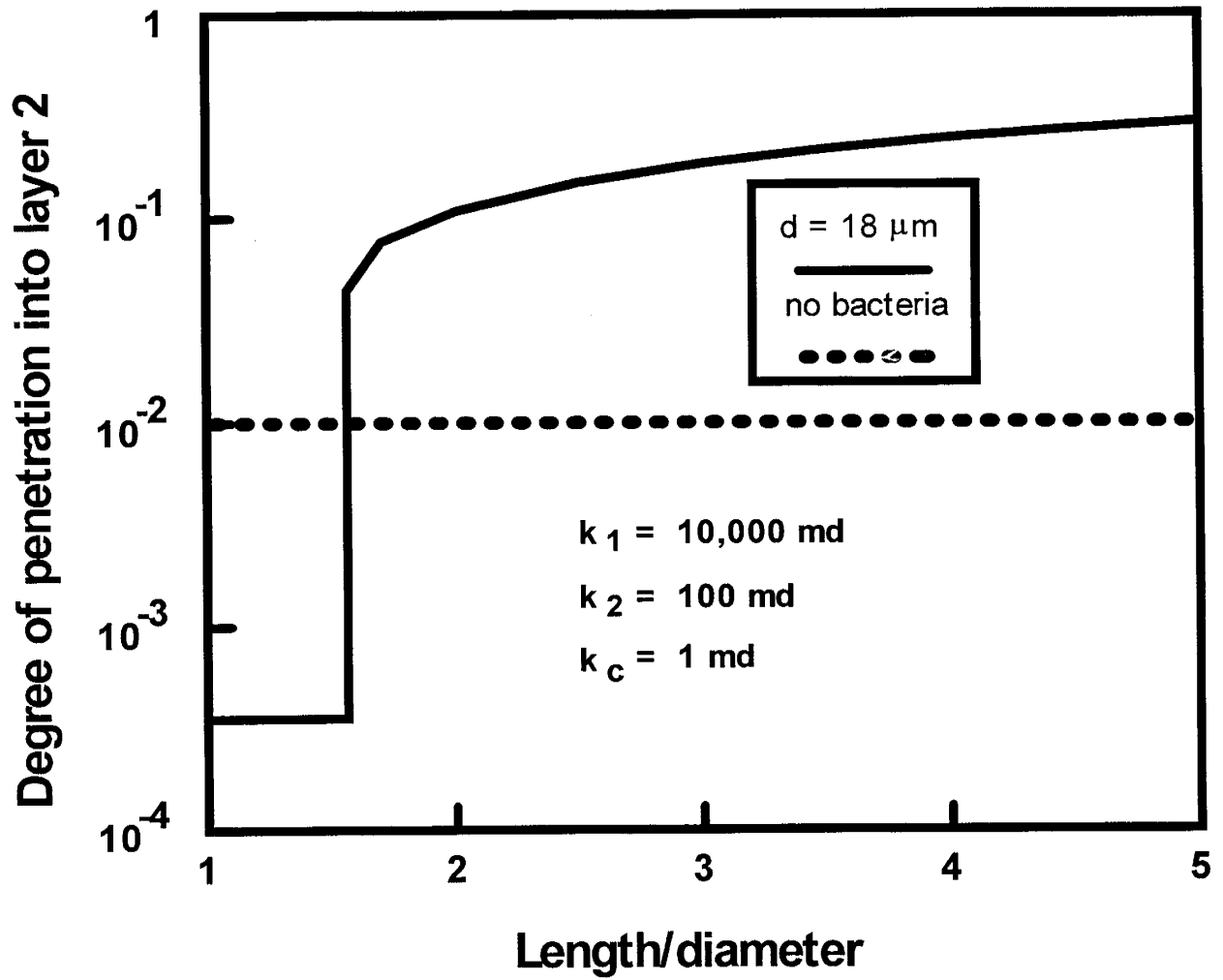


Fig. 64. Effect of aspect ratio of rod-shaped bacteria on selective placement,  $(k_1/k_2)=100$ .

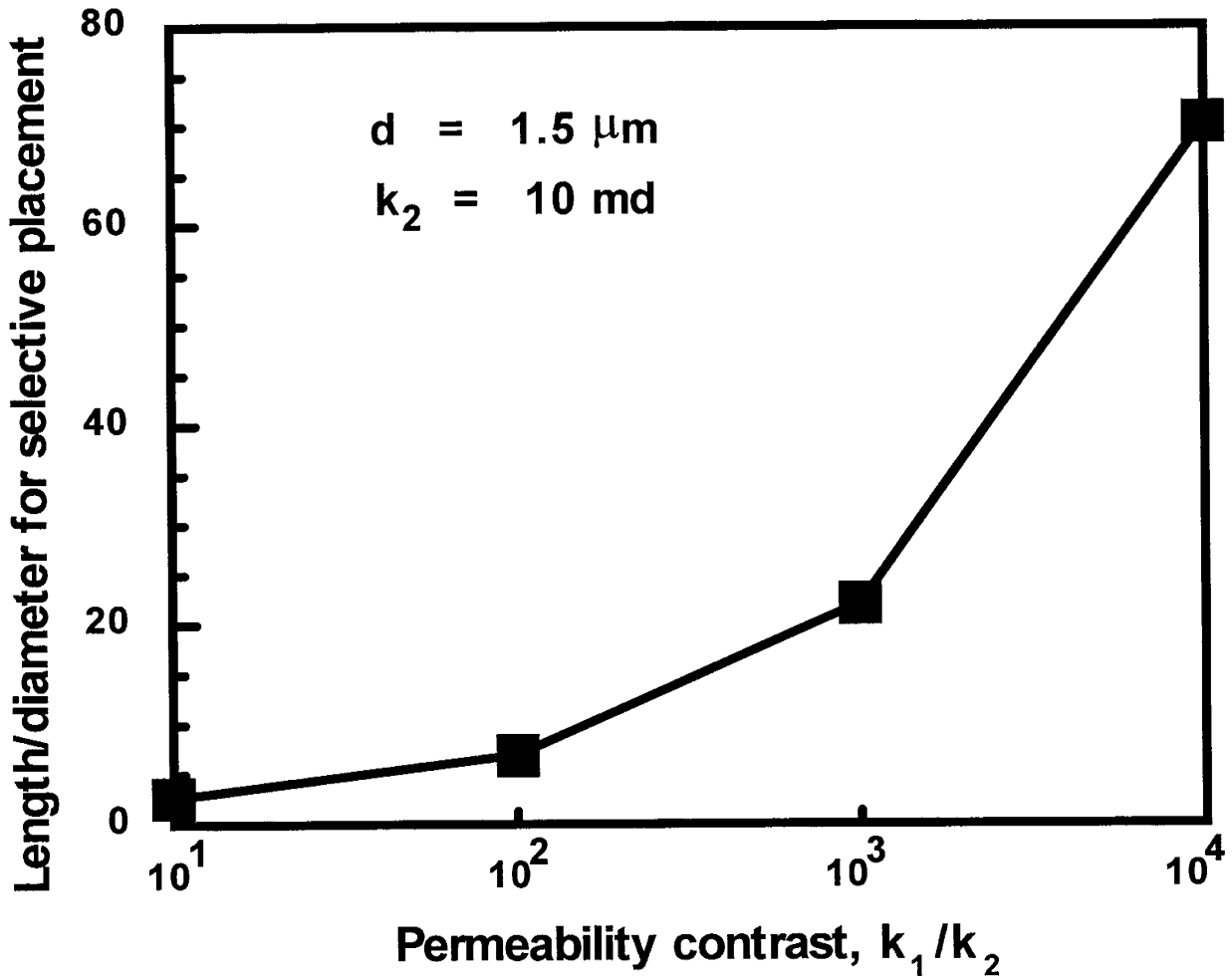


Fig. 65. Effect of permeability contrast on maximum allowable aspect ratio of rod-shaped bacteria for selective placement.

## In-Depth Placement

Near-wellbore plugging is another limiting factor when using microorganisms as blocking agents. This phenomenon results from microbial activities near-wellbore during the placement process. Near-wellbore plugging can inhibit the in-depth placement of the biological materials in the formation. A common method used to minimize near-wellbore plugging involves injecting microorganisms and nutrients sequentially into a formation with or without a brine spacer.<sup>36-46,52-54,57,59,60</sup> The following is a summary of some other methods proposed in the literature for minimizing near-well plugging.

**In Situ Gelation of Exopolymer.** Silver *et al.*<sup>47</sup> proposed the use of an inorganic polyphosphate compound (e.g., sodium tripolyphosphate) in a bacteria nutrient medium. The authors found that the polyphosphate compound would not precipitate from the solution under ambient conditions. The authors asserted that this polyphosphate compound could chelate metal ions (e.g.,  $\text{Cr}^{3+}$ ) so that they could be transported with the bacteria to the desired position in the reservoir. The metal ions would then react with the exopolymer produced in situ to form a polymer gel, thereby reducing the formation permeability. However, the authors did not provide any coreflood or field data to support their ideas.

**Microorganism-Induced Precipitation.** Several researchers<sup>48,49</sup> proposed the use of microorganisms to induce precipitation of minerals from aqueous solutions in situ for formation plugging. This process is commonly known as biomineralization. Ferris and Stehmeier<sup>48</sup> and Jack *et al.*<sup>49</sup> claimed that this in situ precipitation process could reduce face plugging during placement. Microorganisms act as nuclei to induce crystal growth. The metabolism of the microorganisms can change solution conditions by producing new chemicals in solution. In their method, the mineral medium (e.g., colloidal silica) should be near or at saturation so that precipitation could be induced by altering the variables which affect the solubility (e.g., pH). The growth of certain bacteria (e.g., *Leuconostoc mesenteroides* B253) could produce acids in situ. The produced acids could then change the solution pH and stimulate mineral precipitation. Since the precipitation occurred evenly throughout the porous medium after placement, face plugging should be minimal. Results from sandpack experiments showed that this process is effective in causing significant permeability reduction to the porous medium. (No information regarding the sandpack permeabilities were provided.) The authors stated that no face plugging was observed.

**Sequential Nutrient Injection.** Clark *et al.*<sup>50</sup> proposed a sequential nutrient-injection method to prevent near-wellbore plugging in MEOR processes. The authors suggested that in-depth placement could be achieved by sequentially injecting nutrients deficient in the formation. The nutrients are injected individually in order of decreasing tendency of being retained by the porous medium. In this way, microbes would not grow until the last required nutrient is in place, thereby reducing the possibility of face plugging during the placement process. However, their coreflood examples showed that with this method, face plugging still constituted about 46% of the total permeability reduction. Core plugs obtained from the Burbank field, Osage County, Oklahoma were used in the example cases. The core plugs had a nominal permeability of about 500 md.

**Microencapsulation of Nutrients.** One possible way to avoid face plugging is to protect the nutrients from the microbes until the desired location in the formation is reached. Rogers<sup>51</sup> performed a preliminary study to evaluate the possibility of microencapsulating the nutrients for in-depth placement. To achieve in-depth placement, two important factors must be considered; namely, the particle size of the microcapsules and the delayed-release mechanism. The wall materials investigated included poly(methylmethacrylate) (PMMA), poly(ethyleneterephthalamide) (PET), poly(hexamethyleneterephthalamide) (PHT), and poly(N,N-L-lysinediethylterephthaloyl) (PLT). Different techniques were used to prepare the microcapsules, including in situ polymerization, interfacial polymerization, and spray-drying. Electron microscopic studies revealed that the PMMA microcapsules were spherical, smooth, and non-aggregated. They were uniform with an average particle size of about 1  $\mu\text{m}$ . In contrast, the PET microcapsules were spherical with very rough surfaces. Also, they were slightly larger (average particle size of 2  $\mu\text{m}$ ) and had a greater tendency to aggregate. No information was provided regarding the shape and size of PHT and PLT microcapsules. Kinetic studies showed that PMMA microcapsules had a much faster nutrient release rate than PET and PLT microcapsules.

### Permeability Reduction by Microorganisms

Lappan and Fogler<sup>52</sup> performed a series of coreflood experiments to determine the effect of bacterial polysaccharide production on reservoir plugging. The bacteria, *Leuconostoc mesenteroides*, used in their core experiments had a unique ability to produce a water-insoluble polymer only when it was fed sucrose. The typical size of the bacteria was 1  $\mu\text{m}$ . Two ceramic cores of different permeabilities were used in the study. A 14.7-darcy high-permeability core had a normal pore-size distribution with a 33.2  $\mu\text{m}$  mean pore size and a standard deviation of 12.1  $\mu\text{m}$ . A 98-md low-permeability core had a log-normal distribution with a 3.27  $\mu\text{m}$  mean pore size and a standard deviation of 0.94  $\mu\text{m}$ . The results from their core experiments showed that the bacteria caused a 70% permeability reduction in the 98-md core. No damage was observed in the 14.7-darcy core after the bacteria injection. After injecting a nutrient feed containing sucrose to stimulate polymer production, both the high- and low-permeability cores suffered significant formation damage ( $F_{\text{rw}} = 1,000$ ). The permeability reduction caused by the bacteria and the in situ polymer production was basically the same for both the high- and low-permeability cores.

Taylor *et al.*<sup>53</sup> performed sandpack experiments to study the relationship between the in situ biological growth and the resulting permeability reduction. The bacteria used in this study were aerobic methanol-utilizing bacteria. All experiments were conducted at 15°C. During each sandpack experiment, a solution of bacterial culture, methanol, and mineral salts medium were pumped continuously into the porous medium at a constant flow rate. Permeability reductions were determined by monitoring the changes in pressure drop across the sandpack. Results from the sandpack experiments showed that microbial activity in the porous medium could reduce the permeability by as much as three orders of magnitude. The permeability reduction was found to be a function of biomass density. The authors also observed a limit on the permeability reduction.

For the system used in this study, the maximum residual resistance factor was 50,000. The authors did not provide initial permeability data for the sandpacks involved.

Crawford<sup>54</sup> claimed that certain bacteria could plug high-permeability sands more effectively than low-permeability sands. The author asserted that the bacteria could reduce the permeability of the high-permeability zones by a factor of two or three and yet cause little or no damage to the low-permeability zones. However, the author did not provide any information about how his data were obtained and what kind of bacteria were involved.

In a different paper, Crawford<sup>55</sup> proposed that the permeability reduction resulting from a microbial process depends not only on the original permeability of the formation but also on the amount of bacteria injected. The author suggested that as injection continued, more-permeable zones were plugged to a much greater extent than the less-permeable zones. This could result in a more homogeneous injection profile for the subsequent fluid injection. The author also suggested that the continuous bacterial injection could cause significant damage to both the high- and low-permeability zones.

Crawford's observations parallel the behavior of gels in a 2-D linear flow system (vertically fractured system). Our previous studies<sup>21,31</sup> showed that for a given permeability contrast, the degree of gelant penetration into the less-permeable layers is less in a 2-D linear flow system than in a 3-D radial flow system (unfractured system). Thus, the resulting injectivity or productivity losses in the low-permeability layers are less in a 2-D linear flow system than in a 3-D radial flow system. Consequently, gels are more likely to favorably modify injection profile in vertically fractured reservoirs than in unfractured wells.

Jenneman *et al.*<sup>56</sup> studied the penetration of motile bacteria into Berea cores of different permeabilities under static conditions (no pumping). The Berea cores had permeabilities ranging from 52 to 520 md. Their data suggest that the rate of bacterial penetration under static conditions was independent of rock permeability for cores with permeabilities greater than 100 md. For cores with permeabilities less than 100 md, the penetration rate decreased by as much as a factor of ten. They suggested that the microorganisms could preferentially grow and plug high-permeability water zones while only causing superficial damage to the low-permeability oil zones. However, the authors did not provide any permeability reduction data to support this claim.

In a separate study,<sup>57</sup> Jenneman *et al.* examined the transport of viable bacteria and nutrients through porous media. Berea sandstone cores with permeabilities ranging from 171 to 488 md were used as the porous media. Nutrients essential for microbial growth (such as glucose, ammonium ions, phosphate, and peptone-protein) were injected into the Berea sandstone cores. Effluent analyses indicated that glucose, ammonium ions, and phosphate transported through the porous media without much retention. For the peptone-protein, however, the effluent concentration only reached 40% of the injected concentration after 16 PV were injected. The bacteria used in this study showed high degrees of retention in the porous media. The bacteria alone caused 10 to 30% permeability reduction. After injecting sufficient amounts of nutrients,

microbial activity caused permeability reductions between 60 and 80%. The injection of nutrients alone caused 30 to 50% permeability reduction, indicating indigenous microbial activity.

**Summary.** Microorganisms small enough to penetrate a significant distance into a formation can cause serious formation damage. However, the literature is unclear whether microorganisms can reduce permeability to a greater extent in high-permeability water zones than in low-permeability oil zones.

## Conclusions

Selective plugging could be achieved if the nutrients or the microorganisms could be placed selectively into high-permeability thief zones. Since the flow properties of the nutrients are no different from those of gelants, their placement characteristics are similar to those of gelants. Specifically, for a given distance of penetration into a high-permeability zone, the distance of penetration into a less-permeable zone will be no less for the nutrient than for a gelant with a water-like mobility. Using a viscous nutrient (e.g., molasses or corn syrup), nutrient penetration into less-permeable zones increases.<sup>9,21,31</sup>

From one perspective, microorganisms could be viewed as particulates. Because of their narrow size distribution, certain microorganisms could, in concept, provide the advantageous placement characteristics associated with monodisperse particulates.<sup>2</sup> A suspension of microorganisms could penetrate readily into a high-permeability zone, while size restrictions prevent them from entering less-permeable zones. However, most microorganisms are rod-shaped.<sup>36,45,59</sup> The rod-shaped microorganisms act as particulates with a size distribution. Our theoretical analyses, based on Darcy's law and basic formation damage concepts, revealed that for a given permeability contrast, there is a maximum aspect ratio (length/diameter) that should not be exceeded for rod-shaped microorganisms to be more selective than a water-like gelant during placement. The maximum allowable aspect ratio for the rod-shaped microorganisms increases with increasing permeability contrast between high- and low-permeability zones. Maximum selectivity is achieved when the aspect ratio approaches one (i.e., near spherical). When they are near spherical, the placement characteristics of uniformly-sized microorganisms approach those of monodisperse particulates.

Another limiting factor when using microorganisms as blocking agents is near-wellbore plugging. Near-wellbore plugging can inhibit the in-depth placement of the biological materials in the formation. Therefore, growth, aggregation of microorganisms, and adsorption onto pore walls must be limited during placement.

Our literature survey showed that microorganisms small enough to penetrate a significant distance into a formation can cause significant formation damage. However, the literature is unclear whether microorganisms can reduce permeability to a greater extent in high-permeability water zones than in low-permeability oil zones.

## **6. EFFECTS OF PORE SIZE DISTRIBUTION ON SELECTIVE GELANT PLACEMENT USING PARTICULATES**

In our second annual report,<sup>2</sup> we examined the use of particulates as blocking agents. Our analyses of the petroleum and patent literatures revealed that most of the proposed placement schemes suffer from the same placement limitations that gels experience. Particulates small enough to penetrate into the formation can cause significant damage to the formation permeability. The degree of permeability reduction increases with decreasing formation permeability. A theoretical model based on Darcy's law and basic formation damage concepts was developed to determine the feasibility of using particulates to prevent gelant penetration into low-permeability oil zones. Our theoretical analyses showed that when used in conjunction with gelants, monodisperse particulates could prevent gelant leakoff into the formation during placement. As shown in Fig. 66, to achieve selective placement, the particulates must be small enough to penetrate readily into the high-permeability zones but large enough to form an external filter cake on the low-permeability zones. To be more selective than a water-like gelant, Fig. 67 shows that the particle size distribution should not exceed a certain width. The maximum standard deviation for selective placement decreases with decreasing permeability contrast (see Fig. 68). Figs. 66 through 68 in this report are Figs. 10, 13, and 15 in Ref. 2, respectively.

In the previous study, we used the concept of critical particle size to determine the degree of gelant penetration into the formation rock. The critical particle size of a given formation was defined as one-third of the square root of the formation permeability.<sup>2</sup> We assumed that for particulates greater than the critical particle size of the formation, an external filter cake forms on the rock face, while particulates smaller than the critical particle size flow through the porous medium without causing any formation damage. However, a question arises as to whether the critical-particle-size concept is realistic. The critical-particle-size concept basically assumes that the rock has a single pore size. In reality, porous rock contains a range of pore sizes. Will the criteria for selective placement using particulates based on the single-pore-size model be too optimistic? To address this question, we assume in this study that rocks contain pores with normal size distributions. The objective is to determine the effects of pore size distribution on selective gelant placement using particulates.

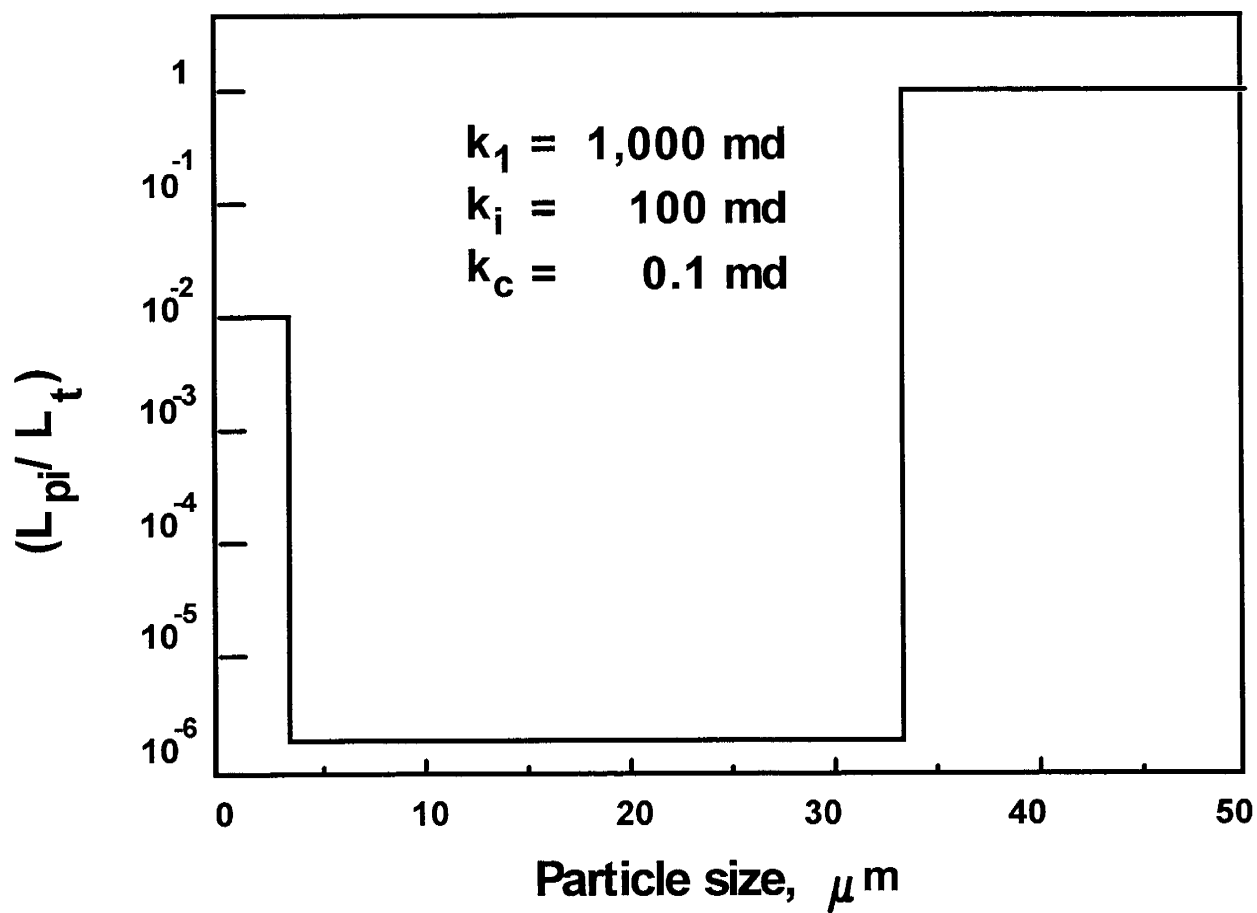


Fig. 66. Effect of particle size on the degree of gelant penetration for particulates with a monodisperse size in porous rock with single pore sizes.

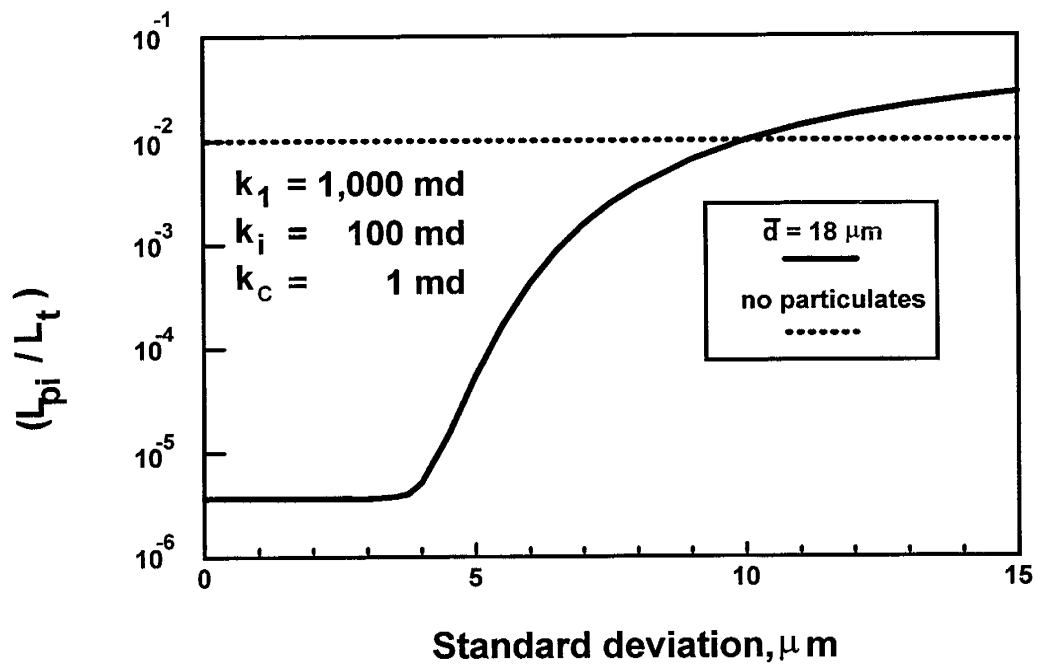


Fig. 67. Effect of standard deviation of particle size distribution on the degree of gelant penetration in porous rock with single pore size.

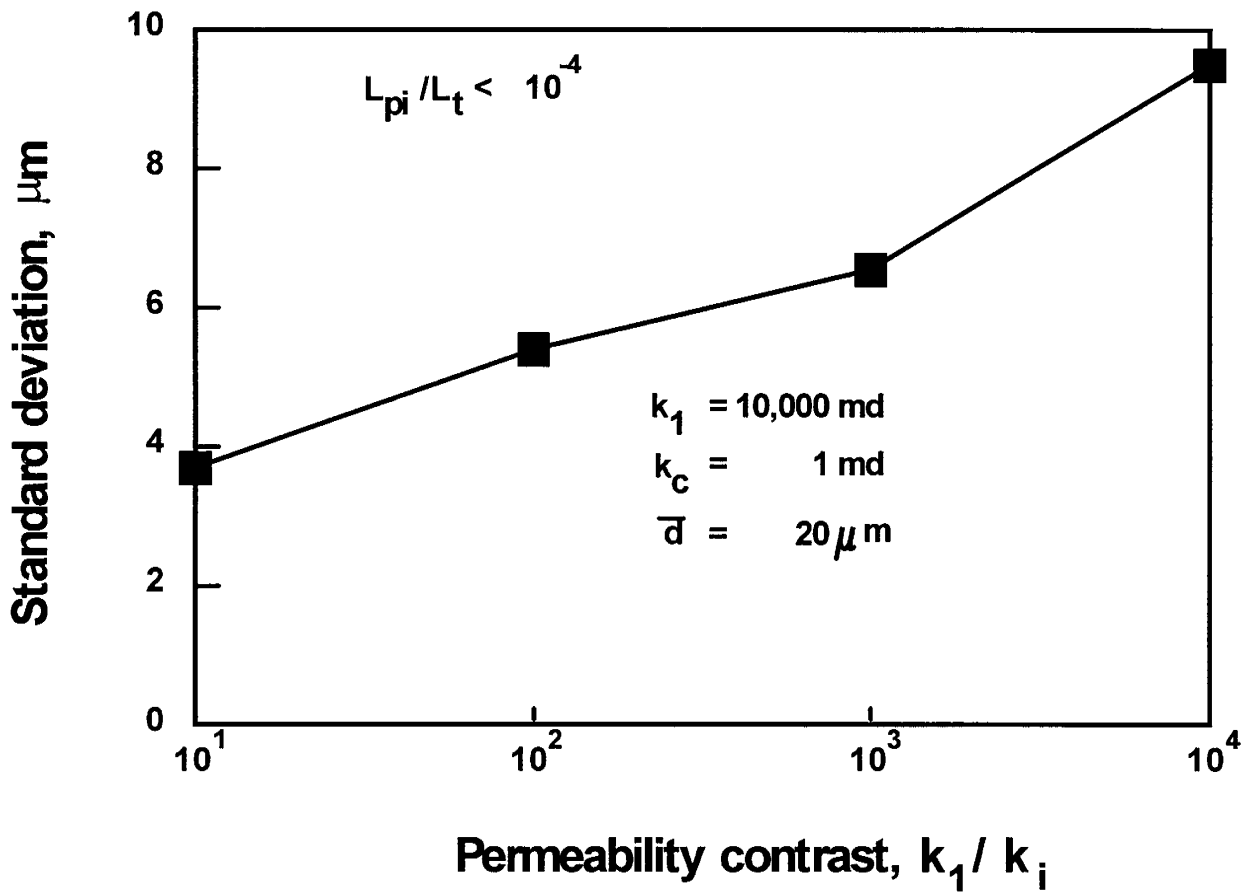


Fig. 68. Effect of permeability contrast on the maximum standard deviation of particle size distribution for a given selectivity.

## Theoretical Model

The theoretical model developed in our previous study was used to examine the effects of pore size distribution on selective gelant placement using particulates.<sup>2</sup> In this study, we assume that the porous rock contains pores with normal size distributions. According to the Carman-Kozeny equation,<sup>61</sup> the median pore size of a given formation is proportional to the square root of the formation permeability. For a normal pore size distribution, the median pore size is equal to the mean pore size. The filter-cake-buildup efficiency,  $\alpha$ , is assumed to be inversely proportional to the fraction of the pores smaller than the maximum particle size in the solution. This implies that during the placement process, particulates will eventually be caught in the rock matrix unless they are smaller than all the pores in the porous medium. The other assumptions involved in this study are the same as those in the previous study. Please refer to Ref. 2 for a detailed description of the theoretical model.

### Effects of Pore Size Distribution on Selective Gelant Placement Using Particulates

To quantify the effect of pore size distribution on the effectiveness of using particulates to achieve selective gelant placement, consider injecting a water-like gelant mixed with particulates into two parallel linear homogeneous cores of equal length from a common injection port. We assume in this study that the porous rock contains pores with normal size distributions. For a normal pore size distribution, the mean pore size locates the center of the distribution and the standard deviation measures its spread. In the following examples, the high-permeability core has a permeability of 10,000 md and the low-permeability core has a permeability of 100 md. According to the Carman-Kozeny equation,<sup>61</sup> the corresponding mean pore sizes are 100  $\mu\text{m}$  and 10  $\mu\text{m}$  for the high- and low-permeability zones, respectively. The rock and fluid properties involved in the examples are summarized in Table 24.

Table 24. Rock and Fluid Properties for Degree of Penetration Calculations

$S_{w1} = 1.0$	$S_{wi} = 1.0$
$\mu_w = 1 \text{ cp}$	$\mu_p = 1 \text{ cp}$
$k_1 = 10,000 \text{ md}$	$k_i = 100 \text{ md}$
$k_c = 1 \text{ md}$	$\phi_c = 0.2$
$\phi_1 = 0.2$	$\phi_i = 0.2$
$\alpha = 0.21$	$\Delta p_D = 0$
$L_t = 50 \text{ ft}$	

**Monodisperse Particulates.** We begin our analyses by using particulates with a monodisperse size of  $18\ \mu\text{m}$ . Fig. 69 shows the effects of pore size distribution on the degree of gelant penetration into the less-permeable core (Core i). As shown in Fig. 69, the degree of gelant penetration into the less-permeable core increases with increasing standard-deviation-to-mean-pore-size ratio. To be more selective than a water-like gelant, Fig. 69 shows that the standard-deviation-to-mean-pore-size ratio must not exceed 0.45. In other words, the standard deviations for the pore sizes in the high- and low- permeability zones should not exceed  $45\ \mu\text{m}$  and  $4.5\ \mu\text{m}$ , respectively. Fig. 69 also shows that when the standard-deviation-to-mean-pore-size ratio is smaller than 0.2, the degree of gelant penetration into Core i is the same as that with monodisperse pore sizes. Orr and Taber<sup>62</sup> studied thin sections of Berea and Frannie sandstone cores. Results from their study revealed that for these relatively uniform porous rock, pore sizes are distributed in a single, narrow mode. The pore size distributions can be approximated by normal distributions. By assuming normal size distributions, the standard-deviation-to-mean-pore-size ratios for both the Berea and the Frannie cores are less than 0.3. These results suggest that selective gelant placement using monodisperse particulates can be achieved in porous media with realistic pore size distributions.

**Particulates with a Size Distribution.** Next, we examine the effects of pore size distribution on selective gelant placement using particulates with a normal particle size distribution. In this example, we assume that the particulates have a mean particle size of  $18\ \mu\text{m}$  and a standard deviation of  $4\ \mu\text{m}$ . The standard-deviation-to-mean-particle-size ratio in this case is 0.22. Is this particle size distribution realistic in field applications? Thomeer and Abrams used different plugging solids for formation plugging.<sup>63</sup> The plugging solids ranged from fine bentonite clay to coarse gravel. Assuming normal size distribution, most of the plugging solids had a standard-deviation-to-mean-particle-size ratio of less than 0.22. Therefore, particulates with a standard-deviation-to-mean-pore-size ratio of 0.22 are sometimes available in field applications. The other parameters involved in this example are the same as those in the previous example. Fig. 70 shows that with particulates having a normal size distribution, the degree of gelant penetration into the less-permeable core increases with increasing standard-deviation-to-mean-pore-size ratio. The effect of pore size distribution becomes negligible when the standard-deviation-to-mean-pore-size ratio is smaller than 0.2. To achieve better selectivity than a water-like gelant, Fig. 70 shows that the standard-deviation-to-mean-pore-size ratio must be smaller than 0.38. A comparison of Figs. 69 and 70 shows similar trends with particulates having a normal size distribution and with monodisperse particulates. In both cases, the importance of pore size distribution on gelant placement diminishes when the standard-deviation-to-mean-pore-size ratio is smaller than 0.2. However, to achieve better selectivity than a water-like gelant, the maximum allowable standard-deviation-to-mean-pore-size ratio is more restrictive using particulates with a normal size distribution than in the case with monodisperse particulates.

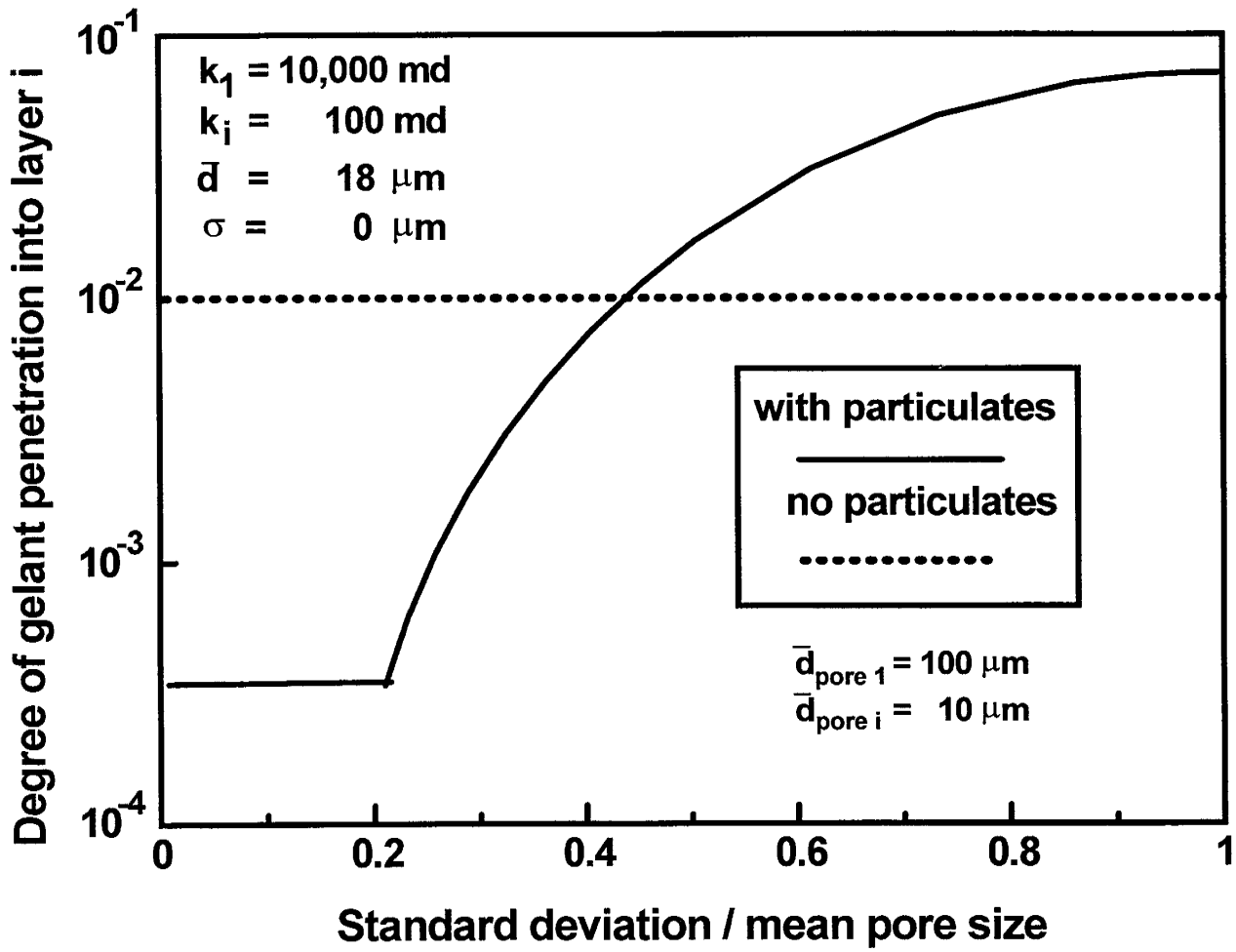


Fig. 69. Effect of pore size distribution on placement of a water-like gelant with particulates having a monodisperse size.

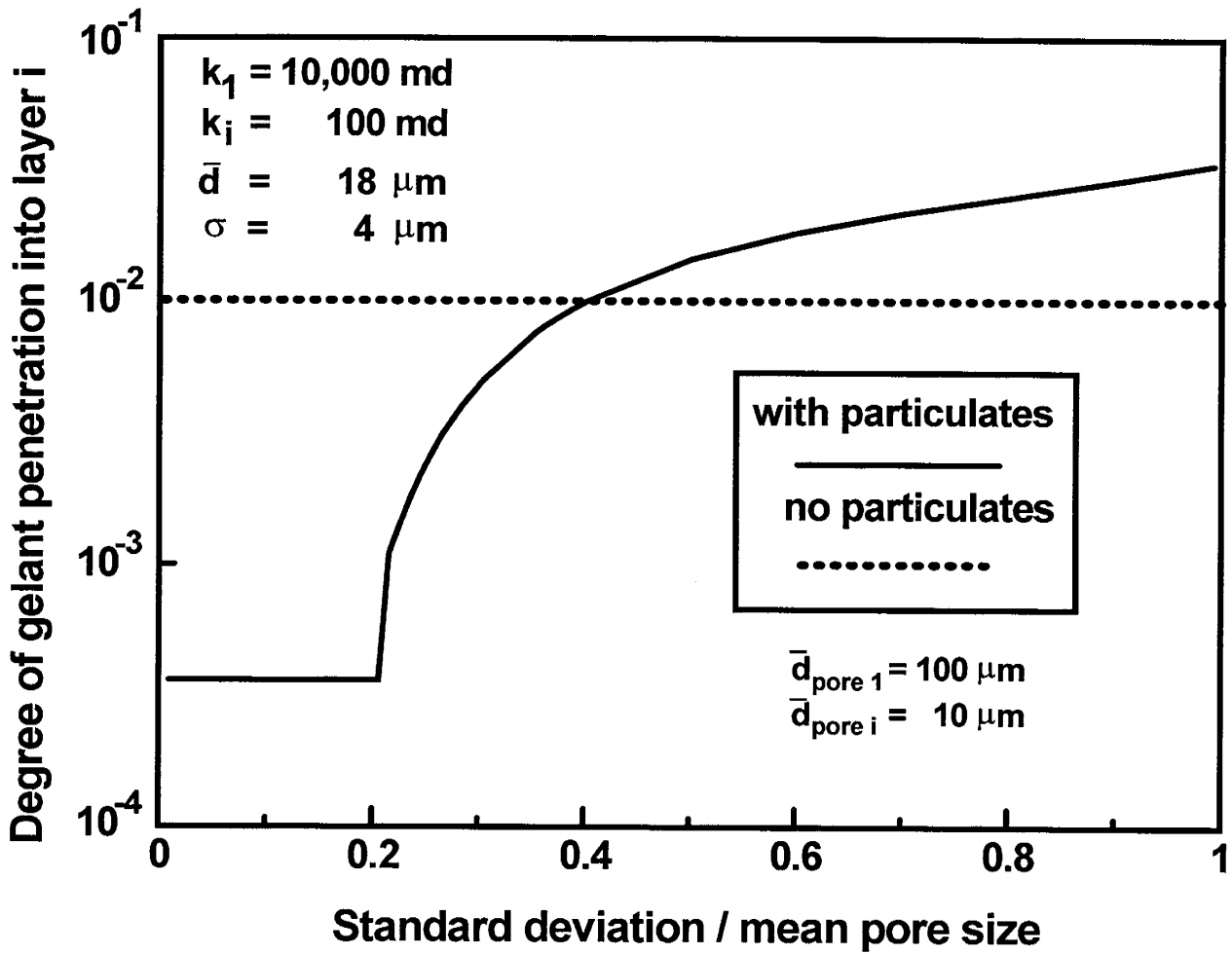


Fig. 70. Effect of pore size distribution on placement of a water-like gelant with particulates having a normal size distribution.

The next question is, for a given permeability contrast, would porous rock containing pores with size distributions require a more restrictive particle size distribution for selective gelant placement? To answer this question, we assume in the next example that the standard deviations of pore size are 25  $\mu\text{m}$  and 2.5  $\mu\text{m}$  for the high- and low-permeability zones, respectively. The other parameters are the same as those in the previous example. Fig. 71 shows that the degree of gelant penetration into the less-permeable core increases with increasing standard deviation of particle size. Fig. 71 also shows that the standard deviation of particle size must be smaller than 9  $\mu\text{m}$  to achieve better selectivity than a water-like gelant. This result is somewhat surprising since this number is similar to that obtained in our previous study (10  $\mu\text{m}$ ) where the critical-particle-size concept was used (see Fig. 67). In other words, for a given permeability contrast, porous rock containing pores with size distributions does not necessarily require a more restrictive particle size distribution for selective gelant placement using particulates (compared to rock with monodisperse pores). However, the selectivity can be very sensitive to the mean and standard deviation of the particle size distribution.

## Conclusions

1. Selective gelant placement can be achieved in porous media with realistic pore size distributions using monodisperse particulates.
2. The maximum allowable standard-deviation-to-mean-pore-size ratio for selective gelant placement is more restrictive using particulates with a normal size distribution than in the case with monodisperse particulates.
3. For a given permeability contrast, porous rock containing pores with size distributions does not necessarily require a more restrictive particle size distribution for selective gelant placement using particulates (compared to rock with monodisperse pores). However, the selectivity can be very sensitive to the mean and standard deviation of the particle size distribution.

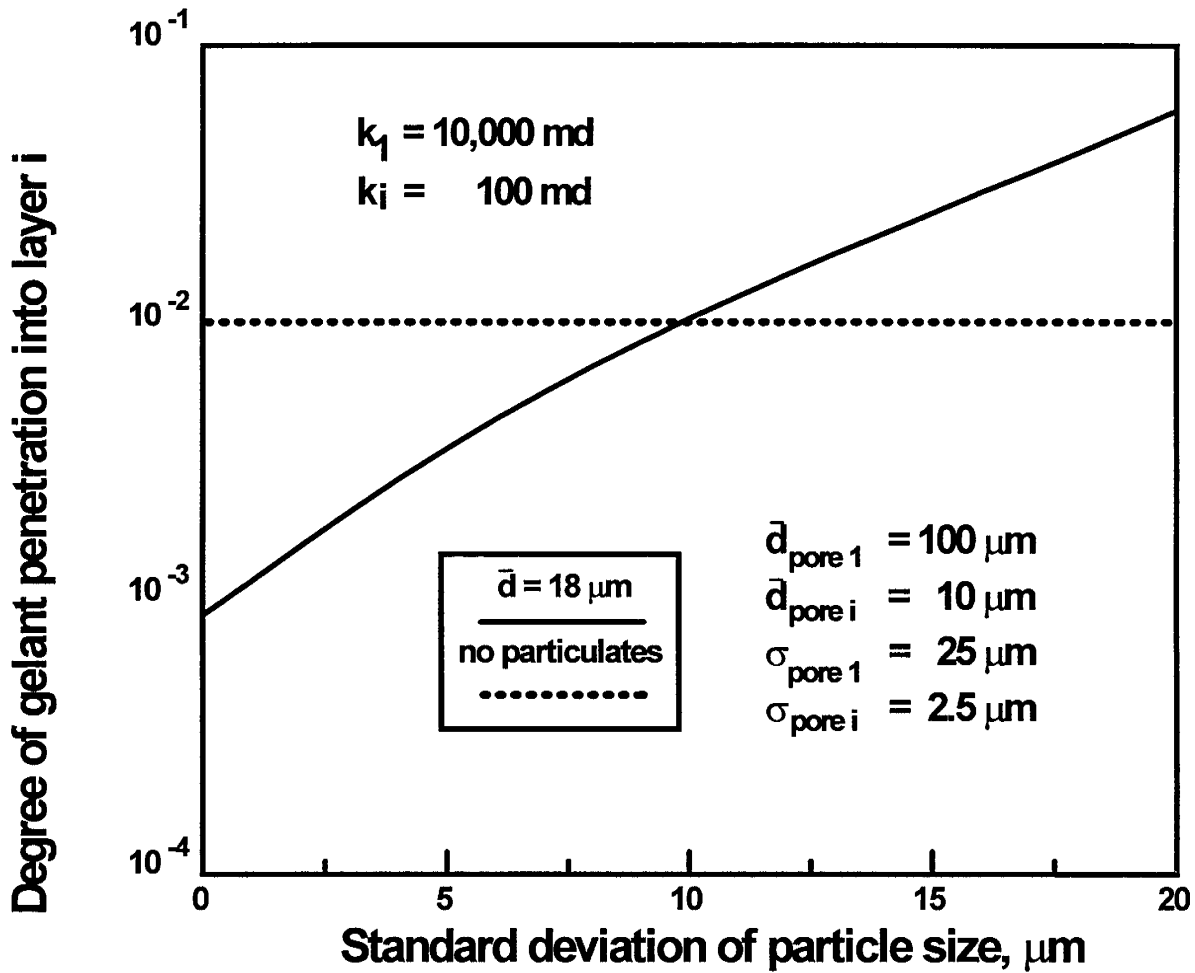


Fig. 71. Effect of particle size distribution on placement of a water-like gelant in porous media with pore size distributions.

## 7. USE OF FOAMS AS BLOCKING AGENTS

This chapter investigates the use of foams as blocking agents. Although foam has been suggested as a blocking agent, much of the literature focuses on the use of foams as mobility-control agents. In blocking applications, the foam must substantially restrict flow in high-permeability zones while causing minimum permeability reduction in the less-permeable zones. In contrast, in mobility-control applications, the foam formulation should penetrate as far as possible into the less-permeable zones, with much less regard for the permeability reduction that results.<sup>2</sup>

Although many researchers have studied foam generation and propagation in porous media, controversy still exists regarding different parameters affecting foam flow in porous media. Foam mobility in porous media has been reported to decrease<sup>64</sup>, increase,<sup>65-70</sup> or remain constant<sup>71</sup> with increasing flow rate. While most published data indicates that foam mobility increases with increasing flow rates, the extent of the effects vary significantly. Chou<sup>72</sup> suggested that some of the confusion probably results from the lack of protocol in conducting foam experiments: some experiments were performed at constant foam quality, some at constant flow rate, some under constant gas pressure, and others under unsteady state conditions. Generally, most of the experiments were performed within a low range of velocities (Darcy velocity between 0.1 and 10 ft/d) and/or in high-permeability porous media. For any foam field application, the rheology of foam should be known for a wide range of velocities and in different rock permeabilities. To our knowledge, such comprehensive data is not available in the literature.

In concept, several phenomena could allow foams to be superior to gels as blocking agents, however, only in certain circumstances.<sup>2</sup> At present, these circumstances are hypothetical; very few conditions have been verified experimentally or in field applications. One phenomenon (the limiting capillary pressure<sup>73</sup>) could allow low-mobility foams to form in high-permeability zones but not in low-permeability zones. The limiting capillary pressure is defined as the capillary pressure at which foam coalesces.<sup>73</sup> Exploiting this phenomenon during foam placement requires that<sup>2</sup> (1) under given reservoir conditions, a gas/liquid composition must be identified that will foam in high-permeability zones but not in low-permeability zones, (2) the foam must not easily collapse or wash out from the high-permeability zones, and (3) the aqueous phase must not contain a gelant or other reactive blocking agent.

In this chapter, we examine whether the limiting-capillary-pressure concept can be exploited to aid placement of foam blocking agents. This determination required that mobilities be measured over a broader range of permeabilities and fluid velocities than have been reported in the literature. Using a C<sub>14-16</sub>  $\alpha$ -olefin sulfonate, we measured mobilities of a nitrogen foam in cores with permeabilities from 7.5 to 900 md (750 psi back pressure, 41°C) with foam qualities ranging from 50% to 95% and with Darcy velocities ranging from 0.5 to 100 ft/d. We also extensively studied the residual resistance factors provided during brine injection after foam placement. The results from our experimental studies were used during numerical analyses to establish whether foams can exhibit placement properties that are superior to those of gelants.

## Apparatus and Experimental Procedure

**Coreflood Equipment.** Our coreflood equipment is illustrated in Fig. 72. The design was based on coreflood experiments performed during previous research with gels<sup>58,74,75</sup> (with some modifications). All equipment was housed in a temperature-controlled chamber. Two pumps (Isco 500D) were used for liquid injection (brine, surfactant, or tracer solution). Two mass flow controllers, with two different flow ranges (0-100 and 0-5,000 standard ml/min), were used to measure the mass flow rate of the gases. Both controllers (5850TR) were manufactured and calibrated by Brooks Co. Tracer studies were performed using an absorbance detector (Waters 486<sup>®</sup>, Millipore Corporation, Milford, MA) that was connected to the coreflood equipment.

**Brine and Surfactant Solution.** The brine used in this work contained 1% NaCl and 0.1% CaCl<sub>2</sub>, prepared in distilled water. The brine was mixed with a magnetic stirrer for at least 15 minutes and then filtered through a 0.45 μm filter. The surfactant used was Bio-Terge<sup>®</sup> AS-40 (Stepan Co.), a C<sub>14-16</sub> alpha-olefin sulfonate with an activity of 38.71%. One surfactant concentration (0.3% by active weight) was used throughout the course of this work unless otherwise mentioned. The critical micelle concentration (cmc) for the surfactant was reported to be 0.25% by active weight in distilled water.<sup>76</sup> We determined the cmc to be 0.01% in our brine (1% NaCl, 0.1% CaCl<sub>2</sub>) at 40°C.

**Core Preparation.** The detailed procedure for core preparation was given in previous reports.<sup>74,77</sup> None of the cores used in this work were fired. Cerrotru<sup>®</sup> alloy was used to cast the cores. The casting temperature was 270°C. The typical length of the cores was about 15 cm and the cross-sectional area was about 10 cm<sup>2</sup>. Two pressure taps were drilled in the core. They were located about 2.5 cm from each end of the core. The first section of the core (about 2.5 cm) was used as a filter and foam generator. The second section of the core (approximately 10 cm) was used for the measurements that we report.

**General Experimental Procedure.** To examine the potential of foams as blocking agents, a comprehensive study of foam rheology was performed. Rheological data are reported that cover a wide range of velocities in different cores with different permeabilities. In addition to the conventional methods for rheology studies, tracer experiments were conducted to evaluate the blockage effect caused by nitrogen foam. The effect of foam quality on foam rheology is also presented. In addition, the effect of velocity as well as the number of pore volumes of brine on residual resistance factor were studied.

All coreflood experiments were performed using the equipment illustrated in Fig. 72. The equipment was housed in a chamber where temperature was constant at 40°C (104°F). All experiments described in this chapter used nitrogen foams and were performed using a backpressure of 750 psig. The general experimental procedure is given in Table 25. Experimental results using carbon-dioxide foams are included in Appendix C. Results from the tracer studies are documented in Appendix D. The effect of shut-in on brine residual resistance factor was also examined (Appendix E).

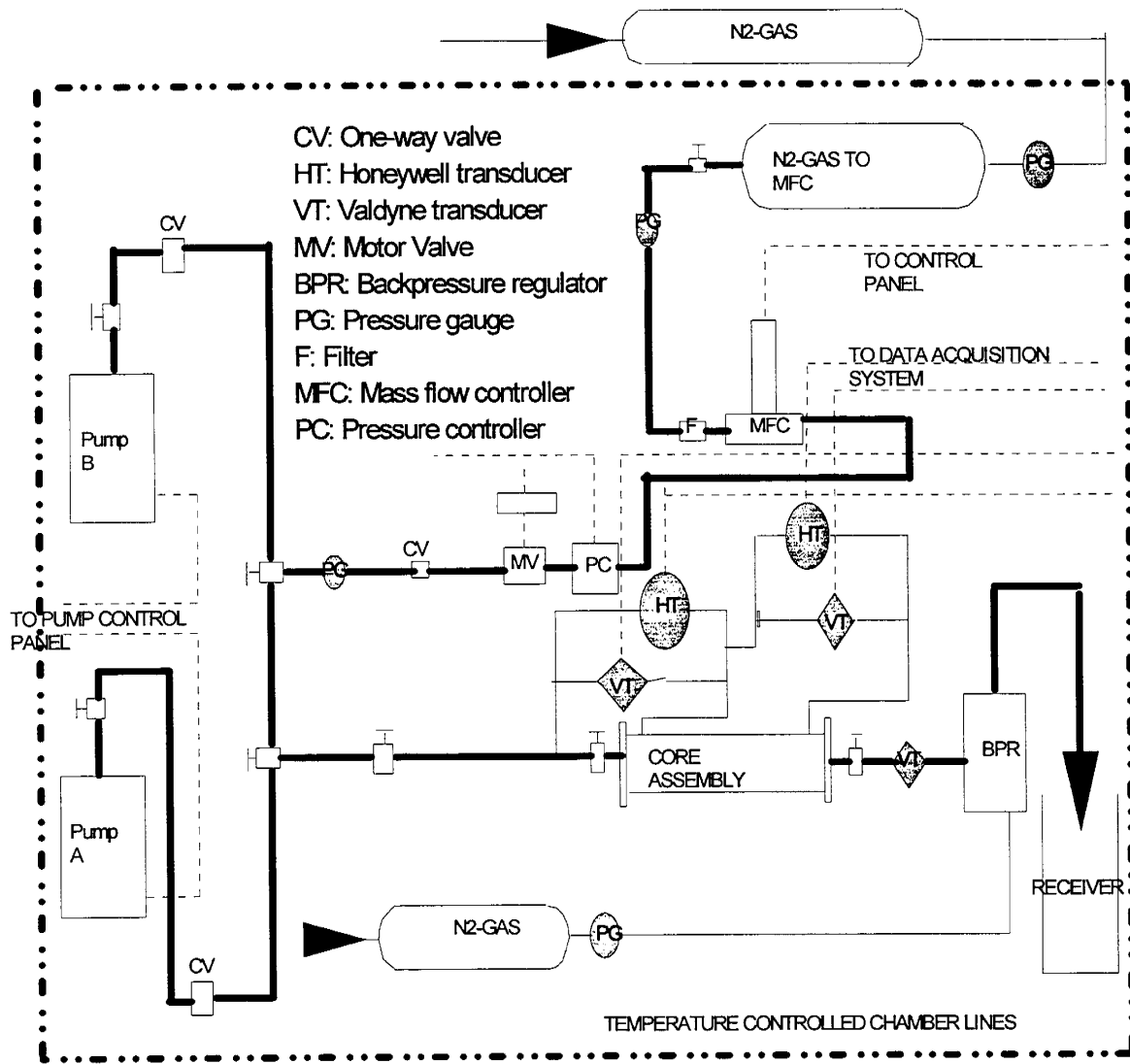


Fig. 72. Schematic of the foam coreflood equipment.

Table 25. General Experimental Procedure

1. Perform brine mobility measurements at constant backpressure and different flow rates. Usually the backpressure applied in this step was the same one at which the foam was generated.
2. Perform water-tracer experiments at different flow rates.
3. Saturate the core with 3-5 PV of surfactant solution and measure the mobility. This step was performed to satisfy the surfactant adsorption requirements of the core.<sup>76</sup> Elemental analysis for sulfur showed that after passing 2 PV of surfactant through Berea sandstone, the concentrations of the surfactant in the inlet and outlet were similar.
4. Simultaneously inject of gas and surfactant at the required gas quality at a specific total flow rate (total flow rate = gas flow rate + surfactant flow rate). When a steady state (constant pressure drop) is achieved, print out the results and change the flow rate to another value.
5. Stop gas injection, and inject brine at different flow rates (flow rate not to exceed 50 ml/hr or 4 ft/d) and measure brine mobility. The total number of pore volumes of brine injected in this step were not to exceed 18 PV. There were two reasons for performing this step: (1) to determine the brine mobility after foam generation and (2) to minimize gas evolution from the core (because gas interferes with tracer detection).
6. Conduct a tracer experiment at 40 ml/hr (3.1 ft/d).
7. Inject at least 3 PV of brine at 100 ml/hr (8 ft/d) and measure brine mobility.
8. Perform a tracer experiment at 100 ml/hr.
9. Inject 3 PV of brine at 200 ml/hr (16 ft/d)
10. Perform a tracer experiment at 200 ml/hr.
11. Release the backpressure gradually, allowing time for the pressure to equilibrate. Inject brine at different flow rates, while the backpressure is sequentially released and reapplied. This procedure was necessary to restore the brine mobility. From 50 to 100 PV of brine were required to restore the original brine mobility.
12. Release the backpressure and flush the transducer lines with distilled water (all lines to the core were closed) and make sure that all transducers were zeroed.
13. Perform a tracer study to confirm that the pore volume was restored.

**Cores Used.** Four cores were used in this work. Three cores were Berea sandstone, and one core was Indiana limestone. Table 26 shows the properties of the cores used.

Table 26. Properties of Cores Used

Core ID:	FHPSS4	FHPSS1	FLPSS2	FLPLS3
Lithology	Berea sandstone	Berea sandstone	Berea sandstone	Indiana limestone
Permeability, md	899	482	80	7.5
Porosity	0.235	0.232	0.185	0.170

## Effects of Permeability, Fluid Velocity, and Foam Quality on Nitrogen-Foam Rheology

Foam was generated by simultaneously injecting gas and surfactant solution. The mobility and superficial-velocity (Darcy velocity) data were fitted using a power-law model. In Figs. 73 to 76, the results for a foam quality of 80% were obtained first. Foam was then generated at 50% quality and finally at 95% quality. This sequence of generation was used to show that hysteresis did not affect our results.

**Results Using the 899-, 482-, and 80-md Berea Sandstone Cores.** Figs. 73 to 75 illustrate the effect of quality on nitrogen-foam rheology in the three Berea sandstone cores. A shear-thinning behavior was observed with all foam qualities studied. Generally, the shear-thinning behavior was more pronounced as the foam quality decreased. At low to moderate rates, Figs. 73 to 75 show that lower mobilities were produced as the quality decreased. However, at high flow rates, the effect of foam quality on mobility was less pronounced.

**Results Using the 7.5-md Indiana Limestone Core.** Fig. 76 compares foam mobilities for simultaneous injection of surfactant and nitrogen into a surfactant-saturated 7.5-md core. For three different qualities (50, 80, and 95%), Newtonian behavior was observed. Higher mobilities were observed as the quality increased. This result indicates very weak or no foam generation (two-phase surfactant and nitrogen flow with no gas-blocking effect). When the quality decreased, the mobility decreased because of the higher liquid fraction. The resistance factors were 2.2, 1.9, and almost 1 for qualities of 50%, 80%, and 95%, respectively. For comparison, the resistance factor varied from 40 to 1,000 in the 899-md core, from 60 to 1,500 in the 482-md core, and from 20 to 300 in the 80-md core, depending on the flow rate and the quality of the foam.

To confirm these results, surfactant-free brine and nitrogen were simultaneously injected into a brine-saturated core at the foam qualities of either 50 or 95%. The results with surfactant/gas and brine/gas combinations are shown in Figs. 77 and 78. Similar behavior was observed for each quality. These results confirm that the core contained a very weak foam or no foam.

**Power-Law Correlations for Foam Rheology.** Table 27 lists power-law correlations between foam mobilities ( $\lambda_f$ , in md/cp) and Darcy velocities ( $u$ , in ft/d) for the three Berea cores and the three foam qualities.

Table 27. Variation of Mobility With Darcy Velocity for Different Nitrogen-Foam Qualities

Foam Quality, %	FHPSS4 (899 md)		FHPSS1 (482 md)		FLPSS2 (80 md)	
	Correlation	R <sup>2</sup>	Correlation	R <sup>2</sup>	Correlation	R <sup>2</sup>
50	$\lambda_f = 1.21 u^{0.73}$	0.99	$\lambda_f = 0.419 u^{0.70}$	0.98	$\lambda_f = 0.36 u^{0.62}$	0.86
80	$\lambda_f = 3.16 u^{0.52}$	0.96	$\lambda_f = 1.28 u^{0.45}$	0.94	$\lambda_f = 1.51 u^{0.37}$	0.96
95	$\lambda_f = 9.9 u^{0.26}$	0.91	$\lambda_f = 2.65 u^{0.28}$	0.96	$\lambda_f = 1.52 u^{0.39}$	0.99

\* R<sup>2</sup> is the correlation coefficient.

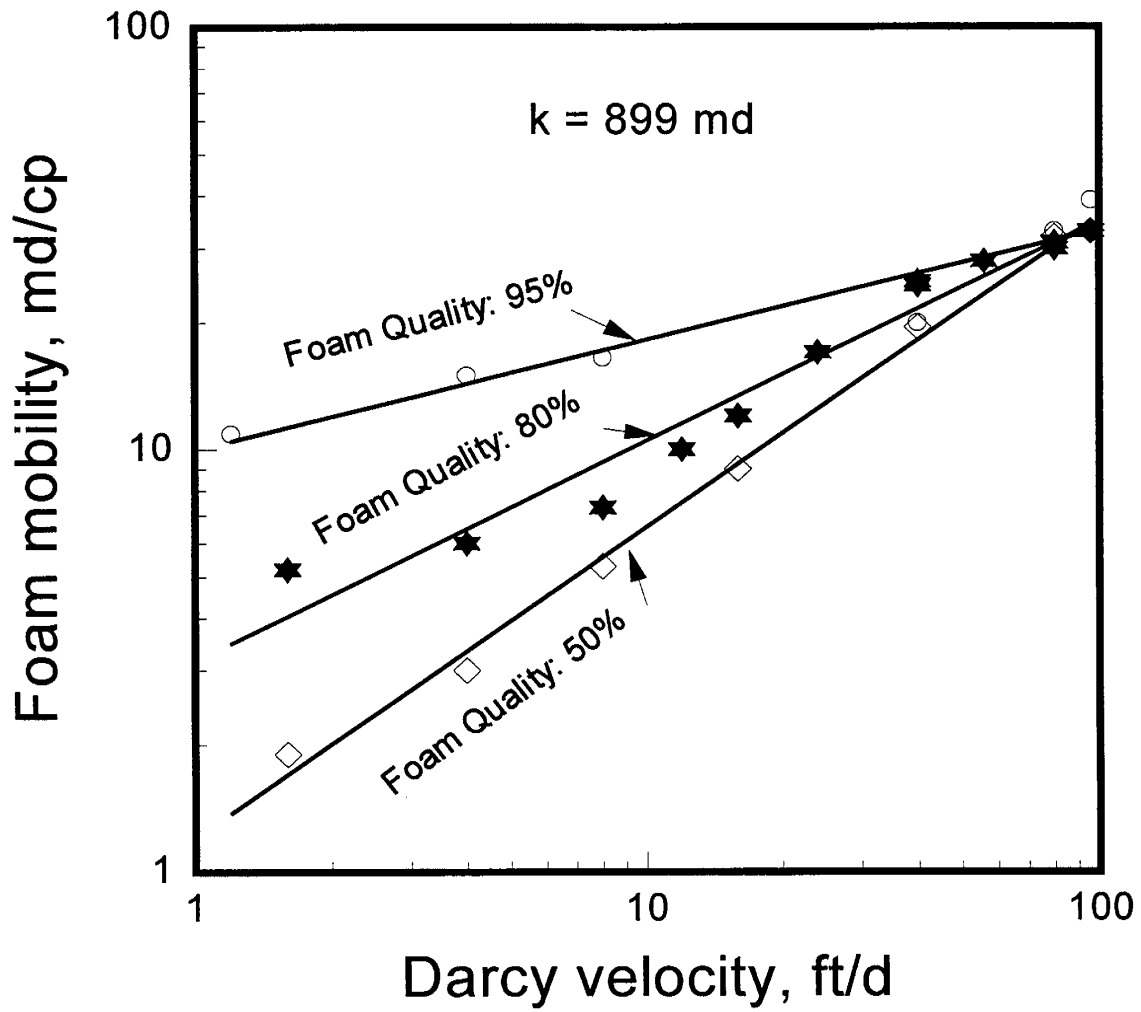


Fig. 73. Effect of quality on foam rheology.  $k=899$  md.

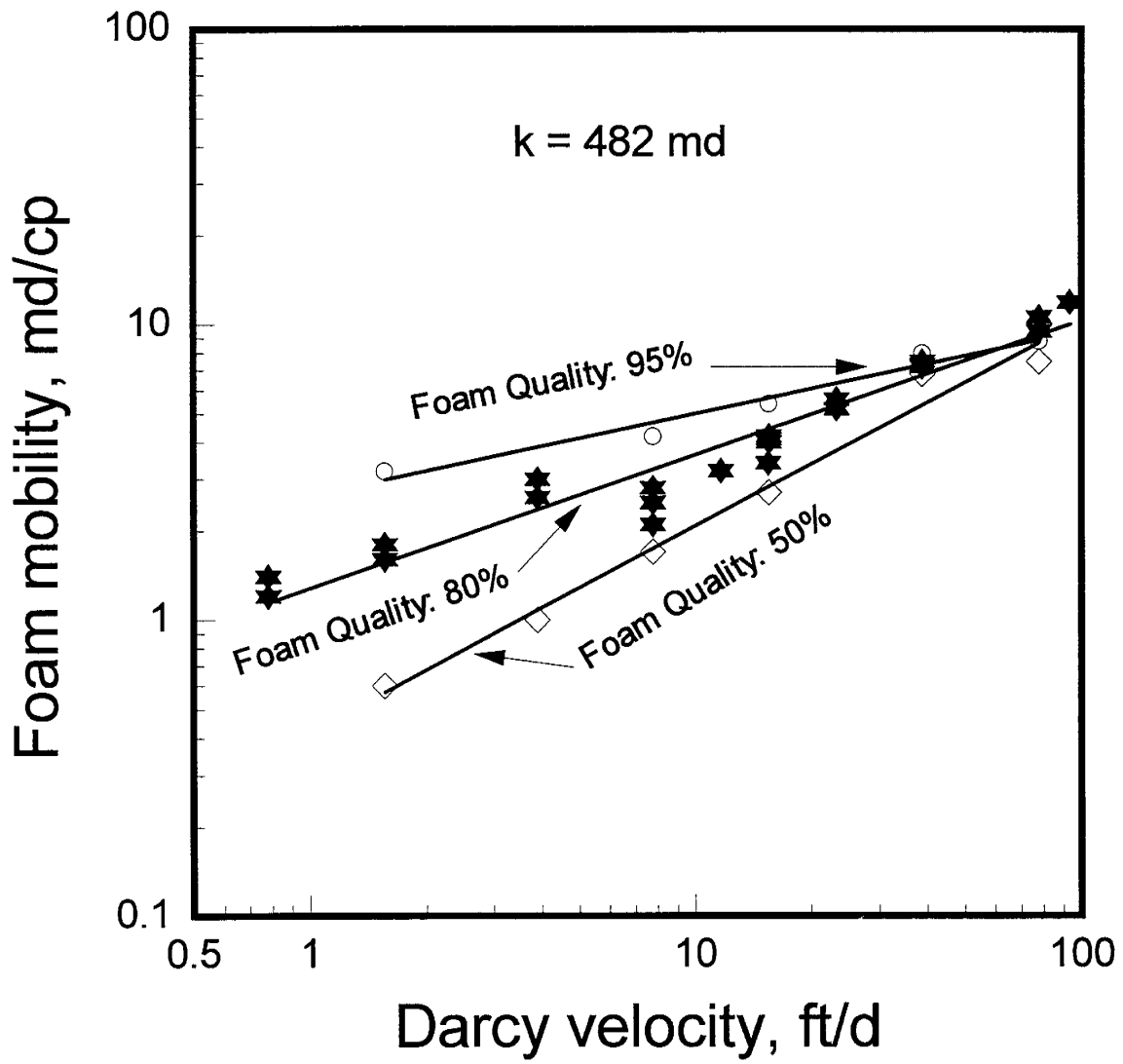


Fig. 74. Effect of quality on foam rheology.  $k=482$  md.

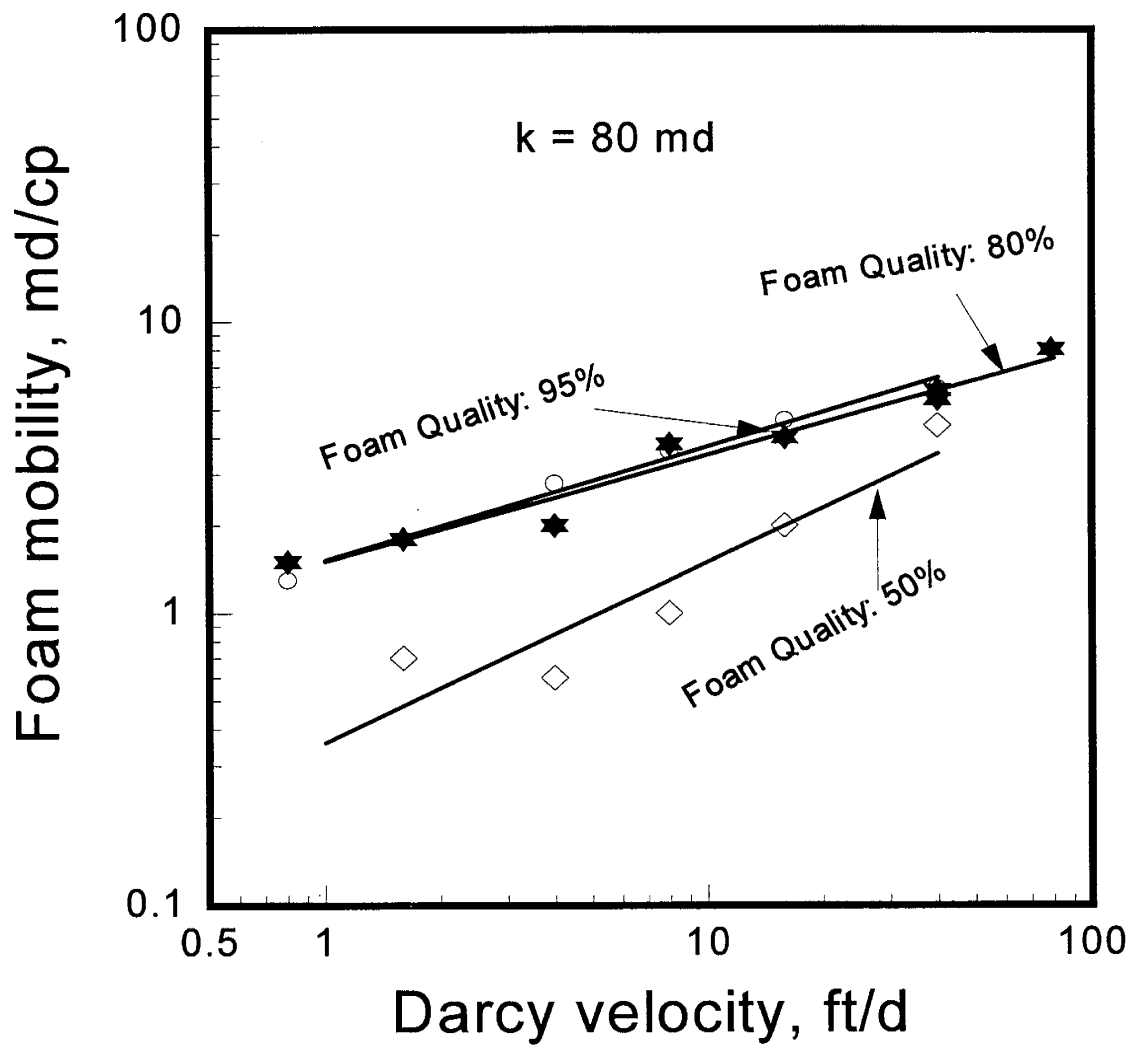


Fig. 75. Effect of quality on foam rheology.  $k=80$  md.

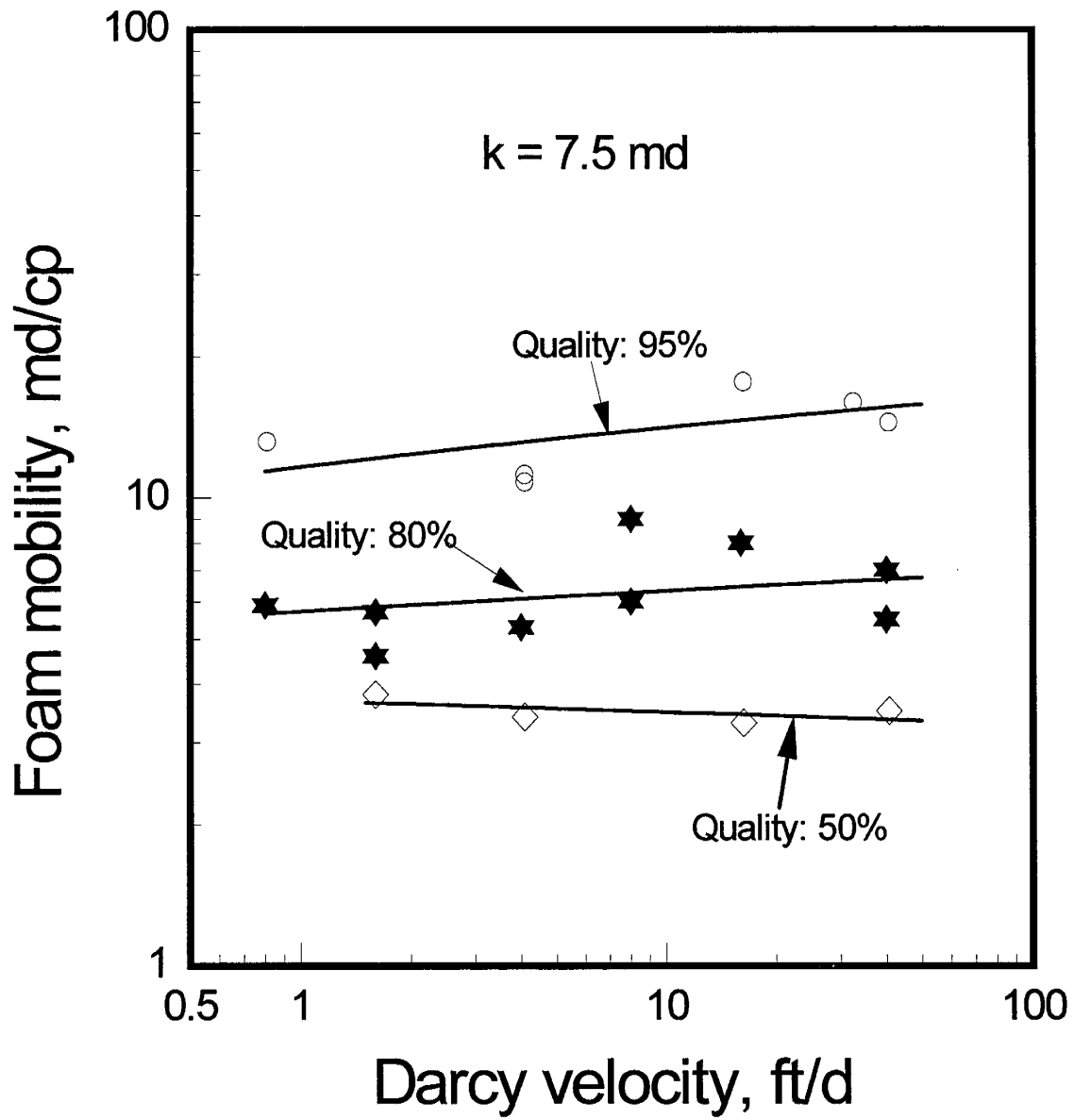


Fig. 76. Effect of quality on foam rheology.  $k=7.5 \text{ md}$ .

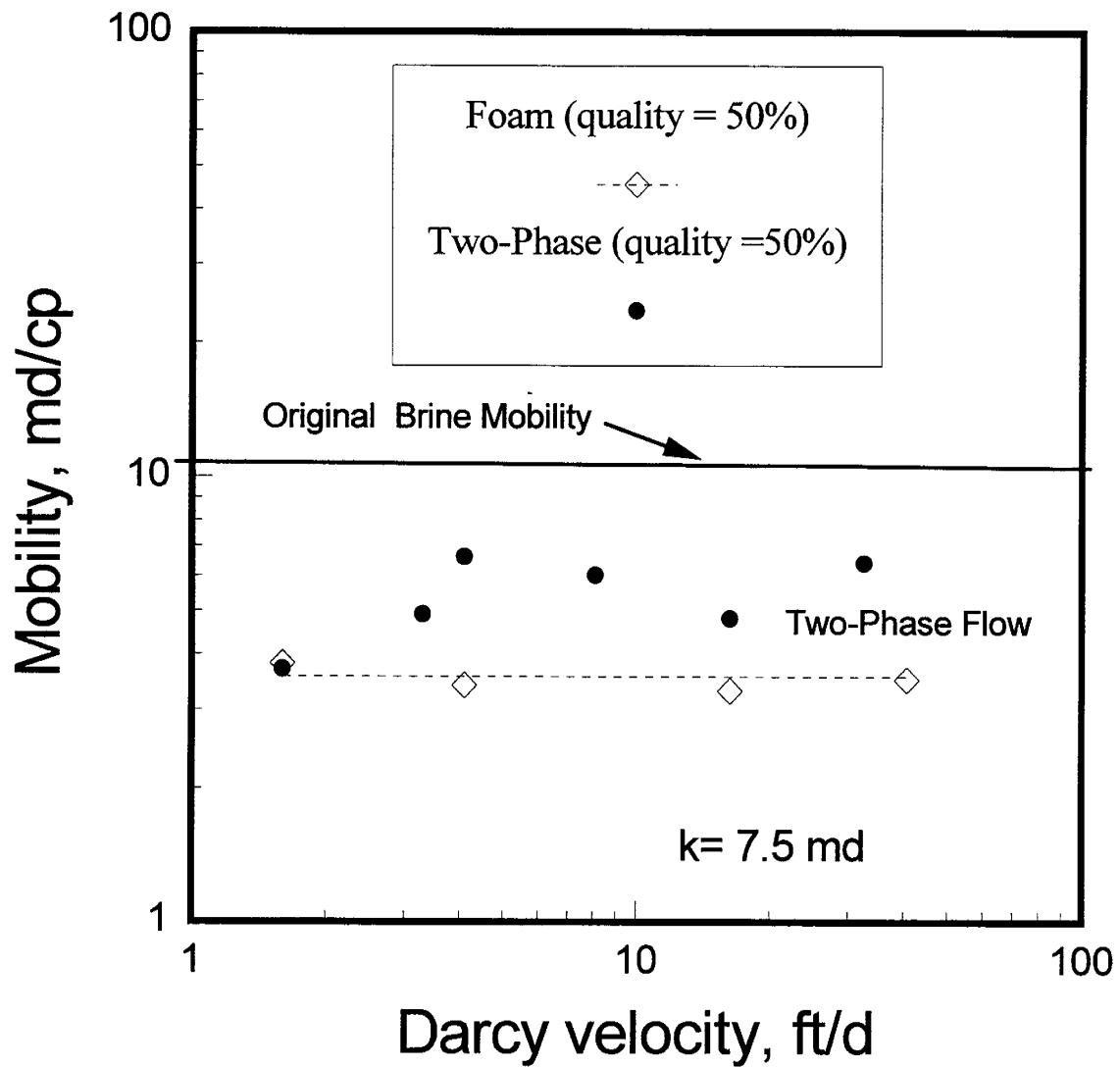


Fig. 77. Comparison of foam flow and two-phase flow. 50% quality foam.

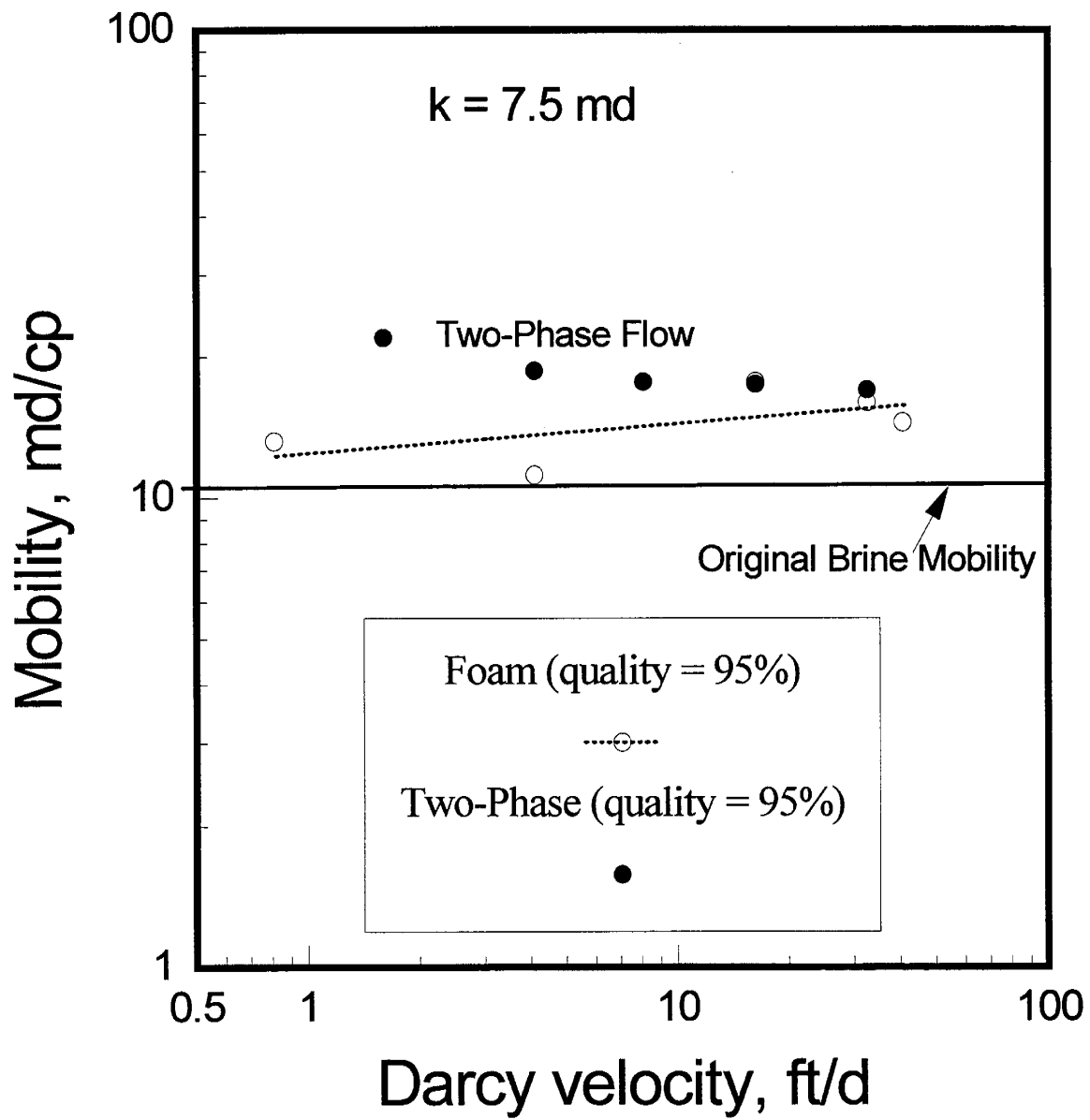


Fig. 78. Comparison of foam flow and two-phase flow. 95% quality foam.

In the Berea cores, shear-thinning behavior was observed for all qualities studied. Contrary to one report,<sup>66</sup> a greater shear-thinning behavior was seen with decreasing foam quality (down to 50%). Our results shown in Table 27 were compared to two sets of published data that covered a wide range of velocities (2 ft/day to 130 ft/day), i.e., from Friedmann *et al.*<sup>79</sup> and Zerhboub *et al.*<sup>80</sup> The data of Friedmann *et al.* showed the effect of gas velocity on pressure gradient for foam in a 950-md Berea sandstone core. The gas used was N<sub>2</sub> and the quality was 95%. The surfactant used was Chaser SD 1000<sup>®</sup> (1% by weight). The length of the core was 10 cm. The results were correlated using Eq. 7.

$$dp/dl = 6.24 v_g^{0.71} \quad (7)$$

where  $dp/dl$  was the pressure gradient in psi/ft, and  $v_g$  was the gas frontal advance velocity in ft/d.

Our results for the same quality (95%) were:

$$k_w = 899 \text{ md: } dp/dl = 16.0 u^{0.74} \quad (8)$$

$$k_w = 482 \text{ md: } dp/dl = 59.6 u^{0.72} \quad (9)$$

$$k_w = 80 \text{ md: } dp/dl = 104 u^{0.61} \quad (10)$$

where  $dp/dl$  was the pressure gradient in psi/ft, and  $u$  was the Darcy velocity in ft/day.

The data of Zerhboub *et al.*<sup>80</sup> were generated in unconsolidated sand using permeabilities from 0.225 to 48 darcys. The surfactants used were not identified in the paper (1% concentration). N<sub>2</sub>-foam was generated at 65% quality. The data of Zerhboub *et al.*<sup>80</sup> (Fig. 5 of Ref. 80) for variation of pressure gradient with velocity (for a velocity range from 0.72 to 7.2 cm/min) were correlated by Eqs. 11 and 12.

For a permeability of 2,700 md,

$$dp/dl = 129 u^{0.31}, \quad (11)$$

and for a permeability of 225 md,

$$dp/dl = 448 u^{0.16}. \quad (12)$$

The correlation coefficients were 0.93 and 0.96, respectively.

For comparison with our work, for a foam quality of 50%, the pressure gradient varied with velocity to a power close to 0.33 (0.27 for 899-md core, 0.30 for 482-md core, and 0.38 for 80-md core). (This information can be obtained from Darcy's law and the equations in Table 27.)

We note the agreement between the power-law indexes (for similar foam qualities) of our results and the results of Falls *et al.*<sup>81</sup> Falls *et al.* measured the apparent viscosity of foams of known texture in glass bead packs. They showed that (for a foam quality > 95%) the apparent foam viscosity varied with velocity to the  $-\frac{1}{3}$  power when the average bubble size was larger than the pore size and to the  $-\frac{2}{3}$  power when the bubble size was smaller than the pore size. Falls *et al.*<sup>81</sup> used nitrogen gas and 1% Siponate DS sodium dodecylbenzene sulfonate in distilled water. The permeability of the glass bead packs varied from 5,000 to 9,000 darcy.

For a foam quality of 95%, our results (listed in Table 27) showed that the apparent foam viscosity varied with velocity to a power close to  $-\frac{1}{3}$  (-0.26 in the 899-md core, -0.28 in the 482-md core, and -0.39 in the 80-md core). For 50% foam quality, on the other hand, our results showed that viscosity varied with velocity to a power close to  $-\frac{2}{3}$  (-0.73 in the 899-md core, -0.70 in the 482-md core, and -0.62 in the 80-md core). In view of the work of Falls *et al.*,<sup>81</sup> our results suggest that the bubble size was smaller than the pore size at a quality of 50% and greater than the pore size at a quality of 95%. (The dependence of the texture on the foam quality was also discussed by Holm,<sup>65</sup> who stated that a high-quality foam contains larger diameter bubbles than a low-quality foam.)

### Implications for Selective Fluid Diversion

For the surfactant solution studied, we identified a range for the threshold permeability where no foam or a very weak foam was generated. This range was between 7.5 md and 80 md. (Of course, lithological differences may affect this range.) The implication of these results is that a potential placement advantage exists when the permeability is 7.5 md or less in the low-permeability zones and 80 md or more in the high permeability zones.

Figs. 79 to 81 show how our data support the limiting-capillary-pressure concept.<sup>73</sup> These figures suggest four different slopes for the variation of foam mobility with core permeability. For 95%-foam quality, the dashed lines (Figs. 79-81) between 1 and 7.5 md suggest that normal gas and liquid flow occurred (i.e., no foam generation). The upper limit of the normal two-phase flow region for 95% quality was not specifically identified by our data, although the limit must be less than 80 md. At qualities of 80% and 50%, weak foams were generated in the 7.5-md core, and much less-mobile foams were observed in the 80-md core. Therefore, between 7.5 and 80 md, lines with negative slopes represent this data in Figs. 79-81 (in most cases). Figs. 79-81 indicate that the foam mobility generally did not vary much between 80 and 482 md. Also, in all cases shown in Figs. 79-81, foam mobilities increased sharply between 482 and 899 md. These trends are qualitatively consistent with those predicted by Khatib *et al.*<sup>73</sup>

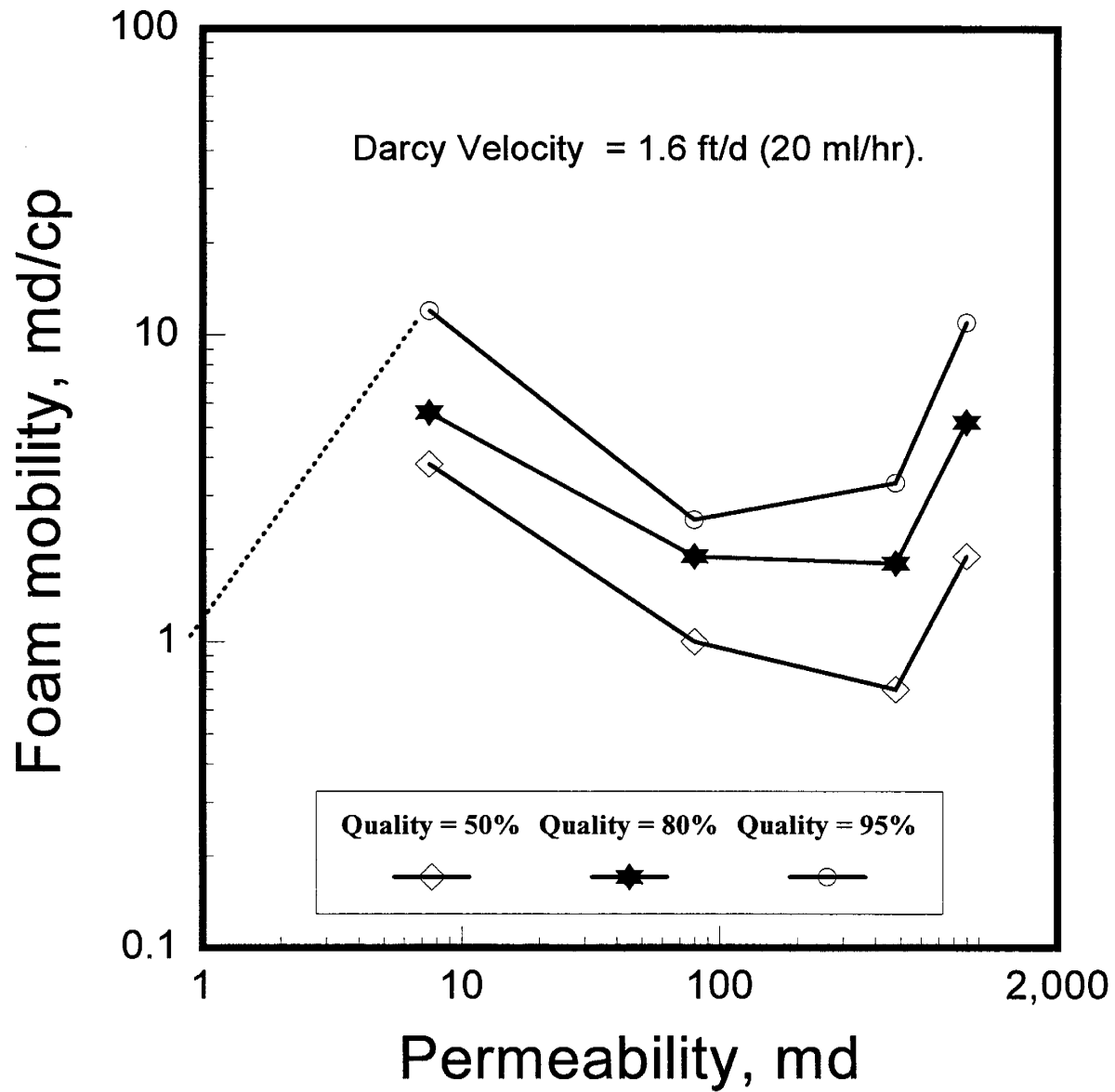


Fig. 79. Variation of foam mobility with permeability. 1.6 ft/d.

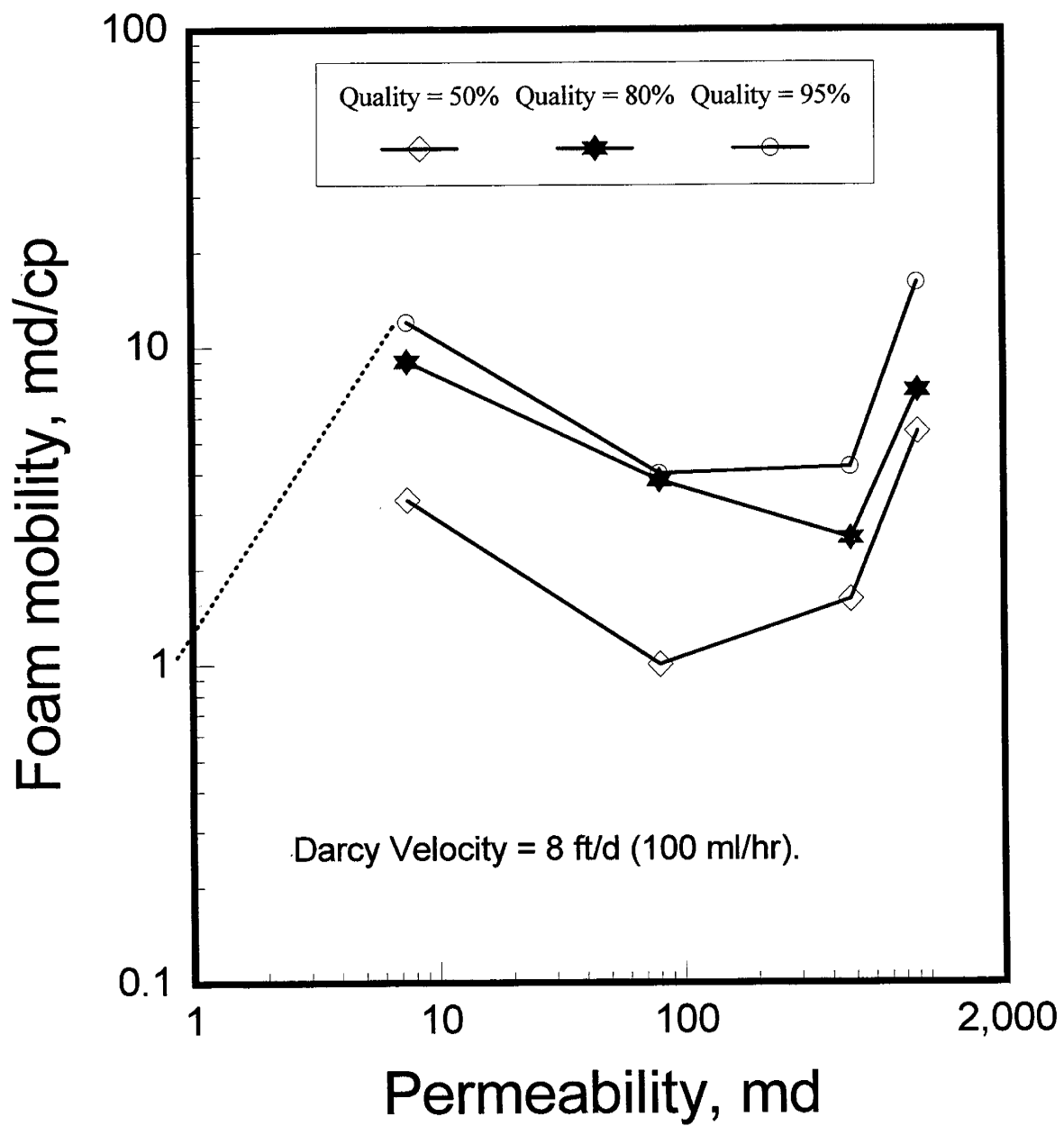


Fig. 80. Variation of foam mobility with permeability. 8 ft/d.

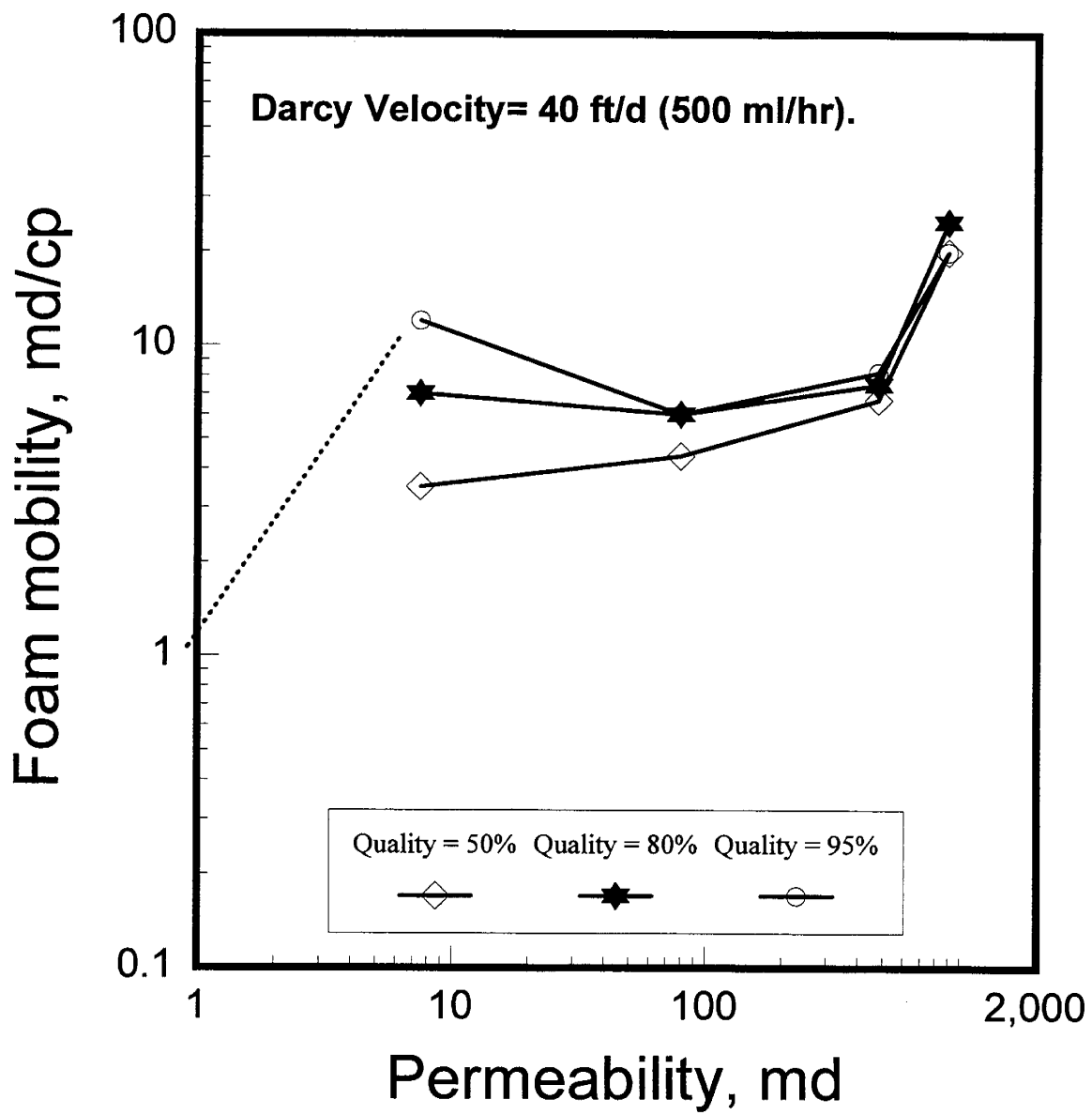


Fig. 81. Variation of foam mobility with permeability. 40 ft/d.

For comparison, Table 28 lists some literature resistance factors for foams generated in different cores (0.4 to 231 md). These results were performed with carbon-dioxide foams for different surfactants, permeabilities, and lithologies. The data shown in this table are not sufficient to establish the effect of lithology on foam behavior. However, the table suggests that resistance factors are low for many foams when permeabilities are less than 15 md, both in sandstones and carbonates. Of course, the surfactant type, surfactant concentration, brine salinity and permeability may have an important effect on foam generation.

Table 28. Effect of Lithology on Foam Generation

Workers	Surfactant & concentration	Lithology	k, md	F <sub>r</sub>
Lee <i>et al.</i> <sup>66</sup>	Enordet X2001 (0.1%)	West Jordan limestone	0.4	3
		Baker dolomite	6	17
		Rock Creek sandstone	11.1	50
Lee & Heller <sup>71</sup>	Chembetine BC-50 (0.1%)	Rock Creek sandstone	14.8	5
Kuehne <i>et al.</i> <sup>82</sup>	Correxit (ethoxy alcohol)	dolomite	231	20
	Chaser CD1040 (α-olefin sulfonate)	dolomite	231	80

### Parameters Affecting Foam Persistence During Brine Injection

To determine the potential of foams as blocking agents, we must investigate the parameters that affect foam persistence during brine injection. For a successful treatment, foam in the high-permeability zones should not washout easily during brine flow. This section examines several variables that may affect residual resistance factors for nitrogen foams.

**Effects of Brine Velocity and Throughput.** For the 482-md Berea core, Fig. 82 illustrates results for brine injection after foam was generated at a quality of 80% and a flow rate of 500 ml/hr (40 ft/day). The first experiment (solid circles in Fig. 82) was conducted after generating foam until steady state was achieved, followed by brine injection at a flow rate of 1,300 ml/hr (100 ft/day). The second experiment (solid diamonds) was identical to the first experiment, except that brine was injected at 13 ml/hr (1.0 ft/day). In both cases, the steady-state foam mobilities before brine injection were approximately 7.5 md/cp, and the foam throughput values required to reach steady state were similar. For a given brine throughput, Fig. 82 shows that higher F<sub>rr</sub> values were observed at 1 ft/d than at 100 ft/d. Similar results were observed in the 899-md and 80-md Berea cores (see Figs. 83 and 84).

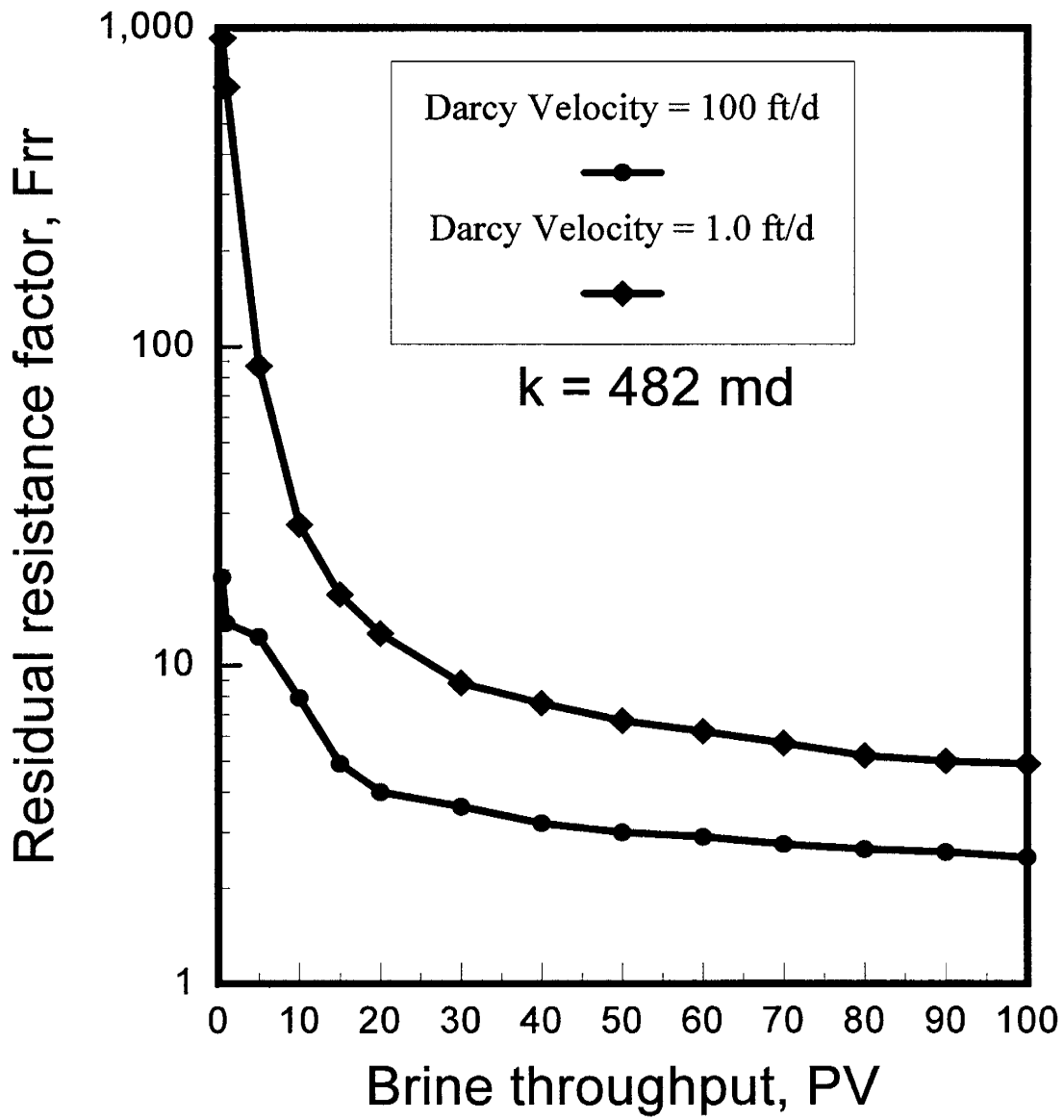


Fig. 82. Effects of brine throughput and velocity on foam persistence. 482 md.

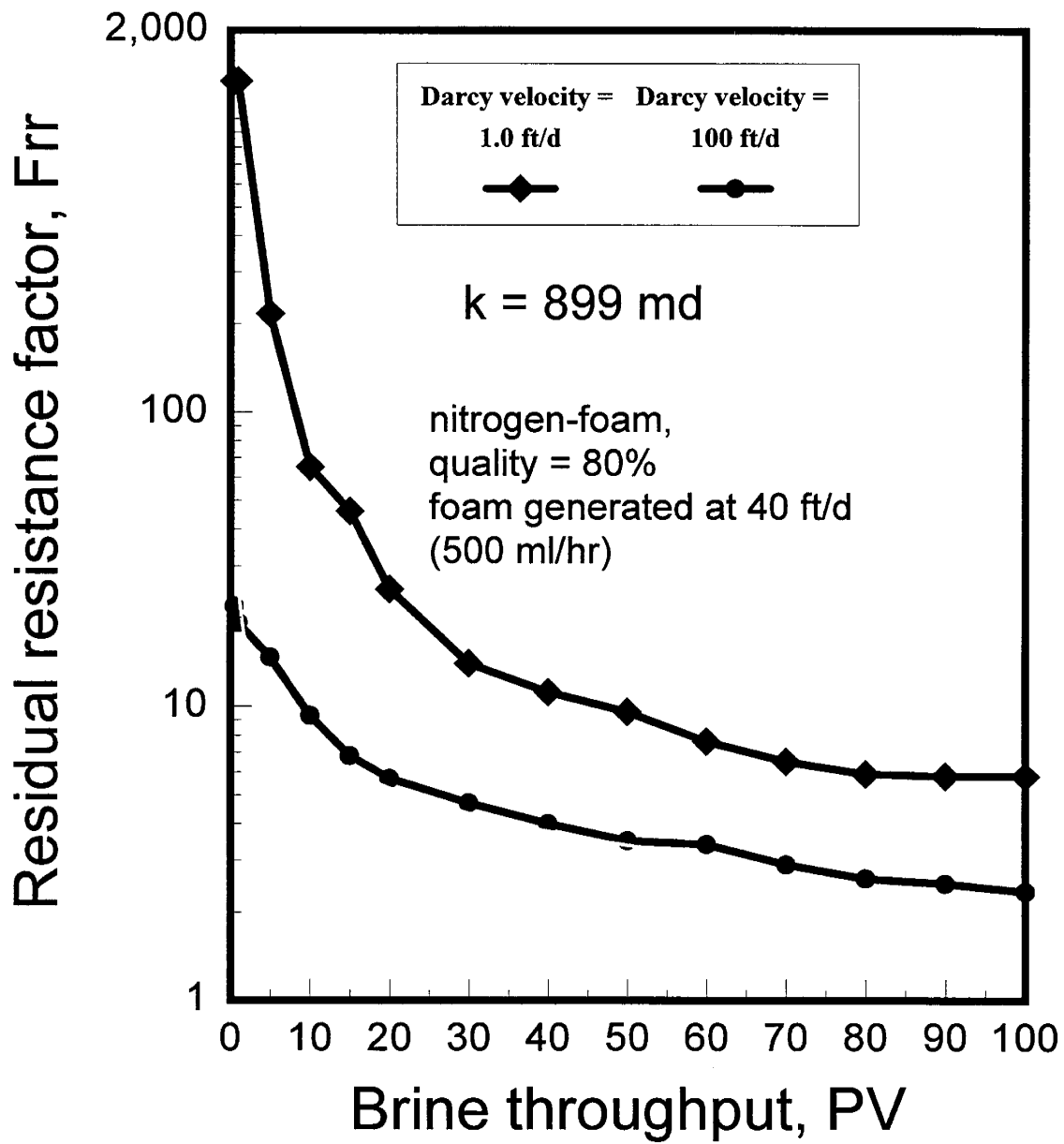


Fig. 83. Effects of brine throughput and velocity on foam persistence. 899 md.

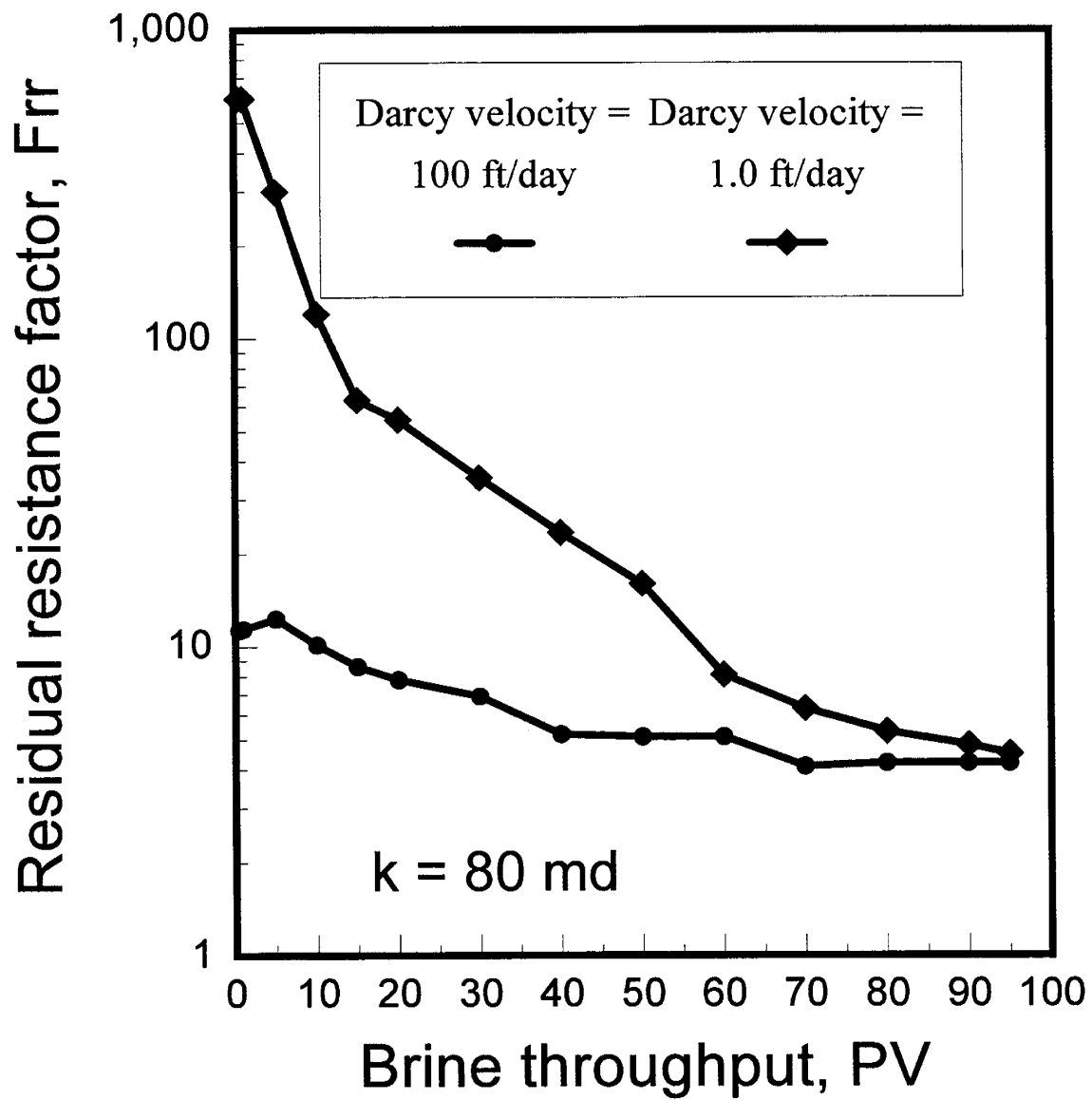


Fig. 84. Effects of brine throughput and velocity on foam persistence. 80 md.

**Other Parameters Affecting Nitrogen-Foam Persistence.** Table 29 and Fig. 85 illustrate other factors that may affect the persistence of nitrogen foam during brine injection in the 482-md core. Brine or dilute surfactant solution (in Case f) was injected at a flow rate of 1,300 ml/hr (100 ft/day) unless otherwise mentioned. The cases tested were as follows:

- Case a. Foam generated at 80% quality and flow rate of 500 ml/hr (40 ft/day).
- Case b. Foam generated at 80% quality and flow rate of 50 ml/hr (4 ft/day).
- Case c. Foam generated at 50% quality and flow rate of 500 ml/hr.
- Case d. Foam generated at 95% quality and flow rate of 500 ml/hr.
- Case e. Foam generated at 20% quality and flow rate of 500 ml/hr.
- Case f. Foam generated at 80% quality and flow rate of 500 ml/hr, followed by injection of 0.03%-surfactant solution instead of surfactant-free brine.
- Case g. Foam was generated at higher surfactant concentration (1% instead of 0.3%) at 80% quality and generation rate of 500 ml/hr, followed by brine injection.
- Case h. Foam was generated at 1,000 ml/hr (1% surfactant concentration) and 50% quality, followed by brine injection at 1,300 ml/hr (100 ft/day).

The residual resistance factors were not very sensitive to (1) the rate of foam generation (Cases a and b), (2) the foam quality (Cases a, c, d, and e), (3) the presence of surfactant in the brine post-flush (Cases a and f), or (4) the surfactant concentration during foam generation (Cases a, g, and h).

Table 29. Effect of Different Factors on Residual Resistance Factors

PV brine injected	Residual Resistance Factor							
	Case a	Case b	Case c	Case d	Case e	Case f	Case g	Case h
0.5	18.9	12.5	15.5	17.3	15.1	30.4	19.1	29.8
1	13.6	11.4	16.7	12.7	14.4	14.1	14.4	25
5	12.3	8.3	12.2	10	13	11.4	11.1	18.6
10	7.9	5.3	8.8	7.1	8.7	8.4	8.1	15
15	4.9	4.1	6.8	5.4	6.3	6.9	6.5	8.4
20	4	3.6	5.8	4.5	4.9	5.6	5.3	7.7
30	3.6	3.2	5.7	3.8	5	4.8	5.5	7.3
40	3.2	2.9	4.2	3.4	4.3	4.2	4.8	6.7
50	3	2.7	3.8	2.6	4	4	4.5	6
60	2.9	2.5	3.5	2.3	3			5.8
70	2.75	2.4	3.3		2.8			4.7
80	2.65							4.3
90	2.6							
100	2.5							

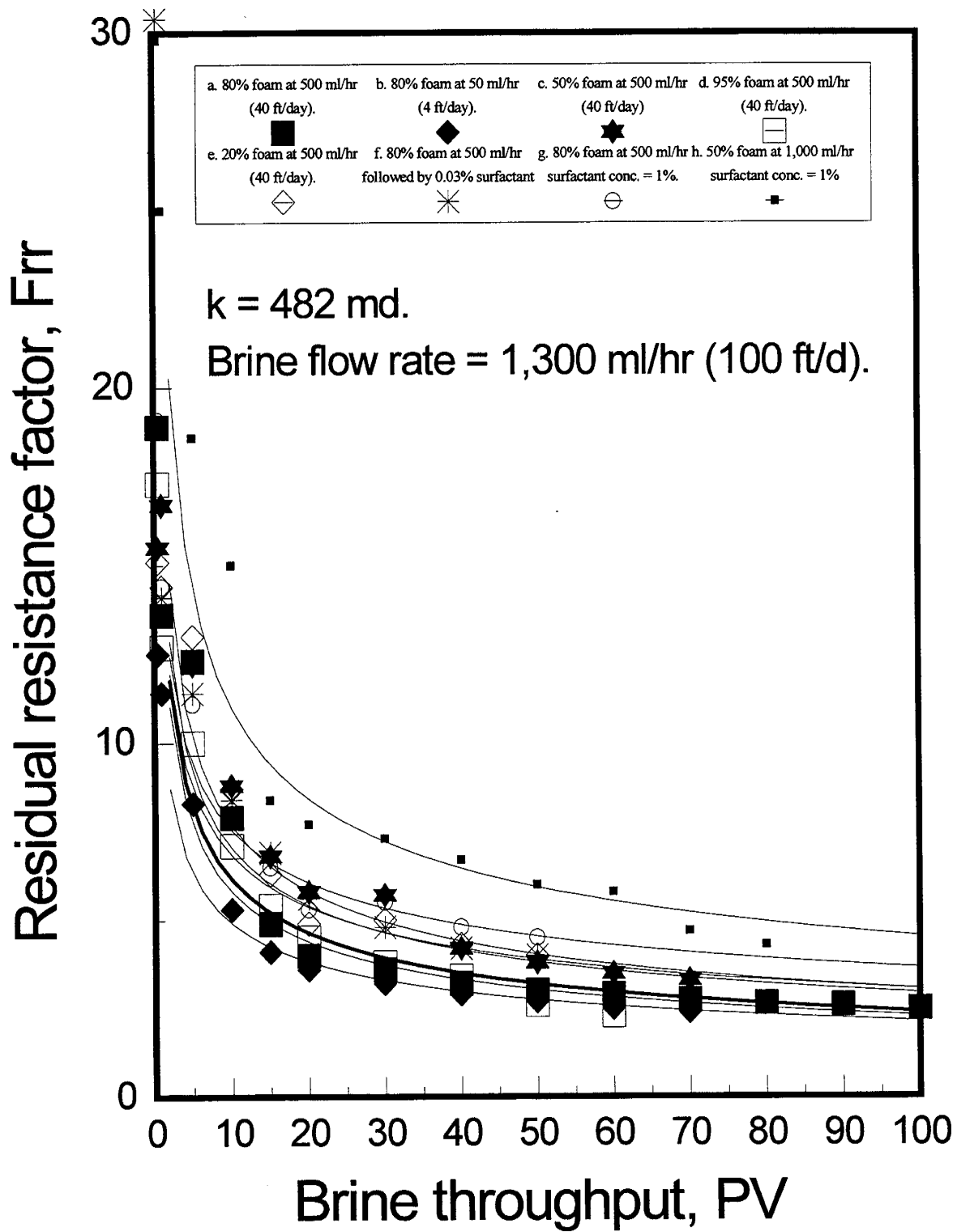


Fig. 85. Factors affecting foam persistence.

## Discussion of Foam Persistence During Brine Injection

During brine injection, our nitrogen foam provided some permeability reduction even at high flow rates (1,300 ml/hr or 100 ft/d) and throughput values (100 PV). Fig. 86 shows nitrogen-foam residual resistance factors versus brine throughput. After injecting about 20 PV of brine, the residual resistance factors in the Berea three cores levelled off at different values. Higher residual resistance factors were observed as the permeability decreased. Surfactant dilution probably caused the decrease in the residual resistance factor with the increased brine throughput.<sup>78</sup> As the surfactant concentration decreased, the ability of foam to hold the trapped gas was reduced. As a result, gas evolved from the backpressure outlet during brine injection. As the gas was removed from the core, the water saturation increased. Fig. 87 plots  $V_p/V_{po}$  values (from our tracer results in Appendix D) versus the reciprocal residual resistance factors, measured before performing the tracer studies. The reciprocal residual resistance factor,  $1/F_{rr}$ , may provide information about the relative permeability of brine in the presence of foam, and the pore volume available for flow may be viewed as an indicator of water saturation in the core. The relationship between  $1/F_{rr}$  and  $V_p/V_{po}$  for the 899-md core was

$$1/F_{rr} = 0.06 e^{2.51(V_p/V_{po})} \quad (13)$$

The correlation coefficient was 0.87.

For the 482-md core,

$$1/F_{rr} = 0.06 e^{2.64(V_p/V_{po})} \quad (14)$$

The correlation coefficient was 0.93.

For the 80-md core,

$$1/F_{rr} = 0.08 e^{2.48(V_p/V_{po})} \quad (15)$$

The correlation coefficient was 0.88.

Averaging all the data from the three cores,

$$1/F_{rr} = 0.07 e^{2.48(V_p/V_{po})} \quad (16)$$

The correlation coefficient was 0.87.

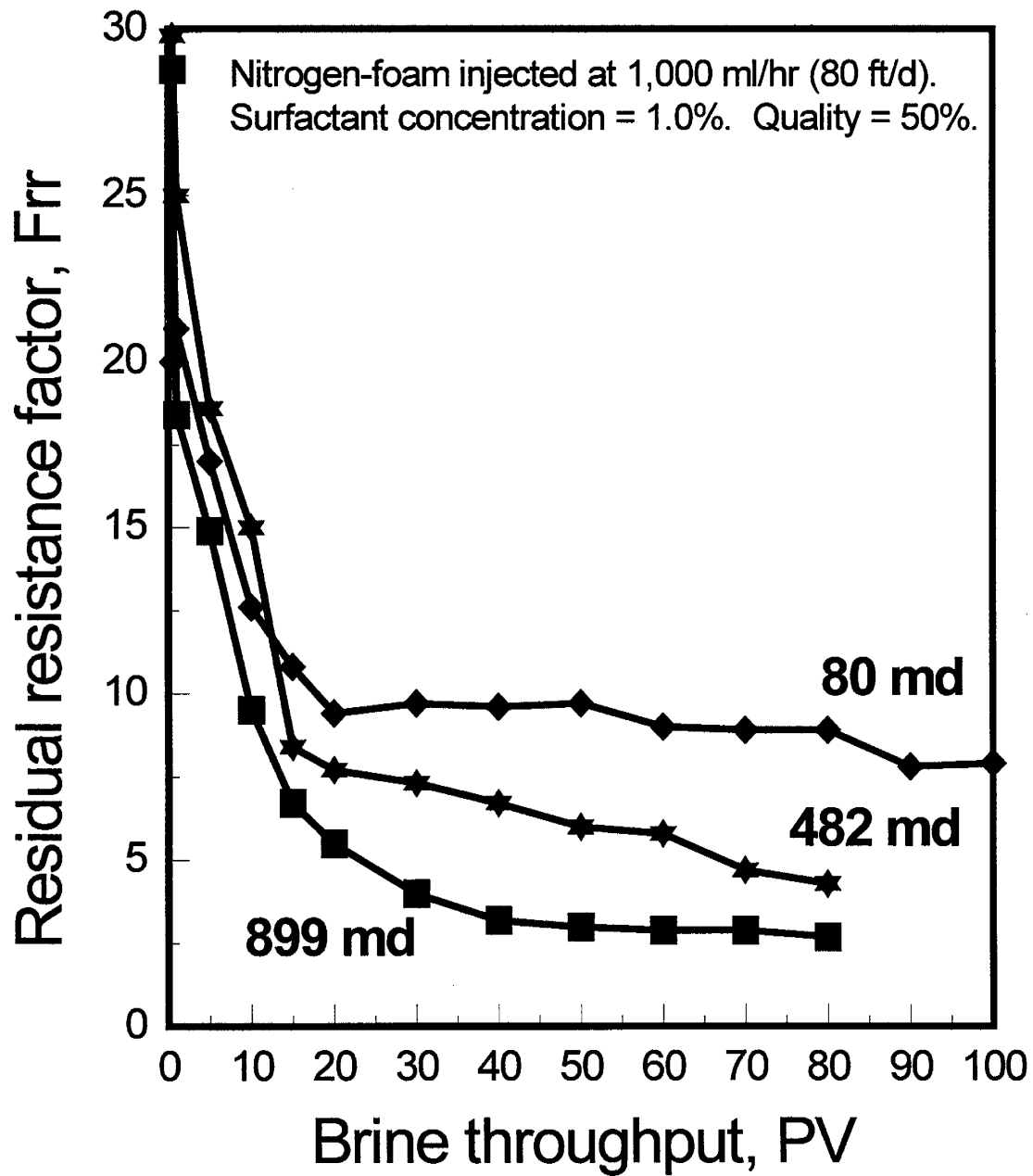


Fig. 86. Effect of permeability on foam persistence.

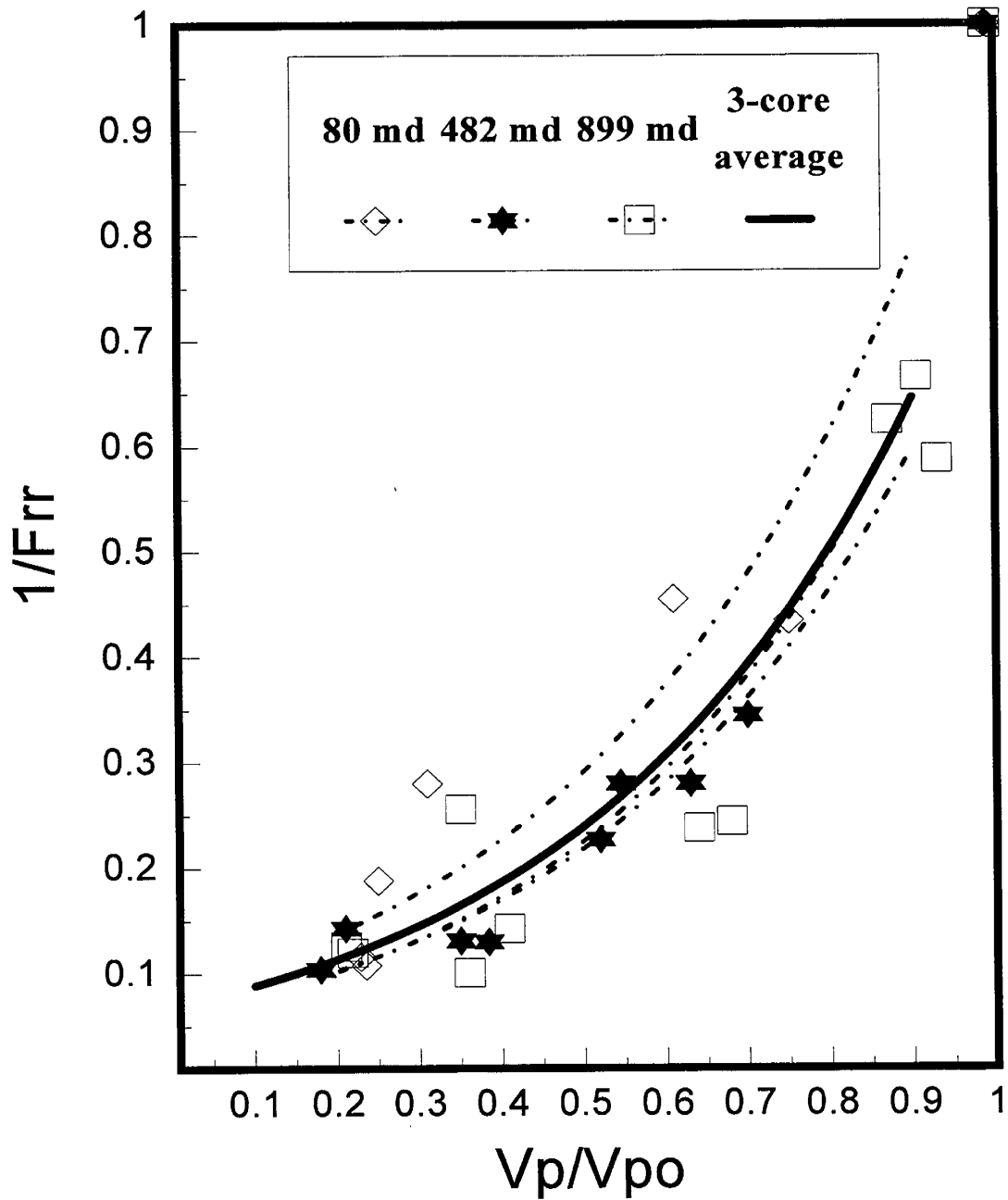


Fig. 87. Relative permeability curve from tracer and residual resistance factor data.

## Comparison With Gel Treatments

Extensive theoretical and experimental work<sup>58,74,75</sup> has shown that gel treatments are not expected to be effective in unfractured injection wells unless hydrocarbon-productive zones are protected during gel placement. The purpose of this analysis is to determine conditions where foam treatments might be superior to gel treatments.

To address this issue, two processes must be analyzed. In the first process, the blocking agent is placed. During placement, the penetration of blocking agent into the low-permeability zones should be much less than that into high-permeability streaks. The second process involves injection of water or gas after the placement process. In this process, the blocking agent must persist (not wash out) in the high-permeability zone during fluid injection, and the treatment must restrict the flow capacity of the high-permeability zones by a greater factor than in the low-permeability zones.

**Placement of Foam Versus Placement of a Water-Like Gelant.** Using eight rheological models, Seright<sup>84</sup> concluded that the non-Newtonian rheology of polymeric gelants will not reduce the degree of penetration into the low-permeability zones below the value achievable with a water-like gelant (i.e.,  $F_r = 1$ ). Therefore, we will use the behavior of water-like gelants as a standard for comparison during placement.

For linear flow, the degree of penetration is defined as the distance,  $L_{p2}$ , of penetration in a low-permeability layer (Layer 2) divided by the distance,  $L_{p1}$ , reached in the most-permeable layer (Layer 1). In radial flow, the degree of penetration is defined as  $(r_{p2}-r_w)/(r_{p1}-r_w)$ , where  $r_{p2}$  is the radius of penetration in a low-permeability layer when the blocking agent reaches a predetermined radius of penetration,  $r_{p1}$ , in the most-permeable layer.  $r_w$  is the wellbore radius.<sup>21</sup>

For water-like gelants, the degree of penetration was calculated using Eq. 17 for linear flow and Eq. 18 for radial flow.<sup>21</sup>

$$L_{p2}/L_{p1} = (k_2\phi_1)/(k_1\phi_2) \quad (17)$$

$$(r_{p2}^2-r_w^2)/(r_{p1}^2-r_w^2) = (k_2\phi_1)/(k_1\phi_2) \quad (18)$$

To calculate values for the degree of penetration for our non-Newtonian foams, we used our experimental results (Figs. 73-76, Table 27, Table D-10) along with the numerical methods that we applied in Ref. 84.

Table 30 compares the results of foam placement to that of water-like gelants for different permeability values in the high- and low-permeability layers. The reservoir model included two non-communicating layers. Both linear and radial flow geometries were considered. For each flow geometry, six cases are presented. For the three cases where the permeability of Layer 2 was 7.5 md (Cases 1, 2, and 3 in Table 30), no foam was formed in Layer 2, so the degree of

penetration was effectively zero. Of course, this situation is the best case that can be achieved. When foam forms in the high-permeability zones but not in the low-permeability zones, the foam has a distinct placement advantage over gelants.

Table 30. Gelant Placement Versus Foam Placement in Two-Layered Systems

Case	$k_1$ , md	$k_2$ , md	Blocking agent	$L_{p2}/L_{p1}$	$(r_{p2}-r_w)/(r_{p1}-r_w)$	Best placement?
1	899	7.5	1. Water-like gelant 2. Foam	0.008 0.000	0.091 0.000	Foam
2	482	7.5	1. Water-like gelant 2. Foam	0.016 0.000	0.125 0.000	Foam
3	80	7.5	1. Water-like gelant 2. Foam	0.094 0.000	0.306 0.000	Foam
4	899	80	1. Water-like gelant 2. Foam	0.09 0.32	0.30 0.52	Gelant
5	482	80	1. Water-like gelant 2. Foam	0.17 0.98	0.41 0.93	Gelant
6	899	482	1. Water-like gelant 2. Foam	0.53 0.37	0.73 0.55	Foam (apparently)

For Cases 4 and 5 in Table 30, foam was formed in both Layers 1 and 2, and the degree of penetration was greater for the foam than for the water-like gelant. For example, for Case 5 in linear flow, the distance of gelant penetration in Layer 2 was 17% of that in Layer 1. In contrast, the distance of foam penetration in Layer 2 was 98% of that in Layer 1. Table 30 indicates that the water-like gelant has a placement advantage over the foam in Cases 4 and 5, both for linear flow and radial flow.

For Case 6 in Table 30, the degree of penetration was less for the foam than for the water-like gelant. For example, in linear flow, the distance of gelant penetration in Layer 2 was 53% of that in Layer 1. In contrast, the distance of foam penetration in Layer 2 was only 37% of that in Layer 1. For this permeability combination, the degree of foam penetration in radial flow was also less than that for the water-like gelant. Upon first consideration, this result suggests that the foam will be superior to a gelant when used as a blocking agent. However, the next section will demonstrate that this suggestion is not correct. Although the foam placement was apparently better than that for a water-like gelant, the permeability-reduction properties ultimately favor the gel instead of the foam for Case 6.

**Relative Injectivity Losses After Foam Placement.** To evaluate the success of a treatment, we must determine how the flow profiles are modified in each layer. This determination requires both the distances of blocking-agent penetration into the various layers (as shown in the previous section) and the permeability-reduction properties (residual resistance factors) in the various layers. The data in Figs. 82 to 87 provided the foam residual resistance factors that we used in our analysis.

In a successful treatment, the brine injectivity in high-permeability zones should be reduced by a much greater factor than in the low-permeability zones. Therefore, to assess the success of a treatment, injectivity values must be compared before versus after placement of the blocking agent. Eq. 19 gives the injectivity retained ( $I/I_o$ ) in Layer  $i$  in an unfractured well (radial flow).<sup>21,74</sup>

$$\frac{I}{I_o} = \frac{(\psi_i + 1) \ln(r_{pm}/r_w)}{F_{rr} \ln(r_{pi}/r_w) + \ln(r_{pm}/r_{pi}) + \psi_i \ln(r_{pm}/r_w)} \quad (19)$$

In Eq. 19,  $r_{pm}$  is the maximum radius of penetration of blocking agent in the reservoir, and  $\psi_i$  is the pressure drop between  $r_{pm}$  and the production well divided by the pressure drop between the injection well and  $r_{pm}$  in Layer  $i$  prior to the placement of the blocking agent. (A similar equation was developed for linear flow.<sup>21,74</sup> However, our analysis here will focus on radial flow.)

Based on our earlier work,<sup>74</sup> the following analysis was conducted to account for the non-Newtonian flow of brine after placement of foam. During water injection before the treatment, the total pressure drop between the injection well and the production well in Layer 1 (the most-permeable layer) is given by Eq. 20,

$$\Delta p_t = \Delta p_{w1} + \Delta p_{\psi_1} \quad (20)$$

where  $\Delta p_{w1}$  is the pressure drop in Layer 1 between the injection well and the maximum radius of penetration ( $r_{pm}$ ) and  $\Delta p_{\psi_1}$  is the pressure drop between  $r_{pm}$  and the production well. Let  $\psi_1$  be defined by Eq. 21

$$\psi_1 = \Delta p_{\psi_1} / \Delta p_{w1} \quad (21)$$

Accordingly,  $\Delta p_t$  is given by Eq. 22

$$\Delta p_t = (\psi_1 + 1)(u_1 r_w)(\mu_w/k_1)[\ln(r_{pm}/r_w)] \quad (22)$$

For  $r_{pm} = 50$  ft,  $r_w = 0.5$  ft,  $\mu_w = 0.67$  at 40°C, and  $\psi_1 = 2$ , Eq. 22 reduces to

$$u_1 = 4.83 \times 10^{-4} (\Delta p_t k_1) \quad (23)$$

where  $u_1$  is in cm/sec,  $k_1$  is in darcys, and  $\Delta p_t$  is in psi.

During water injection after foam placement,  $\Delta p_t$  is given by Eq. 24,

$$\Delta p_t = \Delta p_{p1} + \Delta p_{w1} + \Delta p_{\psi 1} \quad (24)$$

where  $\Delta p_t$  is the pressure drop across the foam bank in Layer 1, i.e., between the injector and the outer radius ( $r_{p1}$ ) of the foam bank in Layer 1. Also,  $\Delta p_{w1}$  is the pressure drop between  $r_{p1}$  and  $r_{pm}$ . In this case, Eqs. 25 and 26 give  $\Delta p_{w1}$  and  $\Delta p_{\psi 1}$

$$\Delta p_{w1} = (u_1 r_w)(\mu_w/k_1)[\ln(r_{pm}/r_{p1})] \quad (25)$$

$$\Delta p_{\psi 1} = \psi_1(u_1 r_w)(\mu_w/k_1)[\ln(r_{pm}/r_w)] \quad (26)$$

For shear-thinning behavior,  $F_{rr}$  is given by Eq. 27

$$F_{rr} = Ku^n \quad (27)$$

and  $\Delta p_{p1}$  is given by Eq. 28

$$\Delta p_{p1} = (u_1)^{1+n} r_w (\mu_w/k_1) (-K/n) [(r_{p1}/r_w)^{-n} - 1] \quad (28)$$

In Eq. 24,  $\Delta p_{w1}$  reduces to zero since  $r_{p1}$  equals  $r_{pm}$ . Using Eqs. 25 through 28,  $u_1$  was found by iteration to be within the range covered by our experimental data.

Similar equations were applied to the low-permeability layer (Layer 2). The relative injectivity in each layer (Layer  $i$ ) is estimated using Eq. 29

$$I/I_o = u_i(\text{after the treatment})/u_{i0}(\text{before the treatment}) \quad (29)$$

Equation 29 was used to determine the values listed in the sixth and seventh columns of Table 31.

Table 31 compares six cases that show how a foam treatment modifies brine-injection profiles in two-layered radial systems (no communication between layers). The fourth and fifth columns of this table list values of the residual resistance factors that were assumed in Layers 1 and 2, respectively. These values were based on our experimental results that were reported earlier.

To obtain velocity values within the range that was covered by our experimental correlation of  $F_{rr}$  versus velocity, the pressure drop was taken to be 10,000 psi for the 80/7.5-md system, 3,000 psi for the 482/7.5-md system, and 2,000 psi for the 899/482-md system. For each combination of high- and low-permeability zones, the radii of penetration were taken from Table 30.

As shown in Table 31, profiles were successfully improved only when no foam ( $F_{rr2}=1$ ) or a very weak foam (low residual resistance factor) was generated in the low-permeability layer and a persistent low-mobility foam was formed in the high-permeability layer ( $F_{rr1} \gg 1$ ). This result is illustrated by Cases 1 through 4 in Table 31, where the permeability was 7.5 in the low-permeability zone.

Cases 5 and 6 show the results when Layers 1 and 2 had permeabilities of 899 md and 482 md, respectively. Even though Case 6 of Table 30 indicated that foam placement was apparently superior to that for a water-like gelant, Table 31 shows that the profile was not improved. Therefore, in radial flow, foams may only be superior to gels when the foam does not form in the less-permeable zones (Cases 1 through 4 in Table 31).

Table 31. Profile Modification During Brine Injection  
After Foam Treatments in Two-Layered Systems (Radial Flow)

Case	$k_1$ , md	$k_2$ , md	$F_{rr1}$	$F_{rr2}$	$I_1/I_{10}$ , %	$I_2/I_{20}$ , %	Profile improved?
1	80	7.5	$279 u^{-0.81}$	6	0.02	30.5	yes
2	80	7.5	$279 u^{-0.81}$	1	0.02	100	yes
3	482	7.5	$686 u^{-0.85}$	3.6	0.004	60	yes
4	482	7.5	$686 u^{-0.85}$	1	0.004	100	yes
5	899	482	$387 u^{-0.95}$	$686 u^{-0.85}$	0.138	0.013	no
6	899	482	3	3.6	60	56	no

## Conclusions

The following conclusions are relevant to nitrogen foams and for the surfactant used [Bio-Terge AS-40<sup>®</sup>, a C<sub>14-16</sub> alpha-olefin sulfonate 0.3% active weight in brine (1% NaCl and 0.1% CaCl<sub>2</sub>)] at 40°C:

1. A permeability (7.5 md) was identified for this surfactant system, where no foam or only weak foam was generated. At a quality of 95%, no foam was generated in the 7.5-md core. As the quality decreased, only weak foams were observed (that were readily washed out by brine).
2. For the 80-, 482-, and 899-md cores, foams were much less mobile. Shear-thinning behavior was typical in the three cores. Foam resistance factors varied from 20 to 300 for the 80-md core, from 60 to 1,500 for the 482-md core, and from 40 to 1,000 for the 899-md core.

3. During foam injection, the apparent viscosity correlated with Darcy velocity to a power close to  $-\frac{1}{3}$  when the foam quality was 95% (-0.26 for the 899-md core, -0.28 for the 482-md core, and -0.39 for the 80-md core). The apparent viscosity in the three Berea cores correlated with the velocity to a power close to  $-\frac{2}{3}$  when the foam quality was 50% (-0.73 for the 899-md core, -0.70 for the 482-md core and -0.62 for the 80-md core).
4. During brine injection after foam placement, residual resistance factors decreased as both the velocity of the brine and the pore volume throughput increased. The residual resistance factors decreased as the permeability increased.
5. During brine injection, foam persistence (resistance to washout) can be slightly enhanced by generating foams at low quality (50%), at high surfactant concentration (1%), or by injecting dilute surfactant solutions (0.03% instead of brine).
6. Compared with water-like gelants, foams showed better placement properties when the permeabilities were 7.5 md or less in the low-permeability zones and 80 md or more in the high-permeability zones.

## NOMENCLATURE

A	= core cross-sectional area, $\text{cm}^2$
$a_r$	= retention or delay factor, PV
$a_{r1}$	= retention or delay factor in Zone 1, PV
$a_{r2}$	= retention or delay factor in Zone 2, PV
C	= tracer concentration in the effluent, $\text{g}/\text{cm}^3$
$C_o$	= injected tracer concentration, $\text{g}/\text{cm}^3$
d	= particle or microorganism diameter, $\mu\text{m}$
$d_{\text{crit}i}$	= critical particle size of Zone i, $\mu\text{m}$
$d_{\text{crit}1}$	= critical particle size of Zone 1, $\mu\text{m}$
$\bar{d}$	= mean particle size, $\mu\text{m}$
$F_r$	= resistance factor (brine mobility before placement of blocking agent divided by blocking-agent mobility before setting or gelation)
$F_{r1}$	= resistance factor in Zone 1, Core 1, or Fracture 1
$F_{r2}$	= resistance factor in Zone 2, Core 2, or Fracture 2
$F_{rr}$	= residual resistance factor (mobility before placement of blocking agent divided by mobility after placement of blocking agent)
$F_{rr1}$	= residual resistance factor in Zone 1
$F_{rr2}$	= residual resistance factor in Zone 2
$F_{rro}$	= oil residual resistance factor
$F_{rrw}$	= water residual resistance factor
H	= constant in Eqs. D-5 and D-6
h	= formation thickness, ft [m]
$h_f$	= fracture height, ft, [cm]
$h_{f1}$	= height of Fracture 1, ft [m]
$h_{f2}$	= height of Fracture 2, ft [m]
I	= injectivity, $\text{bbl}/\text{D}\text{-psi}$ [ $\text{m}^3/\text{s}\text{-Pa}$ ]
$I_o$	= initial injectivity, $\text{bbl}/\text{D}\text{-psi}$ [ $\text{m}^3/\text{s}\text{-Pa}$ ]
K	= consistency index
$K_{\text{ave}}$	= average consistency index
k	= permeability, md [ $\mu\text{m}^2$ ]
$k_{\text{av}}$	= average permeability of a fractured core, md [ $\mu\text{m}^2$ ]
$k_c$	= permeability of the filter cake, md [ $\mu\text{m}^2$ ]
$k_f$	= effective fracture permeability, md [ $\mu\text{m}^2$ ]
$k_i$	= permeability in Zone i or direction i, md [ $\mu\text{m}^2$ ]
$k_m$	= effective rock permeability, md [ $\mu\text{m}^2$ ]
$k_1$	= permeability in Zone 1, md [ $\mu\text{m}^2$ ]
$k_2$	= permeability in Zone 2, md [ $\mu\text{m}^2$ ]
L	= length of a microorganism, $\mu\text{m}$
$L_f$	= fracture length, ft [m]
$L_{f1}$	= effective length of Fracture 1, ft [m]
$L_{f2}$	= effective length of Fracture 2, ft [m]

$L_{pi}$	= distance of gelant penetration into Layer i, Core i, or Fracture i, ft [m]
$L_{pm}$	= maximum distance of gelant penetration into the most-permeable layer (Zone 1), ft [m]
$L_{p1}$	= distance of gelant penetration into Layer 1, Core 1, or Fracture 1, ft [m]
$L_{p2}$	= distance of gelant penetration into Layer 2, Core 2, or Fracture 2, ft [m]
$L_t$	= total core length, ft [m]
$n$	= power-law exponent
$P_c$	= capillary pressure, psi [Pa]
PV	= pore volume
$p$	= pressure, psi, [Pa]
$\Delta p$	= pressure drop, psi [Pa]
$\Delta p_i$	= pressure drop in Zone i, psi [Pa]
$\Delta p_{p1}$	= pressure drop in Zone 1 defined by Eq. 28, psi [Pa]
$\Delta p_t$	= total pressure drop, psi [Pa]
$\Delta p_{w1}$	= pressure drop in Zone 1 defined by Eq. 25, psi [Pa]
$\Delta p_{\psi 1}$	= pressure drop in Zone 1 defined by Eq. 26, psi [Pa]
$dp/dl$	= pressure gradient, psi/ft [Pa/m]
$q$	= volumetric injection or production rate, bbl/D [ $m^3/s$ ]
$q_i$	= injection rate in Zone i, bbl/D [ $m^3/d$ ]
$q_1$	= injection rate in Zone 1, bbl/D [ $m^3/d$ ]
$q_2$	= injection rate in Zone 2, bbl/D [ $m^3/d$ ]
$q_{io}$	= total brine injection rate before gelant placement, bbl/D [ $m^3/d$ ]
R	= correlation coefficient
$r$	= radius or pore radius, ft [m]
$r_e$	= external drainage radius, ft [m]
$r_{pi}$	= radius of penetration into Layer i, ft [m]
$r_{pm}$	= maximum radius of penetration in the reservoir, ft [m]
$r_{p1}$	= radius of penetration into Layer 1, ft [m]
$r_{p2}$	= radius of penetration into Layer 2, ft [m]
$r_w$	= wellbore radius, ft [m]
$S_{gel}$	= gel saturation (fraction of PV occupied by gel)
$S_{or}$	= residual oil saturation
$S_o$	= oil saturation
$S_w$	= water saturation
$S_{wr}$	= irreducible water saturation
$S_{wi}$	= water saturation in Zone i
$S_{wr}$	= irreducible water saturation
$S_{w1}$	= water saturation in Zone or Core 1
$S_{w2}$	= water saturation in Zone or Core 2
$t$	= time, seconds
$u$	= superficial or Darcy velocity or flux, ft/d [cm/s]
$u_i$	= superficial velocity in Zone i after the treatment, ft/d [cm/s]
$u_{io}$	= superficial velocity in Zone i before the treatment, ft/d [cm/s]

$u_1$	= superficial velocity in Zone 1 after the treatment, ft/d [cm/s]
$u_{10}$	= superficial velocity in Zone 1 before the treatment, ft/d [cm/s]
$V_f$	= fracture volume, cm <sup>3</sup>
$V_p$	= apparent remaining pore volume, cm <sup>3</sup>
$V_{po}$	= initial pore volume of the core, cm <sup>3</sup>
$V_t$	= total filtration volume, ft <sup>3</sup> [m <sup>3</sup> ]
$v_g$	= gas frontal velocity, ft/d [cm/s]
$w_f$	= fracture width, cm
$\alpha$	= dispersivity, cm; or filtration coefficient
$\alpha_i$	= filtration coefficient of Zone i
$\alpha_o$	= initial dispersivity of the core, cm
$\theta$	= angle between the long axis of the microorganism and the direction of flow at the pore entrance
$\lambda$	= mobility, md/cp [ $\mu\text{m}^2/\text{mPa}\cdot\text{s}$ ]
$\lambda_{\text{average}}$	= average foam mobility, md/cp [ $\mu\text{m}^2/\text{mPa}\cdot\text{s}$ ]
$\lambda_f$	= foam mobility, md/cp [ $\mu\text{m}^2/\text{mPa}\cdot\text{s}$ ]
$\mu$	= fluid viscosity, cp [mPa-s]
$\mu_{\text{app}}$	= apparent foam viscosity, cp [mPa-s]
$\mu_o$	= oil viscosity, cp [mPa-s]
$\mu_p$	= gelant viscosity, cp [mPa-s]
$\mu_w$	= water viscosity, cp [mPa-s]
$\sigma$	= standard deviation, $\mu\text{m}$ ; or interfacial tension, dynes/cm <sup>2</sup>
$\phi$	= porosity
$\phi_c$	= porosity of filter cake
$\phi_{f1}$	= effective porosity in Fracture 1
$\phi_{f2}$	= effective porosity in Fracture 2
$\phi_i$	= effective aqueous-phase porosity in Zone i
$\phi_1$	= porosity of Zone 1
$\phi_2$	= porosity of Zone 2
$\psi_1$	= ratio defined by Eq. 21 (see Ref. 21 for a more detailed discussion)

## REFERENCES

1. Seright, R.S.: "Improved Techniques for Fluid Diversion in Oil Recovery Processes," first annual report, DOE/BC/14880-5, U.S. DOE (Dec. 1993) 101-140.
2. Seright, R.S.: "Improved Techniques for Fluid Diversion in Oil Recovery Processes," second annual report, DOE/BC/14880-10, U.S. DOE (March 1995) 2-20, 30-50, 63-113, 129-143.
3. Crawford, P.B. and Collins, R.E.: "Estimated Effect of Vertical Fractures on Secondary Recovery," *Trans.*, AIME, **201** (1954) 192-196.
4. Dyes, A.B., Kemp, C.E., and Caudle, B.H.: "Effect of Fractures on Sweep-out Pattern," *Trans.*, AIME, **213** (1958) 245-249.
5. Seright, R.S.: "Gel Placement in Fractured Systems," *SPEPF* (Nov. 1995) 241-248.
6. Sydansk, R.D. and Moore, P.E.: "Gel Conformance Treatments Increase Oil Production in Wyoming," *Oil & Gas J.* (Jan. 20, 1992) 40-45.
7. Moffitt, P.D.: "Long-Term Production Results of Polymer Treatments on Producing Wells in Western Kansas," *JPT* (April 1993) 356-362.
8. Seright, R.S. and Liang, J.: "A Survey of Field Applications of Gel Treatments for Water Shutoff," paper SPE 26991 presented at the 1994 SPE Permian Basin Oil & Gas Recovery Conference, Midland, March 16-18.
9. Sorbie, K.S. and Seright, R.S.: "Gel Placement in Heterogeneous Systems with Crossflow," paper SPE 24192 presented at the 1992 SPE/DOE Symposium on Enhanced Oil Recovery, Tulsa, April 22-24.
10. Dake, L.P.: *Fund. of Reservoir Engineering*, Elsevier Scientific Publishing Co., New York (1982) 110, 343-430.
11. Bird, R.B., Stewart, W.E., and Lightfoot, E.N.: *Transport Phenomena*, John Wiley & Sons, New York (1960) 62.
12. Seright, R.S. and Martin, F.D.: "Impact of Gelation pH, Rock Permeability, and Lithology on the Performance of a Monomer-Based Gel," *SPEPE* (Feb. 1993) 43-50.
13. Seright, R.S.: "Impact of Permeability and Lithology on Gel Performance," paper SPE 24190 presented at the 1992 SPE/DOE Symposium on Enhanced Oil Recovery, Tulsa, April 22-24.

14. Kia, S.F., Fogler, H.S., and Reed, M.G.: "Effect of pH on Colloidally Induced Fines Migration," *J. Colloid & Interfac. Sci.* **118**(1) (1987) 158-168.
15. Sydansk, R.D.: "A Newly Developed Chromium (III) Gel Technology," *SPE* (Aug. 1990) 346-352.
16. Lockhart, T.P. and Albonico, P.: "New Chemistry for the Placement of Chromium(III)/Polymer Gels in High-Temperature Reservoirs," *SPEPF* (Nov. 1994) 273-279.
17. Albonico, P., Burrafato, G., and Lockhart, T.P.: "Polyacrylamide Gels Formed with  $\text{Cr}^{+3}$  Ion and  $\text{Cr}(\text{Acetate})_3$ : Thermodynamically and Kinetically Controlled Crosslinking Reactions," *J. Polym. Sci.: Polym. Chem.* (1992) **30**, 1071.
18. Liang, J., Sun, H., Seright, R.S.: "Why Do Gels Reduce Water Permeability More Than Oil Permeability?," *SPE* (Nov. 1995) 282-286.
19. Liang, J., Sun, H., Seright, R.S.: "Reduction of Oil and Water Permeabilities Using Gels," paper SPE 24195 presented at the 1992 SPE/DOE Symposium on Enhanced Oil Recovery, Tulsa, April 22-24.
20. Seright, R.S.: "Reduction of Gas and Water Permeabilities Using Gels," *SPE Production & Facilities* (May 1995) 103-108.
21. Seright, R.S.: "Placement of Gels to Modify Injection Profiles," paper SPE/DOE 17332 presented at the 1988 SPE/DOE Enhanced Oil Recovery Symposium, Tulsa, April 17-20.
22. Needham, R.B., Threlkeld, C.B., and Gall, J.W.: "Control of Water Mobility Using Polymers and Multivalent Cations," paper SPE 4747 presented at the 1974 SPE-AIME Improved Oil Recovery Symposium, Tulsa, April 22-24.
23. Avery, M.R. and Wells, T.A.: "Field Evaluation of a New Gelant for Water Control in Production Wells," paper SPE 18201 presented at the 1988 SPE Annual Technical Conference and Exhibition, Houston, Oct. 2-5.
24. Sandiford, B.B. and Graham, G.A.: "Injection of Polymer Solutions in Producing Wells," *AIChE Symposium Series*, (1973) **69**, No. 127, 38.
25. Schneider, F.N. and Owens, W.W.: "Steady-State Measurements of Relative Permeability for Polymer/Oil Systems," *SPEJ* (Feb. 1982) 79.
26. Sparlin, D.D.: "An Evaluation of Polyacrylamides for Reducing Water Production," *JPT* (Aug. 1976) 906-914.

27. White, J.L., Goddard, J.E., and Phillips, H.M.: "Use of Polymers To Control Water Production in Oil Wells," *JPT* (Feb. 1973) 143-150.
28. Zaitoun, A. and Kohler N.: "Two-Phase Flow Through Porous Media: Effect of an Adsorbed Polymer Layer," paper SPE 18085 presented at the 1988 SPE Annual Technical Conference and Exhibition, Houston, Oct. 2-5.
29. Zaitoun, A. and Kohler N.: "Thin Polyacrylamide Gels for Water Control in High-Permeability Production Wells" paper SPE 22785 presented at the 1991 SPE Annual Technical Conference and Exhibition, Dallas, Oct. 6-9.
30. Seright, R.S., Liang, J., and Sun, H.: "Gel Treatments in Production Wells with Water-Coning Problems," *In Situ* (1993) 17, No. 3, 243-272.
31. Liang, J., Lee, R.L., and Seright, R.S.: "Gel Placement in Production Wells," *SPEPF* (Nov. 1993) 276-284; *Trans.*, AIME 295.
32. Dawe, R.A. and Zhang, Y.: "Mechanistic Study of the Selective Action of Oil and Water Penetrating into a Gel Emplaced in a Porous Medium," *Journal of Petroleum Science and Engineering* (1994) 12, 113-125.
33. Zaitoun, A. and Kohler N.: "Modification of Water/Oil and Water/Gas Relative Permeabilities After Polymer Treatment of Oil or Gas Wells," *In Situ* (1989) 13, No. 1&2, 55-77.
34. Zaitoun, A. and Potie, B.: "Limiting Conditions for the Use of Hydrolyzed Polyacrylamide in Hard Brines Containing Divalent Ions," paper SPE 11785 presented at the 1983 International Symposium on Oilfield Chemistry, Denver, June 1-3.
35. Doughty, D. and Tomutsa, L.: "Status Report of Investigation of Wettability by NMR Microscopy and Spin Lattice Relaxation," NIPER 720, Sept. 1993.
36. Bae, J.H., Chambers, K.T., and Lee, H.O.: "Microbial Profile Modification Using Spores," paper SPE 28617 presented at the 1994 SPE Annual Technical Conference and Exhibition, New Orleans, Sept. 25-28.
37. Silver, R.S., Bunting, M., Moon, W.G., and Acheson, W.P.: "Bacteria and Its Use in a Microbial Profile Modification Process," U.S. Patent No. 4,799,545 (1989).
38. Costerton, J.W.F., Cusack, F., and MacLeod, F.A.: "Microbial Process for Selectively Plugging a Subterranean Formation," U.S. Patent No. 4,800,959 (1989).

39. Cusack, F., MacLeod, F.A., Costerton, J.W.F., and Lappin-Scott, H.M.: "Formation and Utilization of Ultramicrobacteria to Enhance Oil Recovery by Selective Plugging," *Proc.*, 1st Inst. Gas Technol. Gas, Oil, & Environ. Biotechnol. Int. Symp. (1988) 343-354.
40. Cusack, F., Costerton, J.W.F., and Novosad, J.: "Ultramicrobacteria Enhance Oil Recovery," *Proc.*, 4th Inst. Gas Technol. Gas, Oil, & Environ. Biotechnol. Int. Symp. (1991) 491-504.
41. Cusack, F., Lappin-Scott, H.M., and Costerton, J.W.F.: "Selective Plugging of High Permeability Zones with Ultramicrobacteria to Enhance Oil Recovery," *Proc.*, 2nd Inst. Gas Technol. Gas, Oil, & Environ. Biotechnol. Int. Symp. (1989) 507-521.
42. Jack, T.R., Diblasio, E., Thompson, B.G., and Ward, V.: "Bacterial Systems for Selective Plugging in Secondary Oil Production," *Proc.*, American Chemical Society Symposium on Biological Pressures Related To Petroleum Recovery, Seattle (1983) 773-784.
43. Jack, T.R. and Stehmeier, L.G.: "Selective Plugging in Watered Out Oil Wells," *Proc.*, US DOE Application of Microorganisms to Petroleum Technology Symposium, Bartlesville (1987) VII-1—VII-13.
44. Knapp, R.M., McInerney, M.J., Coates, J.D., Chisholm, J.L., Menzie, D.E., and Bhupathiraju, V.K.: "Design and Implementation of a Microbially Enhanced Oil Recovery Field Pilot, Payne County, Oklahoma," paper SPE 24818 presented at the 1992 SPE Annual Technical Conference and Exhibition, Washington, DC, Oct. 4-7.
45. Li, Y., Yang, C.Y., Lee, K., and Yen, T.F.: "Subsurface Application of *Alcaligenes eutrophus* for Plugging of Porous Media," *Proc.*, 1992 International Conference on Microbial Enhanced Oil Recovery, 65-77.
46. Chang, M-M., Chung, F.T-H., Bryant, R.S., Gao, H.W., and Burchfield, T.E.: "Modeling and Laboratory Investigation of Microbial Transport Phenomena in Porous Media," paper SPE 22845 presented at the 1991 SPE Annual Technical Conference and Exhibition, Dallas, Oct. 6-9.
47. Silver, R.S. and Bunting, P.M.: "Phosphate Compound That Is Used in a Microbial Profile Modification Process," U.S. Patent 4,906,575 (1990).
48. Ferris, F.G. and Stehmeier, L.G.: "Bacteriogenic Mineral Plugging," U.S. Patent 5,143,155 (1992).
49. Jack, T.R., Ferris, F.G., Stehmeier, L.G., Kantzas A., and Marentette, D.F.: "Bug Rock: Bacteriogenic Mineral Precipitation Systems for Oil Patch Use," *Proc.*, 1992 International Conference on Microbial Enhanced Oil Recovery, 27-35.

50. Clark, J.B. and Jenneman, G.E.: "Nutrient Injection Method for Subterranean Microbial Process," Australia Patent No. 636,518 (1991).
51. Rogers, J.A.: "Microencapsulation of Enhanced Oil Recovery Materials," final report for AOSTRA project #793, Sept. 1990.
52. Lappan, R.E. and Fogler, H.S.: "Effect of Bacterial Polysaccharide Production on Formation Damage," *SPEE* (May 1992) 167-171.
53. Taylor, S.W. and Jaffe, P.R.: "Biofilm Growth and the Related Changes in the Physical Properties of a Porous Medium, 1. Experimental Investigation," *Water Resource Research* (1990) **26**, No. 9, 2153-2159.
54. Crawford, P.B.: "Possible Bacterial Correction of Stratification Problems," *Producers Monthly* (Dec. 1961) 10-11.
55. Crawford, P.B.: "Continual Changes Observed in Bacterial Stratification Rectification," *Producers Monthly* (Feb. 1962) 12.
56. Jenneman, G.E., McInerney, M.J., and Knapp, R.M.: "Microbial Penetration Through Nutrient-Saturated Berea Sandstone," *Appl. Env. Microbial.* (1985) **50**, 383-391.
57. Jenneman, G.E., Knapp, R.M., McInerney, M.J., Menzie, D.E., and Revus, D.E.: "Experimental Studies of In Situ Microbial Enhanced Oil Recovery," *SPEJ* (Feb. 1984).
58. Seright, R.S. and Martin, F.D.: "Fluid Diversion and Sweep Improvement with Chemical Gels in Oil Recovery Processes," second annual report (DOE/BC/14447-10), Contract No. DE-FG22-89BC14447, U.S. DOE (Nov. 1991) 61-110.
59. Thomas, C.P., Duvall, M.L., Robertson, E.P., Barrett, K.B., and Bala, G.A.: "Surfactant-Based EOR Mediated by Naturally Occurring Microorganisms," *SPEE* (Nov. 1993) 285-291.
60. Bryant, R.S. and Douglas J.: "Evaluation of Microbial Systems in Porous Media for Enhanced Oil Recovery," *SPEE* (May 1988) 489.
61. Dullien, F.A.L.: *Porous Media: Fluid Transport and Pore Structure*, Academic Press, London (1979) 170-171.
62. Orr, F.M. Jr. and Taber, J.J.: "Displacement of Oil by Carbon Dioxide," Final report, DOE/BC/10331-13, U.S. DOE (March 1984), 163-178.

63. Thomeer, J.H. and Abrams, A.: "A Shallow Plugging-Selective Re-Entry Technique for Profile Correction," *JPT* (May, 1977) 571-578.
64. Patton, J.T., Holbrook, S.T., and Hsu, W.: "Rheology of Mobility-Control Foams," *SPEJ* (June, 1983) 456-460.
65. Holm, L.W.: "The Mechanism of Gas and Liquid Flow Through Porous Media in the Presence of Foam," *SPEJ* (Dec. 1968) 359-369.
66. Lee, H.O., Heller, J.P., and Hoefler, A.M.W.: "Change in Apparent Viscosity of CO<sub>2</sub>-Foam With Rock Permeability," *SPEJ* (Nov. 1991) 421-428.
67. Mitchell, B.J.: "*Viscosity of Foam*," PhD dissertation, U. of Oklahoma (1969).
68. Ettinger, R.A. and Radke, C.J.: "Influence of Foam Texture on Steady Foam Flow in Berea Sandstone," *SPEJ* (Feb. 1992) 83-90.
69. Huh, D.G. and Handy, L.L.: "Comparison of Steady and Unsteady-State Flow of Gas and Foaming Solution in Porous Media," paper SPE 15078, presented at the 1986 California Regional Meeting, Oakland, April 2-4.
70. deVries, A.S. and Wit, K.: "Rheology of Gas/Water Foam in Quality Range Relevant to Steam Foam," *SPEJ* (May 1990) 185-192.
71. Lee, H.O. and Heller, J.P.: "Laboratory Measurements of CO<sub>2</sub>-Foam Mobility," *SPEJ* (May 1990) 193-197.
72. Chou, S.L.: "Percolation Theory of Foam in Porous Media," paper SPE 20239 presented at the 1990 SPE/DOE Symposium on Enhanced Oil Recovery, Tulsa, April 22-25.
73. Khatib, Z.I., Hirasaki, G.J., and Falls, A.H.: "Effects of Capillary Pressure on Coalescence and Phase Mobilities in Foams Flowing Through Porous Media," paper SPE 15442 presented at the 1986 SPE Annual Technical Conference and Exhibition, New Orleans, Oct. 5-8.
74. Seright, R.S. and Martin, F.D.: "Fluid Diversion and Sweep Improvement with Chemical Gels in Oil Recovery Processes," first annual report, DOE/BC/14447-8, U.S. DOE (June 1991) 51-54.
75. Seright, R.S. and Martin, F.D.: "Fluid Diversion and Sweep Improvement with Chemical Gels in Oil Recovery Processes," final report, DOE/BC/14447-15, U.S. DOE (Sept. 1992) 77-93.

76. Flumerfelt, R.W., Chen, H.L., Ruengphrathungsuk, W., Chung, T.K., Hsu, W.F., and Ke, M.J.: "Capillary and Trapping Phenomena of Foam in Porous Media," *AICHE EOR Symposium Series*, **87**, (1991).
77. Sun, H.: "*Gel Applications in Production Wells*," PhD Dissertation, New Mexico Institute of Mining and Technology, Socorro, NM, (May 1994).
78. Kovseck, A.R. and Radke, C.J.: "Fundamentals of Foam Transport in Porous Media," in *Foams: Fundamentals and Applications in the Petroleum Industry*, Schramm, L.L., ed, *Advances in Chemistry Series*, **242**, American Chemical Society, Washington, D.C. (1994) 115-163.
79. Friedmann, F., Chen, W.H., and Gauglitt, P.: "Experimental and Simulation Study of High-Temperature Foam Displacement in Porous Media," *SPE* (Feb. 1991) 37-45.
80. Zerhboub, M., Touboul, E., Ben Naceur, K., and Thomas, R.L.: "Matrix Acidizing: A Novel Approach to Foam Diversion," paper SPE 22854 presented at the 1991 Annual Technical Conference and Exhibition of the SPE, Dallas, Oct. 6-9.
81. Falls, A.H., Musters, J.J., and Ratulowski, J.: "The Apparent Viscosity of Foam in Homogeneous Bead Packs," *SPE* (May 1989) 155-164.
82. Kuehne, D.L., Frozier, R.H., Cantor, J., and Horn, W.: "Evaluation of Surfactants for CO<sub>2</sub>-Mobility Control in Dolomite Reservoirs," paper SPE 24177 presented at 1992 SPE/DOE Symposium on Enhanced Oil Recovery, Tulsa, April 22-24.
83. Prieditis, J. and Paulett, G.S.: "CO<sub>2</sub> Foam Mobility Tests at Reservoir Conditions in San Andres Cores," paper SPE 24178 presented at the 1992 SPE/DOE Symposium on Enhanced Oil Recovery, Tulsa, April 22-24.
84. Seright, R.S.: "Effect of Rheology on Gel Placement," *SPE* (May, 1991) 212-218.
85. Chou, S.I.: "Conditions for Generation of Foam in Porous Media," paper SPE 22628 presented at the 1991 SPE Annual Technical Conference and Exhibition, Dallas, Oct. 6-9.
86. Rossen, W.R.: "Rheology of Foam in Porous Media at Limiting Capillary Pressure," *Revue de L'institut Francais du pe'trole*, **47**, No. 1, (Janvier-Fevrier 1992).
87. Crawford, H.R., Neil, G.H., Bucy, B.J., and Crawford, P.B.: "Carbon Dioxide: A Multipurpose Additive for Effective Well Stimulation," *JPT* (March 1964) 237-242.
88. Holm, L.W. and Josendal, V.A.: "Mechanisms of Oil Displacement by Carbon Dioxide," *JPT* (Dec. 1974) 1427-1438.

89. Yaghoobi, H. and Heller, J.P.: "Laboratory Investigation of Parameters Affecting CO<sub>2</sub>-Foam Mobility in Sandstone at Reservoirs Conditions," paper SPE 29168 presented at the 1994 SPE Eastern Regional Meeting, Charleston, Nov. 8-10.
90. Wang, G.C.: "Laboratory Study of CO<sub>2</sub>-Foam Properties and Displacement Mechanisms," paper SPE 12645 presented at the 1984 SPE/DOE Symposium on Enhanced Oil Recovery, Tulsa, April 15-18.
91. Burman, J.W. and Hall, B.E.: "Foam Diverting Technique Improved Sandstone Acid Jobs," *World Oil* (Nov., 1987) 31-36.
92. Persoff, P., Radke, C.J., Pruess, K., Benson, S.M., and Witherspoon, P.A.: "A Laboratory Investigation of Foam Flow in Sandstone at Elevated Pressure," *SPE* (Aug. 1991) 365-371.
93. Kovscek, A.R. and Radke, C.J.: "Comprehensive Description of Transient Foam Flow in Porous Media," presented at the 1993 DOE/NIPER Symposium on Field Applications of Foams for Oil Production, Bakersfield, Feb. 11-12.
94. Rossen, W.R. and Zhou, Z.H.: "Modelling Foam Mobility in Porous Media," paper SPE 22627 presented at the 1991 Annual Technical Conference and Exhibition, Dallas, Oct. 6-9.
95. Kovscek, A.R., Patzek, T.W., and Radke, C.J.: "Mechanistic Prediction of Foam Displacement in Multidimensions: A Population Balance Approach," paper SPE 27789 presented at the 1994 SPE/DOE Symposium on Improved Oil Recovery, Tulsa, April 17-20.
96. Heller, J.P. and Kuntamukkula, M.S.: "Critical Review of the Foam Rheology Literature," *Ind. Eng. Chem. Res.* (1987) **26**, 318-325.
97. Kolb, G.E.: "*Several parameters Affecting the Foam-Drive Process for the Removal of Water from Consolidated Porous media*," MS thesis, Penn State University (1964).
98. Bond, D.C. and Bernard, G.G.: "Rheology of Foams in Porous Media," presented at the 1966 AIChE Annual Meeting, Dallas, Sept. 26-29.
99. Hirasaki, G.J. and Pope, G.A.: "Analysis of Factors Influencing Mobility and Adsorption in Flow of Polymer Solutions Through Porous Media," *SPEJ* (August 1974) 337.

**APPENDIX A**  
**Derivation of Eq. 5.**

This appendix derives Eq. 5, which predicts the distance of gel penetration ( $L_{p2}$ ) into a fracture (Fracture 2) when the gel reaches a distance,  $L_{p1}$ , in an alternative fracture pathway (Fracture 1). Fig. 29 (reproduced below) provides a schematic of the case that we are considering. The two fractures share a common starting point and a common ending point. Generally, Fracture 1 is assumed to be shorter ( $L_{f1}$ ) and more permeable ( $k_1$ ) than Fracture 2 (with an effective length of  $L_{p2}$  and an effective permeability of  $k_2$ ).

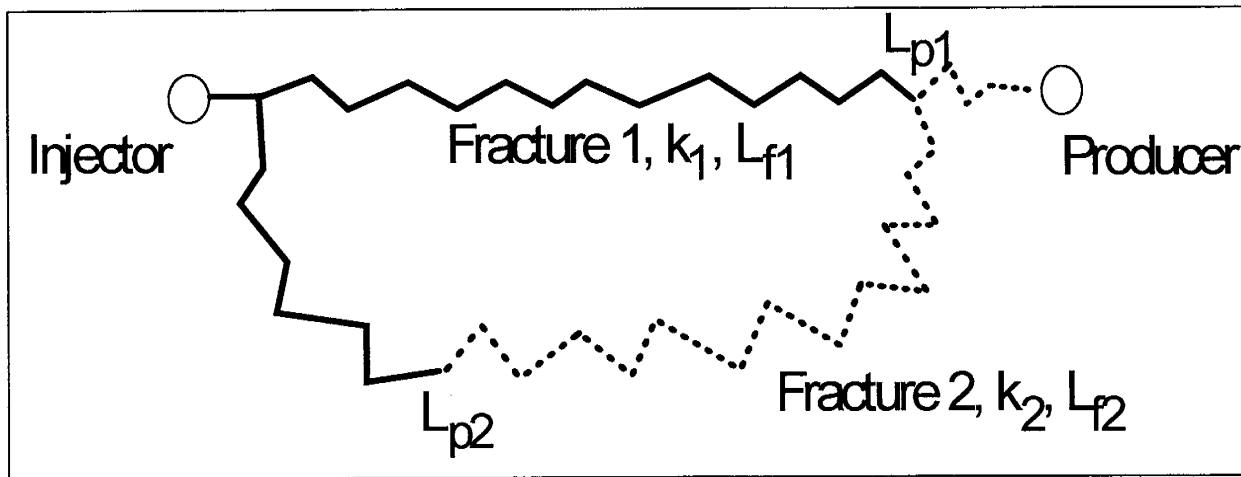


Fig. 29. Schematic of an injector-producer pair connected by two fractures.

In the simple model developed here, we focus on flow of preformed gels through the fractures. These gels cannot propagate through porous rock, so we only consider flow through the fractures. However, we do account for gel dehydration and the retardation of gel propagation through the propagation delay factor,  $a_r$ .

Some of the assumptions in our derivation are as follows:

1. Fluids are incompressible.
2. Displacement is miscible and piston-like.
3. Dispersion, capillary effects, and gravity effects are negligible.
4. All factors that can retard gel propagation (such as dehydration, leakoff, adsorption, and mechanical entrapment) are included in the propagation delay factor,  $a_r$ .
5. In a given fracture,  $a_r$ ,  $k$ ,  $w_f$  (fracture width),  $h_f$  (fracture height), and  $F_r$  (gel resistance factor) are constant. (These parameters may have different values in different fractures.)
6. Flow of gel in a given fracture is effectively linear.
7. The fractures are initially filled with fluids with water-like viscosities.

Since Fractures 1 and 2 have common starting and ending points, they experience the same total pressure drop,  $\Delta p$ , between these points. In Fracture 1, let the gel (with a resistance factor,  $F_{r1}$ ) penetrate to a distance  $L_{p1}$ .

$$\Delta p = \left( \frac{q_1 \mu_w}{k_1 h_{f1} w_{f1}} \right) [F_{r1} L_{p1} + L_{f1} - L_{p1}] \quad (A1)$$

In Eq. A1,  $q_1$  is the gel volumetric flow rate in Fracture 1,  $h_{f1}$  is the height of Fracture 1,  $w_{f1}$  is the width of Fracture 1, and  $\mu_w$  is the viscosity of water. The volumetric flow rate for gel,  $q_1$ , is related to the rate of propagation of the gel front,  $d(L_{p1})/dt$ , by Eq. A2.

$$q_1 = (h_{f1} w_{f1} \phi_{f1}) (1 + a_{r1}) \frac{d(L_{p1})}{dt} \quad (A2)$$

Substituting Eq. A2 into Eq. A1 yields Eq. A3.

$$\Delta p = \left[ \frac{\phi_{f1} (1 + a_{r1}) \mu_w}{k_1} \right] [F_{r1} L_{p1} + L_{f1} - L_{p1}] \frac{d(L_{p1})}{dt} \quad (A3)$$

A similar equation (Eq. A4) applies to gel propagation through Fracture 2,

$$\Delta p = \left[ \frac{\phi_{f2} (1 + a_{r2}) \mu_w}{k_2} \right] [F_{r2} L_{p2} + L_{f2} - L_{p2}] \frac{d(L_{p2})}{dt} \quad (A4)$$

where the subscript, 2, refers to properties in Fracture 2. Equating Eqs. A3 and A4 gives

$$\left[ \frac{\phi_{f1} (1 + a_{r1})}{k_1} \right] [(F_{r1} - 1)L_{p1} + L_{f1}] d(L_{p1}) = \left[ \frac{\phi_{f2} (1 + a_{r2})}{k_2} \right] [(F_{r2} - 1)L_{p2} + L_{f2}] d(L_{p2}) \quad (A5)$$

Integrating Eq. A5 leads to Eq. A6.

$$\left[ \frac{\phi_{f1} (1 + a_{r1})}{k_1} \right] \left[ \frac{(F_{r1} - 1)L_{p1}^2}{2} + L_{f1} L_{p1} \right] = \left[ \frac{\phi_{f2} (1 + a_{r2})}{k_2} \right] \left[ \frac{(F_{r2} - 1)L_{p2}^2}{2} + L_{f2} L_{p2} \right] \quad (A6)$$

Using the quadratic equation to solve for  $L_{p2}/L_{p1}$  yields Eq. A7.

$$\frac{L_{p2}}{L_{p1}} = \frac{\left[ \left( \frac{L_{f2}}{L_{p1}} \right)^2 + 2 (F_{r2} - 1) \left( \frac{k_2 \phi_{f1}}{k_1 \phi_{f2}} \right) \left( \frac{1 + a_{r1}}{1 + a_{r2}} \right) \left( \frac{L_{f1}}{L_{p1}} + \frac{F_{r1} - 1}{2} \right) \right]^{0.5} - \frac{L_{f2}}{L_{p1}}}{F_{r2} - 1} \quad (A7)$$

If the effective porosities ( $\phi$ ) for the two fractures are similar, Eq. A7 reduces to Eq. A8, which is identical to Eq. 5.

$$\frac{L_{p2}}{L_{p1}} = \frac{\left[ \left( \frac{L_{f2}}{L_{p1}} \right)^2 + 2 (F_{r2} - 1) \left( \frac{k_2}{k_1} \right) \left( \frac{1 + a_{r1}}{1 + a_{r2}} \right) \left( \frac{L_{f1}}{L_{p1}} + \frac{F_{r1} - 1}{2} \right) \right]^{0.5} - \frac{L_{f2}}{L_{p1}}}{F_{r2} - 1} \quad (A8)$$

**APPENDIX B**  
**Data Supplement for Chapter 4**

Table B-1a. Summary of Endpoint Water and Oil Mobilities Before Treatment  
(Core SSH-91, High-Permeability Berea Sandstone, Strongly Water-Wet, 41°C)

$(k/\mu)_w$ , md/cp @ $S_w=1.0$	$(k/\mu)_o$ , md/cp @ $S_{wr}=0.30$	$(k/\mu)_w$ , md/cp @ $S_{or}=0.33$	$(k/\mu)_o$ , md/cp @ $S_{wr}=0.31$
754	424	149	431

Table B-1b. Summary of Endpoint Water and Oil Mobilities Before Treatment  
(Core SSH-92, High-Permeability Berea Sandstone, Strongly Water-Wet, 41°C)

$(k/\mu)_w$ , md/cp @ $S_w=1.0$	$(k/\mu)_o$ , md/cp @ $S_{wr}=0.26$	$(k/\mu)_w$ , md/cp @ $S_{or}=0.37$	$(k/\mu)_o$ , md/cp @ $S_{wr}=0.23$
800	473	124	440

Table B-1c. Summary of Endpoint Water and Oil Mobilities Before Treatment  
(Core SSL-100, Low-Permeability Berea Sandstone, Strongly Water-Wet, 41°C)

$(k/\mu)_w$ , md/cp @ $S_w=1.0$	$(k/\mu)_o$ , md/cp @ $S_{wr}=0.32$	$(k/\mu)_w$ , md/cp @ $S_{or}=0.40$
146	77	27

Table B-1d. Summary of Endpoint Water and Oil Mobilities Before Treatment  
(Core SSL-102, Low-Permeability Berea Sandstone, Strongly Water-Wet, 41°C)

$(k/\mu)_w$ , md/cp @ $S_w=1.0$	$(k/\mu)_o$ , md/cp @ $S_{wr}=0.31$	$(k/\mu)_w$ , md/cp @ $S_{or}=0.41$
145	81	24

Table B-1e. Summary of Endpoint Water and Oil Mobilities Before Treatment  
(Core SSL-103, Low-Permeability Berea Sandstone, Strongly Water-Wet, 41°C)

$(k/\mu)_w$ , md/cp @ $S_w=1.0$	$(k/\mu)_o$ , md/cp @ $S_{wr}=0.34$	$(k/\mu)_w$ , md/cp @ $S_{or}=0.38$
154	82	24

Table B-1f. Summary of Endpoint Water and Oil Mobilities Before Treatment  
(Core NB-9, Fused Glass-Bead Core, 41°C)

$(k/\mu)_w$ , md/cp @ $S_w=1.0$	$(k/\mu)_o$ , md/cp @ $S_{wr}$	$(k/\mu)_w$ , md/cp @ $S_{or}$
1,460	820	720

Table B-1g. Summary of Endpoint Water and Oil Mobilities Before Treatment  
(Core NB-11, Fused Glass-Bead Core, 41°C)

$(k/\mu)_w$ , md/cp @ $S_w=1.0$	$(k/\mu)_o$ , md/cp @ $S_{wr}$	$(k/\mu)_w$ , md/cp @ $S_{or}$
1,380	750	590

Table B-1h. Summary of Endpoint Water and Oil Mobilities Before Treatment  
(Core NB-12, Fused Glass-Bead Core, 41°C)

$(k/\mu)_w$ , md/cp @ $S_w=1.0$	$(k/\mu)_o$ , md/cp @ $S_{wr}$	$(k/\mu)_w$ , md/cp @ $S_{or}$
1,300	710	623

Table B-1i. Summary of Endpoint Water and Oil Mobilities Before Treatment  
(Core NB-16, Fused Glass-Bead Core, 41°C)

$(k/\mu)_w$ , md/cp @ $S_w=1.0$	$(k/\mu)_o$ , md/cp @ $S_{wr}$	$(k/\mu)_w$ , md/cp @ $S_{or}$	$(k/\mu)_o$ , md/cp @ $S_{wr}$
1,300	720	660	727

Table B-1j. Summary of Endpoint Water and Oil Mobilities Before Treatment  
(Core NB-17, Fused Glass-Bead Core, 41°C)

$(k/\mu)_w$ , md/cp @ $S_w=1.0$	$(k/\mu)_o$ , md/cp @ $S_{wr}$	$(k/\mu)_w$ , md/cp @ $S_{or}$	$(k/\mu)_o$ , md/cp @ $S_{wr}$
1,448	805	878	800

Table B-1k. Summary of Endpoint Water and Oil Mobilities Before Treatment  
(Core XB-4, Fused Glass-Bead Core, Oil, Xylene, 26°C)

$(k/\mu)_w$ , md/cp @ $S_w=1.0$	$(k/\mu)_o$ , md/cp @ $S_{wr}$	$(k/\mu)_w$ , md/cp @ $S_{or}$	$(k/\mu)_o$ , md/cp @ $S_{wr}$	$(k/\mu)_w$ , md/cp @ $S_{or}$
965	621	514	623	518

Table B-1l. Summary of Endpoint Water and Oil Mobilities Before Treatment  
(Core XB-5, Fused Glass-Bead Core, Oil, Xylene, 26°C)

$(k/\mu)_w$ , md/cp @ $S_w=1.0$	$(k/\mu)_o$ , md/cp @ $S_{wr}$	$(k/\mu)_w$ , md/cp @ $S_{or}$	$(k/\mu)_o$ , md/cp @ $S_{wr}$	$(k/\mu)_w$ , md/cp @ $S_{or}$
960	620	513	614	509

Table B-1m. Summary of Endpoint Water and Oil Mobilities Before Treatment  
(Core XB-6, Fused Glass-Bead Core, Oil, 3,5-Bis(trifluoromethyl)bromobenzene, 26°C)

$(k/\mu)_w$ , md/cp @ $S_w=1.0$	$(k/\mu)_o$ , md/cp @ $S_{wr}$	$(k/\mu)_w$ , md/cp @ $S_{or}$
1,100	453	540

Table B-2a. Summary of Residual Resistance Factors ( $F_{rrw}$ ,  $F_{rro}$ )-Core SSL-100  
 Core: Low-Permeability Berea Sandstone  
 Polymer: 0.5% HPAM (Alcoflood 935) + 1% NaCl

1st waterflood after polymer treatment		
Flux, ft/d	$F_{rrw}$ (1st short core section)	$F_{rrw}$ (Center core section)
3.15	3	3.6
1.575	4.7	3.9
0.787	7.3	4
0.394	11.1	3.9
0.197	18	3.9
Average $F_{rrw}$ (across center section) = 4		
1st oilflood after polymer treatment		
Flux, ft/d	$F_{rro}$ (1st short core section)	$F_{rro}$ (Center core section)
6.3	5.1	3.9
3.15	7.2	3.7
1.575	4.7	4.6
0.787	4.6	4.6
0.394	4.9	4.7
0.197	5	4.7
6.3	4.1	4.5
Average $F_{rro}$ (across center section) = 5		
2nd waterflood after polymer treatment		
Flux, ft/d	$F_{rrw}$ (1st short core section)	$F_{rrw}$ (Center core section)
12.6	1	2.4
6.3	1.2	2.6
3.15	1.9	2.6
1.575	5.5	2.7
0.787	12	2.7
0.394	12.8	2.6
0.197	13.5	2.4
12.6	1	2.3
Average $F_{rrw}$ (across center section) = 3		

Table B-2a. Summary of Residual Resistance Factors ( $F_{rrw}$ ,  $F_{rro}$ )-Core SSL-100 (Cont'd)  
 Core: Low-Permeability Berea Sandstone  
 Polymer: 0.5% HPAM (Alcoflood 935) + 1% NaCl

2nd oilflood after polymer treatment		
Flux, ft/d	$F_{rro}$ (1st short core section)	$F_{rro}$ (Center core section)
12.6	2.8	2.9
6.3	4.9	2.6
3.15	2.9	2.8
1.575	3.3	2.8
0.787	2.4	2.9
0.394	1	3.1
0.197	1	3
12.6	3.1	2.9
Average $F_{rro}$ (across center section) = 3		

Table B-2b. Summary of Residual Resistance Factors ( $F_{rrw}$ ,  $F_{rro}$ )-Core SSL-102  
 Core: Low-Permeability Berea Sandstone  
 Polymer: 0.1% HPAM (Alcoflood 1175A) + 1% NaCl

1st waterflood after polymer treatment		
Flux, ft/d	$F_{rrw}$ (1st short core section)	$F_{rrw}$ (Center core section)
6.3	2.5	3.5
3.15	2.9	4.1
1.575	3.5	4.9
0.787	6.7	8
0.394	13.2	10
6.3	5.4	3.4
$F_{rrw}$ (across center section) = $6.7 u^{-0.39}$ , $r=0.9636$		
1st oilflood after polymer treatment		
Flux, ft/d	$F_{rro}$ (1st short core section)	$F_{rro}$ (Center core section)
6.3	3.6	4.2
3.15	4.3	4.7
1.575	4.7	3.7
Average $F_{rro}$ (across center section) = 4		
2nd waterflood after polymer treatment		
Flux, ft/d	$F_{rrw}$ (1st short core section)	$F_{rrw}$ (Center core section)
6.3	2.7	2.9
3.15	6.9	3.7
1.575	10	4.2
0.787	14	3.9
0.394	25	4.1
Average $F_{rrw}$ (across center section) = 4		

Table B-2c. Summary of Residual Resistance Factors ( $F_{rrw}$ ,  $F_{rro}$ )-Core SSL-103  
 Core: Low-Permeability Berea Sandstone  
 Polymer: 0.4% CPAM (Floperm 500P) + 2% KCl

1st waterflood after polymer treatment		
Flux, ft/d	$F_{rrw}$ (1st short core section)	$F_{rrw}$ (Center core section)
0.197	200	148
0.098	275	220
0.05	222	450
0.05	370	518
0.025	418	910
0.013	460	1150
$F_{rrw}$ (across center section) = $39 u^{-0.81}$ , $r=0.9849$		
1st oilflood after polymer treatment		
Flux, ft/d	$F_{rro}$ (1st short core section)	$F_{rro}$ (Center core section)
1.575	5.9	16.3
6.3	2.7	6.9
Final $F_{rro}$ (across center section) = 7		
2nd waterflood after polymer treatment		
Flux, ft/d	$F_{rrw}$ (1st short core section)	$F_{rrw}$ (Center core section)
1.575	1.7	15.1
0.787	7.4	20.2
0.394	11	26.8
0.197	15	48
$F_{rrw}$ (across center section) = $18 u^{-0.54}$ , $r=0.982$		
2nd oilflood after polymer treatment		
Flux, ft/d	$F_{rro}$ (1st short core section)	$F_{rro}$ (Center core section)
3.15	3.9	12.5
6.3	2.6	7.4
Final $F_{rro}$ (across center section) = 7		

## APPENDIX C

### Supplement to Chapter 7: CO<sub>2</sub>-Foam Results

This appendix supplements Chapter 7 by documenting our studies of the behavior of carbon-dioxide foams. The equipment and experimental procedures are described in Chapter 7. Fig. C-1 shows mobilities during carbon-dioxide-foam generation in a 482-md Berea core. Three runs were performed at different flow rates. The backpressure was 1,000 psig. The quality of the foam was 80% unless otherwise mentioned. Foam was first generated at 50 ml/hr (stars in Fig. C-1). The drop in mobility from 30 to 10 md/cp was speculated to be due to iron dissolution and precipitation processes. The flow rate was then changed to 10 ml/hr (open diamonds) and finally to 500 ml/hr (open circles). For two of these runs, the mobility leveled out (at least temporarily) after approximately 1 PV of foam formulation was injected. The stabilization of the mobility indicates that the capillary pressure was maintained at the critical capillary pressure (i.e., the critical water saturation was reached<sup>85,86</sup>). Steady-state foam flow was observed after this stabilization of mobility. Fig. C-2 shows the results for foam generation performed after the first set of experiments at the same backpressure (1,000 psig). Foam was injected in a sequence of decreasing rates (i.e., 700, 350, 100, 40, and 10 ml/hr). Achieving steady state for this set of experiments required more pore volumes compared to the first set of experiments. During CO<sub>2</sub>-foam generation, an orange-colored effluent was observed. Rust was suspected to be the cause of this color. When the equipment was checked for rust, no rust was seen on the equipment or on the core endcaps. Therefore, we suspected that the Berea core was the source of the produced iron.

Qualitative analyses were conducted to determine the source of the iron. Seven flasks were prepared that contained the following:

- a. Flask 1: Surfactant solution + CO<sub>2</sub> + Berea sandstone (crushed).
- b. Flask 2: Surfactant + CO<sub>2</sub>.
- c. Flask 3: Surfactant + Berea sandstone (crushed).
- d. Flask 4: Surfactant + N<sub>2</sub> + Berea sandstone (crushed).
- e. Flask 5: Surfactant + CO<sub>2</sub> + Indiana limestone (crushed).
- f. Flask 6: Brine + CO<sub>2</sub> + Berea sandstone (crushed).
- g. Flask 7: Surfactant + CO<sub>2</sub> + alloy used in casting.

The surfactant concentration was 0.3% by weight. CO<sub>2</sub> or N<sub>2</sub> gas was bubbled directly into the flasks (p=10 psi) for 10-15 minutes. All flasks were tightly closed and placed in the temperature-controlled box (40°C). After approximately 12 hours, the color in Flask 1 started to change, and an orange precipitate was seen. After about 24 hours, the color in Flask 6 changed to yellow and a precipitate was also detected, but it was lighter colored than that in Flask 1. The solution in Flask 7 changed color after two days, but no precipitate was seen until approximately one week had passed. All other flasks were colorless, and no precipitate was observed for months. Effluent chemical analyses for Flask 1 (performed by NM Bureau of Mines laboratory) confirmed the presence of iron (21 ppm), zinc (1.7 ppm), and manganese (1.5 ppm). The results indicated that

the Berea sandstone was the primary source of the iron. This may explain why the steady state required a longer time to be established in the second set of experiments. Two processes were taking place. We speculated that an iron dissolution process preceded foam generation. This may have been responsible for the mobility increase illustrated in Fig. C-2. Increases in mobility were seen for foam generated at velocities of 27 and 54 ft/day. No such increase in mobility was seen with foam generated at lower velocities. This effect of carbon-dioxide foam on rock has been observed by others during coreflood experiments.<sup>87,88</sup> Carbon dioxide has also been reported to increase the injectivity of water by direct action on the carbonate portions of the rock and by a stabilizing action on clays in the rock.<sup>87,88</sup>

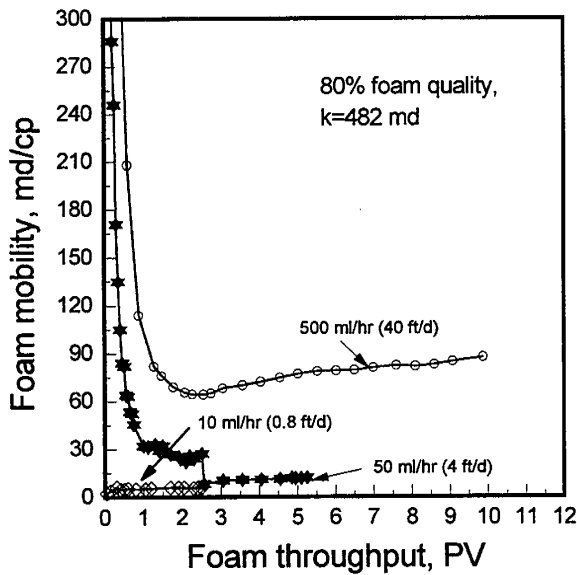


Fig. C-1. CO<sub>2</sub>-foam generation.  
First set of experiments.

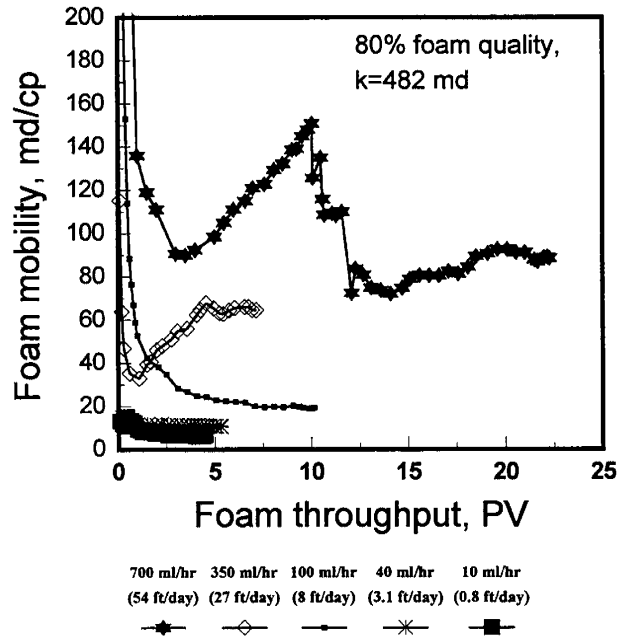


Fig. C-2. CO<sub>2</sub>-foam generation.  
Second set of experiments.

Fig. C-3 illustrates the steady-state values for variation of mobility with velocity for CO<sub>2</sub>-foams. Three sets of experiments were shown in this figure; two sets of experiments were performed using a backpressure of 1,000 psig and the third was performed using a backpressure of 1,500 psig. The rheology data can be correlated by a power-law model as follows:

Backpressure = 1,000 psig (increasing flow rate):

$$\lambda_f = 6.6 u^{0.64} \tag{C-1}$$

Backpressure = 1,000 psig (decreasing flow rate):

$$\lambda_f = 5.5 u^{0.68} \tag{C-2}$$



Our results for the CO<sub>2</sub>-foam mobility performed in the 482-md core were comparable to the results reported by Yaghoobi and Heller<sup>89</sup> in a 490-md Berea core (for the surfactant CD 1040). Yaghoobi and Heller performed CO<sub>2</sub>-foam generation at a backpressure of 2,100 psig for several surfactant solutions as shown in Table C-1 for velocities between 0.8 and 8 ft/day.

Table C-1. Comparison of Carbon-Dioxide-Foam Mobilities

Darcy velocity, ft/day	Mobility measured by Yaghoobi and Heller <sup>89</sup> , md/cp			Mobility measured in the present work, md/cp
	Chaser <sup>®</sup> CD 1040	Enrodet <sup>®</sup> X2001	Chaser <sup>®</sup> CD 1050	Bioterge <sup>®</sup> AS-40
0.8	4.5	4	3	5
3.1	7.5	4	4	8
8	13	5	7	19

The mobility of the foam measured at a backpressure of 1,000 psig was higher than that measured at a backpressure of 1,500 psig. This behavior was not surprising since as the pressure increases, CO<sub>2</sub> becomes more dense and foams formed with dense CO<sub>2</sub> are expected to be more viscous.<sup>78,90</sup>

The reproducibility of our experiment is demonstrated in Fig. C-4. Four experimental runs were performed using carbon dioxide. The total flow rate was 500 ml/hr (40 ft/day), and the foam quality was 80%. Run 1 was performed first, as shown in Fig. C-1. Run 2 was performed after foam had been generated at different flow rates, as shown in Fig. C-2. After Run 2, 16 PV of nitrogen foam were injected at 500 ml/hr. Then, Run 3 was performed using carbon dioxide. Finally, Run 4 was performed directly after Run 3. A minimum in mobility was seen with Run 1 and Run 2. When carbon-dioxide foam was injected after injection of nitrogen foam (Run 3), the mobility appeared to stabilize. During the injection of nitrogen foam, the effluent color became colorless after 6 to 10 PV of injection, indicating that iron dissolution stopped or slowed.

When carbon-dioxide foam was injected following the nitrogen foam, no minimum in the mobility was seen. These CO<sub>2</sub>-foam results are shown in Fig. C-5. Our interpretation was consistent with that of Burman and Hall<sup>91</sup> concerning foam behavior during stimulation processes. They reported that foam transported released fines away from the near-wellbore area.

Fig. C-6 shows that under similar conditions, nitrogen foam mobility was about four times lower than carbon-dioxide foam mobility (at a backpressure of 1,500 psig). This difference between carbon-dioxide and nitrogen foams was reported by Chou.<sup>85</sup> Chou conducted experimental work in Berea sandstone cores using Chaser CD1040 surfactant. His results showed nitrogen foam to have a mobility five to ten times lower than that for carbon-dioxide foam. Chou<sup>72,85</sup> attributed this difference to a lower gas-liquid surface tension for CO<sub>2</sub>-foam than for N<sub>2</sub>-foam. Chou stated that the mobility of foam increased with decreasing gas-liquid surface tension. He measured the

surface tension for both systems (i.e., CO<sub>2</sub> and N<sub>2</sub>) and found the surface tension for CO<sub>2</sub> to be eight times lower than that for N<sub>2</sub>.

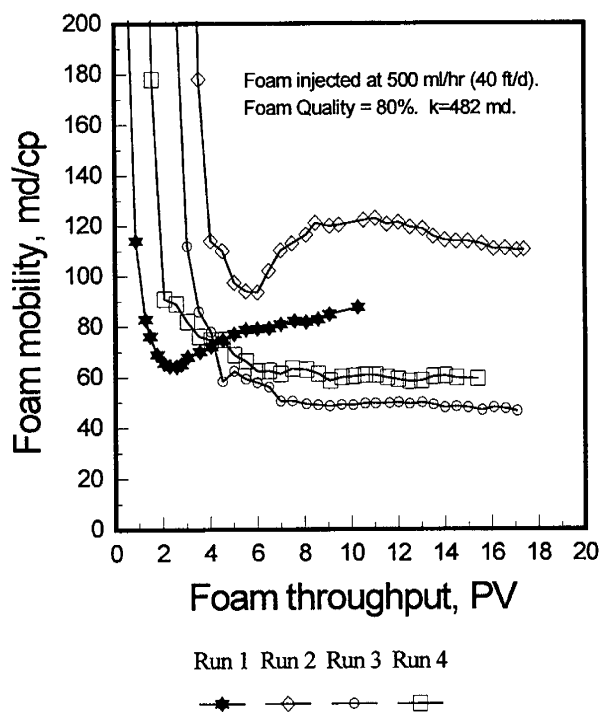


Fig. C-4. Reproducibility of CO<sub>2</sub>-foam generation.

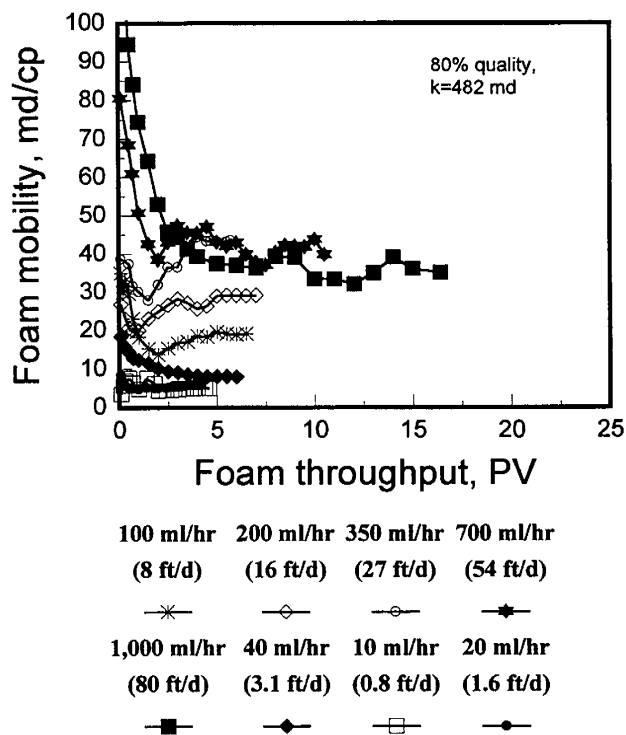


Fig. C-5. Effect of rate and throughput on CO<sub>2</sub>-foam mobilities.

Rossen<sup>86</sup> stated that CO<sub>2</sub>-foams are "weak" compared to nitrogen and steam foams. In view of the minimum pressure gradient for generation and propagation of foam, Rossen<sup>86</sup> speculated that the lamellae do not move from pore to pore, but break and reform at fixed locations. For CO<sub>2</sub>-foams, a minimum pressure gradient from 0.8 to 1.4 psi/ft was estimated for both foam generation and propagation. For other foams, this minimum pressure gradient varied from 5 to 11 psi/ft. Lower gas/liquid surface tension was also claimed to be the cause of the lower estimates for CO<sub>2</sub>-foams. Our results suggest a new method for improving CO<sub>2</sub>-foam performance for direct enhancement of sweep efficiency in Berea sandstone formations. This method involves alternately injecting CO<sub>2</sub> and N<sub>2</sub> foams. After a specified time of carbon-dioxide-foam injection (and if the mobility starts to increase because of iron dissolution), N<sub>2</sub>-foam may be injected for a limited period of time before resuming CO<sub>2</sub>-foam generation. Fig. C-5 suggests that a lower CO<sub>2</sub>-foam mobility will be achieved after injection of N<sub>2</sub>-foam. Nitrogen-foam, which has lower mobility compared to the CO<sub>2</sub>-foam, appeared to stabilize the fines that resulted from the iron dissolution.

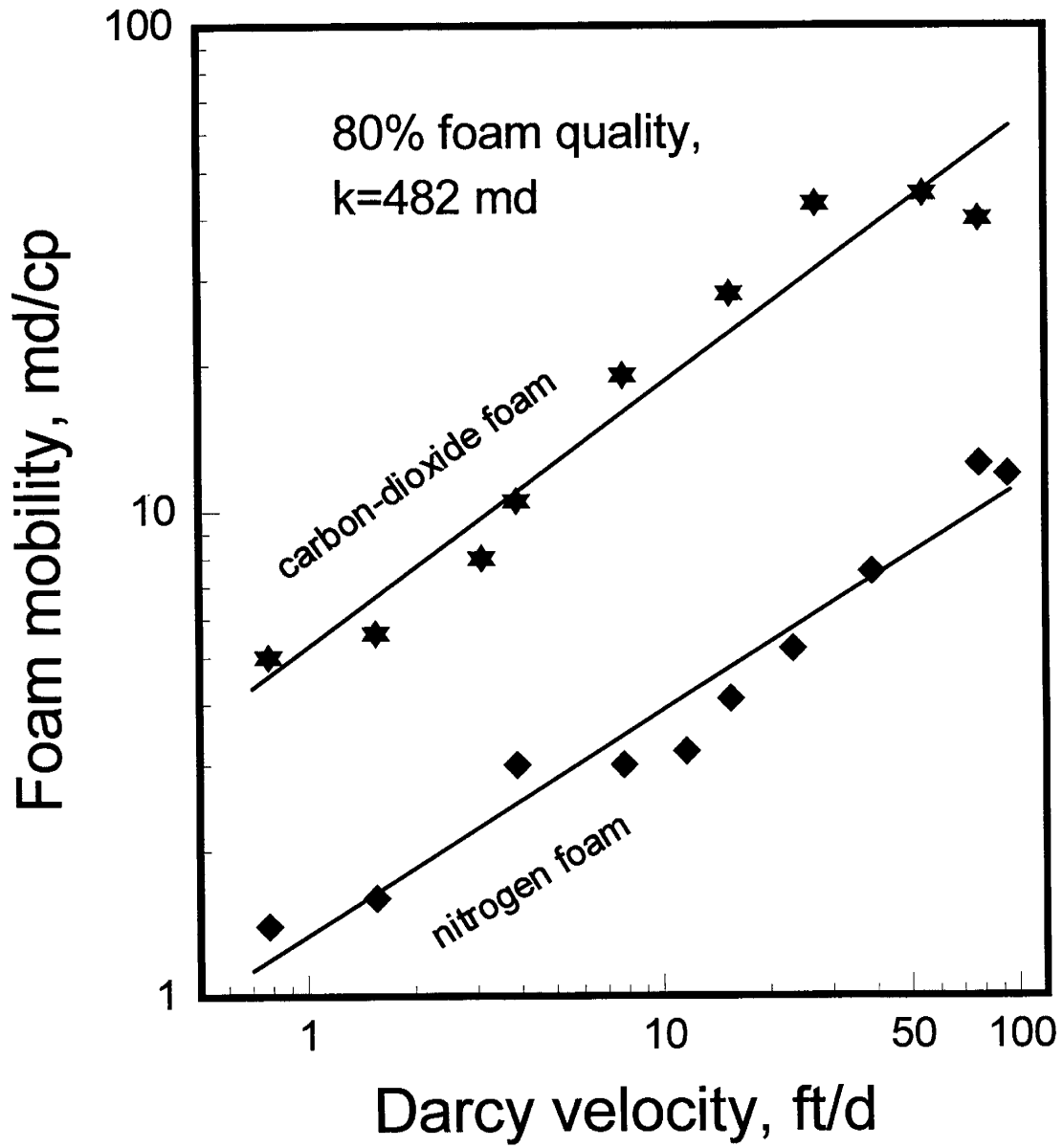


Fig. C-6. Mobility versus velocity for nitrogen and carbon-dioxide foams.

**Residual Resistance Factors After Foam Placement.** To study foam persistence to brine injection, CO<sub>2</sub>-foam was generated in the 482-md core at 40 ml/hr (80% quality). The backpressure was 1,500 psig. After steady-state foam generation was observed, both gas and surfactant-solution injection were stopped, and surfactant-free brine was injected at different flow rates, as shown in Table C-2. This procedure was repeated for foam generation at 1,000 ml/hr. F<sub>rr</sub> values decreased as the brine flow rate and the volume throughput increased. There was no significant difference between F<sub>rr</sub> values after placement of foam generated at 40 ml/hr (3.1 ft/day) and that for foam generated at 1,000 ml/hr (80 ft/day).

CO<sub>2</sub>-foam placed under our experimental conditions was quickly washed from the core (Table C-2). During brine injection, gas was seen coming out of the backpressure outlet. After injecting a total of 7.7 PV of brine, residual resistance factor values decreased dramatically (two orders of magnitude decrease).

Table C-2. Brine F<sub>rr</sub> After CO<sub>2</sub>-Foam Generation

Foam generated at 40 ml/hr (80% quality).			Foam generated at 1,000 ml/hr (80% quality).		
Cumulative PV	u, ft/day	F <sub>rr</sub>	Cumulative PV	u, ft/day	F <sub>rr</sub>
0.4	0.08	481	0.5	0.08	408
1.2	0.78	66	1.0	0.78	80
2.2	1.56	8	2.0	1.56	8.4
5.4	3.89	3.3	5.1	3.89	3.9
7.7	7.78	2.1			

## Conclusions

The following conclusions are relevant to carbon-dioxide foams and for the surfactant used [Bio-Terge® AS-40, a 0.3% C<sub>14-16</sub> alpha olefin sulfonate in brine (1% NaCl and 0.1 CaCl<sub>2</sub>)]:

1. From limited results with CO<sub>2</sub>-foams (performed in a 482-md Berea sandstone core and using a foam quality of 80%), N<sub>2</sub>-foam generated under similar conditions produced a mobility approximately four times lower than that of the CO<sub>2</sub>-foam.
2. From the preliminary results, placement of a nitrogen foam after a carbon-dioxide foam appeared to stabilize a subsequently injected carbon-dioxide foam.

**APPENDIX D**  
**Supplement to Chapter 7: Results from Tracer Studies**

This appendix documents the results from tracer studies that were performed during the experiments described in Chapter 7. In this work, constant-rate water-tracer experiments were usually performed before and after foam placement to compare the actual pore volume available for fluid flow and the change in the dispersivity of the core. The tracer solution contained potassium iodide. After foam placement, and after brine was injected at low flow rates (1 to 50 ml/hr), tracer experiments were performed at the same backpressure at which foam was placed (750 psig). Our attempt to perform tracer studies directly after foam generation showed no success because of the large amount of released gas that affected the detector. Table D-1 shows the sequence of steps followed before and during the tracer studies.

Table D-1. Sequence Followed During Tracer Studies

Step	Description
1	Perform tracer studies before foam generation at two or three flow rates (40, 100, and 200 ml/hr).
2	Generate foam at 80% quality (at 50 or 500 ml/hr).
3	Inject brine at 1 ml/hr (0.08 ft/day).
4	Change the brine flow rate to 10 ml/hr.
5	Change the brine flow rate to 20 ml/hr.
6	Change the brine flow rate to 50 ml/hr.
7	Change the brine flow rate to 10 ml/hr. Continue injection until no gas comes out of the backpressure outlet.
8	Change the brine flow rate to 50 ml/hr.
9	Perform the first tracer after foam at flow rate of 40 ml/hr.
10	Inject brine at 100 ml/hr until the tracer is flushed from the core.
11	Perform tracer study at 100 ml/hr.
12	Repeat Steps 10 and 11 with a flow rate of 200 ml/hr

**Tracer Results in 899-md Rock.** Table D-2 shows brine residual resistance factors,  $F_{rr}$ , after  $N_2$ -foam generation at two different flow rates in the 899-md core. Residual resistance factor is defined by Eq. D-1,

$$F_{rr} = \lambda_{brine}(\text{before foam})/\lambda_{brine}(\text{after foam}) \quad (D-1)$$

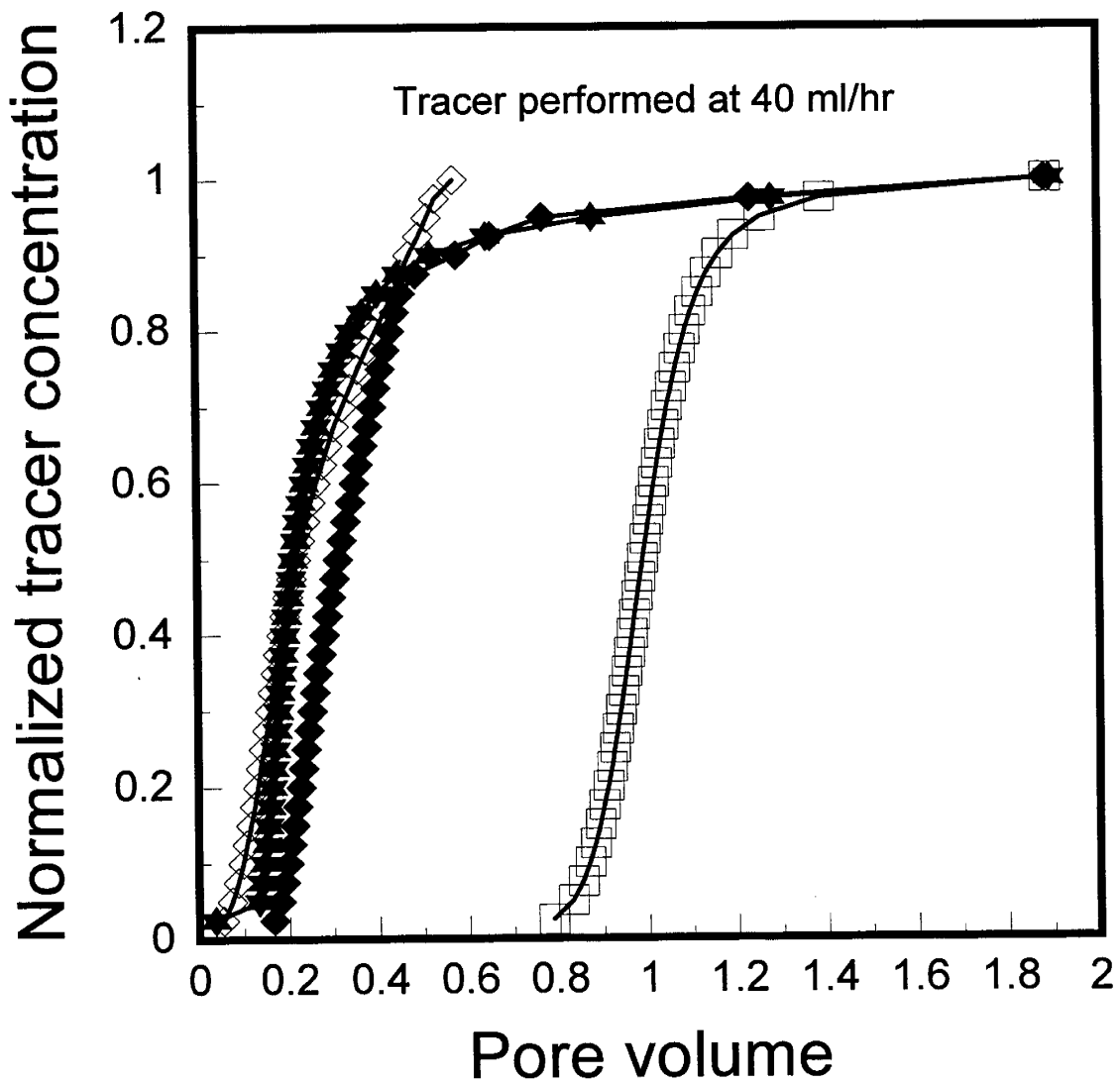
where  $\lambda_{brine}$  was the brine mobility. After 2.6 PV of brine injection, no significant difference was seen between  $F_{rr}$  values for foam generated at 50 ml/hr versus at 500 ml/hr.

Table D-2.  $F_{rr}$  Values Before and During Tracer Studies in the 899-md Core

Cumulative PV of brine	q, ml/hr	u, ft/day	$F_{rr}$ after foam was generated at 50 ml/hr	$F_{rr}$ after foam was generated at 500 ml/hr
1.1	1	0.08	1,356	383
1.6	10	0.8	956	362
2.1	20	1.6	566	209
2.6	50	4	110	117
15.1	10	0.8	14.4	15.2
18.5	50	4	8.2	10.2
20.9	100	8	4	7.2
22	200	16	1.6	2.2
24	100	8	2	1.8
26	50	4	1.8	1.7

Results of the tracer studies are shown in Table D-3. From tracer studies at 40 ml/hr, the fraction of pore volume available for flow ( $V_p/V_{po}$ ) was slightly higher after foam was generated at a flow rate of 500 ml/hr compared to that generated at 50 ml/hr ( $V_p/V_{po}$  was 0.33 after foam generation at 500 ml/hr compared to 0.21 after foam generation at 50 ml/hr). However, when the tracer experiment (after foam generation at 500 ml/hr) was repeated, the  $V_p/V_{po}$  value was close to that after foam at 50 ml/hr (see Fig. D-1). This value was 0.23. Tracer results shown in Table D-3 and Fig. D-2 indicate that foam was affected by both the velocity and the number of pore volumes of brine injected. As the velocity or brine throughput increased, the pore volume available for flow increased. The increase in  $V_p/V_{po}$  probably occurred because gas was produced from the core as the foam collapsed. The foam collapse was mainly attributed to the dilution of the surfactant solution by brine.<sup>78</sup> Performing tracer studies at higher flow rates (100 and 200 ml/hr) resulted in comparable  $V_p/V_{po}$  values for both foams (foam generated at 50 ml/hr and 500 ml/hr). After this flow rate (200 ml/hr), the residual resistance factor remained approximately constant at a value close to 2 (as shown in Table D-2 at cumulative PV from 22 to 26).

The dispersivity ratio,  $\alpha/\alpha_o$ , showed similar trends after foam was generated at two different flow rates (50 and 500 ml/hr). There was an initial increase in the dispersivity ratio as the tracer was performed at a flow rate of 100 ml/hr, compared to the dispersivity ratio for tracer studies performed at 40 ml/hr. After the tracer study at 200 ml/hr, the dispersivity ratio decreased dramatically (approximately 9 times for both cases, Table D-3). Subsequent tracer experiments (performed at 100 ml/hr and 40 ml/hr) showed comparable (low) dispersivity ratios.



After foam at 50 ml/hr    Repeated after foam at 500 ml/hr

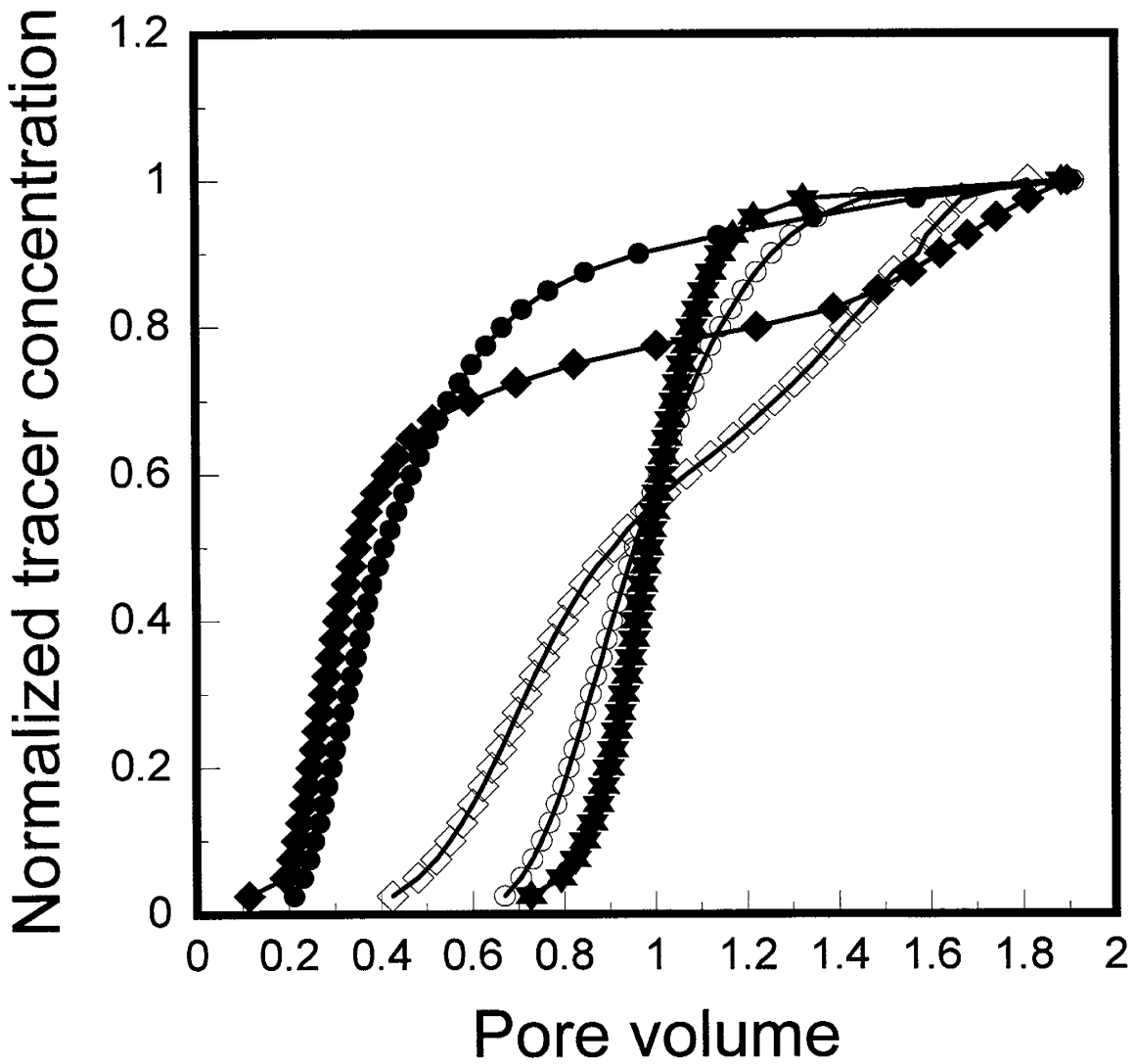


After foam at 500 ml/hr

Before foam



Fig. D-1. Tracer results in the 899-md core, 40 ml/hr.



Tracer flow rate = 100 ml/hr (Before foam)	After foam at 50 ml/hr Tracer at 100 ml/hr	After foam at 500 ml/hr Tracer at 100 ml/hr
◆	◆	●
After foam at 50 ml/hr Tracer at 200 ml/hr	After foam at 500 ml/hr Tracer at 200 ml/hr	
◇	○	

Fig. D-2. Tracer results in the 899-md core, various rates.

Table D-3. Tracer Results in 899-md Core  
(Core ID: FHPSS4)

Status	q, ml/hr	$V_p$	$V_p/V_{p0}$	$\alpha$ , cm	$\alpha/\alpha_0$
Before foam	40	0.989		0.072	
	100	0.986		0.091	
	200	0.984		0.134	
After foam generation at 50 ml/hr	40	0.212	0.21	1.887	26
	100	0.35	0.35	5.25	58
	200	0.905	0.93	0.815	6
	100	1.001	1	0.391	4.3
	40	0.927	0.94	0.301	4.2
After restoring brine mobility	40	0.948		0.098	
	100	1.007		0.112	
	200	1.004		0.138	
After foam generation at 500 ml/hr	40	0.312	0.33	1.298	13.2
	100	0.409	0.41	2.05	18.3
	200	0.956	0.96	0.296	2.1
	100	0.959	0.96	0.21	1.9
	40	0.87	0.92	0.2	2

**Tracer Results in 482-md Rock.** Table D-4 shows results of  $F_{rr}$  measurements performed in the 482-md core before and during tracer experiments for two foams generated at two different flow rates (50 and 500 ml/hr) at 80% quality. No significant difference between  $F_{rr}$  values was seen, except for the low-flow-rate case (1 ml/hr).

Table D-4.  $F_{rr}$  Values Before and During Tracer Studies in the 482-md Core

Cumulative PV of brine	q, ml/hr	u, ft/day	$F_{rr}$ after foam generated at 50 ml/hr	$F_{rr}$ after foam generated at 500 ml/hr
0.5	1	0.08	3,250	6,500
1.5	10	0.78	812	970
2.1	20	1.56	464	382
2.7	50	3.9	144	186
14.5	10	0.8	11	13.6
18.2	50	3.9	6.9	7
22.8	100	7.8	3.2	3.9
26.8	200	15.6		2.6

Table D-5 and Fig. D-3 show results obtained from the tracer studies in the 482-md Berea core. Foam generated at a flow rate of 50 ml/hr and 80 ml/hr appeared to occupy pore volumes comparable to those for foam generated at 500 ml/hr.

Table D-5. Tracer Results in 482-md Core  
(CORE ID: FHPSS1)

Description	q, ml/hr	$V_p$	$V_p/V_{po}$	$\alpha$ , cm	$\alpha/\alpha_o$
Before foam generation.	40	0.98		0.109	
	200	0.98		0.128	
After foam generation at 50 ml/hr.	40	0.38	0.39	4.55	41.7
	100	0.545	0.55	2.08	16.2
After restoring the permeability.	40	0.98		0.154	
	200	0.97		0.168	
After foam generation at 500 ml/hr.	40	0.353	0.36	1.337	8.7
	100	0.517	0.53	3.4	22.1
	200	0.699	0.72	2.2	13.2
After restoring the permeability.	40	0.965		0.28	
After foam generation at 500 ml/hr and injecting 100 PV of brine at 1 ft/day.	13	0.632	0.65	0.81	2.9
After foam generation at 80 ml/hr.	40	0.348	0.36	3.95	14.1

Comparing tracer results performed at an injection rate of 100 ml/hr [after foam generation at two different flow rates (50 and 500 ml/hr)] suggested a similar blocking effect (Fig. D-4). These results are consistent with the results shown in Table D-4. After foam generation at 50 and 500 ml/hr, the residual resistance factor values (just before the tracer experiments, at 18.2 PV in Table D-4) were similar (6.9 and 7).

After foam generation at 50 ml/hr, the dispersivity ratio of the core was 41.7 during a tracer study at 40 ml/hr (see Table D-5). When the tracer flow rate was increased to 100 ml/hr the dispersivity ratio decreased to 16.2, indicating that the foam collapsed. After foam generation at 500 ml/hr, a different trend was observed. The dispersivity ratio was 8.7 for a tracer performed at 40 ml/hr. This value increased when the tracer flow rate was changed to 100 ml/hr. For this foam, the dispersivity ratio decreased when the tracer was performed at a higher flow rate (200 ml/hr). As the flow rate of brine increased, the foam appeared to collapse, resulting in greater  $V_p/V_{po}$  values.

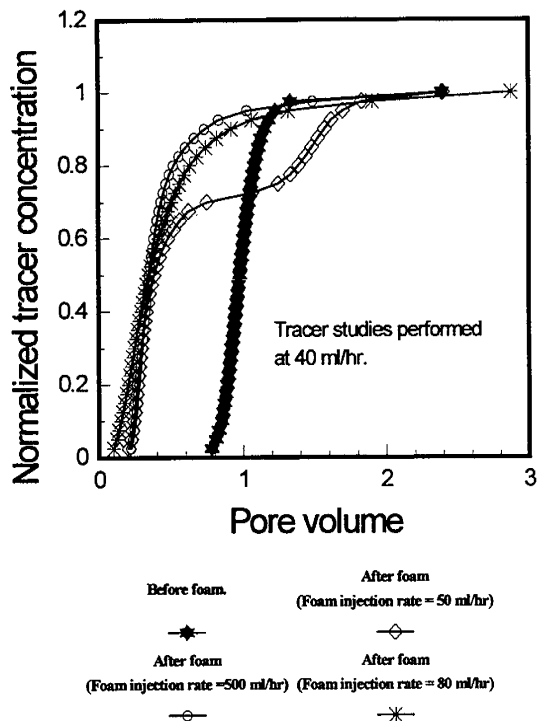


Fig. D-3. Tracer results in the 482-md core, 40 ml/hr.

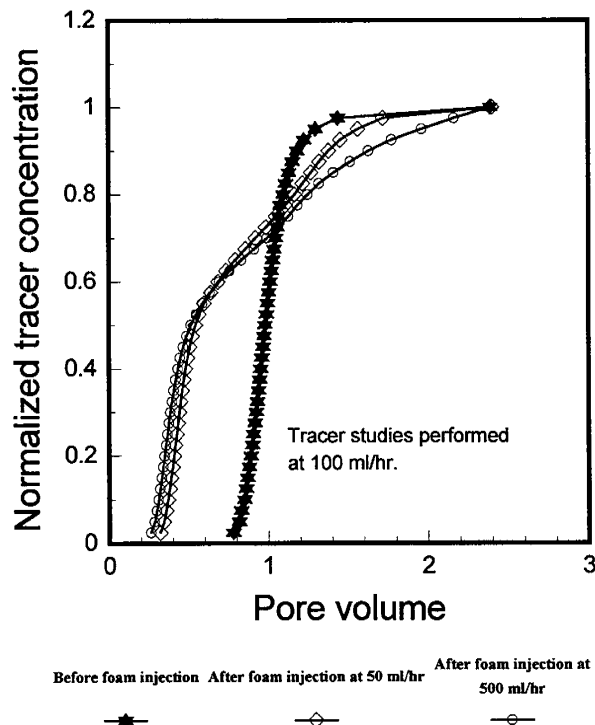


Fig. D-4. Tracer results in the 482-md core, 100 ml/hr.

**Tracer Results in 80-md Rock.** Table D-6 shows results of  $F_{rr}$  measurements in the 80-md core before and during tracer experiments for two foams generated at two different flow rates (50 and 500 ml/hr) at 80% quality.  $F_{rr}$  values after foam generation appeared to have different values for the first set of brine flow rates (1,200 versus 3,000 at  $u = 0.08$  ft/d). When the tracer study was started, the  $F_{rr}$  values were comparable (at a cumulative pore volume of 18.2,  $F_{rr}$  was 11.4 for foam that was generated at 50 ml/hr and 16 for foam that was generated at 500 ml/hr). For foam that was generated at 50 ml/hr, the  $F_{rr}$  values were 4 and 1.8 before performing tracer studies at 100 ml/hr and 200 ml/hr, respectively. After foam was generated at 500 ml/hr, the corresponding  $F_{rr}$  values were 5.3 and 2.2.

Results from several tracer studies in this core are shown in Table D-7. For tracer studies performed at 40 ml/hr, the  $V_p/V_{p0}$  value was almost the same for foams generated at two different flow rates (50 ml/hr and 500 ml/hr). Fig. D-5 illustrates this similarity. The second tracer study was performed after passing about 4 PV of brine at 100 ml/hr through the core in order to measure the residual resistance factor and to restore the basic tracer concentration,  $C_o$ . Results from Table D-6 show that at the cumulative PV of brine injected (just before starting this tracer study, 22.8 PV), comparable residual resistance factors were produced for foams generated at the two different flow rates (i.e.,  $F_{rr}$  values of 4 and 5.3). Fig. D-6 compares tracer studies performed at 100 ml/hr for two different foam generation rates (open circles and open diamonds). For foam generated at 50 ml/hr, the pore volume fraction available for flow increased from 0.23

(which was the  $V_p/V_{po}$  value measured at the tracer flow rate of 40 ml/hr) to 0.31 (the  $V_p/V_{po}$  value measured at the tracer flow rate of 100 ml/hr). The corresponding increase in pore volume for foam generated at 500 ml/hr was from 0.23 to 0.25. The third tracer study was performed at 200 ml/hr (after performing the tracer study at 100 ml/hr). The results are also shown in Fig. D-6 (squares and asterisks). The pore volume available for flow also increased with increased flow rate. This probably occurred because of gas being produced from the core. This result was consistent with our results from the 899- and 482-md cores.

Table D-6.  $F_{rr}$  Values Before and During Tracer Studies in the 80-mdCore

Cumulative PV	q, ml/hr	u, ft/day	$F_{rr}$ after foam generation at 50 ml/hr	$F_{rr}$ after foam generation at 500 ml/hr
0.5	1	0.08	1,200	3,000
1.5	10	0.8	240	308
2.1	20	1.6	200	150
2.7	50	4	54	67
14.5	10	0.8	16.2	36
18.2	50	4	11.4	16
22.8	100	8	4	5.3
27	200	16	1.8	2.2

In the 80-md core, we observed an inconsistent trend for the change in dispersivity ratio  $\alpha/\alpha_0$ . After foam generation at 50 ml/hr,  $\alpha/\alpha_0$  slightly increased (from 33 to 38) when the tracer flow rate was changed from 40 to 100 ml/hr, indicating foam persistence to brine flow. The corresponding  $V_p/V_{po}$  value also slightly increased (from 0.23 to 0.31). In contrast, the dispersivity ratio decreased after performing tracer at a flow rate of 200 ml/hr (from 38 to 12). This change was accompanied by an increase in  $V_p/V_{po}$  value from 0.31 to 0.71.

However, after foam generation at 500 ml/hr and performing tracer studies at the same flow rates as before, different results were observed. The  $\alpha/\alpha_0$  value decreased when the tracer flow rate was changed from 40 to 100 ml/hr (from 30 to 17) with very little change in  $V_p/V_{po}$  value (from 0.23 to 0.25). When the tracer was performed at 200 ml/hr, the dispersivity ratio increased to a value similar to that after tracer result at 40 ml/hr. The  $V_p/V_{po}$  changed from 0.25 to 0.62.

At this point, no specific explanation can be given for this inconsistency. Generally, foam placement was expected to affect the heterogeneity of the core. To understand what was happening during the tracer experiments, more work is needed.

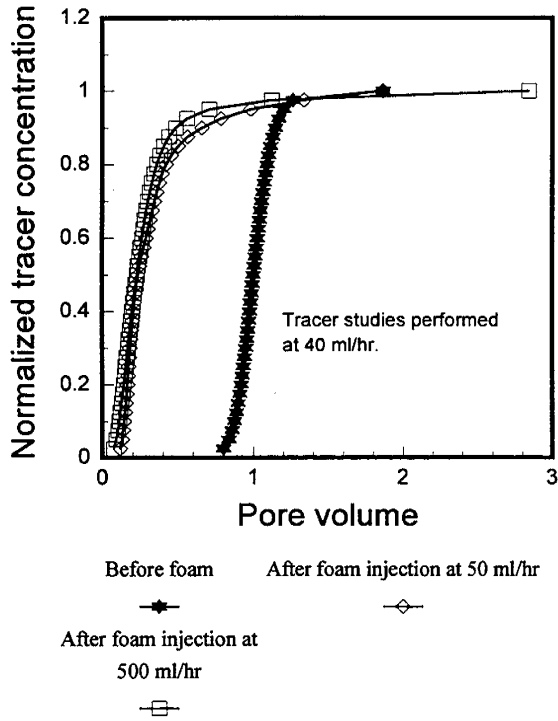


Fig. D-5. Tracer results in the 80-md core, 40 ml/hr.

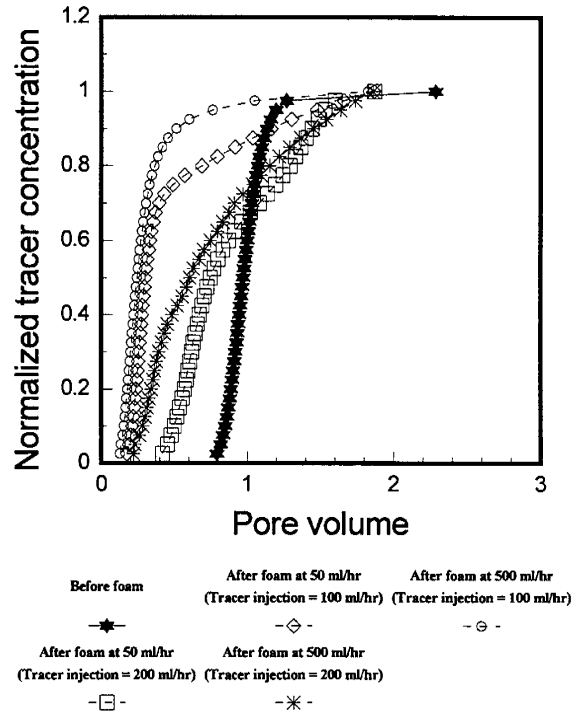


Fig. D-6. Tracer results in the 80-md core, various rates.

Table D-7. Tracer Results in 80-md Core (CORE ID: FLPSS2)

Status	q, ml/hr	$V_p$	$V_p/V_{p0}$	$\alpha$ , cm	$\alpha/\alpha_o$
Before foam.	100	0.974		0.095	
	40	1.001		0.082	
	100	1.052		0.108	
	40	0.992		0.088	
After foam generation at 50 ml/hr	40	0.235	0.23	2.73	33
	100	0.302	0.31	3.69	38
	200	0.748	0.71	1.3	12
After restoring brine mobility	40	0.99		0.083	
	100	0.98		0.102	
After generating foam at 500 ml/hr	40	0.23	0.23	2.53	31
	100	0.246	0.25	1.7	17
	200	0.608	0.62	3.16	31
After restoring brine mobility	100	0.98		0.4	
	200	1.03		0.35	

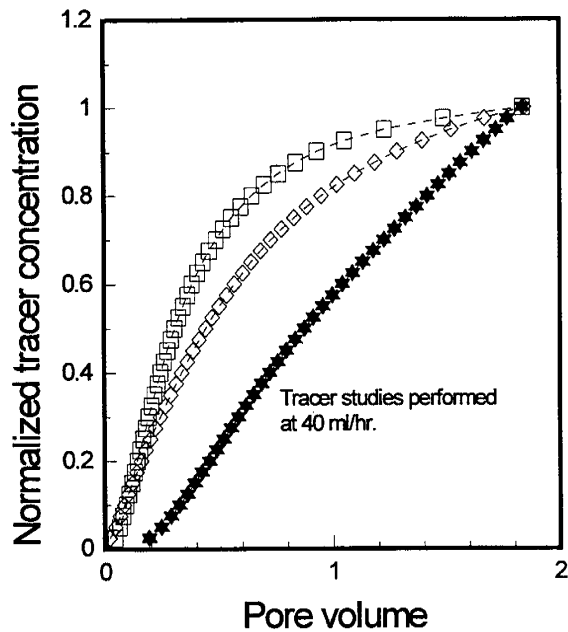
**Tracer Results in 7.5-md Rock.** In the 7.5-md core, water-tracer studies were conducted following the sequence shown in Table D-1. Before foam placement, the tracer dispersivity results for limestone were 30 to 60 times higher than those for sandstone cores. For comparison, a previous report<sup>74</sup> showed the dispersivity of Indiana limestone to be 5 to 10 times higher than that for Berea sandstone cores. Tracer studies were performed after foam generation at 80% quality for two different foam generation rates (50 and 500 ml/hr). Brine was then injected at different flow rates as shown in Table D-1. Before the tracer study at 40 ml/hr, the residual resistance factors were 1.6 for the foam generated at 50 ml/hr and 2.2 for the foam generated at 500 ml/hr. The corresponding pore volumes sampled by the tracer were 0.5 and 0.35, respectively (see Table D-8 and Fig. D-7). Before performing tracer studies at 100 ml/hr, the residual resistance factor was 1.2 for the foam generated at 50 ml/hr and 1.3 for the foam generated at 500 ml/hr. The corresponding pore volumes sampled by the tracer were 0.53 and 0.56, respectively (see Table D-8 and Fig. D-8). This result showed that although the permeability of the core was nearly restored, almost half of the pore volume was still occupied by gas.

Table D-8. Tracer Results in 7.5-md Core  
(Core ID: FLPLS3)

Status	q, ml/hr	V <sub>p</sub>	V <sub>p</sub> /V <sub>po</sub>	α, cm	α/α <sub>o</sub>
Before foam	50	0.874		2.9	
	100	0.887		5.9	
After foam at 50 ml/hr	40	0.442	0.50	9.4	3.2
	100	0.467	0.53	3.7	0.63
After foam at 500 ml/hr	40	0.306	0.35	6.35	2.2
	100	0.5	0.56	5.35	0.9

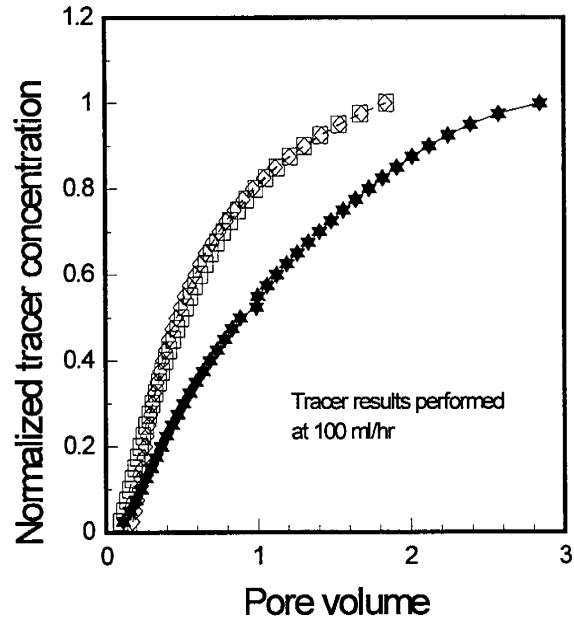
### Discussion of the Tracer Studies

Results illustrated in the previous section indicated that even after injecting approximately 18 PV of surfactant-free brine at low flow rates (1 to 50 ml/hr), the available pore volume for flow remained at a value close to 30% of the original pore volume. Our results were consistent with the tracer results of Holm<sup>65</sup> and Friedmann *et al.*<sup>79</sup>



Before foam. After foam at 50 ml/hr. After foam at 500 ml/hr.  
 -\*-      -◇-      -□-

Fig. D-7. Tracer results in the 7.5-md core, 40 ml/hr.



Before foam After foam at 50 ml/hr After foam at 500 ml/hr  
 -\*-      -◇-      -□-

Fig. D-8. Tracer results in the 7.5-md core, 100 ml/hr.

Other reports in the literature quantified the liquid-phase saturation when foam was flowing at steady state and discussed this phenomenon in view of the concept of limiting capillary pressure.<sup>73</sup> Persoff and co-workers<sup>92</sup> studied flow of foam in Boise sandstone having a permeability of 1.3 darcy. They reported that the liquid-phase saturation remained fixed at about 37% during steady-state foam generation. Kovscek and Radke<sup>93</sup> reported a similar value. They found liquid saturations during steady-state foam flow to be a few units above connate (around 30%). Ettinger and Radke<sup>68</sup> measured the liquid saturation during foam flow using scanning microwave attenuation. In their study, liquid saturations during foam generation were reported to be between 30 and 40%.

Our tracer studies for the 482-md core gave results for water saturations (30% to 40%) that were similar to those reported by Persoff *et al.*<sup>92</sup> and Kovscek and Radke.<sup>93</sup> However, our results for the 80-md and 899-md sandstone cores gave lower  $V_p/V_{po}$  values. This value was about 23% of the core pore volume. This value was comparable to the values reported by Friedmann *et al.*<sup>79</sup> (10% to 25%). Chou<sup>85</sup> reported similar results, with water saturation during foam generation reported to be approximately 18%. Chou concluded that foam was generated during a drainage process, and the water saturation in the presence of foam remained slightly higher than the connate water saturation.

## Implications of Combined Rheology and Tracer Results

A controversial issue in modeling foam flow in porous media emerged from the difficulty in explaining the non-Newtonian behavior of foam flow.<sup>95</sup> The separate effects of apparent viscosity and permeability reduction terms were not specifically addressed in the literature. Kovscek *et al.*<sup>94</sup> suggested that the solution of this issue is important when modeling foam flow. However, Heller and Kuntamukkula<sup>96</sup> criticized this idea. Based on the theoretical expectation and on the experimental evidence, they concluded that the apparent viscosity in a capillary or rotational viscometer with bulk foam would not be appropriate for use in porous media.

One idea that emerged from our experimental observations may shed some light on separating the two terms, apparent viscosity and permeability reduction. At steady-state, it can be assumed that the blocking effect reached its constant, steady limit for all flow rates. This was supported by the tracer results performed after foam was generated at two different flow rates (50 and 500 ml/hr) in each core. After foam placement, the term  $V_p/V_{po}$ , which is an indication of the blocking status of the core, was almost constant in each core (see Tables D-3, D-5, and D-7). In the literature, several researchers showed that the water saturation was in the range from 20% to 30% when the steady state was reached. After generating  $N_2$ -foam at two different flow rates (50 and 500 ml/hr) and injecting brine, similar residual resistance factors were observed in each core (Tables D-2, D-4, and D-6).

Another observation was relevant to the rheological data in the three Berea cores where foam was generated. In each core, we noted that at high velocity, all mobilities (for three different qualities) converged approximately to one value (see Figs. 73 to 75). This result means that the fluid was sheared to a viscosity close to the solvent viscosity. At this limit (assuming the viscosity to be the surfactant solution viscosity), the blocking effect can be quantified. Since this blocking effect is constant (constant permeability) at any other low flow rate, the apparent viscosity of foam can be found by dividing the constant permeability value by the mobility measured at that flow rate.

The data produced in this work will be used to illustrate this idea. The constant mobility value in each Berea core for each foam quality was calculated using the rheological equations given in Table 27. At high shear rate (assumed to be 100 ft/day), where similar values of mobility were obtained, this mobility was averaged for each rock. The average mobility value was used to calculate the average permeability of each core. The viscosity used was 0.67 cp, i.e., the surfactant-solution viscosity at 40°C. The data point for 50% foam quality in the 80-md core was not included because of the poor correlation coefficient (0.86).

At steady state, we assumed that foam flow would occur at the reduced permeability values given in Table D-9. Some experimental reports have suggested a similar mechanism.<sup>97,98</sup> Kolb<sup>97</sup> suggested that during foam flow, a large portion of gas is trapped and a small fraction flows as free gas, following Darcy's law. Bond and Bernard<sup>98</sup> suggested that foam flows as a combination of liquid and gas in a foam body and the liquid flow in porous media following fixed channels that depend solely on the liquid saturation. For each core at a given foam quality, apparent viscosities

were calculated at different velocities, using the averaged permeability value and the equations given in Table 27.

Table D-9. Permeability Reduction During Foam Flow

CORE ID and Permeability	Foam quality	$\lambda_f$ at 100 ft/day, md/cp	$\lambda_{average}$ , md/cp	Average k, md
Core ID: FHPSS4 k = 899 md	50	34.9	34.1	22.8
	80	34.6		
	95	32.9		
Core ID: FHPSS1 k = 482 md	50	10.3	10.0	6.7
	80	10.3		
	95	9.5		
Core ID: FLPSS2 k = 80 md	80	8.1	8.6	5.8
	95	9.1		

Fig. D-9 shows the results for the three foam qualities (50%, 80%, and 95%) studied in the three cores (FHPSS1, FLPSS2, and FHPSS4).

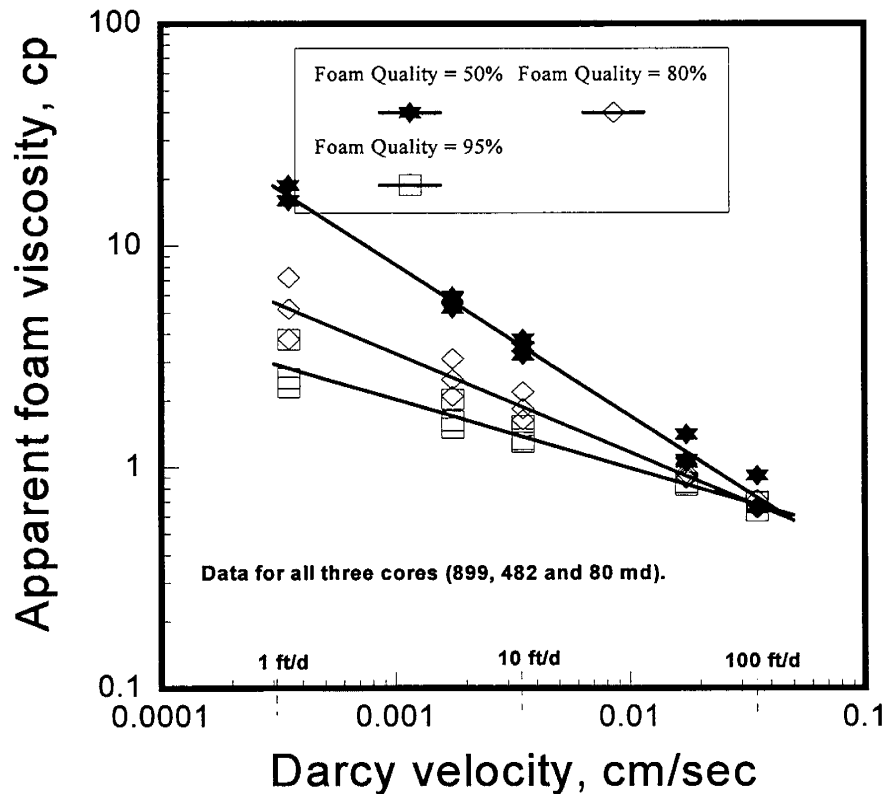


Fig. D-9. Apparent foam viscosity in Berea cores.

At 50% foam quality,

$$\mu_{\text{app}} = 0.074 u^{-0.682} \quad (\text{D-2})$$

and the correlation coefficient was 0.99.

At 80% foam quality,

$$\mu_{\text{app}} = 0.151 u^{-0.455} \quad (\text{D-3})$$

and the correlation coefficient was 0.96.

At 95% foam quality,

$$\mu_{\text{app}} = 0.24 u^{-0.31} \quad (\text{D-4})$$

and the correlation coefficient was 0.96. In the equations,  $\mu_{\text{app}}$  is the apparent viscosity in centipoise and  $u$  is the Darcy velocity in cm/sec.

Eqs. D-2 to D-4 were used to calculate the power-law parameters, i.e., the power-law exponent,  $n$ , and the consistency index,  $K$ . For flow of polymer solutions in porous media, Hirasaki and Pope<sup>99</sup> gave the following expression to calculate the apparent viscosity,

$$\mu_{\text{app}} = H u^{n-1}, \quad (\text{D-5})$$

where  $u$  was the Darcy velocity in consistent units,  $n$  was the power-law exponent, and  $H$  was given by

$$H = (K/12)[(9n+3/n)]^n (150k\phi)^{1-n/2}. \quad (\text{D-6})$$

$K$  was the consistency index, and  $\phi$  was the porosity.

Eqs. D-2 to D-4 together with Eq. D-5 were used to calculate the power-law exponent and the average consistency index for each foam quality. The porosity was assumed to remain constant (since the change in permeability was the same order of magnitude, the porosity was not expected to vary dramatically). Table D-10 lists these results. In Table D-10, the reduced permeability values were taken from Table D-9.

Table D-10. Power-Law Parameters

Permeability before foam, md	Permeability during foam flow, md	$\phi$	Foam quality, %	n	K $\text{cp}/(\text{cm}/\text{sec})^{1-n}$	$K_{\text{avg.}}$
899	22.8	0.235	50	0.318	585	603
482	6.7	0.232			588	
80	5.8	0.185			635	
899	22.8	0.235	80	0.555	52.3	53.2
482	6.7	0.232			52.3	
80	5.8	0.185			55.1	
899	22.8	0.235	95	0.69	14.1	14.3
482	6.7	0.232			14.1	
80	5.8	0.185			14.6	

One advantage of separating the viscosity from the permeability in the mobility term is that the permeability dependence of the shear rate is kept constant at a value of -0.5 (as in the capillary model used for polymeric solutions).

### Conclusions

1. Results from tracer studies and residual resistance factors suggested that the blocking effect provided by nitrogen foams is independent of the flow rate for foam generation.
2. We proposed an idea for separating the apparent viscosity and permeability terms of the mobility of foam.

**APPENDIX E**  
**Supplement to Chapter 7:**  
**The Effect of Shut-In on the Residual Resistance Factor**

This appendix documents a brief study of the effects of a shut-in period on residual resistance factors observed during brine injection after placement of nitrogen foams in three Berea sandstone cores. Much of the background experimental procedures can be found in Chapter 7.

A shut-in period was suggested to provide two potential benefits for fluid diversion applications.<sup>80</sup> First, if foam remains trapped in the high-permeability layer as gas expands and water saturation ( $S_w$ ) decreases, the water relative permeability in that layer can be reduced further. Second, if foam collapses when gas expands (as suggested by the limiting-capillary-pressure model<sup>73</sup>) and collapses faster in the low-permeability layer, then diversion could be enhanced. The data of Zerhboub *et al.*<sup>80</sup> supported the second mechanism.

To study the effect of a shut-in period on residual resistance factor, the following steps were performed: (1) Foam was generated at 80% quality and 500 ml/hr (40 ft/day). (2) The injection of both gas and surfactant was stopped and the core was shut in for 24 hours. (3) After the shut-in period, brine was injected at different flow rates as shown in Table E-1. The percentage change in residual resistance factor (defined as the difference between the  $F_{rr}$  values when no shut-in was applied and those when a shut-in was applied) was calculated in Table E-1. Our results (excluding the first 3 PV, where the trend was not clear) indicated more foam collapsed with decreasing permeability of the core. These results support the results reported by Zerhboub *et al.*,<sup>80</sup> who showed in parallel coreflood experiments that foam collapsed faster in the low-permeability cores.

Table E-1. Shut-In Effect  
(80% quality foam generated at 500 ml/hr, shut in 24 hours)

Cumulative brine PV	u, ft/d	% Change in $F_{rr}$ *		
		Core ID: FLPSS2 k = 80 md	Core ID: FHPSS1 k = 482 md	Core ID: FHPSS4 k = 899 md
0.55	0.08	40	0	88
1.65	0.8	-12.3	4.2	64
2.15	1.6	-37	-31	-19
2.75	4	-27	25	-34
4.75	0.8	73	26	-39
9.75	0.8	73	62.7	-24
14.55	0.8	62	24.7	-6
17.85	4	45	9.6	-18

\* % change in  $F_{rr} = 100(F_{rr1} - F_{rr2})/F_{rr1}$ , where  $F_{rr1}$  was the residual resistance factor when no shut-in was applied, and  $F_{rr2}$  was the residual resistance factor after a 24-hour shut-in period.

## **Conclusion**

After foam generation, applying a shut-in time (for 24 hours) decreased the residual resistance factor. The effect was more pronounced as the rock permeability decreased.

## **APPENDIX F**

### **Technology Transfer**

#### **PROJECT REVIEW MEETINGS**

August 15-16, 1995 in Socorro. 27 people from 11 oil companies in attendance.  
November 10, 1994 in Socorro. 20 people from 10 oil companies in attendance.  
February 8, 1994 in Socorro. 17 people from 9 oil companies in attendance.  
May 19, 1993 in Socorro. 14 people from 8 oil companies in attendance.  
November 5, 1992 in Socorro. 14 people from 8 oil companies in attendance.  
May 21, 1992 in Socorro. 13 people from 7 oil companies in attendance.  
May 13, 1991 in Socorro. 12 people from 7 oil companies in attendance.  
June 4, 1990 in Socorro. 8 people from 6 oil companies in attendance.

#### **ORGANIZATIONS SUPPORTING THE PROJECT**

Arco Exploration and Production Technology Co.,  
British Petroleum Company,  
Chevron Petroleum Technology Co.,  
Conoco Inc.,  
Exxon Production Research Company,  
Marathon Oil Co.,  
Mobil Research and Development Corp.,  
Phillips Petroleum Co. (including Drilling Specialties),  
Texaco Inc.,  
Unocal,  
United States Department of Energy,  
State of New Mexico.

#### **PAPERS RESULTING FROM DOE PROJECTS DE-AC22-92BC14880 AND DE-FG22-89BC14447**

Seright, R.S.: "Use of Gelants Versus Preformed Gels for Conformance Control in Fractured Systems," paper SPE 35351 presented at the 1996 SPE/DOE Symposium on Improved Oil Recovery, Tulsa, April 21-24.

Nimir, H.B. and Seright, R.S.: "Placement Properties of Foams Versus Gelants When Used as Blocking Agents," paper SPE 35172 presented at the 1996 SPE Permian Basin Oil & Gas Recovery Conference, Midland, March 27-29.

Ye, M. and Seright, R.S.: "Gel Placement in Anisotropic Flow Systems," *In Situ* (1996) **20**, No.2.

Seright, R.S.: "Gel Placement in Fractured Systems," *SPE Production & Facilities* (Nov. 1995), 241-248.

Liang, J., Sun, H., Seright, R.S.: "Why Do Gels Reduce Water Permeability More Than Oil Permeability?," *SPE Reservoir Engineering* (Nov. 1995) 282-286.

Seright, R.S.: "Reduction of Gas and Water Permeabilities Using Gels," *SPE Production & Facilities* (May 1995), 103-108.

Seright, R.S. and Liang, J.: "A Comparison of Different Types of Blocking Agents," paper SPE 30120 presented at the 1995 SPE European Formation Damage Control Conference, The Hague, May 15-16.

Seright, R.S. and Liang, J.: "A Survey of Field Applications of Gel Treatments for Water Shutoff," paper SPE 26991 presented at the 1994 SPE Permian Basin Oil & Gas Recovery Conference, Midland, March 16-18.

Liang, J., Lee, R.L., Seright, R.S.: "Placement of Gels in Production Wells," *SPE Production & Facilities* (Nov. 1993) 276-284; *Transactions AIME* **295**.

Seright, R.S.: "Effect of Rock Permeability on Gel Performance in Fluid-Diversion Applications," *In Situ* (1993) **17**, No.4, 363-386.

Seright, R.S., Liang, J., and Sun, H.: "Gel Treatments in Production Wells with Water Coning Problems," *In Situ* (1993) **17**, No.3, 243-272.

Seright, R.S. and Martin, F.D.: "Impact of Gelation pH, Rock Permeability, and Lithology on the Performance of a Monomer-Based Gel," *SPE Reservoir Engineering* (Feb. 1993) 43-50.

Seright, R.S.: "Impact of Permeability and Lithology on Gel Performance," paper SPE 24190 presented at the 1992 SPE/DOE Symposium on Enhanced Oil Recovery, Tulsa, April 22-24.

Sorbie, K.S. and Seright, R.S.: "Gel Placement in Heterogeneous Systems with Crossflow," paper SPE 24192 presented at the 1992 SPE/DOE Symposium on Enhanced Oil Recovery, Tulsa, April 22-24.

Liang, J., Sun, H., Seright, R.S.: "Reduction of Oil and Water Permeabilities Using Gels," paper SPE 24195 presented at the 1992 SPE/DOE Symposium on Enhanced Oil Recovery, Tulsa, April 22-24.

Seright, R.S. and Martin, F.D.: "Effect of  $\text{Cr}^{3+}$  on the Rheology of Xanthan Formulations in Porous Media: Before and After Gelation," *In Situ* (1992) **16**, No.1, 1-16.

Seright, R.S.: "Impact of Dispersion on Gel Placement for Profile Control," *SPE Reservoir Engineering* (Aug. 1991) 343-352.

Seright, R.S.: "Effect of Rheology on Gel Placement," *SPE Reservoir Engineering* (May 1991), 212-218; *Transactions AIME* **291**.

## **PRESENTATIONS (WITHOUT PAPERS)**

**"Cost Effective Methods to Reduce Water Production,"** SPE Distinguished Lecture presented at the following local sections of the Society of Petroleum Engineers (costs paid by the SPE Foundation):

1. New Plymouth, New Zealand, April 15, 1994.
2. Darwin, Australia, April 13, 1994.
3. Perth, Australia, April 12, 1994.
4. Adelaide, Australia, April 8, 1994.
5. Melbourne, Australia, April 7, 1994.
6. Sydney, Australia, April 6, 1994.
7. Brisbane, Australia, April 5, 1994.
8. Roswell, New Mexico, March 22, 1994.
9. Midland, Texas, March 17, 1994.
10. Bakersfield, California, March 10, 1994.
11. Santa Maria, California, March 9, 1994.
12. Edmonton, Alberta, Canada, March 8, 1994.
13. Ponca City, Oklahoma, February 17, 1994.
14. Bartlesville, Oklahoma, February 17, 1994.
15. Grayville, Illinois, February 16, 1994.
16. Pittsburgh, Pennsylvania, February 15, 1994.
17. Traverse City, Michigan, February 14, 1994.
18. Liberal, Kansas, January 21, 1994.
19. Gillette, Wyoming, January 19, 1994.
20. Rock Springs, Wyoming, January 18, 1994.
21. Farmington, New Mexico, January 17, 1994.
22. Beijing, China, November 25, 1993.
23. Jakarta, Indonesia, November 22, 1993.
24. Ahmedabad, India, November 18, 1993.
25. Karachi, Pakistan, November 15, 1993.
26. Muscat, Oman, November 14, 1993.
27. Doha, Qatar, November 10, 1993.

28. Dhahran, Saudi Arabia, November 9, 1993.
29. Cairo, Egypt, November 8, 1993.
30. Lubbock, Texas, October 21, 1993.
31. Mobile, Alabama, October 20, 1993.
32. Shreveport, Louisiana, October 19, 1993.
33. Abilene, Texas, October 18, 1993.
34. Port of Spain, Trinidad, September 27, 1993.
35. Maracaibo, Venezuela, September 22, 1993.
36. Santa Cruz, Bolivia, September 21, 1993.
37. Buenos Aires, Argentina, September 16, 1993.
38. Quito, Ecuador, September 14, 1993.
39. Bogota, Colombia, September 13, 1993.
40. Socorro, New Mexico (NM Tech), September 8, 1993.

### **Other Recent Presentations**

"Water Shutoff: An Overview of Diagnostics and Treatments," presented at the Schlumberger-Doll Research Forum on Reservoir Characterization, Ridgefield, CT, October 16-17, 1995.

"Overview of Successful Technology," presented at the SPE Gulf Coast Section Symposium on Subsurface Fluid Control, Houston, TX, September 12, 1995.

"Overview of Conformance and Sweep Improvement Techniques," presented at the SPE Permian Basin Conformance Control and Sweep Improvement Seminar, Midland, TX, October 26, 1994.

"Challenges of Gel Placement in Oil Recovery," presented at the University of Kansas, Department of Chemical and Petroleum Engineering, Lawrence, KS, September 21, 1994.

"Use of Gels to Reduce Water Production During Oil Recovery," presented at the Lawrence Berkeley Laboratory, Berkeley, CA, December 10, 1993.

"Disproportionate Permeability Reduction by Gels," (Jenn-Tai Liang) presented at the SPE Forum, *Advances in Conformance Control*, Snow Mass, CO, August 11, 1993.

### **PREVIOUS REPORTS FROM DOE PROJECTS DE-AC22-92BC14880 AND DE-FG22-89BC14447**

Seright, R.S.: "Improved Techniques for Fluid Diversion in Oil Recovery Processes," second annual report (DOE/BC/14880-10), Contract No. DE-AC22-92BC14880, U.S. DOE (March, 1995).

Seright, R.S.: "Improved Techniques for Fluid Diversion in Oil Recovery Processes," first annual report (DOE/BC/14880-5), Contract No. DE-AC22-92BC14880, U.S. DOE (Dec., 1993).

Seright, R.S. and Martin, F.D.: "Fluid Diversion and Sweep Improvement with Chemical Gels in Oil Recovery Processes," final report (DOE/BC/14447-15), Contract No. DE-FG22-89BC14447, U.S. DOE (Sept, 1992).

Seright, R.S. and Martin, F.D.: "Fluid Diversion and Sweep Improvement with Chemical Gels in Oil Recovery Processes," second annual report (DOE/BC/14447-10), Contract No. DE-FG22-89BC14447, U.S. DOE (Nov. 1991).

Seright, R.S. and Martin, F.D.: "Fluid Diversion and Sweep Improvement with Chemical Gels in Oil Recovery Processes," first annual report (DOE/BC/14447-8), Contract No. DE-FG22-89BC14447, U.S. DOE (June 1991).



